Vol. 1 No. 1 2010

Wrocław
University
of Technology

Journal of Energy Science

Fundamentals, Applications and Safety

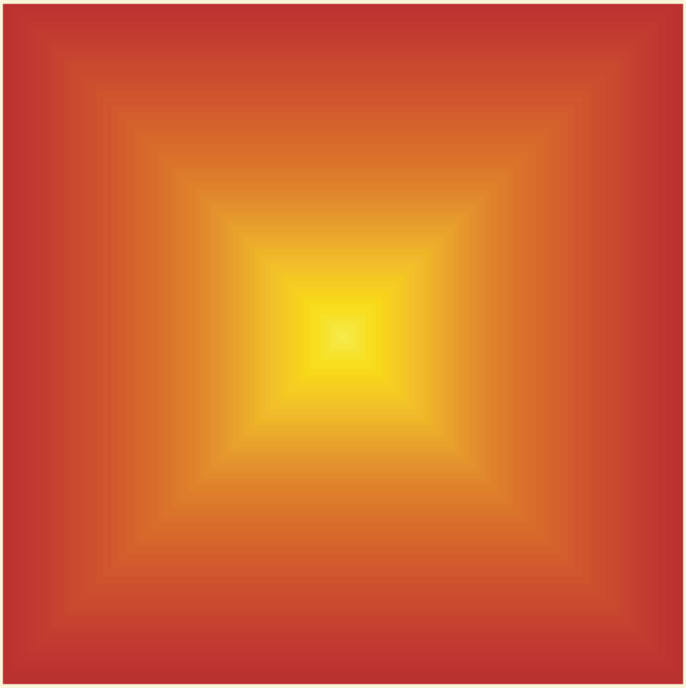

ISSN 1689-8338

Wrocław University of Technology

Journal of
Energy Science

Vol. 1 No. 1 2010

ISSN 1689-8338

Description

Journal of Energy Science is an inter-disciplinary journal published quarterly, devoted to the mechanical, thermal, chemical, electrical and electronic issues of machines, systems and processes related to the various aspects of energy. It serves as a platform for the accumulation and dissemination of pure and applied knowledge arising from theoretical analysis, experiments, and practical experience**. Clean coal energy is a leading problem covered by the journal.** Contributions on fundamental issues, modelling of particular power processes, technical and environmental aspects of coal, nuclear, renewable and other hypothetical energy sources, generation of electric power, and heat transmission, are solicited. The journal is advised by an international board of editors and a pool of highly qualified reviewers.

1. SUBJECT COVERAGE

- Clean coal energy
- Fundamental knowledge about energy
- Combustion and fuels
- Modeling of energy process
- Emission of gaseous and solid pollutions
- Heat engineering and cogeneration
- Optimization of power engineering machines and devices
- Automation and diagnostics of power engineering processes and systems
- Phenomena of flow in energy systems
- Materials for energy systems
- Safety of energy systems
- Energy development – renewable energy (biomasses, solar, wind, hydro power, geothermal, ocean – thermal, wave, flow and ebb), fuel cells system, nuclear fusion systems

EDITOR-IN-CHIEF

SCIENTIFIC SECRETARY

Editorial Committee

International Advisory Board

Editorial office

Andrzej Sitka
Tomasz Tietze

Institute of Heat Engineering and Fluid Mechanics
Wrocław University of Technology
Wybrzeże Wyspiańskiego 27
50-370 Wrocław, Poland
Tel.: 48713202287, 48713204364 fax: 48713204130
energyscience@pwr.wroc.pl

All accept papers are placed on the Web page of the Journal and are available at the web address: www.energyscience.pwr.wroc.pl .

Wrocław University of Technology
Department of Periodics Publications

Contents

Journal of Energy Science, Vol. 1, No. 1, 2010, pp.7-14

The research of the fabric compensators exploitated in power stations

MAREK GAWLIŃSKI, JANUSZ ROGULA

Technical University of Wrocław, Instytut Inżynierii Lotniczej, Procesowej i Maszyn Energetycznych, 50-370 Wroclaw, Poland

A paper presents the test results of the materials for the fabric compensators making easy an estimation of their quality. It was found, that the fabrics characterize themselves with defined rate of anisotropy of the strength properties; this rate diminishes in the course of the compensators exploitation. Second indicator of the materials quality can be the width of the hysteresis loop as well as the stabilization time during fatigue tests. The fabric for the compensators should distinguish itself with narrow hysteresis loop and short time of stabilization of the loop width.

1. Introduction

The fabric compensators are elastic construction (fig.1). They connect the ends of primary and secondary air channels and exhaust gases in chimney systems applied in the power stations. Basic functions of compensator's work are:

- ends of connecting channels displacement compensation,
- during expliatation life to ensure the good tightness level,
- damping of vibrations.

Stresses into fabric compensator follow from their axis (O), perpendicular (P) and angular deformation and static and dynamic load which is produced by pressure of flowing medium.

Work conditions of compensators shows that the material from which compensator is made should mark the proper static and fatigue strength, stiffness and impermeability. Impregnation of fabric is necessary to achieve the proper stiffness and tightness.

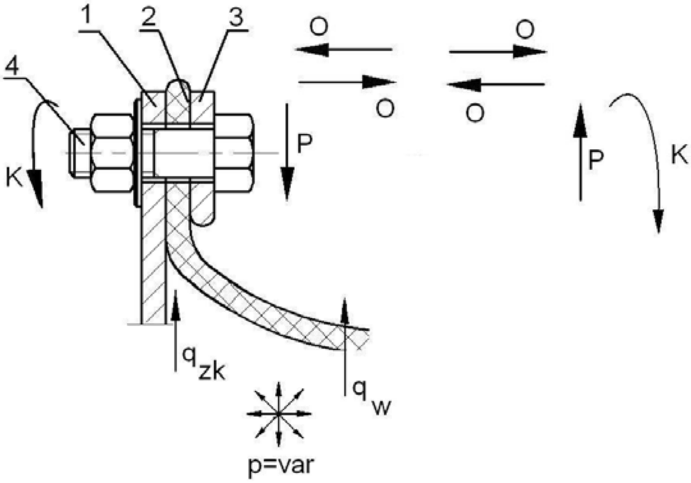

Fig. 1. Fabric compensator installed in the flange, 1 – flange, 2 – compensator, 3 – metal clamp, 4 – bolt, q_w – leakage through the compensator material, q_{zk} - leakage along the flange – compensator interface

2. Static strength determination of compensator materials

Original and exploitated in power station test pieces of materials were examined for tensile strength. One type of tensile specimens were cut along the warp, second type - perpendicular to the warp and third type – at the angle 45^0 to the warp direction of the fibre. From the diagrams of the tensile specimens the following data could be read: maximal force – F_{max} and probe elongation Δl_{max}, mm, unit elongation A_{max}, material strength - R_{max}. The mean values of parameters described above are presented in Table 1 and 2.

Table 1. Mean tensile strength of samples cut along the warp (W) and in perpendicular direction to the warp (P). Original materials

		F_{max} N	**Δl_{max} mm**	**R_{max} MPa**	**A_{max} %**
SW	W	7080	6,1	163	10,2
	P	4540	15,3	105	25,6
B-4	W	7950	7,9	183	13,2
	P	4733	19,4	109	32,3
B-3	W	3077	7,5	110	12,5
	P	1973	8,1	71	13,4

Table 2. Mean tensile strength of probes cut along the warp (W) and in perpendicular direction to the warp (P). Samples made from exploitated compensators.

		F_{max} **N**	**Δl_{max}** **mm**	**R_{max}** **MPa**	**A_{max}** **%**
A-1	W	3140	8,2	76	13,7
	P	2420	11,4	58	19,0
A-2	W	2350	10,2	57,7	16,9
	P	1953	9,9	46,7	16,5
A-3	W	4867	7,7	117,7	13,0
	P	3375	10,9	81,5	18,2
A-5	W	3345	6,7	78	11,1
	P	1700	11,3	39,5	18,8

The sample surface view shows that the layer of artificial material adhered to the fabric cracks on the warp fibres only. They are transmitting the longitudinal load (fig. 2).

On the base of the tensile strength results it was found:

- Original materials of the fabric compensators characterize themselves with anisotropy of strength properties. The anisotropy level in the materials from exploitated compensators is lower than in original ones.
- The highest strength have the materials loaded by force acting in the warp direction of the fabric,
- The plastic coating is cracking along the warp fibres only. During the samples elongation being cut in perpendicular direction to the warp inquires into microcracks of impregnated material on the whole area in points of crossroads fibres of warp and weft. It results from relative elongation which is two-three times bigger in weft direction than in warp direction cut probes.
- Decrease of allowable load value is a result of fatigue and ageing of exploitated materials. It leads to fibres crackings and to the decrease of relative elongation of material.

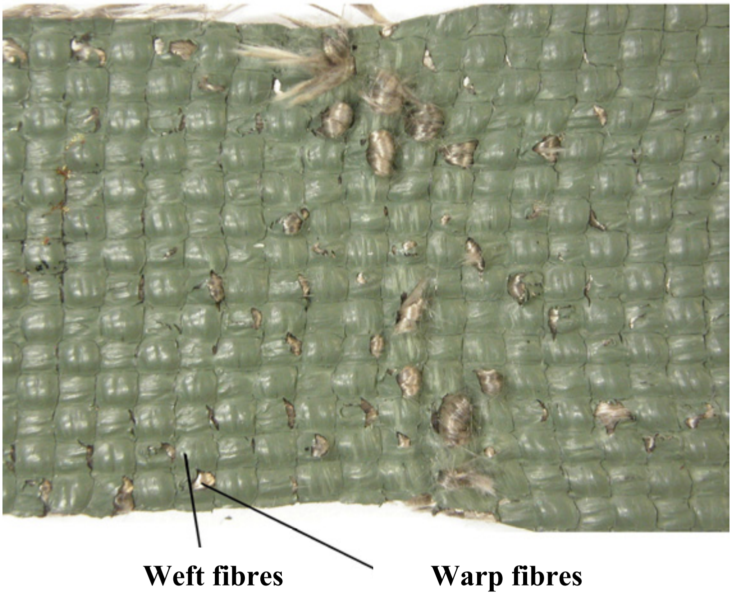

Fig. 2. Topography of microcracks on the surface of the plastic covering the original fabric

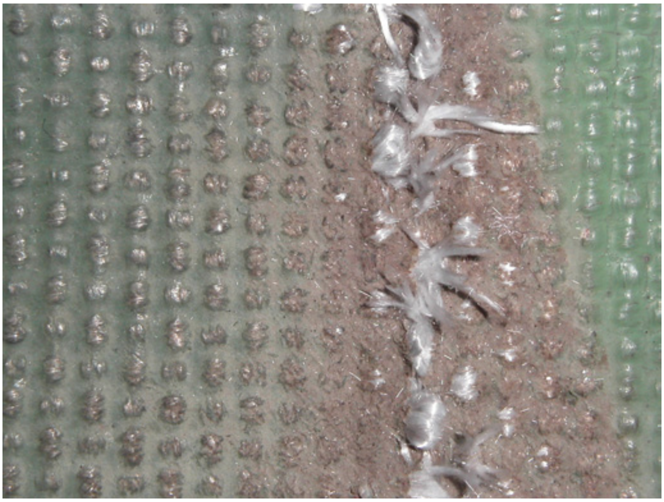

Fig. 3. Topography of microcracks on the plastic covering the sample cut out from the exploitated compensator

3. Fatigue strength determination of compensator material

Transient medium flow through the channels exists during the start up the boilers. It causes the fatigue wear cycles into compensator material. It was decided to determine the fatigue strength of material. The aim of these investigations was to check the material structure degradation which favours leakage through the compensator material after certain number of fatigue cycles. Samples destruction during the fatigue test makes easy measurement of the leakage. One-direction sinusoidal fatigue cycle was assumed (tensile-tensile) around constant minimal force value F_{Zmin} =100 N. Maximal force value F_{Zmax} depended of the compensator material type and direction of samples cutting with respect to the warp fibres. Load frequency was constant and was equal f = 4Hz. The investigations were done on the fatigue test machine MTS 858MINI BIONIX. Force value, elongation of probes, number of load cycles and temperature of samples surface was recorded.

3.1. Results of investigation of original material

Results of fatigue strength of samples which were cut out along the warp fibers and in perpendicular direction to the warp fibres are presented on tables 3 and 4.

Table 3. Fatigue strength of samples cut out along the warp fibres

Nr pr.	**Fz_{min} N**	**Fz_{max} N**	**C_{ZS} %**	**N cycles**	**Remarks/Notes**
W8	100	1600	22,6	3200	Damaged
W9	100	1600	22,6	11565	damaged
W10	100	1600	22,6	6234	Destroyed
W11	100	1600	22,6	17500	no marks of destruction
W7	100	2200	31,1	2000	destroyed
W12	100	3700	52,3	2125	Destroyed

It is characteristic, for probes cut out across the fibers warp, that there are no damages for load ratio $C_{ZS} = Fz_{max} / \overline{F}_{max}$ which amounts to 30% of the average maximal load. During the elongation test, the some of samples were damaged with the same maximal load. It is the result of material high flexibility and deformation ability of material tensioned in the fibres weft direction. Analysis of shape and dimensions of first 10 hysteresis loops for samples cut out in two directions seems to acknowledge this observation. The first loop of hysteresis is the highest for samples cut out in two directions (fig. 4 and 5) because during the first cycle starts the initiation of microcracks on the whole material area. The change of shape and dimensions of the next loops is caused by irreversible damages of fibre.

Table 4. Fatigue strength of samples cut out across the fibers warp

Nr pr.	**Fz_{min} N**	**Fz_{max} N**	**C_{ZS} %**	**N cycles**	**Remarks/Notes**
P1	100	1000	22,0	18500	no marks of destruction
P2	100	1150	25,3	10000	no marks of destruction
P3	100	1400	30,8	6600	destroyed
P5	100	1400	30,8	17500	no marks of destruction
P8	100	2300	50,7	3439	destroyed

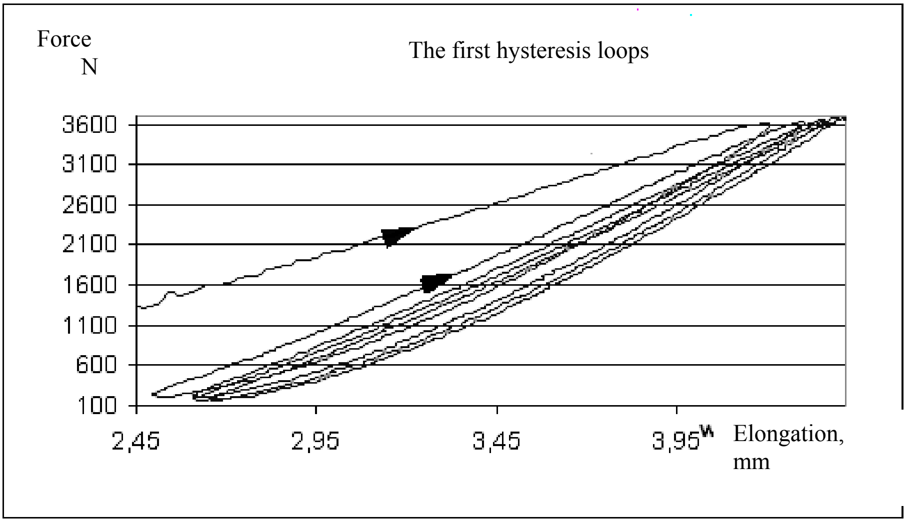

Fig. 4. Variation of the shape and the size of the first hysteresis loops for the sample cut out along the fibers warp

The hysteresis loop (fig. 4) is very fast contracting and stabilising for samples cut out along the fibres warp. Stabilization of 10 loops do not appear for samples cut out across the fibers warp. First four or five loops are very wide. Allocations, friction between warp and weft fibers and microcracs are existing in the material and they have an influence on behaviour of the material tensioned in weft direction only. It was found that the loop length is decreasing with the growth of cycle numbers.

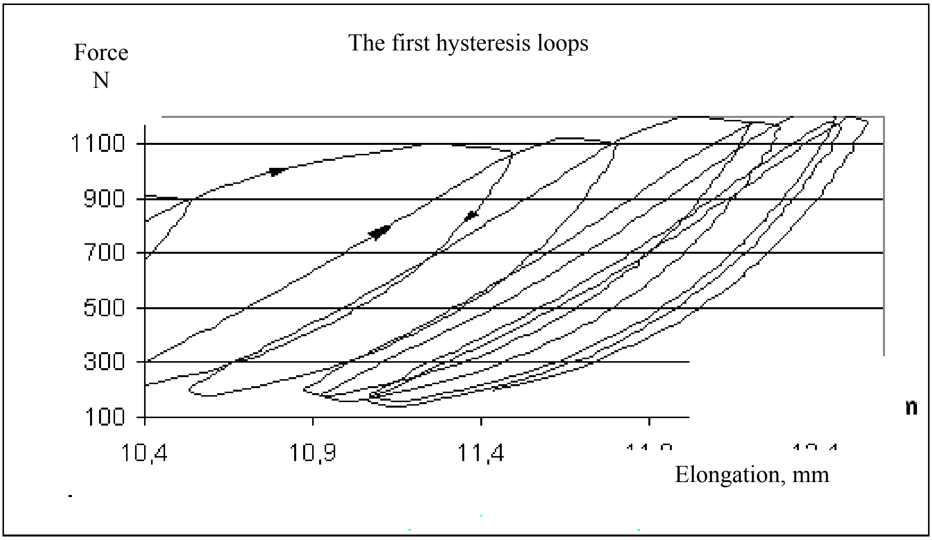

Fig. 5. Variation of the shape and the size of the first hysteresis loops for the sample cut out across the fibers warp

Knowledge of the hysteresis loops enable determination of the elasticity modulus of compensator material according with the fiber direction. Disposing with the adequate number of loops, dependant on the load value, one can conclude about the change of compensator material stiffness, because it is changing with the change of elasticity modulus.

Elasticity modulus of samples cut out along the warp fibers of material SW is equal up to 245 MPa, for samples cut out in opposite direction - 40 MPa. Sudden decrease of elasticity modulus means that, the sample will be damaged after small number of load cycles.

It was generally concluded that hysteresis loops recorded in the first periods of sample loading are adequate parameter of their properties. When the hysteresis loops are wider, and the change of their width necessitates more time of internal friction and more intensive run of the process of the material structure degradation is visible.

3.2. Thermovisional investigation of compensator material

Research of compensator material temperature field was carried out by thermovision camera Therma CAM^{TM} 575. It was possible to record the minimum and maximum temperature values. Thermovision method can help to determine the state of compensator material. Thermogram of sample where the material structure is locally damaged is showed on the fig. 6. The thermogram was made during the fatigue test.

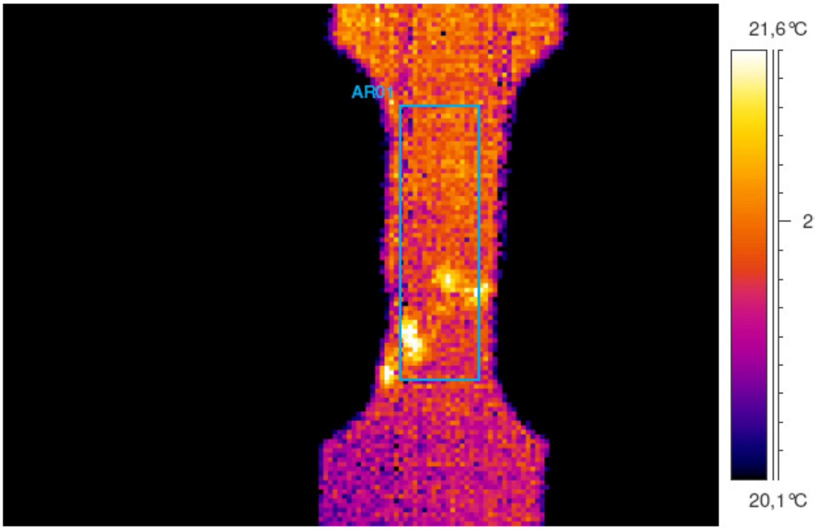

Fig. 6. Thermogram of the heated sample during the fatigue test. The light places indicate the local damages of the sample surface

4. Conclusions

The research of compensator material could be summarized as follows:

1. impregnated materials characterize the anisotrophy of strength. It means, their static and fatigue strength depends on the direction of material load. They have various elasticity modulus value too. The highest strength value of material is then when the load acts along the warp fibres. The designer should remember about the material anisotropy during the manufacturing the fiber compensator,
2. hysteresis can be regarded as quality parameter of the fabric,
3. the leakage is the second quality parameter. Proper tightness level could be achieved when the material is not covered with microcracks and delamination.
4. thermovision should be used to verify the state of compensator material. It is very sensitive method to look for the places of structure defect in the material.

Journal of Energy Science, Vol. 1, No. 1, 2010, pp.15-28

Hydrogen as a fuel and as a coolant - from the superconductivity perspective

BARTŁOMIEJ A. GŁOWACKI[1,2*], W.J. NUTTALL[3]

[1]Department of Materials Science and Metallurgy, University of Cambridge,
Pembroke Street, Cambridge CB2 3QZ, UK
[2]Institute of Power Engineering, ul Augustówka 36, 02-981 Warsaw, Poland
[3] Cambridge Judge Business School, Trumpington Street CB2 1AG, UK

Superconductors have a great potential in the future development of transportation and energy supply applications. Although MgB_2 superconductors that operate at liquid hydrogen temperatures are not yet commercially available, research indicates that these will be feasible in the future. Novel concepts for transportation and energy supply that would be possible using medium-temperature MgB_2 superconductors include the non-polluting 'cryoplane', a self-contained full electric superconducting ship, and cheaper superconducting MgB_2 magnets for the fusion, small energy storage and possibly magnetic resonance imaging (MRI) systems. Superconducting conductors based on magnesium borides have been developed in Cambridge that can be fabricated into cables for power transport with minimal losses. Development of liquid hydrogen cooled MgB_2 superconducting DC cables are also under consideration. Hydrogen used as a coolant, as well as an energy carrier, may spin off new research and developments in superconducting materials and efficient energy use.

1. Introduction

Crude oil prices are rising as stability in the Middle East continues to be elusive. There are fears that energy policy may be heading towards a situation not unlike the dark days of the early 1970s. Back then, nuclear power implied a more reliable and sustainable hope for the future. Recent thinking suggests making use of the unique combination of properties presented by hydrogen, allowing it to serve as both a source of energy and cryogenic medium and provide a modern solution to demanding energy and environmental

---

[*] Corresponding author, e-mail: *bag10@cam.ac.uk or Bartlomiej.glowacki@ien.com.pl*

requirements. The concept "hydrogen as a fuel and hydrogen as a coolant" is fundamental to many applications that fully exploit the various properties of hydrogen, including: nuclear fusion, the cryoplane, energy storage, the electric ship and even magnetic resonance imaging (MRI) magnets. Each of these technologies can operate independently of a wide-scale power distribution network and can be visualised as 'hydrogen-islands'. In this paper nuclear fusion and the cryoplane are highlighted as examples of the implementation of hydrogen technology. The cost-effective, reliable and environmentally benign generation of hydrogen is crucial to successful realisation of these applications. Novel hydrogen generation technologies under intensive development offer new routes to fulfilling these requirements [1].

One of the superconducting materials which can be used successfully in conjunction with hydrogen technology is a magnesium diboride, MgB2, in the form of the powder-in-tube

conductors (see Fig.1) developed originally by the Applied Superconductivity and Cryoscience Group in Cambridge, UK [2,3].

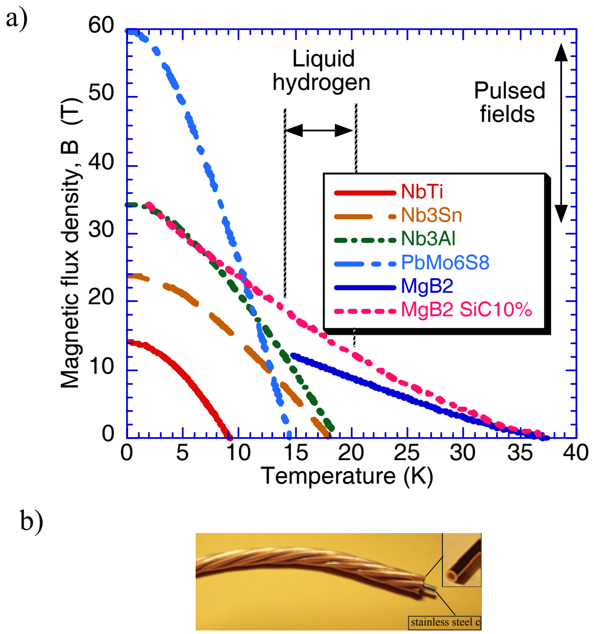

Fig.1 MgB_2 conductors: a) comparison upper critical flux density B_{c2} versus temperature of Nb-based conductors [4] and MgB_2; b) twisted multifilamentary Cu/CuMgB2 with the internal reinforcement can be viable solution [3]

2. Fusion and the Hydrogen Economy

Demand for hydrogen is growing every year. For example in the US the actual mass growth rate is predicted to increase dramatically from n = 2 to n = 6, see Fig.2.

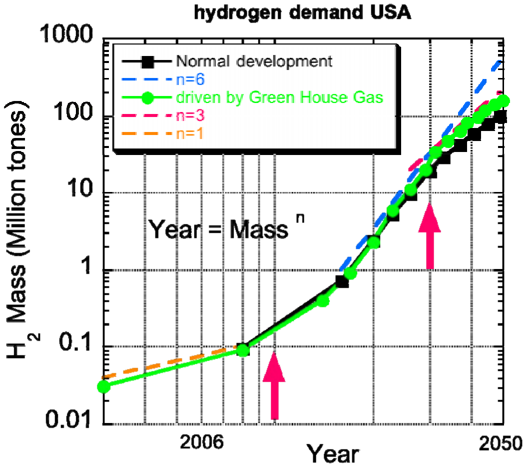

Fig.2 Predicted mass production demanded by the US economy versus time. It is evident that the differences for two scenarios: normal development and demand driven by green-house gas are almost identical until 2050. The n value of the calculated time = mass^n may increase from n = 2 to n = 6 over next ten years

A recent study of the applicability of a 1 GW class hybrid energy transfer line of hydrogen and electricity, has been conducted by Yamada at al. [5] as presented in Fig.3. Current plans are based on a high temperature fission reactor to produce H_2, nearby liquefaction, and transfer of LH_2 by a superconducting DC cable made of MgB_2 through the shipping Mutsu-Ogawara port for wide spread distribution. The target distance of the hybrid energy transfer line is 1000 km. A hydrogen refrigeration station is placed every 10 km of the unit section. The rated current and maximum voltage of the DC power line are 10 kA and 100 kV, respectively. Capacity of the liquid hydrogen transportation is 100 tons per day where a typical hydrogen LH_2 plant delivers 3 tonnes/day. However in the above case a fission reactor was considered as the driver for the hydrogen production process, but we will present the reasons why fusion can benefit from liquid hydrogen since in the future co-generation of H_2 could be driven by a fusion [6-8].

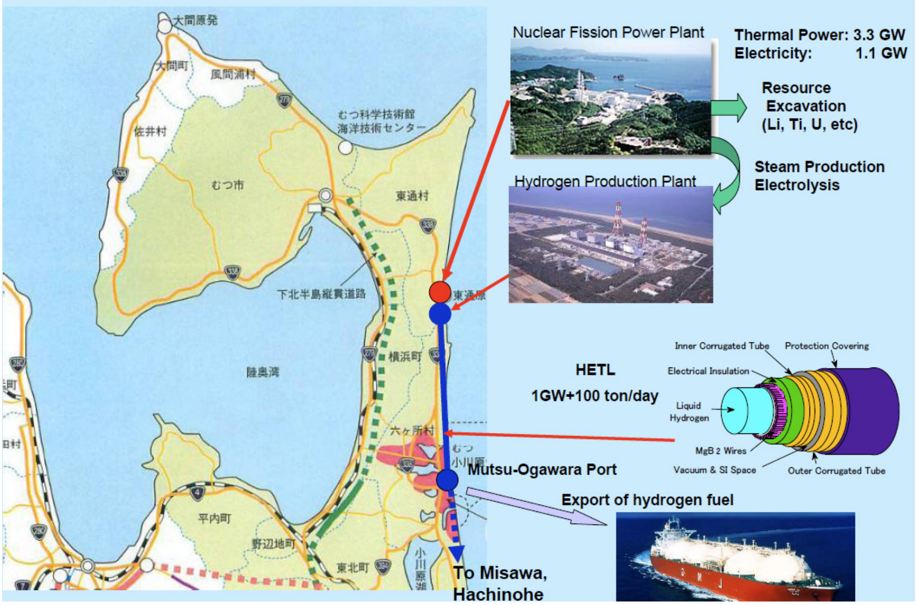

Fig. 3 Schematic representation of the hydrogen generation, liquefaction, transfer and distribution using fission, liquefaction, DC 1GW MgB_2 superconducting cable and H_2 sea tankers distribution; (picture published as a courtesy of Yamada at al [5](all rights reserved)

General Atomics in San Diego first linked nuclear fusion to the possibility of hydrogen production for a 'hydrogen economy'. The term hydrogen economy refers to hydrogen as the dominant energy carrier in our future industrial and commercial economy. At present our main energy carriers are fossil fuels and electricity. Of these, the former is economically storable, while the latter is not an energy resource (or fuel) but merely a pure energy carrier. The hydrogen economy would rely on manufactured hydrogen (here there is a similarity to electricity) yielding a fluid energy product that could be transported and stored relatively straightforwardly (in a manner similar to petrol). Currently there is much discussion of global warming and the need to minimise the release of carbon dioxide from fossil fuel combustion into the atmosphere. Hydrogen on the other hand can release its energy by combustion (or more efficiently in an electrochemical fuel cell) without releasing any carbon dioxide. In order for hydrogen to be a truly environmentally benign energy carrier it will be important to produce the hydrogen in a clean way without the combustion of fossil fuels. Several clean options are available, but General Atomics of San Diego have highlighted the efficiency benefits arising from the direct thermochemical production of hydrogen using high temperature catalytic reactions such as the sulfur-iodine cycle. This method does not rely on wasteful intermediation using electricity for electrolysis, but does require high temperatures above 750°C. Conventional approaches to fusion dedicated to electricity production plan for fusion blanket temperatures (where steam or hot helium would be produced to drive thermal turbines) of around 500°C. If, however, the incentives were sufficient fusion designs could surely be shifted into the 750°-1000°C range. Fusion systems operate at very low pressures despite the high temperatures involved and design are possible with few mechanical moving parts in the system.

Importantly environmental factors are not the only policy-driver for the hydrogen economy. Over the timescale of the development of fusion energy systems energy security issues are likely to motivate a shift towards both hydrogen and fusion. These technologies combine local control of the system with the collaborative research interests of the major energy users in the global economy [9].

2.1. Hydrogen as a Cryogen for Fusion

The thermochemical fusion hydrogen generator described above would produce large amounts of hydrogen requiring safe storage ready for transport to regional and global markets. It seems likely that the energy density benefits of cryogenic hydrogen storage would outweigh the higher costs of compressed gas storage. A radical breakthrough in our thinking is that this existing cryogenic hydrogen reservoir might permit the operation of the superconducting magnets needed to maintain the magnetic 'Tokamak' confinement of the fusion plasma, Fig.4a). Conventionally fusion systems are designed to use niobium titanium and niobium-tin superconducting magnet windings cooled, at great cost, with liquid helium. Our vision is for magnet windings of magnesium-diboride, MgB_2 cooled most likely indirectly by liquid hydrogen using close cycle helium has exchanging heat with hydrogen bath. The liquid boiling temperature of hydrogen is 20 K under normal pressure. Magnesium diboride has the pleasing property that despite being relatively high-temperature superconductor it is also straightforward (with the right know-how) to produce real flexible wires for magnet windings. It is expected that a full-scale fusion reactor will require fields of approximately 8T in the heart of the plasma. It a conventional tokamak geometry this corresponds to a field of 10 T at the windings themselves. With a critical current density of 10^5-10^6 A/m^2 in magnetic field of 10T, MgB_2 is well suited to the electromagnetic requirements of future fusion containment.

Moving to hydrogen based fusion cryogenics may raise some moderate safety concerns and the need to ensure that flammable hydrogen is at all times safely isolated from any liquid oxygen or liquid air, such as might condense on exposed cold metal surfaces. But if there is to be a hydrogen economy using cryogenic systems these problems will already have been easily dealt with.

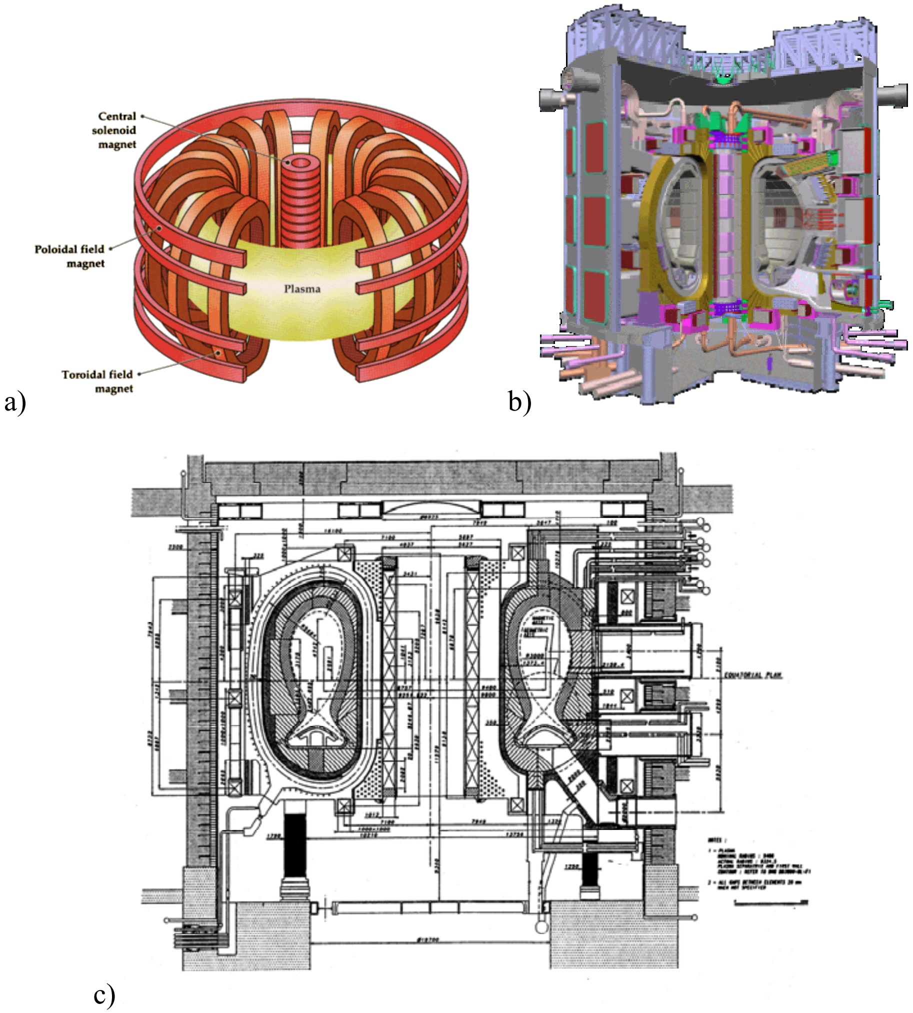

Fig.4: a) Cross-Section of a Tokomak Reactor; b) ITER (fusion power 500 MW, 400 s); c) reactor (DEMO) (fusion power 2000 MW, stationary). The magnetic field generated by the superconducting coils is stronger towards the centre, causing the plasma to tend towards the outer wall. However, another magnetic field generated by a current going through the plasma itself combines with the coils' magnetic field to create magnetic lines that spiral around the torus. This spiralling counteracts the drifting effect on the plasma because of the strong inner field, and effectively traps the plasma. Image courtesy of the Lawrence Livermore National Laboratory; [10]

Table 1 Fusion Devices and Parameters, Fig.2

Parameters	ITER Fig b)	Power Reactor Fig c)
relative size	1	1…1.2
fusion power (MW)	500	2000
power to He-ions (MW)	100	400
total thermal power (MW)		2600
electric power (MW)		1000
efficiency (%)		38
neutron damage (dpa)	5	120 in 5y

It is projected that DEMO fusion reactor presented in Fig.3c) and future concept reactors will require an alternative approach where medium temperature and high temperature superconductors will be used to provide high magnetic induction at elevated cryogenic temperatures [11]. Some of the high temperature superconductors, due to their specific temperature-dependent magnetic properties can be used effectively at LH_2 (20K) or LNe (25K) temperatures. For example a preliminary design of a DEMO, CICC, made with Bi2212 round strands and operating at 20 K and 13 T leads to a value of J_{cable} not very different from a Nb_3Sn CICC cable in the range of 54 A mm^{-2} [10].

Indicative early stage design directives of the future DEMO fusion reactor require toroidal and poloidal electromagnets to be made respectively from $YBa_2Cu_3O_7$ and also MgB_2 conductors enabling reaching a desired magnetic flux density of 20 Tesla for plasma confinement. Especially for large installations a predicted shortage of He and already increased price of helium brings necessity of development of new cooling systems. Little attention has been paid to the hydrogen option, since direct liquid hydrogen cooling would be very challenging. However, by adapting the already-established concept of an intermediate low-loss helium loop, the substantial benefits of using 20K cooling could be harnessed without encountering the direct safety impacts of hydrogen [12,13]. As a coolant, 20K (or possibly 15K) helium gas will have different characteristics than a boiling cryogen. There will be no critical heat flux issue but local heat transfer coefficients may be lower. If micro-channels are engineered into the system substrates then good thermal coupling could be achieved, perhaps surpassing the performance of conventional liquid helium cooling. The technology implications of helium-cooled indirect hydrogen (i-LH_2) versus direct helium and nitrogen cooling are compared and discussed and research needs are identified [13].

Economical calculations of cooling efficiency of the large electromagnetic non-superconducting device conducted by McDonald at. al [14] for LHe, LH_2 and LN_2 shown very clearly that cooling by helium or neon is 70 times and 100 times more expensive than indirect cooling by LH_2, see Fig. 5. Taking to account price of 1l of LH_2 (\$ 0.79), LHe (\$4.74) and Ne (\$ 237) and the fact that hydrogen is the only element that is also an energy carrier, the choice of LH_2 as a cryogenic cooling medium is apparent.

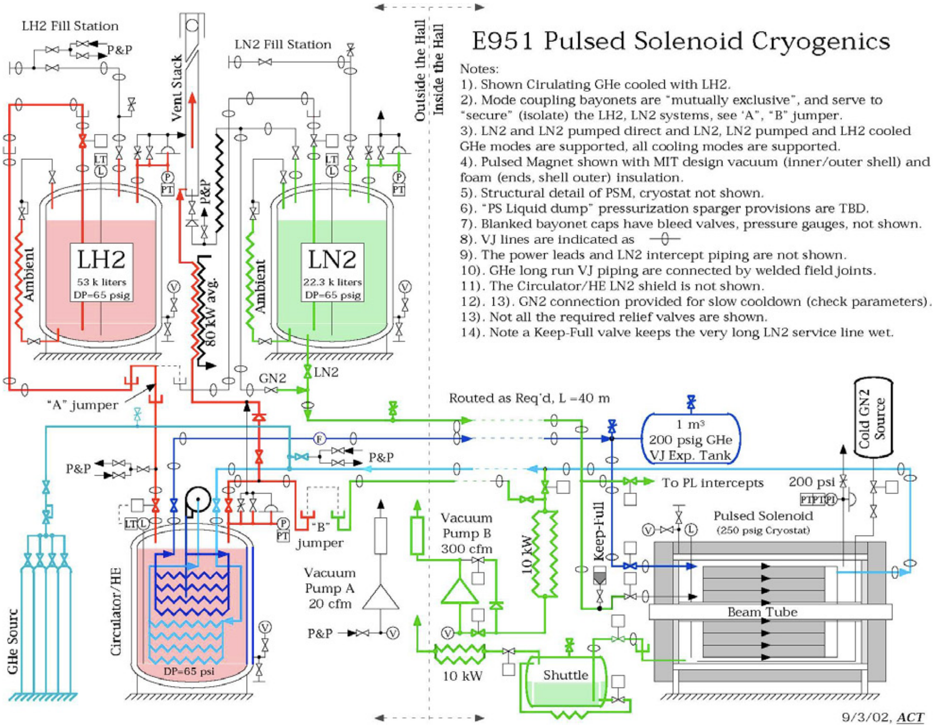

Notes:
1). Shown Cirulating GHe cooled with LH2.
2). Mode coupling bayonets are "mutually exclusive", and serve to "secure" (isolate) the LH2, LN2 systems, see 'A", "B" jumper.
3). LN2 and LN2 pumped direct and LN2, LN2 pumped and LH2 cooled GHe modes are supported, all cooling modes are supported.
4). Pulsed Magnet shown with MIT design vacuum (inner/outer shell) and foam (ends, shell outer) insulation.
5). Structural detail of PSM, cryostat not shown.
6). "PS Liquid dump" pressurization sparger provisions are TBD.
7). Blanked bayonet caps have bleed valves, pressure gauges, not shown.
8). VJ lines are indicated as —0—
9). The power leads and LN2 intercept piping are not shown.
10). GHe long run VJ piping are connected by welded field joints.
11). The Circulator/HE LN2 shield is not shown.
12). 13). GN2 connection provided for slow cooldown (check parameters).
13). Not all the required relief valves are shown.
14). Note a Keep-Full valve keeps the very long LN2 service line wet.

Fig. 5 Piping and instrument diagram for the proposed cryogenic system to operate a 15-T pulsed, copper solenoid magnet at 30 K cooled indirectly by liquid hydrogen (courtesy of the McDonald at al [14])

2.2 Black-Starting the fusion energy system

Conventional plans for fusion energy involve electricity at two levels. First, and obviously, as the product produced for sale; second, however, one must not forget that a fusion power plant will require substantial electrical energy to fire up.

To first impression one might regard this reality as a major argument in favour of fusion's role in an integrated energy system, but upon further reflection this becomes far less clear. For instance a fusion power plant contributing 2.5GWe to the English and Welsh electricity grid (with its overburdened interconnectors to other systems) could be providing several percentage points of total demand at a time of a very low capacity surplus in the system. If, for any reason, the fusion power station were to trip out, then the grids supply-demand balance could be very hard to maintain. The system operator would call upon various open cycle gas turbine systems and pumped water storage systems to cover the shortfall as the coal fired plant at the margin increased its contribution towards maximum levels. If the fusion power plant operators were to call the system operator asking for an extra 200 MWe to restart their machine, it is far from clear that they would receive a positive response. Chances are that they would be asked to wait until the crisis (of their causing) had passed. In our scenario of fusion for hydrogen, the Fusion Island would be supported by its own dedicated large-scale hydrogen gas turbine and/or hydrogen fuel cell park. The capacity of the park would be determined as part of an integrated black-start capacity for the machine which might also involve energy storage flywheels (as used a present on the JET machine for roughly have its start-up power needs) and possibly supercapacitors for the peak of the big electrical push needed for start-up. In normal operations the Fusion Island has a range of on-site temperatures spanning from 20K to more than 800 K [15]. As hydrogen fuel cells require elevated temperatures in order to operate, it is conceivable that there might be benefit in integrating the fuel cell system into the fusion heat extraction system or even the fusion blanket itself. Even if the system were truly cold and dark, the plant could combust stored hydrogen sufficient to warm the hydrogen fuel cells sufficient for their operation.

2.3. The fusion island and big business

After much wrangling an international consortium has started to build an experimental fusion reactor to be known as 'ITER' at Cadarache in Southern France, Fig.4b). It seems unlikely however that a risk averse liberalised and competitive electricity industry will be keen to invest the large sums necessary to construct prototype and early commercial fusion power plants for electricity. Their nervousness would also include a fear that early fusion power plants might suffer from poor operational reliability and suffer from intermittency. As electricity is not an economically storable commodity and supply contracts involve stiff penalties for failure to generate, any such reliability failings could be very expensive indeed. If as we have argued here and previously, early fusion energy systems are dedicated to thermochemical hydrogen production and serving the needs of the transport sector then intermittency is not a concern as hydrogen storage is an integral part of the system and supply-chain. Furthermore hydrogen as an energy carrier has the possibility of becoming the dominant fluid energy product sold by the oil majors once oil becomes depleted later this century.

Three independent timescales are likely to coincide, much to the possible benefit of the *Fusion Island* concept.

- First, as we have already mentioned, over the coming decades oil resources and reserves will diminish and probably be sourced from fewer regions at ever increasing prices
- Second, and at a similar pace, climate change caused by fossil fuel emissions will increase and as environmental harm increases pressure will increase to replace oil and natural gas with a clean alternative. Demand for hydrogen will grow.
- Third fusion energy systems will become ready for commercial deployment over the same period.

Such considerations lead one naturally to consider that the source of private capital for the development of *Fusion Island* systems should come from the oil majors. These companies must transition from being oil companies to become energy companies. Thermochemical hydrogen production from fusion requires many of the skills and competencies already possessed by the oil majors. Importantly these companies retain an adventurous culture of 'exploration' and risk taking well suited to developing a difficult high-stakes technology such as fusion.

In Conclusion we put forward the idea that a *Fusion Island* [15] dedicated to hydrogen production can be achieved entirely independently of the electricity system. Such a system would be relatively simple and efficient relying on Magnesium Diboride superconductors.

Cryogenic liquid hydrogen and high-temperature gaseous hydrogen would serve a range of useful functions within the system and the whole endeavour would be well suited to the competencies, needs and investment preferences of the major oil companies.

2.4. Cryoplane

Air traffic's growing by ~5% every year - there's never been a better time for a clean aircraft. If it gets off the ground, the Cryoplane concept passenger plane [16] will run on liquid hydrogen, leaving a vapour trail of pure water. The actual clean efficiency will be achieved at the height of less than 10 km. At the altitude below 10km, the gaseous products of hydrogen combustion produce a much weaker long-term effect than those of kerosene see Table 2.

Table 2. Relative influence of gaseous combustion products on the greenhouse effect. (Normal cruising altitude for commercial jet traffic) [16]

Altitude	kerosene	hydrogen
15km	175%	275%
12km	107%	84%
10km	88%	6%
5km	100%	1%

Burning 1kg of kerosene produces 3.16 kg of CO_2 and 1.25 kg H_2O. Since 0.36 kg of hydrogen has the same energy content as 1 kg of kerosene, the combustion of 0.36 kg of kerosene will form 3.21 kg of H_2O.

Carbon dioxide is a very long-lived greenhouse gas (residence time ~100 years. Its effect is independent of the altitude. Water vapour is also a greenhouse gas. Its effect increases rapidly with the altitude; the residence time also varies greatly with altitude (several days above ground; six months in the lower stratosphere). If sufficient fuel is to be carried, liquid hydrogen at 20K is needed Fig.6.. Liquid hydrogen has a greater energy density than conventional aviation fuel kerosene.

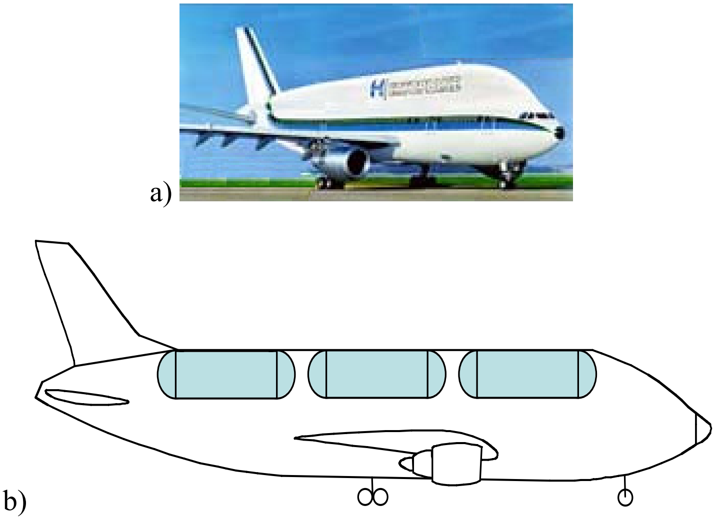

Fig.6 Cryoplane: a) an artist impression of the Cryoplane; b) schematic of the location of the H_2 cryotanks in the Cryoplane aircraft structure [16]

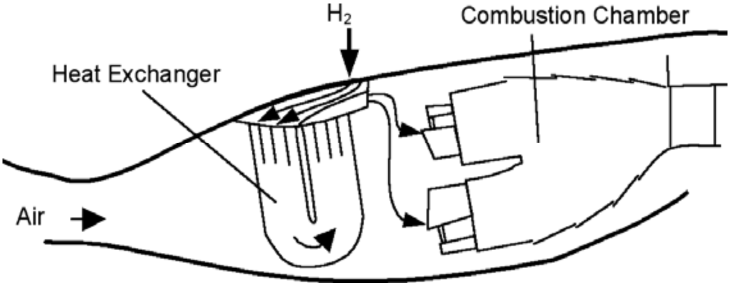

Fig.7 The hydrogen airplane engine. The heat exchange converts the liquid hydrogen to a gas before injection into the combustion chamber [16]

An optimised combustion chamber designed for hydrogen will have favourable properties in comparison to conventional engines. Because hydrogen will be used as a evaporated gas, it mixes well with air during combustion (i.e. 'hot spots'); combustion is possible with a large air surplus (low temperatures) and very high rate of combustion (short dwell times); hence the combustion chamber can be shortened considerably, Fig.7.

A separate issue is a noise pollution created by the aircraft during take off and landing. In a radical departure from current configurations, it has been decided between engine manufacturer Rolls-Royce and the Cambridge-MIT Institute's that in the design for the *Silent Aircraft*, the engines will not hang below the wings, Fig.8 [15]. The project team has decided that the engines will be embedded into the body of the aircraft itself to help minimise the engine noise transmitted to the ground.

Fig.8 a) Artist impression of the 'scilent plane'during landing; b) Simulation of the reduction of sound propagation from the engines mounted on the top of the plane. Pictures courtesy of Cambridge MIT Institute [17]

By managing airflow over the wing and into the engine a much more efficient and quieter propulsion system will be produced. Such integration would be advantageous for the Cryoplane in terms of a hydrogen delivery system. It was found that during take-off the total exhaust area must be about three times as large as that of today's conventional jet engines in order to achieve this balance. During landing the engines of the airplane will throttled back to reduce speed of the aircraft permitting later deployment of under carriage and shorter runways.

3. Conclusions

It can be expected that restrictions of the fossil fuel consumption will force rapid development of such cryoplanes including safety and crash tests. It has to be emphasised that liquid hydrogen offers the advantage of a high vaporization rate compared with liquid natural gas. Hydrogen has a low flash point, and the detonation limit is reached only at much richer mixtures. In a crash no fire carpet can develop; the hydrogen will burn in an upward direction. The burn will progress very rapidly with very little radiation of heat. Thus, the aluminium airframe will not burn but rather protect the passengers and ensure their survival.

The new basic technologies for the production, liquefaction, storage and distribution of hydrogen have to be further developed where production of LH_2 would have to increase from less than currently 20 tons per day to 6000 tons. If the hydrogen were to be generated by electrolysis, it would require the electrical energy output of ten large power plants.

Considering fact that 20 K cryogen and there is a current trend to move away from high frequency electric system (400Hz) on the board of the aircraft and replace it with a DC current devices; these automatically will introduce a number of superconducting applications such as: DC conductors, ultra fast super computers, superconducting DC fault current limiters, also superconducting microwave communication and many other undeveloped superconducting applications. It is also important that recently invented designs of the a fully superconducting bearings [18] will be adopted in the combustion engines since heat exchanges converting liquid hydrogen to gas in the hydro-engines will be introduced.

We suggest that the technological opportunities arising from hydrogen as a fuel and as a coolant could be of a great importance in a range of sectors.

ACKNOWLEDGEMENTS

The authors wish to acknowledge EPSRC SUPERGEN EP/G01244X/1 http://gow.epsrc.ac.uk/ViewGrant.aspx?GrantRef=EP/G01244X/1 Sustainable delivery of Hydrogen and F7 EU project EFECTS 205854 Project area: NMP-2007-3.4-2 http://cordis.europa.eu/fetch?CALLER=FP7_PROJ_EN&ACTION=D&DOC=1&CAT=PROJ&QUERY=012b62d8d34a:77bc:582db170&RCN=89597 for financial assistance.

Fruitful discussions with Leslie Bronberg, Joe Minervini, Bruno Coppi, Richard Clarke, Michael O'Brien, Michael-Alexandre Cardin, Steven Steer, David Dew-Hughes, are greatly acknowledged.

References

[1] http://www.supergen14.org/

[2] GLOWACKI B.A., MAJOROS M., VICKERS M, EVETTS J.E., SHI Y. and MCDOUGALL I., Superconductor Science and Technology, 14 (2001) 193.

[3] GLOWACKI B.A., MAJOROS M., VICKERS M., EISTERER M., S. TOENIES S., WEBER H.W., M. FUKUTOMI M., KOMORI K. and TOGANO K. 'Composite Cu/Fe/MgB_2 superconducting wires and MgB_2 tapes for AC and DC applications' Supercond. Sci. Technol. 16 (2003) 297.

[4] GLOWACKI B.A. 'Development of Nb-based Conductors' in: Frontiers in Superconducting Materials, ed. A. Narlikar, Springer Verlag (2005) 697.

[5] YAMADA S., HISHINUMA Y., UEDU T., SHIPPL K., YANAGI N., MITO T. and SATO M., 'Conceptual Design of 1 GW Class Hybrid Energy Transfer Line of Hydrogen and

Electricity'EUCAS 2009, Journal of Physics: Conference Series 234 (2010) 03206; also 'Design of 1 GW Class Hybrid Energy Transfer Line of Hydrogen and Electricity and Development of its MgB_2 Cable' presented at ICEC 23/ICMC 19-23 July 2010, Wroclaw Poland to be published in Advances in Cryogenic Engineering.

[6] http://www.msm.cam.ac.uk/ascg/lectures/applications/fusion.php

[7] NUTTAL W.J., GLOWACKI B.A., and BROMBERG L., Fusion island – latest considerations concerning magnetic fusion, hydrogen cryomagnetics and thermochemical hydrogen production' Proceedings of Novel Aspects of Surfaces and Materials (NASM 3) Manchester, 11-15 April 2010.

[8] NUTTAL W.J. and GLOWACKI B.A., Nuclear Engineering International, Jul (2008) 38

[9] NUTTALL W.J.,'Nuclear Renaissance - Technologies and Policies for the Future of Nuclear Power', IoP Publishing Bristol 2004 ISBN: 0750309369

[10] http://www.llnl.gov

[11] GLOWACKI B.A. and NUTTALL W.J., '*Assessment of liquid hydrogen cooled MgB_2 conductors for magnetically confined fusion',* Journal of Physics: Conference Series, 97 (2008) 012333.

[12] GLOWACKI B.A., 'Hydrogen cryomagnetics: the way forward for superconductivity' presented at ICEC 23/ICMC 19- 23 July 2010, Wroclaw Poland to be published in Advances in Cryogenic Engineering.

[13] CLARKE R. and GLOWACKI B.A., 'Indirect hydrogen versus helium or nitrogen cooling for fusion cryogenic systems' presented at ICEC 23/ICMC 19-23 July 2010, Wroclaw Poland to be published in Advances in Cryogenic Engineering.

[14] MCDONALD K.T., IAROCCI M., KIRK H.G., MULHOLLAND G.T., TITUS P.H. and WEGGEL R.J 'Use of He Gas Cooled by Liquid Hydrogen with a 15-T Pulsed Copper Solenoid Magnet' presented at ICEC 23/ICMC 19-23 July 2010, Wroclaw, Poland; to be published in Advances in Cryogenic Engineering and also http://www.hep.princeton.edu/~mcdonald/mumu/target/icec_paper.pdf

[15] NUTTALL W., CLARKE R. and GLOWACKI B.A., 'Fusion Island' The Engineer 31 October (2005). p. 16

[16] Russian-German Cooperative Venture Study Report, Cryoplane 1992

[17] Rolls-Royce and the Cambridge-MIT Institute: 'Silence plane' http://www.cambridge-mit.org

[16] PATEL A, PALKA R. and GLOWACKI B.A., 'New fully superconducting hybrid bearing concept using the difference in irreversibility field of two superconducting components' Presented at The 7th International Workshop on Processing and Applications of Superconducting (RE)BCO Large Grain Materials, July 29-31, Washington, D.C. USA and to be published in Supercond Sci. and Technology 2011.

Journal of Energy Science, Vol. 1, No. 1, 2010, pp.29-35

Sustainable LH_2 energy cycle

BARTŁOMIEJ A. GŁOWACKI[1,2*], R. TOMOV[1], M. CHOROWSKI[3], A. PIOTROWSKA-HAJNUS[3], M. KRAUZ4, R. NOWAK[4], J. JEWULSKI[2]

[1] Department of Materials Science and Metallurgy, University of Cambridge, Pembroke Street, Cambridge CB2 3QZ, England
[2] Institute of Power Engineering, Thermal Processes Department, ul Augustówka 6, 02-981 Warsaw, Poland
[3] Instytut Inżynierii Lotniczej, Procesowej i Maszyn Energetycznych, Technical University of Wrocław, 50-370 Wroclaw, Poland
[4] Institute of Power Engineering, Ceramic Department, CEREL, ul Techniczna 1, 36-040 Boguchwała, Poland

Hydrogen energy cycle in a decentralized economy is a subject of discussion and research effort to find justification for usage of liquid hydrogen in conjunction with SOFC and SOEC and superconducting energy storage devices. The renewable energy sources are envisage to provide electricity to split water to H_2 and O_2 using high temperature electrolysis which can be beneficial thanks to the decrease of the energy demand due to the thermodynamics and improved electrochemical kinetics. Additionally O_2 and H_2 can be effective cryogenic liquids with boiling temperatures of 55K (under lower pressure) and 20K respectively. It is proposed that both gases O_2 and H_2 can be used in conjunction with recently developed mix gas cryocooler working at very low pressure and providing refrigeration at temperature below inversion temperature of hydrogen (118K). Liquefied hydrogen at temperature of 20K is a very efficient coolant for high temperature superconducting energy storage devices such flywheel and even SMES made from MgB_2. The H_2 and O_2 can be used in SOFC or PFC generating electricity when it is needed. The fact that SOFC is exothermic and SOEC is endothermic, enable realisation of the thermally balanced heat and electricity cycle. It was concluded that combination of the balanced SOFC/SOEC stacks in conjunction with liquefaction of the H_2 and O_2 products makes the overall LH_2 energy cycle sustainable and applicable to other modern energy storage devices such as superconducting flywheel.

---

[*] Corresponding author, e-mail: *bag10@cam.ac.uk or Bartlomiej.glowacki@ien.com.pl*

1. Introduction

Until multisource renewable energy supply will provide sustainable power delivery the alternative energy storage devices have to be considered. Hydrogen economy does consider storage of hydrogen in many forms: in metal hydrates, compressed gas, and also as a liquid. Hydrogen in the liquid form at 20K has very important cryogenic property as a coolant for superconducting storage devices such as for example flywheel. The applications of medium temperature superconductors, MgB_2, and high temperature superconductors, $YBa_2Cu_3O_7$, can benefit from the low cost cooling by liquid H_2 at 20K. Our work on SOFC and SOEC in frame of the international and national projects and also long-term expertise in hydrogen cryoscience, enable us to present the concept of the sustainable liquid hydrogen cycle in conjunction with energy generation, storage and usage.

2. Model

Liquid hydrogen has two main strands: as a energy carrier and as a cryogenic liquid [1-3]. What concerns energy carrier it is envisage that hydrogen can be used to balance varying renewable supply with varying demand of decentralised energy infrastructure as presented schematically in Fig 1. The aspect of decentralised energy storage can be seen as a calorific value of the liquid hydrogen itself (100%wt H_2), with potential for an additional physical cryosorption of hydrogen (7wt% H_2) and also as an efficient cooling of superconducting energy storage device such as flywheel at level of 10kWh.

As it was described buy W. Doenitz, et al. [4] hydrogen obtained by conventional electrolysis methods appears to have no chance to contribute considerably to the energy supply in the future, since it will become increasingly important to select high efficient secondary energy systems. On the other hand using high temperature electrolysis, electrolytic production of hydrogen can be performed with significantly higher thermal efficiencies of 50 % by operating in the vapour phase, see Fig 2.

Direct provision of O2/H2 gases by SOEC at elevated pressure is a subject of intensive research in the frame of SUPERGEN-14 ‘H-Delivery’ project, the UK initiative [6] and new EU initiative ‘RELHY’[7]. It is important that electro-thermal conditions and absolute humidity, AH, are optimised for the particular type of SOEC such as Ni-YSZ/YSZ8/LSM to achieve the highest efficiency [5].

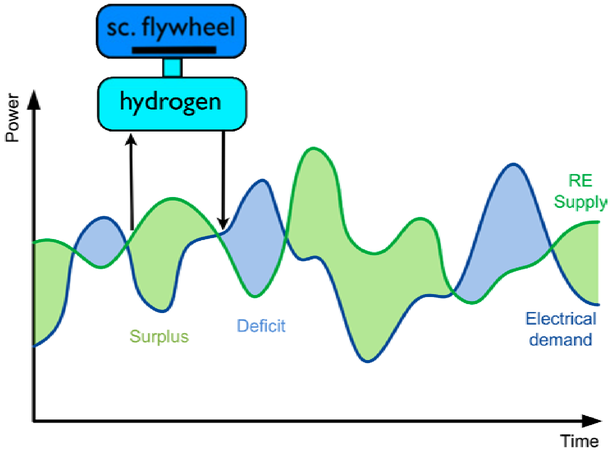

Fig.1 Schematic of the way to balance varying renewable supply with varying demand of decentralised energy infrastructure using liquid hydrogen and superconducting flywheel technology

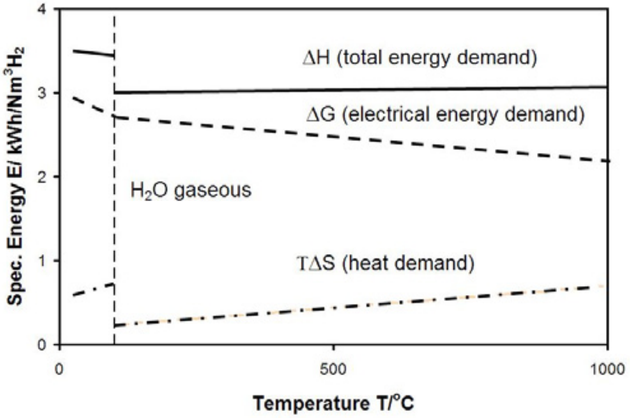

Fig.2 Thermodynamics of steam electrolysis, the energy requirements for splitting water versus temperature. The total energy (ΔH) needed for splitting H_2O into its elements consists of a minimum fraction of electrical energy ΔG and a heat fraction. The overall benefit of this type of electrolysis is a significant reduction of electrical energy and consequently a substantial reduction of primary energy needed; where H- enthalpy; G – Gibbs energy, T – temperature; S – entropy; after [4,5]

As presented in the Fig. 4 the practical high temperature solid oxide electrolyser cell may work in endothermic and exothermic mode. Considering the fact that exemplary cell may work in the reverse mode acting as a exotermic SOFC, see Fig.3, the electro-thermal balace need to be achieved for a decrentralised energy cycle as it will be be discussed later.

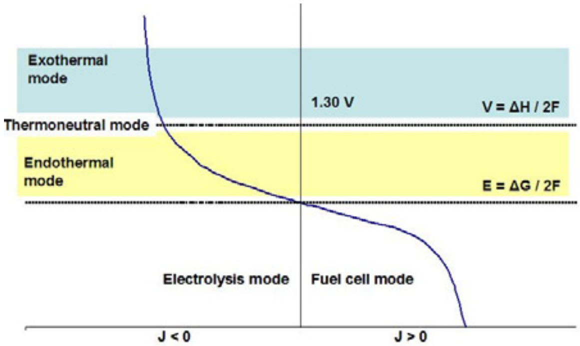

Fig.3 Kinetics of solid oxide cell working as an electrolyser cell (negative current densities J) and as a fuel cell (positive current densities J). However an ideal electrolysers cell consumes heat and the ideal fuel cell generates heat, in the real case due to combination of ohmic losses on electrolyte, electrodes and interconnectors as well as diffusion processes and charge transfer at electrodes at certain voltage – current density conditions SOEC may be in the exotermic mode [7]

The energy requirement for conventional large-scale hydrogen liquefaction is estimated to be as high as 30% of the calorific value of the generated LH_2. New approaches that can lower energy requirement and thus the cost of liquefaction especially at low hydrogen production rate need to be developed for decentralised hydrogen economy [5].

We propose a development of tandem cooling system, presented in Fig.4, where high temperature electrolysis, SOEC, at elevated pressure provides compressed O_2 and H_2 needed to liquefy H_2.

Oxygen has an inversion temperature of 764 K therefore can be effectively cooled by the combination of Joule - Thomson valve and turbine based expanders. In our design lowered temperature liquid oxygen (super-cooled O_2) plays an important role in increasing hydrogen liquefaction efficiency. To improve safety during liquefaction of hydrogen a novel composite solid nitrogen reservoir will be researched as a heat exchanger between liquid O_2 and gH_2. Cryogenic LH_2 is going to be storage in cryogenic super-insulated Dewar integrated with liquefier as presented in the Fig.5. Additionally thermal link from the LH_2 energy storage to the superconducting flywheel is a viable option, Fig. 1 and Fig.5.

Many of current and also future energy and electrotechnology applications require employment of medium and high temperature superconductors working at cryogenic temperatures of approximately 20 K to achieve their desired efficiency. If such cryogenic temperature needed to be created exclusively to enable superconducting devices, with no connection to hydrogen economy, cost will be very high. For example to generate cooling power of 1W at temperature of 20K a 1kW of power of the cryogenic cryocooler is required at room temperature. The overall efficiency of the cooling will dramatically improve if the liquid hydrogen is produced as an energy carrier and can have an additional use as a cryogenic coolant for superconductors deployed in the energy cycle.

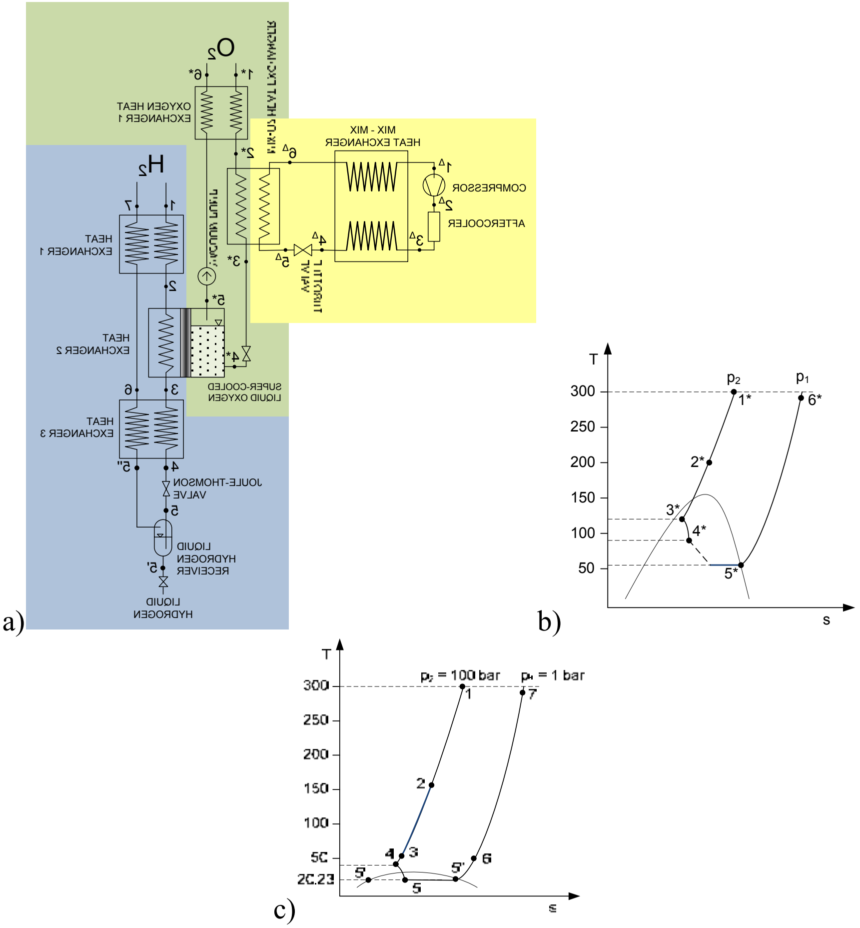

Fig.4 Hybrid O_2/H_2 liquefier: a) Schematic of the novel design of oxygen and hydrogen cycle characterised by efficiency of 40% liquefaction of hydrogen at rate of 1ml of LH_2/min. The O_2/H_2 liquefier is combined at initial cooling stage with developed novel PEN J-T cycle marked in yellow [8]; b) temperature-entropy phase diagram for oxygen liquefaction cycle, point 5* represent LO_2 under low pressure at temperature 55K; c) temperature-entropy phase diagram for hydrogen liquefaction cycle

If one envisages that liquid hydrogen integrated with superconducting storage energy systems may act as energy vector, buffering the energy demand from renewable sources as, Fig.1, one may also consider new approach where electro-thermal integration of the SOEC with SOFC can be viable option, Fig.5.

Considering the fact that solid oxide cell function presented in Fig. 3 may work as SOEC or SOFC the novel hybrid design of the multifuncional stack can be employed enabling electro-thermal balace need for a decrentralised energy cycle. High temperature SOFC benefits in 30% improved performance if pure hydrogen is used in comparison with metane. In the more general picture hydrogen from the storage can be used by polymeric fuel cells that required ultra pure hydrogen gas, which in case of the cryogenic liquid hydrogen storage simply is sourced from LH_2 evaporation.

Another interesting and important issue about proposed LH_2 cycle is that in most cases the input from renewable energy sources to support high temperature electrolysers comes form of dc current and dc voltage. The same holds for the generation of the electricity from high temperature solid oxide fuel cells. Therefore one may recognise that integrated LH2 Energy Cycle, that merges the lower cost H_2 liquefaction and storage with DC energy cycle, becomes distributed energy generic cluster for sustainable cities and industrial applications.

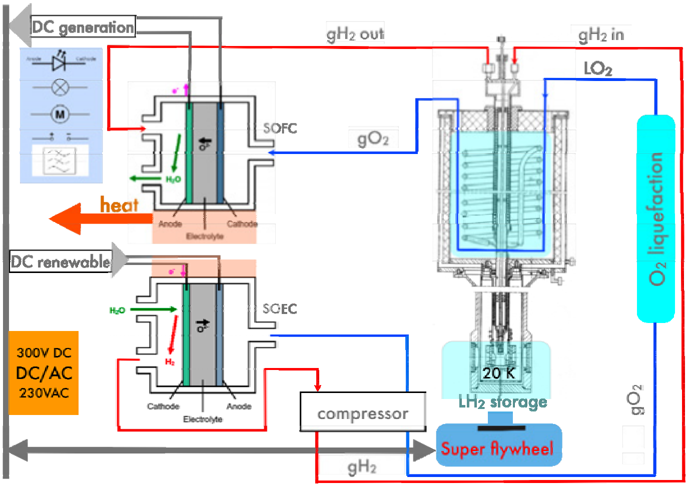

Fig. 5. Integrated sustainable liquid H_2 energy cycle

3. Conclusions

Proposed sustainable LH_2 energy cycle exploring interconnection between SOEC => LH_2 => SOFC requires intensive research to optimise rapid development of the hybrid solid oxide cells which interchangeable functions and integrated electro-thermal management to secure real opportunities for implementation of the sustainable LH_2 Energy Cycle. Integration of well balanced hydrogen generation, compression, storage and usage with DC renewable energy sources can become distributed energy generic cluster for sustainable cities and various decentralised industrial applications.

Acknowledgements

The authors wish to acknowledge The authors wish to acknowledge EPSRC SUPERGEN EP/G01244X/1 'Sustainable delivery of Hydrogen' and F7 EU project EFECTS 205854 Project area: NMP-2007-3.4-2 and EPSRC studentship "Superconducting bearing" for financial support.

References

[1] YAMADA S., Y. HISHINUMA Y., UEDE T., SCHIPPL K. and O. MOOTJIMA, J. Phys.: Conference Series 97 (2008) 012167.
[2] GLOWACKI B.A. and NUTTALL W.J., J. Phys.: Conf. Ser. 97 (2008) 012333.
[3] NUTTALL W.J., CLARKE R. And GLOWACKI B.A., The Engineer, 31 October (2005) 16.
[4] DOENITZ W. SHIMIDBERGER R., STEINHEIL E. and STREICHER R., Int. J. Hydrogen Energy 5 (1980) 55.
[5] ERDLE E., GROSS J. and MEYRIGER V., "Solar thermal central receiver systems", In Proceedings of the Third International Workshop Vol. 2 High temperature and its Applications. June 23-27, 1986, Konstanz, Germany.
[6] 'H-Delivery' SUPERGEN 14; http://www.supergen14.org
[7] 'RELHY' Innovative Solid Oxide Electrolyser Stacks for Efficient and Reliable Hydrogen Production http://cordis.europa.eu/icadc/fetch?CALLER=FP7_PROJ_EN&ACTION=D&DOC=95&CAT=PROJ&QUERY=011aa1a03e88:3444:4077d56a&RCN=85754
[8] PIOTROWSKA-HAJNUS A., PhD Thesis, Technical University of Wrocław, Poland 2009.

Journal of Energy Science, Vol. 1, No. 1, 2010, pp.37-53

Temperature measurements of flowing fluid under unsteady-state conditions

MAGDALENA JAREMKIEWICZ[1], DAWID TALER[2], TOMASZ SOBOTA[1]

[1] Cracow University of Technology, Department of Thermal Power Engineering, Al. Jana Pawła II 37, 31-864 Kraków, Poland
[2] University of Science and Technology, Department of Power Installations, Al. Mickiewicza 30, 30-059 Kraków, Poland

Under steady-state conditions when fluid temperature is constant, there is no damping and time lag and temperature measurement can be accomplished with high degree of accuracy. However, when fluid temperature is varying rapidly as during start-up, quite appreciable differences occur between the actual fluid temperature and the measured temperature. This is due to the time required for the transfer of heat to the thermocouple placed inside a heavy thermometer pocket. In this paper, two different techniques for determining transient fluid temperature based on the first and second order thermometer model are presented. The fluid temperature was determined using the temperature indicated by the thermometer, which was suddenly immersed into boiling water. To demonstrate the applicability of the presented method to actual data, the time constants for the three sheathed thermocouples with different diameters, placed in the air stream, were estimated as a function of the air velocity.

Symbols

A – surface area of the thermocouple cross section, m^2,
A_o – surface area of the housing cross section, m^2,
A_T – outer surface area of the thermocouple, m^2,
α_T – heat transfer coefficient on the outer surface of the thermocouple, $W/(m^2 \cdot K)$,
α_w – heat transfer coefficient on the inner surface of the housing, $W/(m^2 \cdot K)$,
α_z – heat transfer coefficient on the outer surface of the housing, $W/(m^2 \cdot K)$,
c – average specific heat of the thermocouple, $J/(kg \cdot K)$,
c_o – average specific heat of the housing, $J/(kg \cdot K)$,
d, – outer diameter of the thermocouple, m,
D_w – inner diameter of the housing, m,
D_z – outer diameter of the housing, m,
δ_o – housing thickness, m,
ε_o – emissivity of the housing inner surface,
ε_T – emissivity of the thermocouple surface,

k_w – overall heat transfer coefficient between the housing inner surface and outer surface of the thermocouple referred to the inner housing surface, W/(m^2·K)
k_z – overall heat transfer coefficient between the fluid and the housing referred to the outer housing surface, W/(m^2·K)
λ_o – housing thermal conductivity, W/(m·K),
λ_p – thermal conductivity of the air gap, W/(m·K),
m_T – thermocouple mass, kg
P_w – perimeter of the internal surface of the housing, m,
ρ – average density of the thermocouple, kg/m^3,
ρ_o – average density of the housing, kg/m^3,
s – complex variable,
σ – Stefan-Boltzmann constant, $\sigma = 5.67 \cdot 10^{-8}$ W/(m^2·K^4),
T_{cz} – fluid temperature, °C,
T_o – housing temperature, °C,
T_0 – initial thermometer temperature, °C,
$\bar{T}_{cz}(s)$ – Laplace transform of the fluid temperature,
$\bar{T}(s)$ – Laplace transform of the thermometer temperature,
τ – time constant of the thermometer in the first order model, s,
τ_1, τ_2 – time constants of the thermometer in the second order model, s
U – unit-step response of the thermometer,
w – fluid velocity, m/s

1. Introduction

Most of the books on temperature measurements concentrate on steady-state measurements of the fluid temperature [1-9]. Only a unit-step response of thermometers is considered to estimate the dynamic error of the temperature measurement. Little attention is paid to measurements of the transient fluid temperature, despite the great practical significance of the problem [10-12].

The measurement of the transient temperature of steam or flue gases in thermal power stations is very difficult. Massive housings and low heat transfer coefficient cause the actually measured temperature to differ significantly from the actual temperature of the fluid. Some particularly heavy thermometers may have time constants of 3 minutes or more, thus requiring about 15 minutes to settle for a single measurement. There are some thermometer designs where there is more than one time constant involved. In order to describe the transient response of a temperature sensor immersed in a thermowell, the measuring of the medium temperature in a controlled process may have two or three time constants which characterise the transient thermometer response.

The problem of a dynamic error during the measuring of the temperature of the superheated steam is particularly important for the superheated steam temperature control systems which use injection coolers (spray attemperators). Due to a large inertia of the thermometer, a measurement of the transient temperature of the fluid, and thus the automatic control of the superheated steam temperature can be inaccurate. A similar problem is encountered in flue gas temperature measurements, since the thermometer time constant and time delay are large.

In this paper there are presented two methods of determining the transient temperature of the flowing fluid on the basis of the temperature time changes indicated by the thermometer. In the first method the thermometer is considered to be a first order inertia device and in the second one it is considered as a second order inertia device. A local polynomial approximation, based on 9 points was used for the approximation of the temperature changes. This assures that the first and the second derivative from the function representing the thermometer temperature changes in time will be determined with a great accuracy.

An experimental analysis of the industrial thermometer at the step increase of the fluid temperature was conducted. The temperature time histories determined using the two proposed methods at the step increase of the fluid temperature were compared.

2. Mathematical models of the thermometers

Usually the thermometer is modeled as an element with lumped thermal capacity. In this way, it is assumed that the temperature of the thermometer is only the function of time, and temperature differences occurring within the thermometer are neglected. The temperature changes of the thermometer in time T(t) have been described by an ordinary first order differential equation (first order thermometer model)

$$\tau \frac{dT}{dt} + T = T_{cz} . \tag{1}$$

For thermometers with a complex structure used for measuring the temperature of the fluid under high pressure, the accuracy of the first order model (1) is inadequate.

3. Thermometer of a complex structure

To demonstrate that a dynamic response of a temperature sensor placed in a housing, may be described by a second-order differential equation, a simple thermometer model shown in Fig. 1 will be considered.

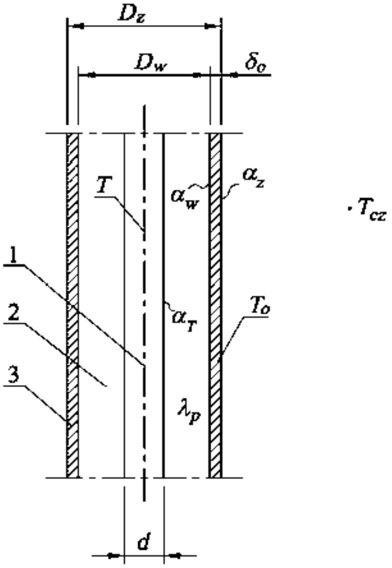

Fig.1. Cross section through the temperature sensor together with the housing

An air gap can appear between the external housing and the temperature sensor. The thermal capacity of this air gap c·ρ is neglected due to its small value (Fig. 1).

Introducing the overall heat transfer coefficient kw referenced to the inner surface of the housing

$$\frac{1}{k_w} = \frac{1}{\alpha_w} + \frac{\left(1 + D_w/d\right)\left(D_w - d\right)}{4\lambda_p} + \frac{D_w}{d} \cdot \frac{1}{\alpha_T}, \tag{2}$$

and accounting for the radiation heat transfer from the housing to the inner sensor, the heat balance equation for the sensor located within the housing assumes the form:

$$A\rho c \frac{dT}{dt} = P_w k_w \left(T_o - T\right) + C\left(T_o^4 - T^4\right), \tag{3}$$

where the symbol C denotes:

$$C = \frac{\pi d \sigma}{\frac{1}{\varepsilon_T} + \frac{d}{D_w}\left(\frac{1}{\varepsilon_o} - 1\right)}.$$

The convection and conduction heat transfer between the fluid and the thermometer housing is characterized by the overall heat transfer coefficient k_z referenced to the outer housing surface:

$$\frac{1}{k_z} = \frac{1}{\alpha_z} + \frac{1 + D_z/D_w}{2} \cdot \frac{\delta_o}{\lambda_o}. \tag{4}$$

The formulas (2) and (4) for the overall heat transfer coefficients were derived using the basic principles of heat transfer [2,4,8]. The heat transfer equation for the housing (thermowell) can be written in the following form:

$$A_o \rho_o c_o \frac{dT_o}{dt} = P_z k_z \left(T_{cz} - T_o\right) - P_w k_w \left(T_o - T\right) - C\left(T_o^4 - T^4\right). \tag{5}$$

In the analysis of the heat exchange between the housing and the thermocouple, the radiation heat transfer will also be disregarded. Such a situation occurs, when a gap between the housing and temperature sensor is filled with non-transparent substance or one of the two emissivities ε_o and ε_T is close to zero.

After determining the temperature T_o from Eq.(3), we obtain:

$$T_o = \frac{A\rho c}{P_w k_w} \frac{dT}{dt} + T. \tag{6}$$

Substituting Eq. (6) into Eq. (5) yields:

$$\frac{\left(A_o \rho_o c_o\right)\left(A\rho c\right)}{\left(P_w k_w\right)\left(P_z k_z\right)} \frac{d^2 T}{dt^2} + \frac{A_o \rho_o c_o}{P_z k_z}\left[1 + \frac{\left(P_z k_z\right)\left(A\rho c\right)}{\left(P_w k_w\right)\left(A_o \rho_o c_o\right)} + \frac{A\rho c}{A_o \rho_o c_o}\right] \frac{dT}{dt} + T = T_{cz}. \tag{7}$$

Introducing the following coefficients:

$$a_2 = \frac{\left(A_o \rho_o c_o\right)\left(A\rho c\right)}{\left(P_w k_w\right)\left(P_z k_z\right)}, \qquad a_1 = \frac{A_o \rho_o c_o}{P_z k_z}\left[1 + \frac{\left(P_z k_z\right)\left(A\rho c\right)}{\left(P_w k_w\right)\left(A_o \rho_o c_o\right)} + \frac{A\rho c}{A_o \rho_o c_o}\right],$$

the ordinary differential equation of the second order (7) can be written in the form:

$$a_2 \frac{d^2T}{dt^2} + a_1 \frac{dT}{dt} + T = T_{cz}. \tag{8}$$

The initial conditions are:

$$T(0) = T_0 = 0, \left. \frac{dT(t)}{dt} \right|_{t=0} = v_T = 0. \tag{9}$$

The initial problem (8-9) was solved using the Laplace transformation. The operator transmittance $G(s)$ assumes the following form:

$$G(s) = \frac{\bar{T}(s)}{\bar{T}_{cz}(s)} = \frac{1}{(\tau_1 s + 1)(\tau_2 s + 1)}. \tag{10}$$

The time constants τ_1 and τ_2 in Eq. (10) are:

$$\tau_{1,2} = \frac{2a_2}{a_1 \pm \sqrt{a_1^2 - 4a_2}}. \tag{11}$$

The differential Equation (8) can be written in the following form:

$$\tau_1 \tau_2 \frac{d^2T}{dt^2} + (\tau_1 + \tau_2) \frac{dT}{dt} + T = T_{cz}. \tag{12}$$

For the step increase of the fluid temperature from $T_0 = 0°C$ to the constant value T_{cz} the Laplace transform of the fluid temperature assumes the form: $\bar{T}_{cz}(s) = \frac{T_{cz}}{s}$ and the transmittance formula can be simplified to:

$$\frac{\bar{T}(s)}{T_{cz}} = \frac{1}{s(\tau_1 s + 1)(\tau_2 s + 1)}. \tag{13}$$

After writing Eq. (12) in the form:

$$\frac{\bar{T}(s)}{T_{cz}} = \frac{1}{s} + \frac{\tau_1}{\tau_2 - \tau_1} \cdot \frac{1}{\left(s + \frac{1}{\tau_1}\right)} - \frac{\tau_2}{\tau_2 - \tau_1} \cdot \frac{1}{\left(s + \frac{1}{\tau_2}\right)}, \tag{14}$$

it is easy to find the inverse Laplace transformation and determine the thermometer temperature as a function of time:

$$u(t) = \frac{T(t)}{T_{cz}} = 1 + \frac{\tau_1}{\tau_2 - \tau_1} \exp\left(-\frac{t}{\tau_1}\right) - \frac{\tau_2}{\tau_2 - \tau_1} \exp\left(-\frac{t}{\tau_2}\right). \tag{15}$$

For the first order model the thermometer response for a unit step fluid temperature change is determined by the simple expression:

$$u(t) = 1 - \exp\left(-\frac{t}{\tau}\right). \tag{16}$$

If we assume in Eq. (15) $\tau_2 = 0$ then we obtain Eq. (16) with $\tau = \tau_1$.

In the time response of a first order system, given by Eq. (16), there is no a time delay (a dead time). Heavy thermometers for measuring fluid temperature at high pressure involve a time delay between the temperature sensor output and the fluid temperature changes. The second order thermometer model is appropriate to describe the response behaviour with a time delay.

The time constant τ in Eq. (16) or time constants τ_1 and τ_2 in Eq. (15) will be estimated from experimental data.

The fluid temperature can be determined on the basis of measured histories of the thermometer temperature $T(t)$ and known time constants τ_1 and τ_2.

The changing in time of fluid temperature $T_{cz}(t)$ can be determined from Eq. (1) or Eq. (12) after a priori determination of the time constant τ or time constants τ_1 and τ_2 – respectively. The thermometer temperature changes $T(t)$, the first and second order time derivatives from the function $T(t)$, can be smoothed using the formulas [3]:

$$\begin{aligned} T(t) = {} & \frac{1}{693} \cdot \big[-63 f(t - 4 \cdot \Delta t) + 42 f(t - 3 \cdot \Delta t) + \\ & + 117 f(t - 2 \cdot \Delta t) + 162 f(t - \Delta t) + 177 f(t) + 162 f(t + \Delta t) + \\ & + 117 f(t + 2 \cdot \Delta t) + 42 f(t + 3 \cdot \Delta t) - 63 f(t + 4 \cdot \Delta t) \big] \end{aligned} \tag{17}$$

$$\begin{aligned} T'(t) = \frac{dT(t)}{dt} = \frac{1}{1188\Delta t} \cdot \big[& 86 f(t-4\cdot\Delta t) - 142 f(t-3\cdot\Delta t) - \\ & -193 f(t-2\cdot\Delta t) - 126 f(t-\Delta t) + 126 f(t+\Delta t) + \\ & +193 f(t+2\cdot\Delta t) + 142 f(t+3\cdot\Delta t) - 86 f(t+4\cdot\Delta t) \big] \end{aligned} \tag{18}$$

$$\begin{aligned} T''(t) = \frac{d^2T(t)}{dt^2} = \frac{1}{462(\Delta t)^2} \cdot \big[& 28 f(t-4\cdot\Delta t) + 7 f(t-3\cdot\Delta t) - \\ & -8 f(t-2\cdot\Delta t) - 17 f(t-\Delta t) - 20 f(t) - 17 f(t+\Delta t) - \\ & -8 f(t+2\cdot\Delta t) + 7 f(t+3\cdot\Delta t) + 28 f(t+4\cdot\Delta t) \big], \end{aligned} \tag{19}$$

in order to eliminate, at least partially, the influence of random errors in the thermometer temperature measurements $T(t)$ on the determined fluid temperature $T_{cz}(t)$. The symbol $f(t)$ in Eq. (17-19) denotes the temperature indicated by the thermometer and Δt is a time step.

If measured temperature histories are not too noisy, the first and second order derivatives can be approximated by the central difference formulas

$$T'(t) = \frac{f(t+\Delta t) - f(t-\Delta t)}{2\Delta t}, \tag{20}$$

$$T''(t) = \frac{f(t+\Delta t) - 2f(t) + f(t-\Delta t)}{(\Delta t)^2}. \tag{21}$$

Equation (1) and Equation (12) can also be used for determining fluid temperature T_{cz} when the time constants of the thermocouple τ or τ_1 and τ_2 are a function of fluid velocity w. After substituting the time constant $\tau(w)$ into Eq. (1) we can determine fluid temperature $T_{cz}(t)$ for different fluid velocities using the proposed method.

4. Experimental determination of time constants

The method of least squares was used to determine the time constants τ_1 and τ_2 in Eq. (15) or the time constant τ in Eq. (16). The values for the time constants are found by minimising the function S:

$$S = \sum_{i=1}^{N} \left[u_m(t_i) - u(t_i) \right]^2 = \min , \tag{22}$$

where $u(t)$ is the approximating function given by Eq. (15) or Eq. (16). The symbol N denotes the number of measurements (t_i, $u_m(t_i)$). That is, the sum of the squares of the deviations of the measured values $u_m(t_i)$ from the fitted values $u(t_i)$ is minimized. Once the time constants τ_1 and τ_2 or τ have been determined they can be substituted into Eq. (22) to find the value for $S_{\min}$.

The uncertainties in the calculated time constants τ_1 and τ_2 or in τ are estimated using the mean square error [13-15]:

$$S_N = \sqrt{\frac{S_{\min}}{N-m}} , \tag{23}$$

where m is the number of time constants ($m = 2$ for Eq. (15) and $m = 1$ for Eq. (16)).

Based on the calculated mean square error S_N, which is an approximation of the standard deviation, the uncertainties in the determined time constants can be calculated using the formulas given in the TableCurve 2D software [15].

5. Determining the fluid temperature on the basis of time changes in the thermometer temperature

An industrial thermometer (Fig. 2) at the ambient temperature was suddenly immersed into hot water with saturation temperature. The thermometer temperature data was collected using the Hottinger-Baldwin Messtechnik data acquisition system. The measured temperature changes were approximated using functions (15) and (16). The time constant τ in Eq. (16) and time constants τ_1 and τ_2 in function (15) were determined using the TableCurve 2D code [15]. The following values with the 95% confidence uncertainty were obtained: $\tau = 14.07 \pm 0.39$ s, $\tau_1 = 3.0 \pm 0.165$ s, and $\tau_2 = 10.90 \pm 0.2$ s.

Next, the fluid temperature changes were determined from Eq. (1) for the first order model and from Eq. (12) for the second order model (Fig. 3). The time step Δt was 1.162 s.

The analysis of the results presented in Fig. 3 indicates that the second order model delivers more accurate results.

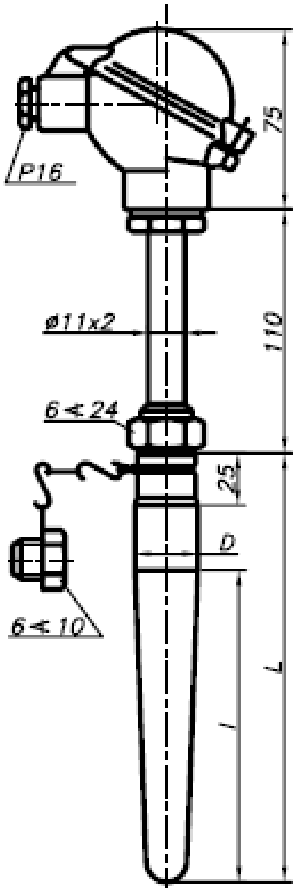

Fig.2. Industrial thermometer and its dimensions: D = 18 mm, l = 65 mm, L = 140 mm

The same tests were repeated for sheathed thermocouple with outer diameter 1.5 mm and the results are presented in Fig. 4. The estimated value of the time constant and the uncertainty at 95% confidence are: $\tau = 1.54 \pm 0.09$ s. As the thermocouple is thin, then Eq. (16) was used as the function approximating the transient response of the thermocouple. First, the transient fluid temperature $T_{cz} = u(t)$ was calculated using Eq. (1) together with Eqs. (17) and (18). Then, the raw temperature data was used. The first order time derivative dT/dt in Eq. (1) was calculated using the central difference quotient (20). The inspection of the results displayed in Fig. 4 indicates, that the central difference approximation of the time derivative in Eq. (1) leads to less accurate results, since it is more sensitive to random errors in the experimental data.

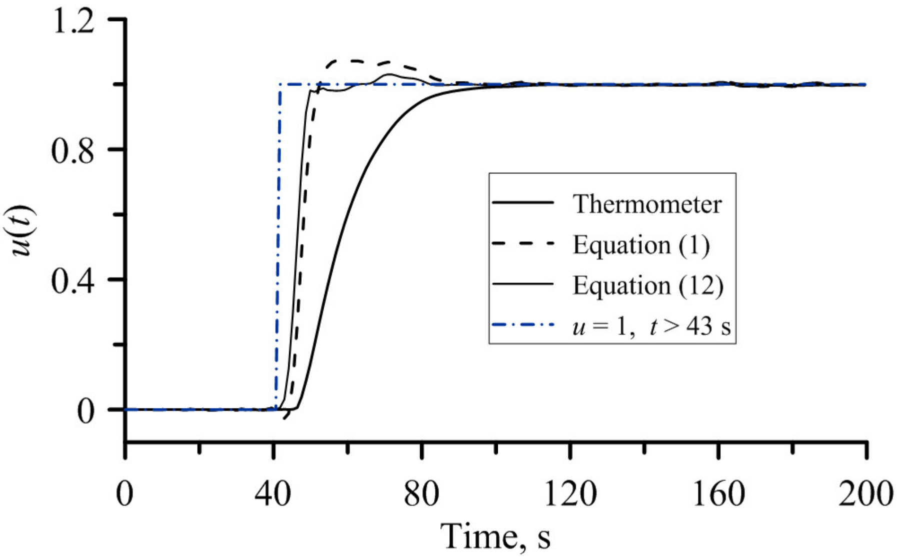

Fig.3. Fluid and industrial thermometer temperature changes determined from the first order Eq. (1) and from the second order Eq. (12)

The thermocouple time constant τ for various air velocities w, were determined in the open benchtop wind tunnel (Fig. 5). The WT4401-S benchtop wind tunnel is designed to give a uniform flow rate over 100 mm × 100 mm test cross section [16].

The experimental data points displayed in Fig. 6 were approximated by the least squares method for three different thermocouple diameters 0.5 mm, 1.0 mm and 1.5 mm. The following function was obtained:

$$\tau = \frac{1}{a + b\sqrt{w}}, \tag{24}$$

where τ is expressed in s, and w in m/s.

The best estimates for the constants a and b, with the 95 % confidence uncertainty in the results, are:

- thermocouple with outer diameter 0.5 mm
  $a = 0.004337 \pm 0.000622$ 1/s and $b = 0.022239 \pm 0.001103$ $(\text{m}\cdot\text{s})^{-1/2}$,

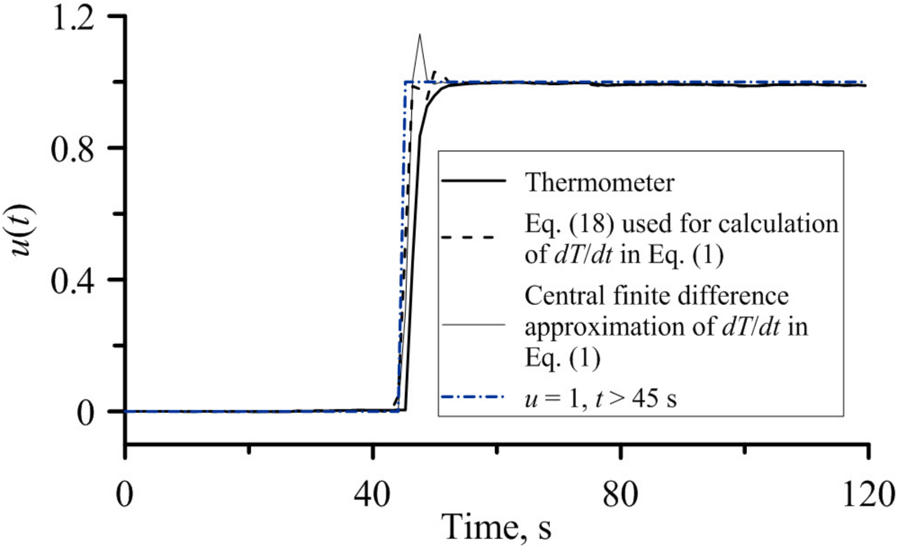

Fig.4. Fluid and thermometer temperature changes determined from the first order Eq. (1) for the sheathed thermocouple with outer diameter 1.5 mm

Fig.5. Benchtop wind tunnel used for determining thermocouple time constant

- thermocouple with outer diameter 1.0 mm
  $a = 0.020974 \pm 0.006372$ 1/s and $b = 0.103870 \pm 0.011240$ $(\mathrm{m\cdot s})^{-1/2}$.
- thermocouple with outer diameter 1.5 mm
  $a = 0.040425 \pm 0.003301$ 1/s and $b = 0.056850 \pm 0.004479$ $(\mathrm{m\cdot s})^{-1/2}$.

The variations of the thermocouple time constants τ with the fluid velocity for the sheathed thermocouples with the outer diameter of 0.5 mm, 1.5 mm and 3.0 mm are shown in Fig. 6.

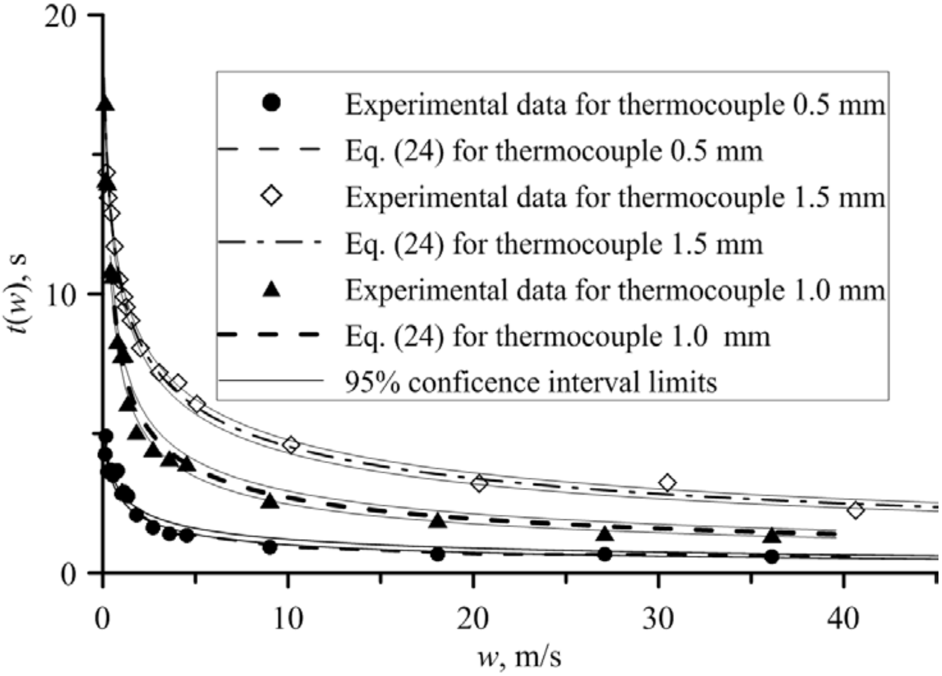

Fig.6. Time constants τ of sheathed thermocouple with outer diameters of 0.5 mm, 1.5 mm and 3.0 mm as a function of air velocity w with 95 % confidence intervals

The time constant of the thermocouple $\tau = m_T c/(\alpha_T A_T)$ depends strongly on the heat transfer coefficient α_T on the outer thermometer surface, which in turn is a function of the air velocity [17].

When the velocity and temperature of the air stream change in time, the velocity dependent time constant (24) can be used in Eq. (1) to estimate the air temperature based on the temperature readings from the sheathed thermocouples.

In order to determine fluid temperature three thermocouples with different diameters of 0.5 mm, 1.0 mm and 1.5 mm were used simultaneously. Time constants τ as a function of air velocity for mentioned above thermocouples are presented in Fig. 6. Air velocity changes during temperature measurement depicts Fig. 7a. Temperature indicated by thermocouples and calculated fluid temperature are shown in Fig. 7b. A significant improvement in air temperature measurement accuracy can be observed when the proposed method was applied for determining air temperature. The agreement between the air temperature for the thermocouple with 0.5 mm and for the thermocouple with 1.0 mm outer diameter is very good. It seems that the thermocouple with 1.5 mm outer diameter is less adequate to follow fast changes fluid temperature, since its time constant is large.

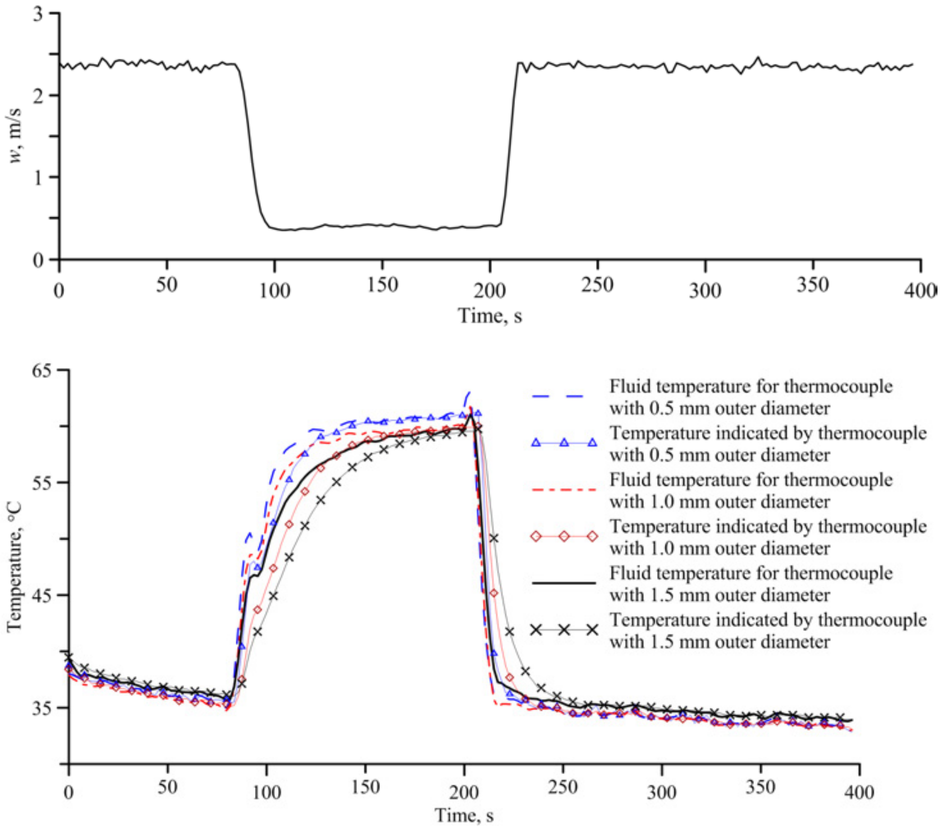

Fig.7. Temperature measurements: a) air velocity changes, b) temperature indicated by thermocouples and calculated air temperature

6. Conclusions

Both methods of measuring the transient temperature of the fluid, presented in this paper, can be used for the on-line determining fluid temperature changes as a function of time.

The first method in which the thermometer is modeled using the ordinary, first order differential equation is appropriate for thermometers which have very small time constants. In such cases, the delay of the thermometer indication is small in reference to the changes of the temperature of the fluid. For industrial thermometers, designed to measure temperature of fluids under a high pressure, there is a significant time delay of the thermometer indication in reference to the actual changes of the fluid temperature. For such thermometers the second order thermometer model, allowing for modeling the signal delay, is more appropriate. Large stability and accuracy of the determination of the actual fluid temperature on the basis of the time temperature changes indicated by the thermometer can be achieved by using a 9 point digital filter.

Fluid temperature changes obtained using the two described methods were compared. It was established that the thermometer model of the second order gave better results for the industrial thermometer having the large thermowell. The techniques proposed in the paper can also be used, when time constants are functions of fluid velocity.

REFERENCES

[1] NICHOLAS J.V. and WHITE D.R., Traceable Temperatures. An Introduction to Temperature Measurement and Calibration, Wiley, New York, 2001.

[2] MICHALSKI L., ECKERSDORF K., McGHEE J., Temperature Measurement, Wiley, Chichester, 1991.

[3] WIŚNIEWSKI S., Temperature Measurement in Engines and Thermat Facilities, WNT, Warszawa, 1983 (in Polish).

[4] TALER J., Theory and Practice of Identification of Heat Transfer Processes, Zakład Narodowy im. Ossolińskich, Wrocław, 1995 (in Polish).

[5] KABZA Z., KOSTYRKO K., ZATOR S., ŁOBZOWSKI A., SZKOLNIKOWSKI W., Room Climate Control, Agenda Wydawnicza, Pomiary Automatyka Kontrola, Warszawa, 2005 (in Polish).

[6] LITTLER D.J. et al., Instrumentation, Controls & Testing. Modern Power Station Practice, Pergamon Press, Oxford, 1991.

[7] CHILDS P.R.N., Practical Temperature Measurement, Buterworth-Heinemann, Oxford, 2001.

[8] O.A. GERASHCHENKO, A.N. GORDOV, V.I. LAKH, B.I. STADNYK, N.A. YARYSHEV, Temperaturnye Izmereniya, Naukova Dumka, Kiev, 1984 (in Russian).

[9] HAN J-Ch., DUTTA S., EKKAD S.V., Gas Turbine Heat Transfer and Cooling Technology in: Experimental Methods, Taylor & Francis, New York, 2000.

[10] SZÉKELY V., RESS S., POPPE A., TÖRÖK S., MAGYARI D., BENEDEK Zs., TORKI K., COURTOIS B., RENCZ M.. New approaches in the transient thermal measurements, Microelectronics J., 31 (2000), 727–733.

[11] CROCKER D.S., PARANG M., Unsteady temperature measurement in an enclosed thermoconvectively heated air, Int. Comm. Heat Mass Transfer, 28(8) (2001), 1015-1024.

[12] CHAU P.C., Process control. A First Course with MATLAB, Cambridge University Press, Cambridge, 2002.

[13] ASME, Policy on reporting uncertainties in experimental measurements and results, J. Heat Transfer, 122 (2000), 411-413.

[14] MOFFAT R.J., Describing the uncertainties in experimental results, Experimental Thermal and Fluid Science, 1 (1988), 3-17.

[15] TableCurve 2D v.5.0, Automated Curve Fitting&Equation Discovery, AISN Software Inc., 2000.
[16] WT4401-S & WT4401-D Benchtop Wind Tunnels, Omega, Stamford, CT, USA, www.omega.com
[17] SANITJAI S., GOLDSTEIN R.J., Forced convection heat transfer from a circular cylinder in crossflow to air and liquids, Int. J. Heat and Mass Transfer, 47 (2004), 4795-4805.

Journal of Energy Science, Vol. 1, No. 1, 2010, pp.53-67

Instability and heuristic problems in high – speed rotor of a micro turbine

JAN KICIŃSKI

Institute of Fluid-Flow Machinery Polish Academy of Sciences, Gdansk, Poland

Nonlinear forms of vibrations in rotors dynamics, especially after exceeding the stability limit, as well as the assessment of not precise and randomly variable input parameters, still constitute the research subject in many institutions all over the world. The results of investigations of the high-speed rotor of a micro turbine, being an element of the micro power plant in dispersed power engineering based on renewable energy sources - are presented in the paper. The basic problem of such devices is to assure a stable rotor operation within the entire range of rotational speeds. Foil bearings and special rotor structure were applied. It turned out that the situation in that the rotor – after loosing its stability – stabilises again when the rotational speed increases, is possible. This is a new phenomenon determined by the author as 'multiple whirls'. Possibilities of stabilizing the situation by the application of hybrid lubrication and siphon pockets are also presented in the paper.

Another topic, discussed in the hereby paper, is an assessment of the influence of a random character of certain input data – in this case - changes of external excitations of the system. This problem is related to the so-called heuristic models often placed in opposition to widely used algorithmic models. The obtained results indicate different influence of disturbances depending on the system working conditions. After exceeding the stability limit, it means in a highly nonlinear operation range, the influence of disturbances significantly decreases. It is rather unexpected result. Research tools such as computer series codes and the method of their experimental verification are also included in the paper.

1. Research tools and their verification

The MESWIR computer code, based on nonlinear models of complex systems rotor – bearings, was applied in research – Fig.1. Theoretical models, basic equations as well as the system itself, have been presented already several times during the conferences and in publications [1,2,3]. Due to that and having in mind the paper space limitation and its different aims, the MESWIR series code will not be presented here in details. However, it is worth mentioning that the most useful feature of this system is the possibility of description of the rotor machine state both in a linear and nonlinear range by means of the same tool - thereby describing new vibration forms at transition the stability limit. The description capability of bearings of a complex geometry of oil clearance including foil bearings is also important. The MESWIR code was experimentally verified both at the research stand and with using real objects such as large power turbosets [1].

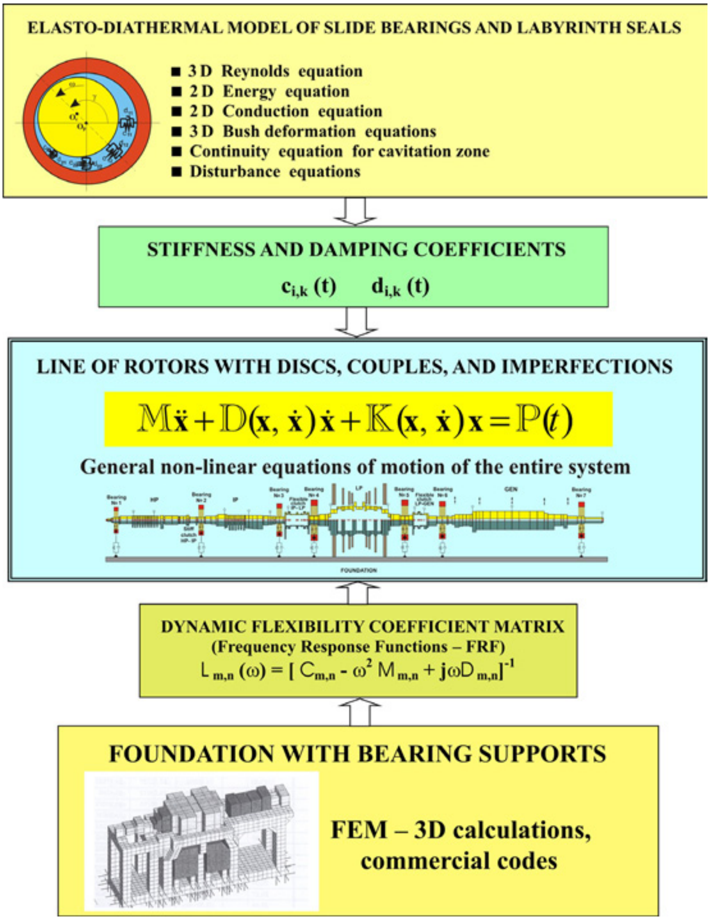

Fig. 1. Basic modules and algorithms of the MESWIR series code applied in the hereby paper [1]

For the needs of the research, this system was coupled with commercial programs of the ABAQUS type to determine dynamic properties of the supporting structure and of the whole system. Thus, bearing and rotor characteristics (MESWIR system) as well as dynamic characteristics of supporting structure (ABAQUS system) were calculated in one iteration loop. However, this type of coupling requires additional verifying of such research tools. The photo of the testing stand operating in the Vibrodiagnostics Laboratory of the Institute of Fluid-Flow Machinery, Polish Academy of Sciences, as well as the FEM discretisation of this system together with details concerning modelling of characteristic structural nodes such as fixing bolts or vibroinsulators – is presented in Fig.2. This is a system of a journal diameter d=0.1 m, discs diameter D=0.4 m and length L=3.2 m. Fig. 3 presents the experimental verification results done by a modal analysis with the application of PC CADA tools. As can be seen, the compatibility of results is quite satisfactory.

The situation is different in the case of experimental verification of dynamic flexibility coefficients. Obtaining a good compatibility - in such systems - is much more difficult and sometimes even impossible. This is illustrated in Fig. 4. The experimental data were obtained by sinusoidal excitations of subsequent supports and recording the bearing bush displacements, whereas the theoretical data constitute the results of calculations performed by means of the ABAQUS commercial software coupled with the MESWIR code. Regardless of such precise theoretical modelling of the entire system (Fig. 2), we did not manage to achieve sufficient compatibility of experimental and theoretical results – see: upper diagrams in Fig. 4. After several tests, only when a crack of one of the fixing bolts was taken into account in calculations that the verification results improved – see lower diagrams in Fig.4. It occurred, that this bolt was actually quite loose and behaved as if being cracked. This example can serve as an illustration of capabilities of the model based diagnostics, since knowing the symptom we can – by means of the computer analysis - localise the defect.

Research tools, prepared and verified in such a way, were applied in the research constituting the basic contents of the hereby paper.

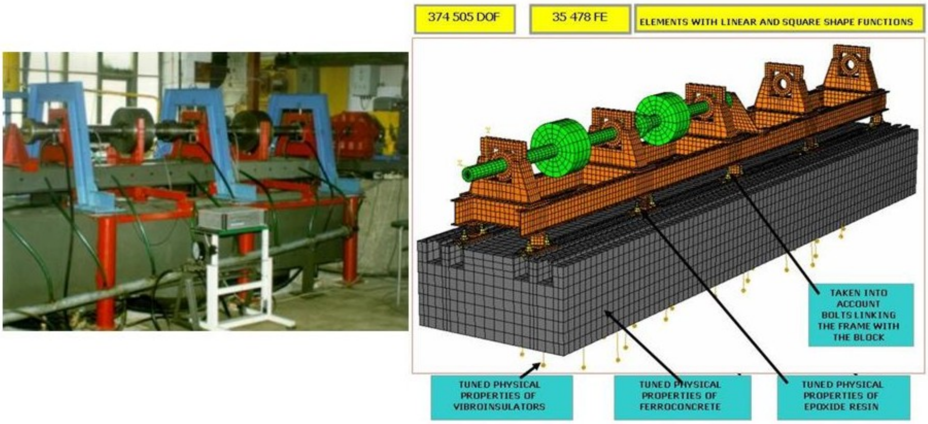

Fig. 2. Photo of the testing stand and the FEM discretisation of rotor and supporting structure (taking into account properties of coupling elements, vibroinsulators and a concrete block [2,4]

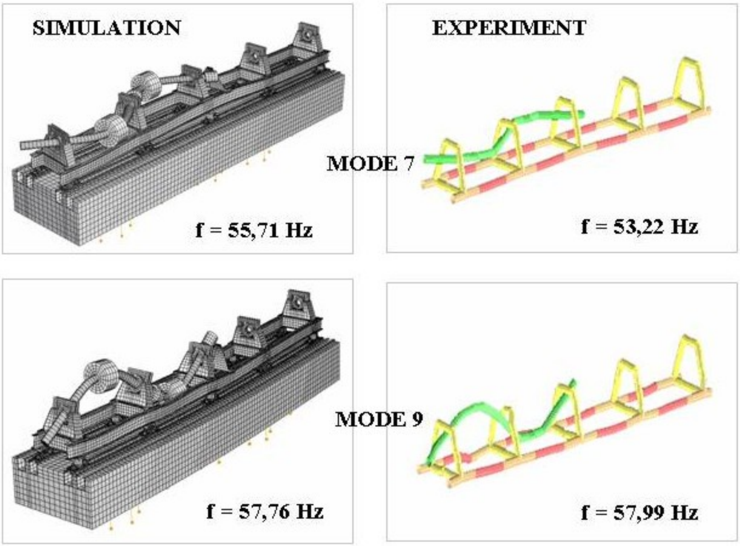

Fig. 3. Results of the experimental verification performed by modal analysis for two main modes (PC CADA system was used in experiments – right-hand side) [2,4]

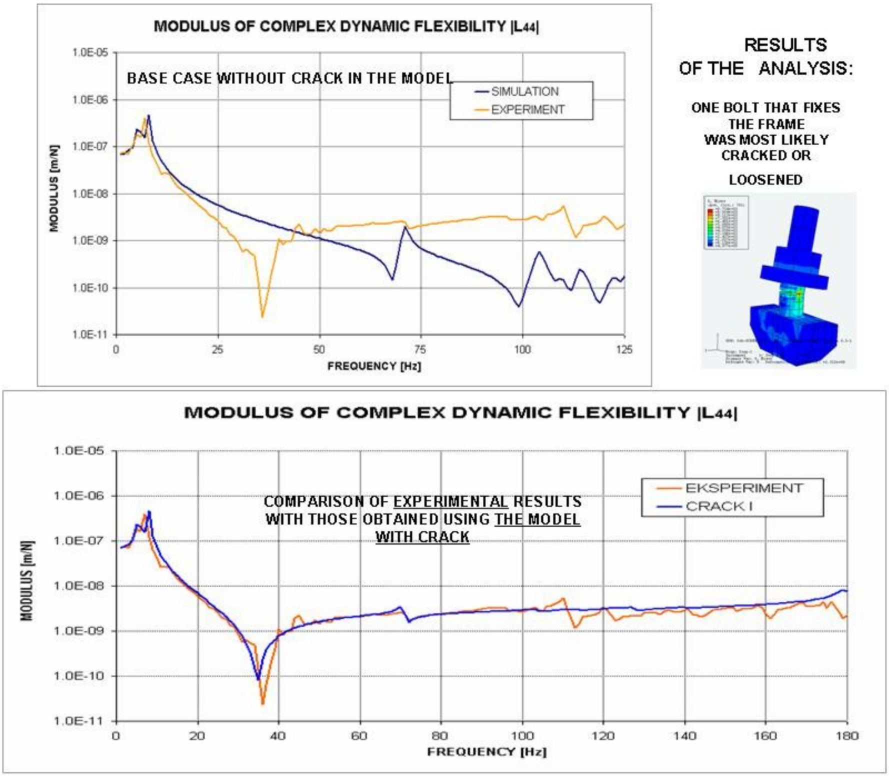

Fig. 4. Verification of dynamic flexibility coefficients for one bearing support of the system shown in Fig. 2. Experimental tests: excitations of one support by a sinusoidal exciter and measuring displacements. Theoretical investigations: calculations by the ABAQUS system coupled with the MESWIR series code. Upper diagram: calculations not taking into account any cracking (loosening); Lower diagram: calculations taking into account the crack of one bolt that fixes the frame [2,4]

2. Stability testing of high-speed rotors. Phenomenon of „multiple whirls"

Problems related to ecological energy generation at a small and dispersed scale become especially actual in recent years. A dispersed power engineering requires the construction of micro power plants, which includes the construction of micro-turbines with outputs ranging from a few to several KW. The idea of building micro turbines for low-boiling agents ORC, which ensures small dimensions of devices and easiness of servicing, has become attractive. Unfortunately it is obtained at the cost of a high rotational speed of the rotor, approaching 100 000 rpm. Thus, the main problem becomes ensuring the stable operation of the device within the entire rotational speed range of the rotor. This type of devices are most often coupled with boilers supplied with renewable energy sources.

A concept of such micro power plant developed in the IF-FM PAS in Gdansk is shown in Fig. 5 [5]. Essential elements of the micro turbine constitute slide bearings of special characteristics ensuring a high stability of a system. The foil bearings were chosen since – due to easiness of changing the oil clearance geometry (deformations of a membrane part of a bearing bush) – they can stabilise the system operation as the rotational speed increases.

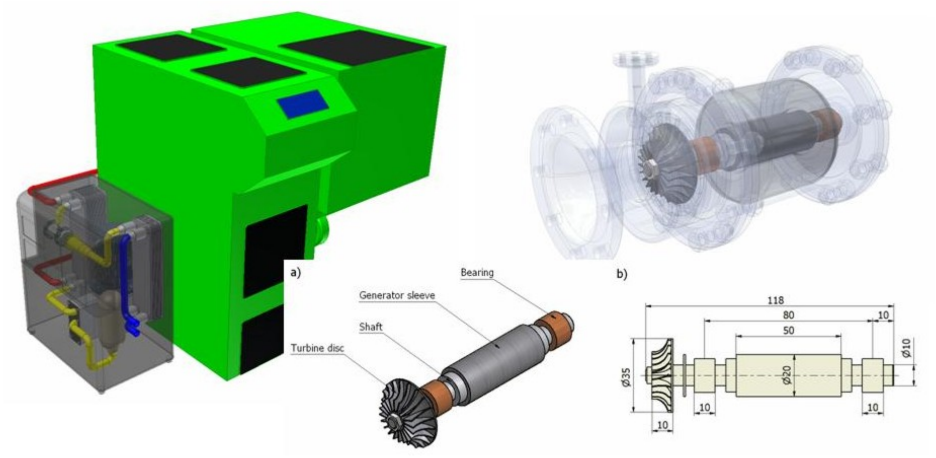

Fig. 5. Object of testing. Micro power plant (a boiler and turbine set) developed in the IF-FM PAS in Gdansk of a thermal and electric power of 20 KW and 3 KW, respectively. Single-stage radial-axial turbine for low-boiling agents ORC and a rotational speed up to 100 000 rpm [5]

Fig. 6 presents a sketch of bearings applied in the object shown in Fig. 5 and the FEM discretisation of the foil system in order to calculate a static substitute stiffness of a bearing, while Fig. 7 presents a verification of the obtained results. Compatibility of theoretical and experimental results is considered to be satisfactory. The notion of the substitute stiffness is essential for the calculation capabilities of the MESWIR code (multiple calculations in one iteration loop).

The system assumed for testing consisted of a rotor (with one disc and a generator) placed on two foil bearings of dimensions shown in Fig. 5. A low-boiling agent ORC was used as bearings lubricant, which significantly simplifies construction of the whole micro power plant. Typical values of the possible unbalancing of a rotor disc (as an excitation force) were assumed as well as some parametric values of damping the foil bearing bush and supporting structure (from the material data sheets).

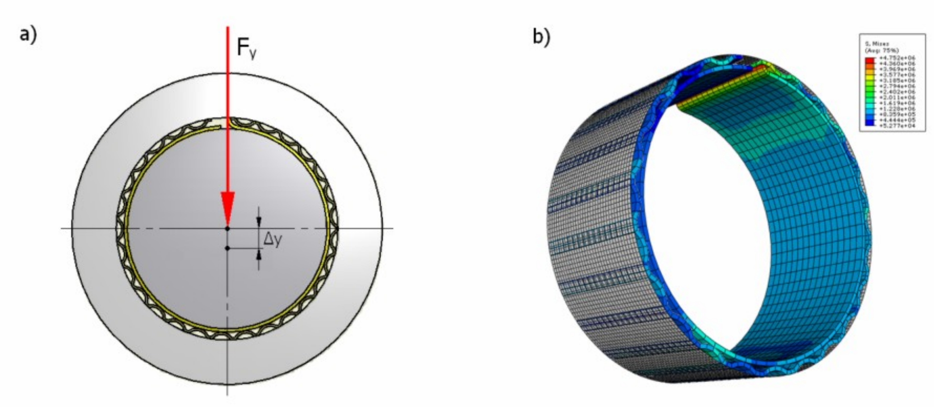

Fig. 6. Sketch of foil bearings applied in a micro turbine from the object shown in Fig. 5 (of a journal diameter 10 mm) and the FEM discretisation of an inner foil, membrane and outer foil – in order to calculate the substitute stiffness of the bearing bush [5]

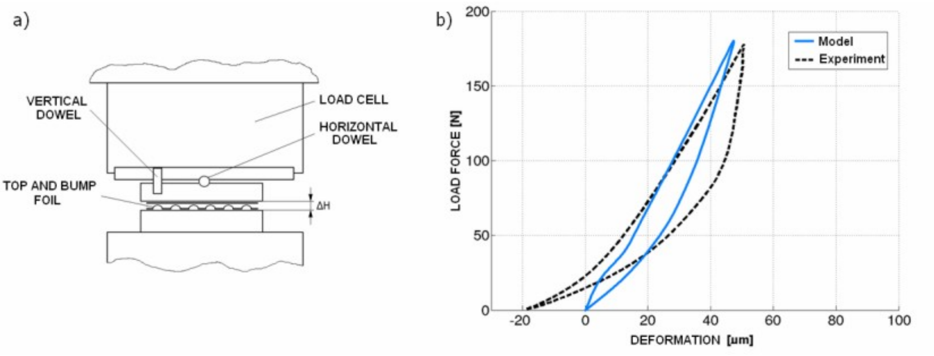

Fig. 7. Verification of a static substitute stiffness of the foil bearing bush. Model and calculations [5], experiment according to [6]

The calculation results in the form of amplitude – speed characteristics within the speed range up to 100 000 rpm are presented in Fig. 8.

The attention is called to quite different operation of bearing No 1 (at the disc) and bearing No 2 (free end). While bearing No 1 is stable within the entire range of rotational speeds, bearing No 2 exhibits two characteristic zones of exceptionally high vibration amplitudes exceeding 70 % of a bearing clearance. To identify this phenomenon and to exclude common resonance, the shape of relative displacement trajectories of the journal and bearing bush in these zones were analysed. The calculation results for the first zone and after passing through it are presented in Fig. 9.

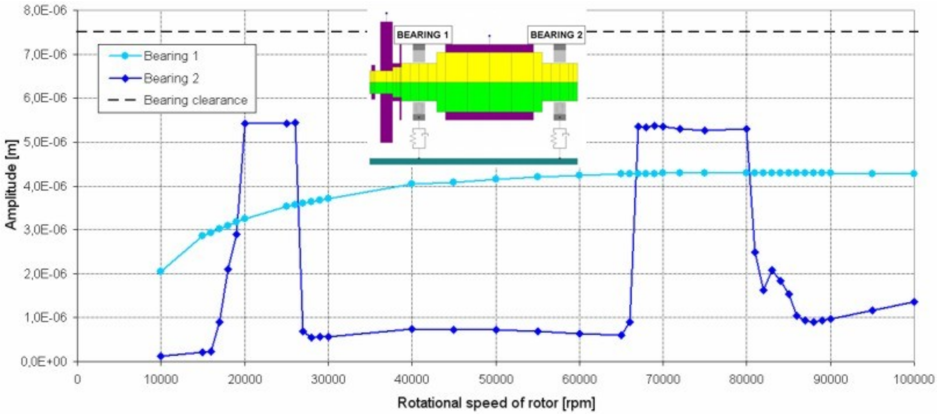

Fig. 8. Amplitude – speed characteristics of the rotor from the micro turbine (shown in Fig. 5) calculated for the relative vibrations of a journal and foil bearing bush. Illustration of the ‘multiple whirls’ phenomenon in bearing No 2 (repeated processes of formation and decaying of high amplitude zones caused by a hydrodynamic instability)

Analysis of fig. 9 explicitly indicates that the displacement trajectory of bearing No 2 at a rotational speed of 25 000 rpm (the first zone of high amplitudes) has features characteristic for the evoluted hydrodynamic instability, the so-called ‘whip’. The ‘whip’ means - in this case - a developed form of whirls of a lubricating agent within the lubrication clearance. This is pointed out by double shaft rotations (it means a vector of external excitations) falling to one full precession, which creates 2 phase markers (FM) on the trajectory. Actually, there are three markers since points for 0 and 720 degrees overlap each other, which not always happens. This means, that the same positions of the excitation force vectors (horizontally to the right: TAL = 0, 360 and 720 degrees) correspond to different positions on the journal trajectory within the bearing clearance.

However, the most unexpected is the observation that after the system has exceeded the first zone of hydrodynamic instability (which means the first ‘whip’) the system returns to a stable operation of bearing No 2 (it means to the typical situation, in which one phase marker on the trajectory corresponds to one rotation of the excitation vector). The situation remains a stable one up to the rotational speed of approximately 65 000 rpm. After the system has exceeded this speed a rapid instability (‘whip’) occurs again followed by a subsequent calming down. Thus, we are dealing here with a multiple ‘whip’ of a lubricating agent, understood as formation and decaying of the hydrodynamic instability as the rotational speed of the rotor increases. If we assume a stiff bearing bush we are unable to model the phenomenon. This allows to assume that variable deformations of the foil bearing bush (corresponding to the turbine rotational speed increase) are responsible for such process. Since this phenomenon is not known - from the references - to the author of this paper he suggests to call it 'multiple whirls'. The phenomenon of 'multiple whirls' has been quite often observed in practice by exploitation crews of large power plants. Small oil whirls were formed and then disappearing on one of the recorded bearings and this did not cause any instability of the entire system. Unfortunately those results have not been published. In our case, it means in the case of a small power micro turbine, we are dealing with large whirls i.e. whips, however, it is a different magnitude scale and a different rotational speed range.

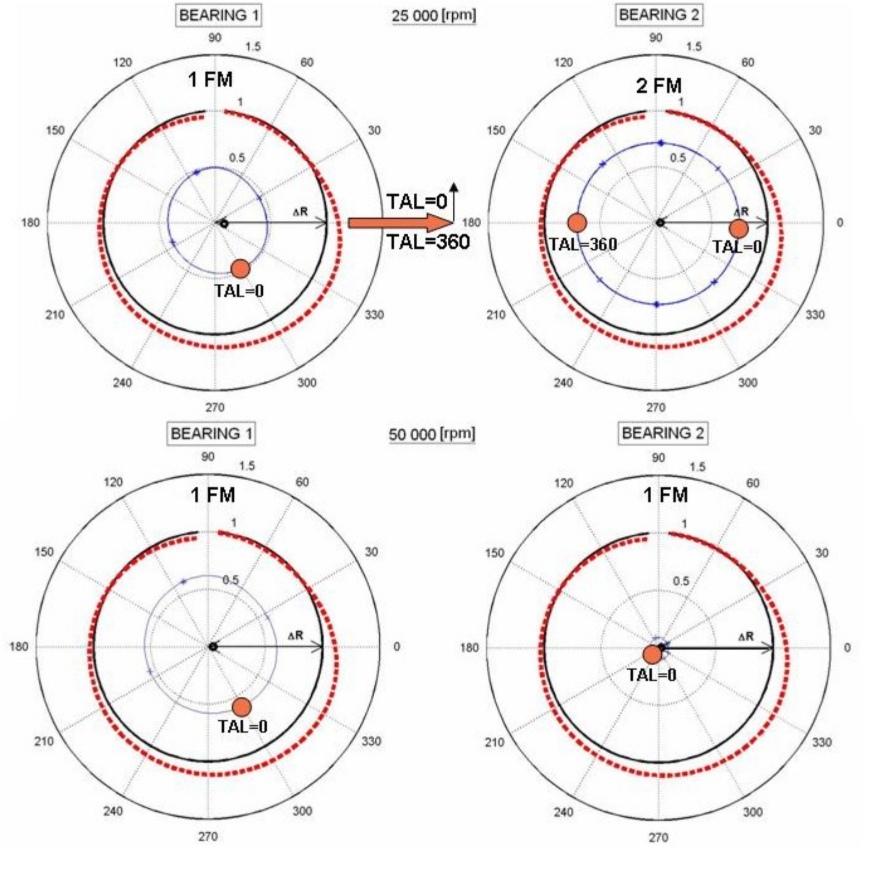

Fig. 9. Displacement trajectories of journal of bearing No 1 and 2 calculated for the first high amplitudes zone (25 000 rpm) and in the transient period (50 000 rpm). Image of the first hydrodynamic 'whip' in the trajectory – 2 phase markers FM (upper right-hand side trajectory). Broken red line indicates deformations of the bearing inner foil

A zone of 'multiple whirls' is very interesting from the point of view of the hydrodynamic pressure distribution. The very fact of existing 2 phase markers corresponds to the situation, in which for the same position of the exciting force vector (TAL = 0 and 360 degrees) we have two different journal positions on the trajectory and two different pressure distributions in the bearing. This is illustrated in Fig. 10.

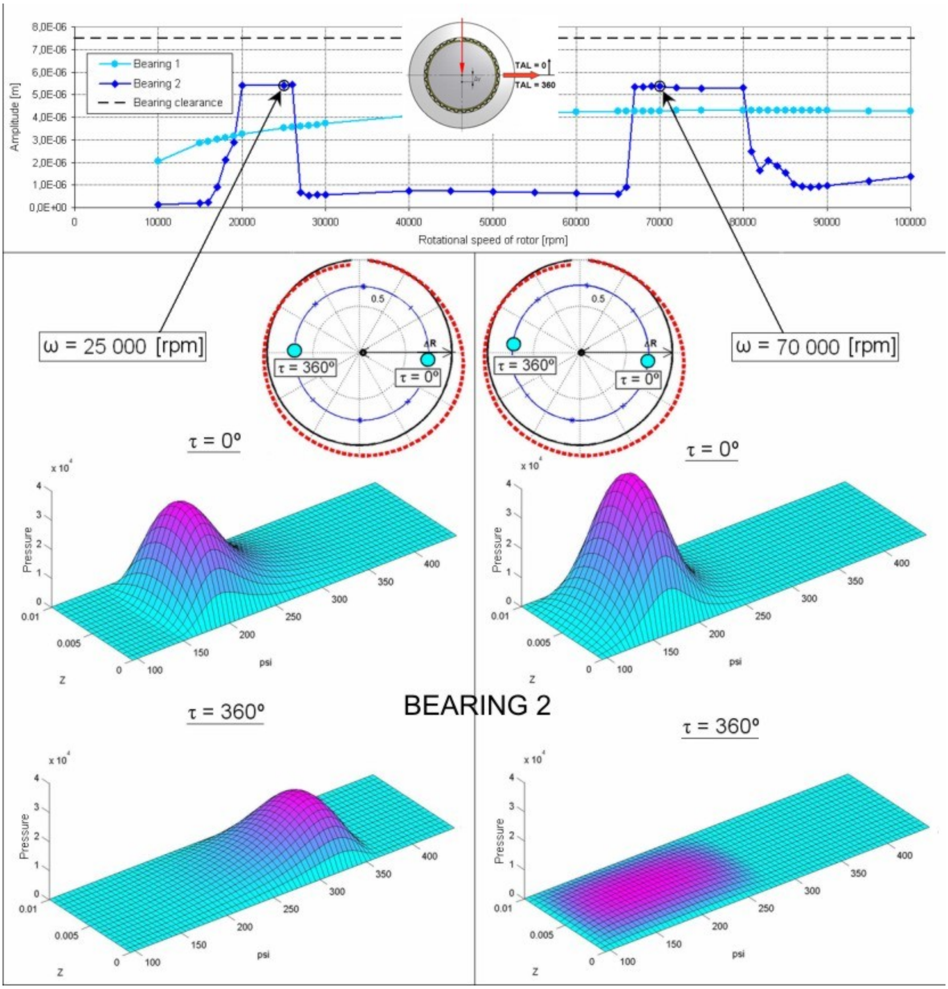

Fig. 10. Pressure distribution calculated for various positions of phase markers within a zone of ‘multiple whirls’ for the same position of the excitation force vector (horizontally to the right, it means for TAL = 0 and 360 degrees)

A question arises: is there any method enabling improvement of the dynamic state of a micro turbine - in this case - characteristics of bearing No 2? Various possibilities were considered. One of them was a concept of a hybrid lubrication with the application of siphon pockets. Several examples have been analysed. The most favourable was the case with 4 siphon pockets (2 in the upper part and 2 in the lower part of the bearing bush – Fig. 11) and siphon pressure at the level of 0.01 MPa. The calculation results are presented in Fig.11. Comparing these results with the amplitude-speed characteristics for bearing No 2 in Fig. 8, we will immediately notice that 'multiple whirls' disappeared and vibration amplitudes are significantly lower in the entire range of rotational speeds. This observation might suggests directions of further research, however, solutions based on hybrid lubrication – in the micro turbine case – significantly complicate design and exploitation side of the problem.

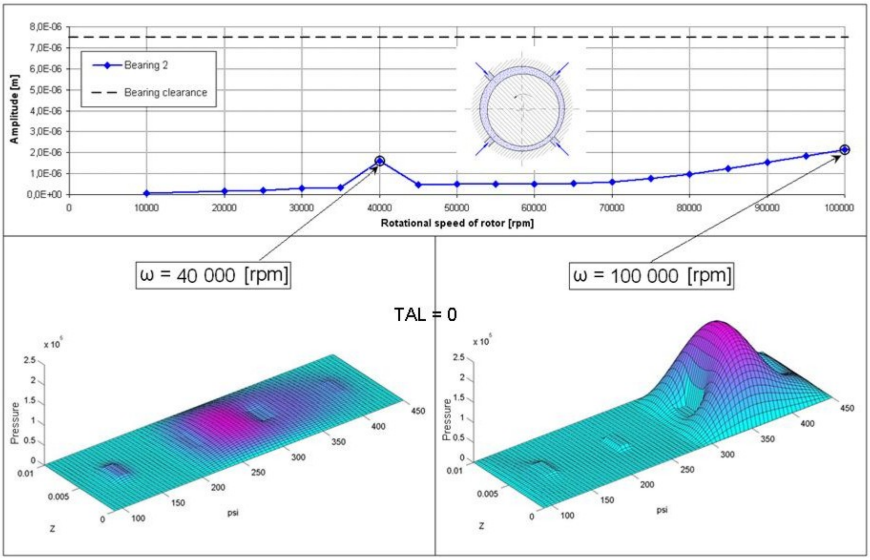

Fig. 11. Influence of siphon pockets and siphon pressure for the time-history of vibration amplitudes and pressure distribution – for bearing No 2 of the object shown in Fig. 5. 4 siphon pockets were applied (upper part of the figure) and pressure = 0.01 MPa

3. Stochastic variability of input data in heuristic modelling of rotors

A classic, traditionally applied for many years, approach to the state modelling of various kinds of machines is the algorithmic approach, i.e. the one in which for the known set of input data we obtain the same, precisely repeatable, set of output data (results). This is the obvious consequence of calculation capability of computers and the applied programs. However, this type of 'traditional' research tools, often highly advanced and applicable in practice, are neither able to correct the already introduced data nor to modify the assumed model depending on external conditions during the calculation procedure being in progress.

Meanwhile natural phenomena and a human nature (and thereby objects created by it) are of a heuristic character**,** which means possible feedbacks occurring in processes, intrinsic data and the previously assumed methodology of state assessment - corrections. It also means the necessity of taking into account influences of various errors and the uncertainty of input data, what is often intuitively done.

It is worth to mention that the trial of heuristic modelling means the necessity of having highly advanced ‘traditional’ research tools. The so called nonlinear description is extremely important since heuristic models are nonlinear by nature. Another substantial feature is the possibility of a smooth transition from the linear to nonlinear description applying the same research tools (the Superposition Principle cannot be used in this case). In consideration of the above, the MESWIR series code was applied in investigations. Fig. 12 presents the object used in tests as well as the concept of random changes of external excitation forces acting on a rotor disc. The randomness of changes was assumed (random-number generator was applied) although within limits +/- ΔP in proportion to the basic value P. Calculations were performed for different ΔP values simulating in this way various possible situations (e.g.: displacement of rotating masses, influence of magnetic fields, etc.).

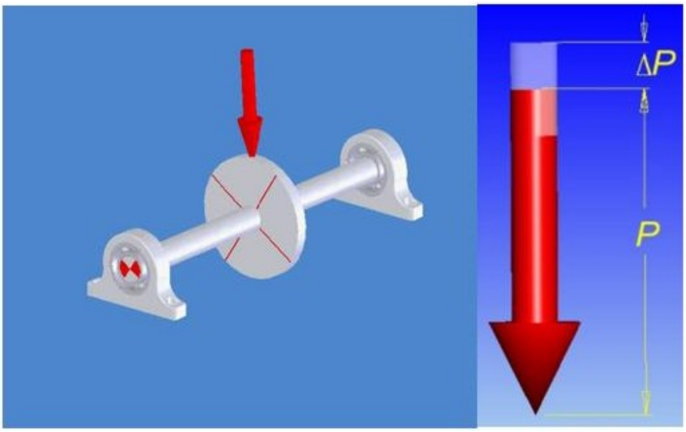

Fig. 12. Object of investigations: twin-support, symmetric rotor of a shaft diameter of 0.1 m, disc diameter 0.4 m, shaft length 1.4 m and a mass of 179 kg. Classic, cylindrical slide bearings lubricated by machine oil were used. The stochastic variability of an external excitation force within limits +/- ΔP= 20% in proportion to the constant (basic) value P was assumed

External rotating excitation forces, which can randomly change within limits +/-20% in proportion to the basic value, P, was assumed for the analysis

- Fig. 12. The calculation results for the rotor shaft rotational speed from 300 rpm to 5550 rpm are shown in Fig. 13 and 14 [7]. The trajectory of the rotor centre loaded by a constant force (basic) - rotating synchronously - is shown for the comparison on the left-hand side of each figure, whereas the trajectory of the rotor loaded by randomly changing force - within limits +/-ΔP=20% in proportion to the basic force P - is shown on the right-hand side of each figure. Images of trajectories in co-ordinate systems related to the maximum value of bearing clearance are placed in the upper part, while images of trajectories magnified as much as possible to exhibit clearly the phenomena - are shown in the lower part of each figure.

The analysis of the figures indicates that influence of randomly changing values of the external excitation force is significant, in the case of small rotational speeds of the rotor. When the speed increases, this influence diminishes, what can be explained by the influence of rotor inertial forces generally attenuating a time-history. At the very stability limit a certain increase in the trajectory disturbance can be observed. However, disturbances caused by the stochastic variability of input data decay when the rotor rotational speed increases, it means when the hydrodynamic instability develops – Fig.14. This is rather a surprising result, since it could have been expected that such perturbations – after exceeding the stability limit – would intensify the instability of the entire system since it has been already unstable. Similar conclusions were found when investigations were performed for various ΔP values and various algorithms of random excitations. Thus, a system defect in the form of the hydrodynamic instability attenuates to a certain degree the defect caused by stochastic effects of input data. It is an interesting observation resulting from the performed research.

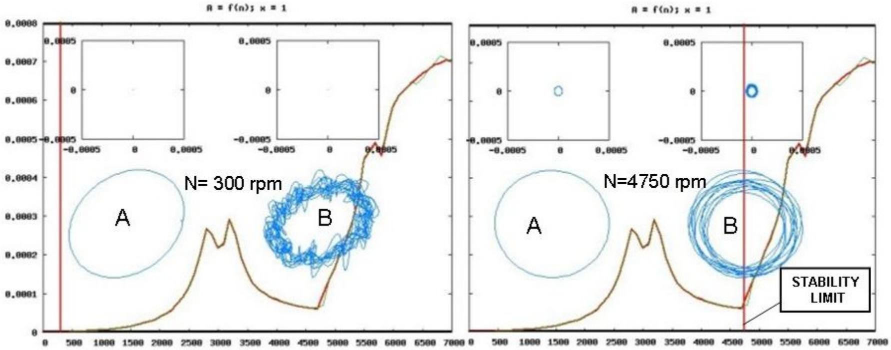

Fig. 13. Displacement trajectories of the rotor centre - within a stable operation range - calculated for the constant excitation force (basic) P (part A) and for the randomly changing – within limits +/- ΔP= 20% (part B) shown at the background of the rotor amplitude-frequency characteristics [7]

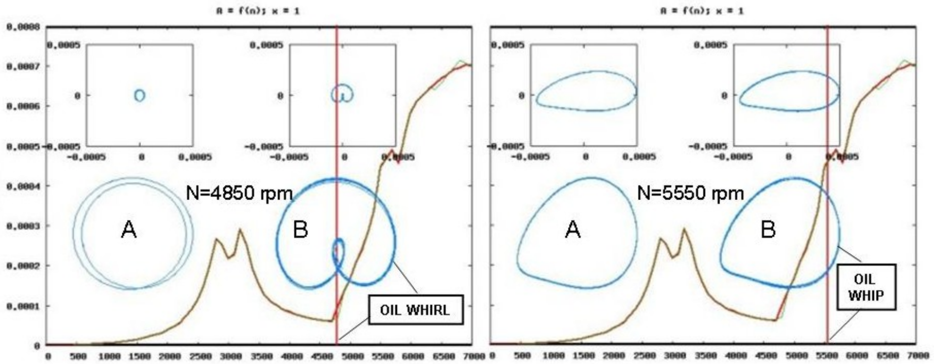

Fig. 14. Displacement trajectories of the rotor centre after the system exceeded the stability limit calculated for the constant basic force P (part A) and for the randomly changing – within limits +/- ΔP= 20% (part B) shown at the background of the rotor amplitude-frequency characteristics [7]

4. Final conclusions

The phenomenon of 'multiple whirls' presented in the hereby paper, found by advanced computer simulations and performed by means of the experimentally verified own and commercial codes, requires further investigations both theoretical and experimental. Experimental investigations in this field are planned in the Gdansk Research Centre. However, they will be put into operation only after building the first prototypes of micro power plants and relevant testing stands. Currently we have only unpublished information that the similar phenomenon was recognised by means of direct measurements of vibrations at large power plants. Interesting hint for further investigations constitute the obtained results of hybrid lubrications. It is possible to stabilise the system by this method but at the cost of significant structural complications.

Preliminary considerations concerning heuristic modelling of rotors are included in the paper. In such modelling we took into account uncertainty and randomness of the calculation input data and mutual couplings. It was found that an influence of the stochastic variability of input data decreases after the system has exceeded the stability limit. This indicates that the defect of the hydrodynamic instability type can attenuate - to a certain degree - the defect in the form of a random scatter of input data.

References

[1] KICINSKI J., Rotor Dynamics, IFFM Publishers, ISBN 83-7204-542-9, pp. 539, Gdansk, 2006.

[2] BATKO W., DABROWSKI Z., KICINSKI J., Nonlinear Effects In Technical Diagnostics, Publishing and Printing House of the Institute for Sustainable Technologies, ISBN 978-83-7204-748-9, pp. 303, Warszawa, 2008.
[3] KICINSKI J., Materials and Operational Imperfections in Rotating Machinery, IFToMM – Seventh International Conference on Rotor Dynamics, Vienna (Austria), Paper-ID 307.
[4] ZYWICA G., Simulation Investigation of the Effect of a Supporting Structure Defect on the Dynamic State of the Rotor Supported on Slide Bearings, ASME International Design Engineering Technical Conference, Las Vegas, DETC2007-34415.
[5] KICIŃSKI J., ŻYWICA G., BANASZEK S., BOGULICZ M., CZOSKA B., Modelling of Thermo-Elastic Deformations of the Foil Bearing Bush with the Application of Authors' Own and Commertial Calculation Codes (in polish), Internal Report No 22/08 of the IF-FM PAS, Gdansk 2008.
[6] KU R., HESHMAT H.: Compliant Foil Bearing Structural Stiffness Analysis: Part II – Experimental Investigation. ASME Journal of Tribology, Vol. 115 (1993), 364-369.
[7] PIETKIEWICZ P., KICIŃSKI J., CZOSKA B., MARKIEWICZ A., Development of Defect Models – with Uncertainty of Input Data Taken into Account (in polish), Internal Report of the IF-FM PAS, Gdansk 2008.

Journal of Energy Science, Vol. 1, No. 1, 2010, pp.69-80

Hydrodynamic effects produced by oscillating foil in fluid

HENRYK KUDELA, TOMASZ KOZŁOWSKI

Wroclaw University of Technology, Department of Numerical Fluid Flow Modelling, 50-370 Wroclaw

In the paper we presented the numerical results related to the unsteady effects produced by the oscillating foil in fluids. The paper was inspired by the studies over insects and birds fly. It was shown that by choosing of the frequency and amplitude of oscillations it can be generated the different kind of the vortex Karman street and this way control the drag, lift and thrust force exerted on the object. For numerical study vortex-in-cell method was used. We establish numerically relationship between Strouhal number amplitude of oscillations and vortices topology behind the oscillating foil by constructing the phase space diagram. The computational result are in consistent with the existent experimental data.

Symbols

ω – z-direction component of the vorticity field
ψ – stream function
$\mathbf{u}$ – fluid velocity vector
A_0 – Amplitude of profile oscillations
f – frequency of oscillations
c – chord length
U_0 – free stream velocity
St_A – Strouchal number defined with respect to the amplitude of oscillation
St – Strouchal number with respect to the chord length
$C_{D,L}$ – drag and lift coefficient respectively

1. Introduction

The great interests in the low Reynolds number unsteady aerodynamics of oscillating foil stems from the increasing importance in the micro air vehicles and from the will to understand the aerodynamics of natural flyers. Flapping motion is a basic mode of locomotion in birds, insects and fishes. The basic question birds and insects flight is how do they generate enough lift and the thrust force to be able to perform remarkable maneuvers with rapid accelerations and decelerations. From the point of the fluid mechanics, we believe that all the phenomena, that are related to the generation of hydrodynamic forces, are ruled by the dynamics of the vorticity. The Karman vortex street in the flow over the steady profile generate the drag force. On the outer side, the flapping motion of the profile may reverse Karman vortex street producing the thrust force. In the paper it was demonstrated the lift force and thrust force production for the basic two dimensional oscillating foil. Although, flight in nature is naturally three-dimensional, when the ratio of the span to the chord is large enough, the two-dimensional model is widely used [11-15]. It's believed that 2D model allow to capture the essence of flapping flight hydrodynamics. The primary parameter, that characterize the oscillating foil, is amplitude of the oscillation (A_C), the Strouhal (St_A) and Reynolds number (*Re*). We demonstrated dependence between the these basic parameter and vortex wake topology, the reversing of the topology of the vortex Karman street and deflection of its from the main direction of the flow. These phenomena directly influenced production of the thrust and lift forces.. For numerical study we choose the Vortex-In-Cell (VIC). The importance of the vortex particle method lies in the possibility of the analyzing more easily and directly the vorticity field due to fact that in computation the vortex particles that carry the information about the vorticity field are used. Attractive feature of the method is also the elimination of pressure from the equation of the fluid motion.

2. Vortex-in-cell method

2.1. governing equations

The Navier-Stokes equation in primitive variables with the coordinates fixed to the moving body has the form [14]

$$\frac{\partial u}{\partial t} + \nabla u \cdot u = -\nabla p + \nu \Delta u - \frac{\partial U_0}{\partial t} + \left[-\frac{\partial \Omega_0}{\partial t} \times r + 2\Omega_0 \times u + \Omega_0 \times (\Omega_0 \times r) \right], \quad (1)$$

$$\nabla \cdot u = 0\,, \quad (2)$$

where Ω_0 is the angular and U_0 is the translation velocity vector of the wing. The last three terms in equation (1) arise from non-inertial coordinate system and denote non-inertial force due to rotational acceleration, the Coriolis force and the centrifugal force respectively. Taking the curl by the both side of the equation (1) and assuming of 2D flow, the evolution equation for the vorticity in the reference system fixed to moving body, one can transform to the form [6]

$$\frac{\partial(\omega^*)}{\partial t} + \nabla\omega^* \cdot u = \nu\Delta\omega^*, \tag{3}$$

$$\Delta\psi^* = -\omega^*, \tag{4}$$

$$u = \nabla \times (0,0,\psi^*), \tag{5}$$

where $\omega^* = \omega + 2\Omega_0$, $\psi^* = \psi - \psi_\infty$ and stream function far from the body, at the infinity ψ_∞ take the form $\psi_\infty = U_0(y\cos\alpha - x\sin\alpha) - (\Omega_0/2)(x^2+y^2)$. Further, the star index (*) was dropped. The detailed description of solution of the Helmholtz equations in moving reference frame can be found in [6].

2.2. Vortex-in-cell method for conformal geometry

To better fit of numerical grid to solid boundary, we transform the non-rectangular physical region (x,y) – variables to the rectangular one (ζ,η). The following conformal transformation was applied, Fig. 1

$$x + iy = \cosh(\zeta + i\eta), \tag{6}$$

In new variables (ζ,η), the equations (3), (4) have the form

$$\frac{\partial\omega}{\partial t} + \nabla\omega \cdot u = \frac{\nu}{J}\Delta\omega, \tag{7}$$

$$\Delta\psi = -\omega \qquad u = \frac{1}{J}\frac{\partial\psi}{\partial\eta} \qquad v = -\frac{1}{J}\frac{\partial\psi}{\partial\zeta}, \tag{8}$$

where J denotes Jacobian of the conformal transformation. The nullifying of the normal velocity component is obtained by setting ψ = const. on the wall. The no-slip condition is realized by introducing a proper portion of vorticity, that ensure the condition $\mathbf{u} \cdot \mathbf{s^0} = 0$, were $\mathbf{s^0}$ is tangential unit vector [8,16]. In the VIC method the continuous vorticity field is approximated with the discrete vortex particles distribution. The flow region is covered with the numerical grid

(ih, jh), $h = \Delta\eta = \Delta\zeta$. In every grid node ($i,j$), the particles with circulation $\Gamma_{ij} = \int_A \omega d\zeta d\eta$ are placed, where $A = h^2$ and

$$\omega(\zeta,\eta) = \sum_{i,j} \Gamma_{ij}\delta(\zeta-\zeta_i)\delta(\eta-\eta_j)\,. \tag{9}$$

The viscous splitting algorithm [3] was used for solution of (7), (8). At first, the inviscid fluid motion equation was solved

$$\frac{\partial\omega}{\partial t} + \nabla\omega\cdot u = 0\,. \tag{10}$$

From (11) stems that vorticity is constant along the trajectory of the fluid particles. According to Helmholtz theorem [18], vortex particles are moving like material fluid particles. The differential equation (10) is replaced by the set of ordinary equations

$$\frac{d\zeta}{dt} = u \quad \frac{d\eta}{dt} = v \quad \zeta(0) = \alpha_1 \quad \eta(0) = \alpha_2\,, \tag{11}$$

where $\alpha = (\alpha_1,\alpha_2) = (\zeta_i, \eta_j)$ means Lagrangian coordinate of fluid particles. The number of the particles are equal to the number of the grid nodes. The finite set of equations (11) was solved by fourth order Runge-Kutta method. The velocity field was obtained by solving Poisson equation (8) on the numerical grid.

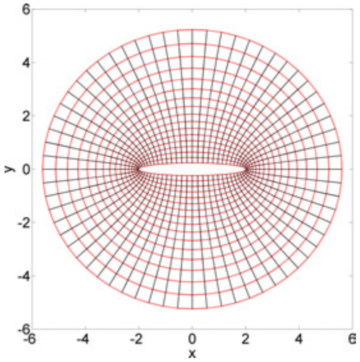

Fig. 1. Elliptical grid in the physical domain

The velocities of the particles that are found between the grid nodes were calculated by the two dimensional bilinear interpolation. At second step the viscosity was taken into account. The diffusion equation was solved

$$\frac{\partial \omega}{\partial t} = \frac{\nu}{J} \Delta \omega, \quad \omega(\zeta, \eta) = 0 \;\; \omega |_{wall} = \omega_s \, , \tag{12}$$

where ω_s was calculated on the basis of the Poisson equation (8). The non–slip condition $u = 0$ is realized by adding proper value of the vorticity on the wall ω_s, [16].

After particles displacement according to equation (11), one have to redistributed the mass of the particles to the grid nodes, Fig. 2. It was done, according to the formula

$$\omega_{ij} = \frac{1}{h^2} \sum_p \Gamma_p \varphi_h(\zeta) \varphi_h(\eta) \, , \tag{13}$$

where $\varphi_h(\cdot)$ denotes the kernel of the interpolation function. Interpolation of particle masses onto the grid nodes has the fundamental meaning for the precision of the VIC method. In present work the redistribution process was performed using Z-splines [2]. After redistribution, the diffusion equation (12) was solved on the numerical grid, with alternating direction implicit (ADI) scheme [13]. Detailed numerical test of the VIC method can be found in [9], [10].

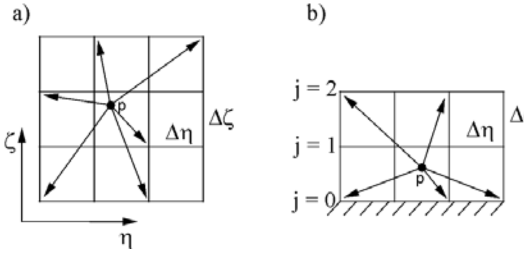

Fig. 2. Redistribution of the particle masses onto the neighboring grid nodes, a) for particles laying inside of the computational domain (at least one cell from the wall), b) for the particles in the vicinity of the wall

3. Numerical simulation

3.1. Formulation of the problem and computation details

In the present study, we used the elliptic foil with prescribed motion in vertical direction according to the equation

$$y(t) = \frac{A_0}{2}\cos(2\pi f t) \quad u = \frac{dy}{dt}, \tag{14}$$

where $y(t)$ denotes instantaneous position of the wing center, A_0 is the amplitude, f is the frequency of the oscillation and u denotes the airfoil vertical velocity. Far from the body we assumed that velocity of the fluid U_0 is constant, Fig. 3. In literature, a motion of the profile described by the equation (14) is known as a plunging. The phenomena related to the plunging foil can be characterized by three non-dimensional numbers, Re – Reynolds number, St – Strouhal number and non-dimensional amplitude of plunging A_C, [1], [4], [5]:

$$\mathrm{Re} = \frac{U_0 c}{v}, \quad St = \frac{fc}{U_0}, \quad A_C = \frac{A_0}{c}, \tag{15}$$

where c is the chord of the foil and v is a kinematic coefficient of fluid viscosity

The chord was set to $c = 2$ and thickness of the profile $e = 0.4$. We perform the calculations for the constant Reynolds number $Re = 100$ and homogeneous fluid with density $\rho = 1$. The plunging frequency was fixed to $f = 0.5$ and the Strouhal number St was changed by varying of the free stream velocity U_0. The calculations were carried on for dimensionless time $T = ft$, in range $T = (0,10)$.

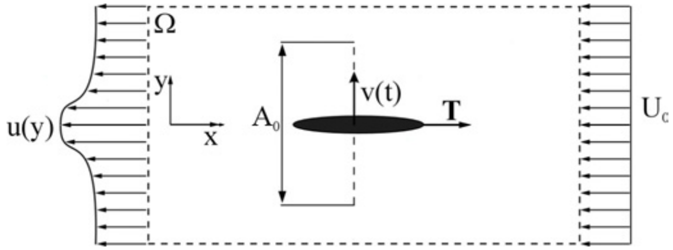

Fig. 3. Scheme of the plunging airfoil immersed in the fluid

In calculation the elliptical mesh, given in Fig. 1 was used, with 256 grid nodes in radial direction and 256 grid nodes in azimuth direction. The time step Δt was constant and set to $\Delta t = 0.01$.

3.1. Numerical results

The hydrodynamic forces exerted on the moving body immersed in the fluid can be explain by the dynamics of vorticity [17,18]. By proper choice of the frequency and amplitude of plunging we can change the position of the vortices in the vortex street. In Fig. 4, 5, 6, 7 and 8 it was shown the different kind of the vortex street. In Fig. 4 ($St = 0.6$, $A_C = 0.25$) it was presented the vortex Karman street (vKs). On the left side of the Fig. 4 the vortex street was visualized by the streak lines (passive particle that was taken by fluid from the surface of the profiles). On the right part of the figures the flow is visualized by vorticity distribution and streamlines. It was drawn also the mean velocity profiles behind the foils. By vortex Karman street, we mean the vortex street when the vortices shed form the upper (lower) side of the profile stay on the upper (lower) side of axis of symmetry. The situation that is presented in Fig. 5 ($St = 0.8$, $A_C = 0.5$) is called align vortices (av). It means that the vortices are placed on the axis of symmetry. The drag force ($F_D = \frac{1}{2} C_D \rho v^2 A_f$), where C_D means drag force coefficient, was dropped but is not equal zero. It is transitional state of vortex street.

Increase of the plunging amplitude ($St = 0.8$, $A_C = 0.75$) leads to the reverse vortex street, (Fig. 6). The vortices shaded on the upper surface of the profile changed the position and went to the below of symmetry axis. The vortices created on the lower part of the profile surface went to the upper positions. In such configuration the thrust force was produced ($C_D < 0$). For inverse vortex street state one can find the parameters for that there was drag force was equal zero. Further increase the plunging amplitude ($St = 0.8$, $A_C = 1.0$) leds to the deflection of the reverse Karman vortex street (drvKs) what results in production of the lift force, Fig.7. In Fig. 8 it was presented that for ($St = 1.2$, $A_C = 1.0$) the random vortex street was obtained. It is worth to note that in this regime the maneuverability will be difficult due to the random distribution of hydrodynamic forces on the profile.

One can summarized the above results in phase space diagrams. In Fig. 9 the relation between the wake type and Strouhal number St and amplitude of oscillation is presented. For given Reynolds number $Re = 100$, at the small amplitude of oscillations, we observed the stationary vortex bubbles behind the foil. They are attached to the profiles.

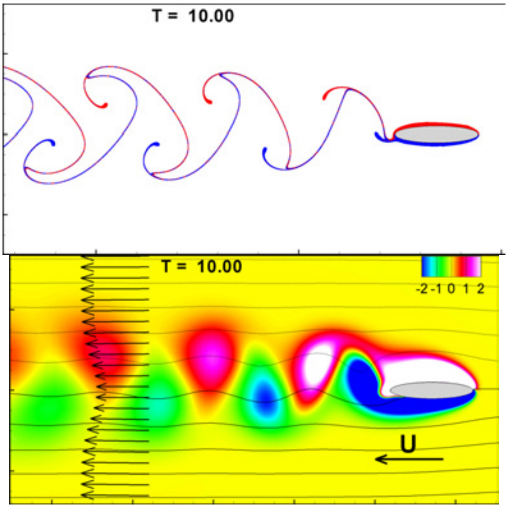

Fig. 4. Vortex Karman street produced by plunging foil with $St = 0.6$ and $A_C = 0.25$. The arrows behind the airfoil denotes averaged fluid velocity profile. The arrow on the bottom right correspond to value of the free stream velocity U_0. In Fig. 9 this case is represented by □

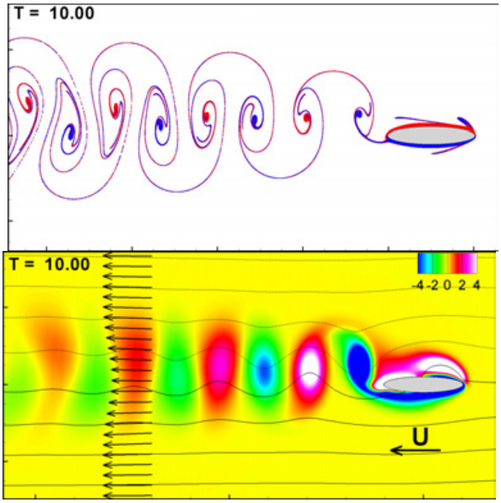

Fig. 5. Aligned vortices ,$St = 0.8$ and $A_C = 0.5$. In Fig. 9, denoted by ■

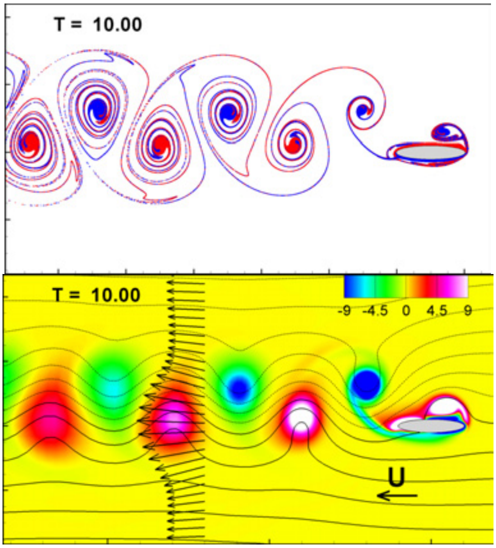

Fig. 6. The reversed Karman vortex street, *St* = 0.8 and A_C= 0.75 (rvKs). In Fig.9 denoted by +

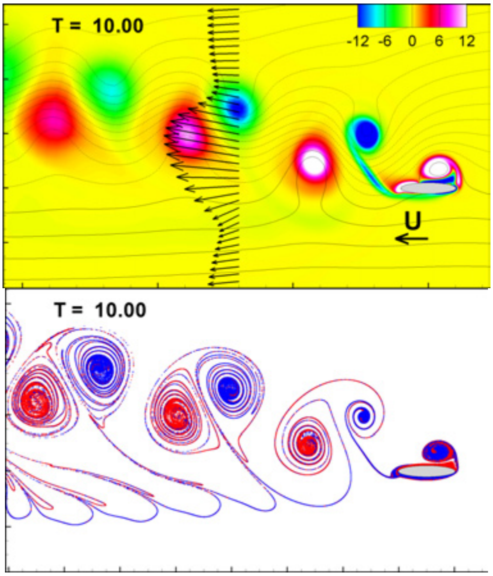

Fig. 7. Deflected reverse vortex Karman (drvKs) *St* = 0.8 and A_C = 1.0. In Fig. 9 denoted by Δ

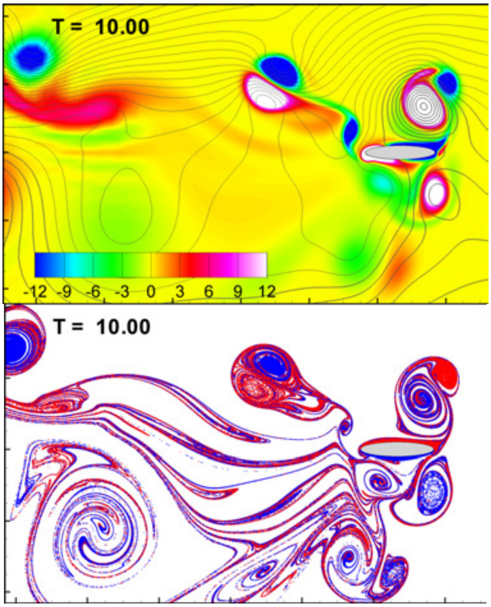

Fig. 8. Random vorticity field , *St* = 1.2 and A_C = 1.0. In Fig. 9 marked by ●

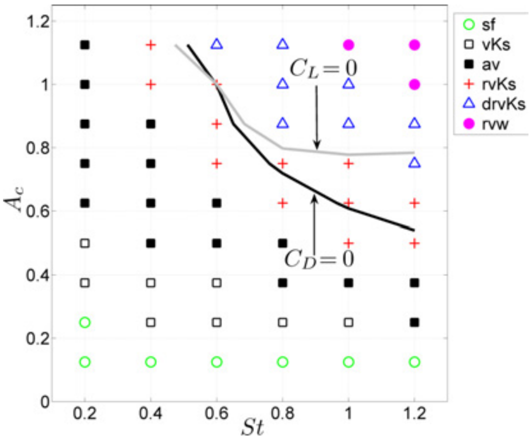

Fig. 9. Relationship between Strouhal number *St*, non-dimensional plunging amplitude A_C and vortex topology in the wake behind of the foil, *Re* = 100. Symbols denotes: ○ - steady vortex bubbles, □ - vortex Karman street (vKs), ■ - transition region with aligned vortices (av), + - reversed vortex Karman street (rvKs), Δ - deflected reverse Karman vortex street, ● - random vortex wake

This regime depicted with ○ in Fig. 9 is independent on the Strouhal number. If the amplitude of oscillation increase, the vortex bubbles are no longer stationary forming Karman vortex street behind the body, denoted by □.

The vortices reduces fluid momentum in the profile wake caused the drug production ($C_D > 0$). The transitional region remarked by ■, are related to the situation when opposite vortices form a row behind the profile, aligned vortices (av).

Inversion of the topology of the vortices (see Fig. 6) led to the revere vortex Karman street (rvKs) that results in the production of thrust force. The counter-rotating vortices in the foil wake increase the fluid momentum forming jet flow. However generation of the thrust force isn't obligatory for this type of the wing wake topology. In the Fig. 9 the curve for $C_D = 0$ is depicted. Only over this $C_D = 0$ curve, the thrust force is generated ($C_D < 0$).

If the Strouhal number and amplitude of oscillations increase, the symmetry of the wake is broken and the deflection of the vortex Karman street (drvKs) from horizontal direction is observed,. This phenomena is related to the lift force production [7]. As for the thrust force, the positive lift force appear over the curve with $C_L = 0$. Further increase of the Strouhal number and amplitude of oscillations results in the random vorticity field generation The similar the phase space diagram for (St, A_C) was obtained experimentally for pitching profile [4,5].

3. CONCLUSIONS

The Vortex-In-Cell method was used to model the hydrodynamics effect of the plunging foil. Despite of the 2D fluid flow simplification, the dynamics of fluid motion is very reach and permit to understand the non-linear nature of the flapping effect and the structure of the vorticity flow. The dynamics of the vorticity field is responsible for production of the lift and thrust forces during the flight of the natural flyers. The computational result are in qualitative agreement with experimental data presented in [4], [5], although we assumed much smaller Reynolds number and perform the basic plunging motion of the profile.

References

[1] ANDERSON J., M., STREITLIEN K., BARRET D., S., TRIANTAFYLLOU M., S. Oscillating foils of high propulsive efficiency J. Fluid. Mech, 360, 1998

[2] BECERRA SAGREDO Moment conserving Cardinal Splines Interpolation of Compact Support for Arbitrarily Spaced Data, Research Report No. -10 Zurich Switzerland, 2003

[3] COTTET G-H., KOUMOUTSAKOS P. Vortex Methods Theory and Practice, Cambridge University Press, Cambridge, 2000

[4] GODOY-DIANA R., AIDER J-L.,WESFREID J., E. Transitions in the wake of a flapping foil Physical Review E, 77, 2008

[5] GODOY-DIANA R., MARAIS C., AIDER J-L., WESFREID J., E. Model for the symmetry breaking of the reverse Benardvon Karman vortex street produced by flapping foil J. Fluid Mech., 622, 2009

[6] GUSTAFSON K., E., LEBEN R., FREYMUTH P. Visualization and computation of hovering mode, Vortex methods and vortex motion, 1991

[7] JONES K., D., DOHRING C., M., PLATZER M., F. Wake Structures Behind Plunging Airfoils: A Comparison of Numerical and Experimental Results, AIAA, 1996

[8] KOUMOUTSAKOS P., LEONARD A., PEPIN F. Boundary conditions for Viscous Vortex Methods, J. Comp. Phys., 113, 1994

[9] KUDELA H., MALECHA Z. M. Viscous flow modelling using the vortex particle method Task Quarterly, 13, 2009

[10] KUDELA H., KOZLOWSKI T. Vortex in cell method for exterior problems, J. Theor. Appl. Mech., 47, 2009

[11] PESKIN CH., S., MILLER L. A. When vortices stick: an aerodynamic transition in tiny insect flight, J. Exp. Biol., 207, 2004

[12] SHYY W., LIAN Y., TANG J., VIIERU D., LIU H. Aerodynamics of Low Reynolds Number Flyers Dover Publications, Dover Publications, Cambridge University Press, 2008

[13] THOMAS J., W. Numerical Partial Differential Equations: Finite Difference Methods, Springer, 1995

[14] WANG Z., J. The role of drag in insect hovering J. Exp. Biol., 207, 2004

[15] WANG Z., J., BIRCH J., M., DICKINSON M., H. Unsteady forces and flows in low reynolds number hovering flight: two-dimensional computations vs robotic wing experiments J. Exp. Biol., 207, 2000

[16] WEINAN E., JIAN-GUO LIU Vorticity Boundary conditions and Related Issues for Finite Difference schemes, J. Comp. Phys. 124, 66, 1996

[17] WU J. C. Theory for aerodynamics force and moment in viscous flows AIAA, 19, 1981

[18] WU J. Z., MA H.Y., ZHOU M.D. Vorticity and Vortex Dynamics, Springer, 2005

Journal of Energy Science, Vol. 1, No. 1, 2010, pp.81-91

Analysis of the possibility of determining the internal structure of composite material by estimating its thermal diffusivity making use of the inverse head conduction method

STANISŁAW KUCYPERA

Silesian University of Technology, Institute of Thermal Technology, Konarskiego 22, 44-100 Gliwice, Poland

The aim of the paper is analysis of the possibility of determining the internal structure of the fibrous composite material by estimating its thermal diffusivity. A thermal diffusivity of the composite material was determined by applied inverse heat conduction method and measurement data. The idea of the proposed method depends on measuring the time-dependent temperature distribution at selected points of the sample and identification of the thermal diffusivity by solving a transient inverse heat conduction problem. The investigated system which was used for the identification of thermal parameters consists of two cylindrical samples, in which transient temperature field is forced by the electric heater located between them. The temperature response of the system is measured in the chosen point of sample. One dimensional discrete mathematical model of the transient heat conduction within the investigated sample has been formulated basing on the control volume method. The optimal dynamic filtration method as solution of inverse problem has been applied to identify unknown diffusivity of multi-layered fibrous composite material. Next using this thermal diffusivity of the composite material its internal structure was determined. The chosen results have been presented in the paper.

Symbols

c – specific heat, J/kg K,
k – thermal conductivity, W/m K,
ρ – density, kg/m^3,
a – thermal diffusivity, m^2/s,
d, H – radial and axial sizes of the sample, m,
L – number of the measurement sensors (thermocouples),
N – number of nodal temperatures,
M – number of the identified parameters,
$\dot{Q}$ – power of the electric heater, W,

t – temperature, ^{o}C,
$\mathbf{V}$ – covariance matrix of the measurements errors,
ω – maximal disturbance of the measurement result,
u – volumetric share of fibres in composite material,
τ – time, s.

Subscripts
i - refers to the node,
k - refers to the time step.

1. Introduction

As known presently produced composite material are most often fibrous many-layered materials with the reproducible structure. Therefore the thermal diffusivity of these material depend on the thermal properties of the matrix and the fibres as well as the volumetric fraction of the fibres in the composite material. Hence, knowledge of the true values of thermal diffusivity of materials is very important to determine of the volumetric fraction of the fibres in composite material (internal structure of the composite) [1]. So basing on the identification of the thermal diffusivity of multi-layered fibrous composite material, the possibilities of determining its internal structure were presented in the paper.

Determination of the thermal diffusivity of composite material is based on the solution of the inverse heat conduction problem in an investigated sample, for given boundary conditions and given geometry [2,3].

The inverse heat conduction problem is generally solved in two stages.

In the first stage, basing on a suitably formulated mathematical model, the direct heat conduction problem is solved. Auxiliary measurements and their characteristics (for example the temperature field) are also determined. These quantities will be used in the second stage of solving the algorithm.

In the second stage, making use of measurement data and previously determined quantities, the inverse problem is solved and the final quantities are determined.

The specific feature of the considered problem is that the objective function does not depend on the identified parameters in the explicit way. In order to find the relationship between the identified parameters and changes of the objective function, we must solve the direct transient heat conduction boundary problem. In this paper to solve the direct boundary problem, the mathematical model has been formulated basing on the control volume method. The inverse problem was formulated as an optimisation problem and solved by using the optimal dynamic filtration method.

Information about input data required to solve the inverse heat conduction problem was obtained by solving the direct heat conduction problem or from measurement stand.

The chosen results of research has been presented.

2. Formulation of the mathematical model and solution of the direct heat conduction problem

One-dimensional heat conduction in the analysed process can be described by a well-known differential equation of the form [4]:

$$\rho \cdot c \frac{\partial t}{\partial \tau} = k \frac{\partial^2 t}{\partial x^2}. \tag{1}$$

The electric heater is located between two identical samples (Fig. 1), hence the problem becomes symmetrical and we can analyse only one of the sample. The boundary conditions for that case can be written in the form:

$$-k \frac{\partial t}{\partial x}\Big|_{x=0} = \frac{\dot{q}}{2}, \tag{2}$$

$$\frac{\partial t}{\partial x}\Big|_{x=\pm\delta} = 0, \tag{3}$$

where x=0 denotes the location of the heater, δ is the thickness of the sample and q is the power of the electric heater.

The initial temperature in the sample is known and kept uniform, so the initial condition for the boundary heat conduction problem has the form:

$$t(x, \tau = 0) = t_0. \tag{4}$$

The considered transient boundary problem belong to non-linear problems and it is difficult to obtain analytical equation describing transient temperature field within the sample. Therefore basing on the control volume method, the discrete mathematical model of the transient temperature field within the sample can be written in the form of the following non-linear system equations:

$$t_1^{k+1} = (1 + b_{11}) \cdot t_1^k + b_{12} \cdot t_2 + \gamma_1,$$

$$t_2^{k+1} = b_{21} \cdot t_1^k + (1 + b_{22}) \cdot t_2^k + b_{23} \cdot t_3 ,$$

$$t_3^{k+1} = b_{32} \cdot t_2^k + (1 + b_{33}) \cdot t_3^k + b_{34} \cdot t_4 , \qquad (5)$$

$$t_4^{k+1} = b_{43} \cdot t_3^k + (1 + b_{44}) \cdot t_4^k + b_{45} \cdot t_5 ,$$

$$t_5^{k+1} = b_{54} \cdot t_4^k + (1 + b_{55}) \cdot t_5^k ,$$

where $\boldsymbol{\gamma}$ is a vector that includes the boundary conduction data, but coefficients $\boldsymbol{b}_{ij}$ contain the thermal diffusivity of layers,.

for node "1” b_{ij} is defined:

$$b_{ij} = -\frac{a \cdot \Delta\tau}{\Delta x_1 \cdot (\Delta x_1 + \frac{\Delta x_2}{2})} , \text{(where } i = j\text{)},$$

$$b_{ij} = \frac{a \cdot \Delta\tau}{\Delta x_1 \cdot (\Delta x_1 + \frac{\Delta x_2}{2})} , \text{(where } i \neq j \text{)}. \qquad (6)$$

Similarly for node "5” b_{ij} is defined:

$$b_{ij} = -\frac{a \cdot \Delta\tau}{\Delta x_5 \cdot (\Delta x_5 + \frac{\Delta x_4}{2})} , \text{(for } i = j\text{)},$$

$$b_{ij} = \frac{a \cdot \Delta\tau}{\Delta x_5 \cdot (\Delta x_5 + \frac{\Delta x_4}{2})} , \text{(for } i \neq j \text{)}. \qquad (7)$$

For remaining nodes b_{ij} is defined as fellow:

$$b_{ij} = -\frac{2 \cdot a \cdot \Delta\tau}{\Delta x_i} \cdot \left(\frac{1}{\Delta x_{i-1} + \Delta x_i} + \frac{1}{\Delta x_i + \Delta x_{i+1}}\right) , \text{(dla } i = j\text{)},$$

$$b_{ij} = \frac{2 \cdot a \cdot \Delta\tau}{\Delta x_i \cdot (\Delta x_i + \Delta x_j)} , \text{(for } i \neq j \text{)}, \qquad (8)$$

where**:**

t_i^k , t_i^{k+1} – temperature in i^{th} node and k and k+1 time steps,

a – determined thermal diffusivity,
$\Delta\tau$ − length of time step,
Δx_i − the thickness of the i^{th} layer in the discrete plate.

3. Description of the test stand

The scheme of the test stand is presented in Fig.1.

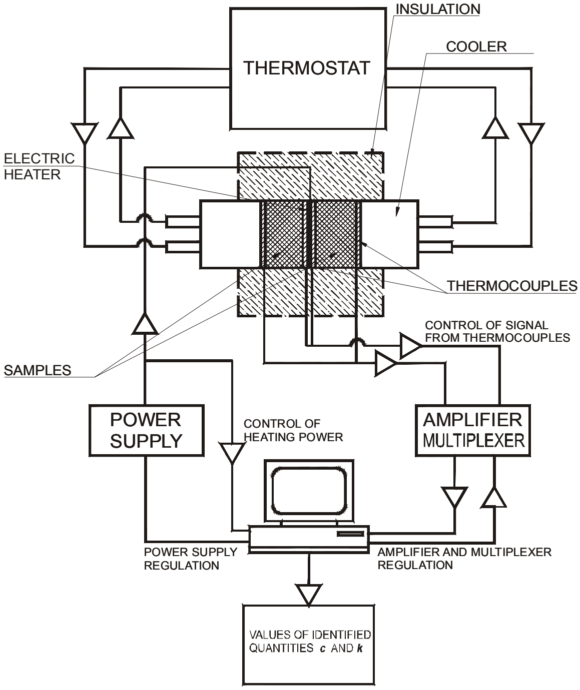

Fig. 1. Scheme of the test stand

In the symmetrical system two samples are located on both sides of the electric heater. The heater is made of plastic foil coated with an electricity-resistant layer to minimise its heat capacity. The important technical problem is to measure the temperature of the four surfaces of the samples - this is done by means of a thin copper plate with Ni-NiCr thermocouple welded in their centres. Those plates are located between the heater and the samples and on the cooled outside surfaces of the samples. The other effect of applying copper plates is that the temperature of the surfaces is more uniform. The samples are cylinders with a diameter *d* and thickness δ. The samples, heater and copper plates are well insulated on the cylindrical surface. The heater is connected to a stabilised electric current-voltage power supply. The power of the heater results from the voltage and current fo the heater:

$$\dot{Q} = P = U \cdot I \,. \tag{10}$$

The heat flux q per surface unit of each sample equals:

$$\dot{q} = \frac{2P}{\pi \cdot \mathrm{d}^2}, \quad \frac{\mathrm{W}}{\mathrm{m}^2} \,. \tag{11}$$

The experiment continues as follows. After assembling the samples and auxiliary equipment, all functions during the experiment are checked by a special computer program. The computer switches on the power supply, controls and registers U and I, registers the temperatures and stops the procedure if one of the given criteria is reached (i.e. time of the experiment or maximum temperature of the sample). The results of measurements are stored in the memory of the computer.

4. Kalman filter to solve the inverse problem

To involve the discrete Kalman filter procedure into solution the inverse heat conduction problem it is necessary to write the discrete transient temperature field within the sample in the form of the following non-linear matrix equation [5-7]:

$$\boldsymbol{y}_{k+1} = \boldsymbol{F}_{k+1,k}(\boldsymbol{y}_k) \,, \tag{12}$$

where y is the state vector, which includes the N nodal temperatures and M evaluated coefficients, F vector valued function of y, which defines the relation between the vector y at two adjacent time steps. In the concerning case the $M = 1$. So the extended vector state we can write down:

$$\mathbf{y}^T = [\,t_1, t_2, \ldots\ldots t_N, a\,] = [\,y_1, \ldots. y_{N,} y_{N+1}, \ldots, y_{N+M}\,] \,. \tag{13}$$

The relationship between the results of temperature measurements z (the so-called vector of observations) in selected L sensors located in the sample and the vector of state y at a given time step k+1 has the form:

$$\mathbf{z}_{k+1} = \mathbf{H}\,\mathbf{y}_k + \mathbf{v}_{k+1}\,, \tag{14}$$

where the matrix $\boldsymbol{H}$ of size $L*M$ consists of the elements equal unity for the corresponding to the measured temperatures and with all others elements equal zero, because only the nodal temperatures are measured. Vector $\mathbf{v}_{k+1}$ represents measurement errors (Gaussian white noise with zero mean) of the covariance matrix $\mathbf{V}_{k+1}$.

Because of products $k{\cdot}t_i$, $\boldsymbol{F}(\boldsymbol{y})$ is non-linear function of the state variables and discrete linear Kalman filter can not be used, so in order to solve the inverse problem by Kalman filter the function $\boldsymbol{F}(\boldsymbol{y})$ must be linearized.

After two steps (prediction and filtration – correction) the Kalman filtering process contains the following equations:

a) **a prediction**

$$\tilde{\mathbf{y}}_{k+1/k} = \mathbf{F}_{k+1,k}(\tilde{\mathbf{y}}_k)\,, \tag{15}$$

and the covariance matrix of the prediction estimate errors can be written as:

$$\mathbf{P}_{\mathrm{k+1/k}} = \mathbf{G}_{\mathrm{k+1/k}}\,\mathbf{P}_{\mathrm{k,k}}\,\mathbf{G}^{\mathrm{T}}_{\mathrm{k+1/k}}\ , \tag{16}$$

where $\boldsymbol{G}$ is the square matrix of the size $((N+M)\cdot(N+M)$.

The elements of matrix $\boldsymbol{G}$ represent derivatives of the state function F_i with respect to the unknown quantity y_j:

$$G_{i,j} = \frac{\partial F_i(y_1,\ldots.y_N, y_{N+1},\ldots, y_{N+M})}{\partial y_j}\,. \tag{17}$$

b) **a correction**

The vector of state $\tilde{\boldsymbol{y}}_{k+1}$ and *a posterior* covariance matrix $\mathbf{W}_{k+1}$ of the estimate errors can be written down:

$$\tilde{\mathbf{y}}_{k+1} = \tilde{\mathbf{y}}_{k+1/k} + \mathbf{K}_{k+1}[\mathbf{z}_{k+1} - \mathbf{H}\tilde{\mathbf{y}}_{k+1/k}], \tag{18}$$

where $\mathbf{K}_{k+1}$ is the so-called Kalman gain matrix and can be expressed as:

$$\mathbf{K}_{k+1} = \mathbf{P}_{k+1/k}\mathbf{H}^T[\mathbf{H}\mathbf{W}_{k+1/k}\mathbf{H}^T + \mathbf{V}_{k+1}]^{-1}\,. \tag{19}$$

The covariance matrix of estimate errors has the form:

$$\mathbf{P}_{k+1} = \mathbf{P}_{k+1/k} - \mathbf{P}_{k+1/k}\mathbf{H}^{\mathrm{T}}[\mathbf{H}\mathbf{P}_{k+1/k}\mathbf{H}^{\mathrm{T}} + \mathbf{V}_{k+1}]^{-1}\mathbf{H}\mathbf{P}_{k+1/k}\,. \tag{20}$$

The calculation procedure starts at the time k=0 for the given *a priori* initial vector $\mathbf{y}_0$ and covariance matrix $\mathbf{P}_{0,0}$. At each time step the algorithm uses the measurement results $\mathbf{z}_{k+1}$ from the number of L sensors (thermocouples) located within the sample.

5. Selected results of the research

At first the accuracy of the proposed method was verified by a numerical experiment [8]. To solve the inverse problem for numerical experiment results of “measurements”, t_i^{meas} were obtained by adding a noise term $(\omega \cdot \nu)$ to the results of solution of the direct boundary heat conduction problem (for given values of a) t_i, according to the relationship:

$$t_i^{meas} = t_i + \omega \cdot \nu\,, \tag{21}$$

where ν is the standard deviation of measurement errors. For normally distributed errors (Gaussian distributed noise) with 99% confidence for the measured data, ω lies in the range $-2.576 \le \omega \le 2.576$, and the value of ω is calculated by a random generator.

In the numerical experiment the shape of the samples was assumed as the cylinders with a diameter d =72 mm, a thickness H = 9.1 mm and a density of material ρ=1700 kg/m^3. The power of the heater varied during each experiment. The example value of power P is 2.49 W, with a heat flux density $\dot{q}$ = 306.12 W/m^2. The measurement sensors were located on the internal (z=0) and external (z=H) surfaces of the samples. The simulated measurement data were obtained using the simulated exact results obtained from the solution of the direct heat conduction problem and disturbed by the different error ν (eq. 21).

The temperature within the sample was measured at $\Delta\tau$=1.

The influence of the measurement errors ν =[0.01÷0.1] K on the results of identification was examined, but results presented below were obtained for error ν = 0.05 K.

The thermal properties assumed for the numerical experiment are: diffusivity a=1.1439*10^{-7} m^2/s. The following entire values of the research parameters were assumed: a=*1.1029**10^{-7} m^2/s. After calculations by means of the Kalman filter method the following results were obtained: a= 1.144*10^{-7}m^2/s.

Next, using real measurement data for different content of the fibres in the composite material and the worked out computer program, the thermal diffusivities were determined. The registered average temperatures of heated and insulated surfaces of the samples for exemplary real measurement data are shown in Fig.2

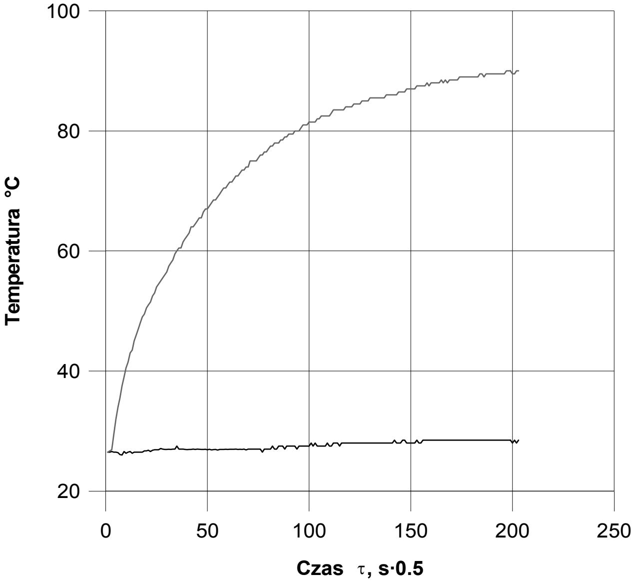

Fig 2 Temperature distribution on the surfaces of the sample as a function of time

The results obtained by means of the proposed algorithm have been presented in the table 1 and in Fig 3.

Table 1. Results of estimation of the thermal diffusivity

nr of sample	content of fibres in composite material. %	Thermal diffusivity ***a**** 10^7, m^2/s
1	5,41	1,35
2	10.40	1.52
3	20.78	1.86
4	28.91	2.21

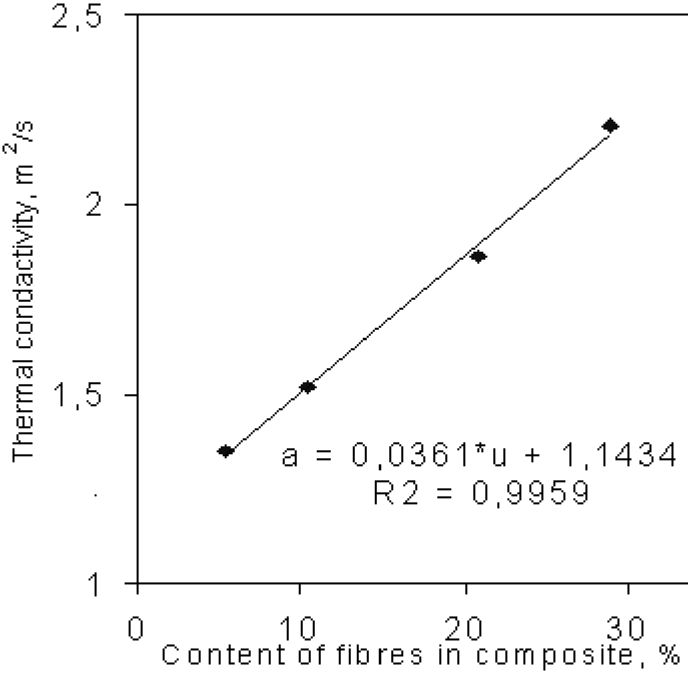

Fig. 3. Thermal diffusivity as a function of a volumetric share of a fibres in the composite material

The appointed values of thermal diffusivity of samples with a thickness 9.1 mm and different contents of fibres in composite material provided the basis for determination of the mathematical relation between thermal diffusivity and share of fibres in the composite. In the presented diagram it is visible that this dependence is linear. The values of the coefficients of this line were determined by applying method of linear regression. The appointed function well describes the relation between diffusivity and content of fibres, which confirms the value of the correlation coefficient.

6. Final conclusions

The final conclusions may be listed as follows:

- The inverse heat conduction solution problem based on the connection control volume method, measurement data and the Kalman filter method constitutes a very effective tool for identification of the thermal diffusivity of the fibrous composite materials.

- The numerical tests have proved that, in spite of the large noise of measured temperatures the identification process is stable and identified parameter are very close to real values.
- The method enables us to estimate the accuracy of identification parameter, what is a very important feature of the algorithm.
- The proposed approach allows us to short the time of experiments which is another advantage of this method.
- On the basis of the received results we can affirm, that exists possibility to determine the share of fibres in the composite material basing on the determined thermal diffusivity.

References

[1] HOSSELMAN D.P.H., DONALDSON K.Y.: Effects of detector nonlinearity and specimen size on the apparent thermal diffusivity of NIST 8425 graphite. International Journal of Thermophysics. 1990, 11, No 3, pp.573-585

[2] BECK J. V., ARNOLD K.: Parameter estimation in engineering and science, Wiley, New York, 1977

[3] KUCYPERA S.: Wyznaczanie parametrów termofizycznych materiałów ortotropowych w oparciu o rozwiązanie odwrotnego zagadnienia przewodzenia ciepła. Materiały XIII Sympozjum wymiany ciepła i masy, Koszalin-Darłówko, 2007, t. 2, str. 633-640

[4] ÖZISIK M. N., ORLANDE H. R.: Inverse heat transfer. Taylor & Francis, New York, 2000

[5] SCARPA F. AND MILANO G..: Kalman smoothing technique applied to the inverse heat conduction problems. Numerical Heat Transfer. Part B. 1995, vol. 28, pp. 79-96

[6] SKOREK J., KUCYPERA S., (2000). Dynamic filtration based on the inverse approach for determination heat conductivity and specific heat of solids. Proc. 34th ASME National heat transfer conference, Symposium on inverse thermal problem, (Compact Disc) Pittsburgh 2000, USA.

[7] MOULTANOVSKY A.V, REKADA M.: Inverse heat conduction problem approach to identify the thermal characteristics of super-hard synthetic materials. Inverse Problems in Engineering, 2002, **10**, No 1, pp. 19-39

[8] MZALI F., ALABOUCHI F., NASRALLAH S. PETIT D.: ptimal experiment design and thermo-physical characterisation of a plastically deformed solid, Inverse Problems, Design and Optimization Symposium, Miami**,** Floryda, U.S.A. April 2007, pp. 16-28

Journal of Energy Science, Vol. 1, No. 1, 2010, pp.93-102

Attempt to estimate exergy balance of a ship's main diesel engine

ZBIGNIEW MATUSZAK[1], GRZEGORZ NICEWICZ[2]

Akademia Morska, Instytut Technicznej Eksploatacji Siłowni Okrętowych,
70-500 Szczecin, ul. Wały Chrobrego 1-2
Akademia Morska, Instytut Nauk Podstawowych Technicznych,
70-500 Szczecin, ul. Wały Chrobrego 1-2;

The article presents an attempt to estimate the exergy balance of a main diesel engine of the vessel in two environment temperatures of the power plant (25°C and 45°C), which correspond to winter and tropical conditions of the operation of the vessel. In the analysis the following forms of energy and ways of its delivery and carrying off, there were considered: the chemical energy (fuel), charging air, lubricating oil, flow of fresh cooling water, exhaust gases. The basis for the data of energy and exergy balances were the parameters of the operation of the vessel engine. They were registered in the conditions of established heat equilibrium of the main engine1.

Symbols

B_d – exergy of fluids put into the system, J
$B_{wuż}$ – useful exergy of fluids put out of the system, J
c_{chp} – mean specific heat of water, kJ/kgK
c_o – mean specific heat of lubricating oil, kJ/kgK
c_p – mean specific heat of charging air, kJ/kgK
c_S – mean specific heat of exhaust gases, kJ/kgK
c_W – mean specific heat of water, kJ/kgK
E_{uk} – the terminal energy of the system; J
E_{up} – the initial energy of the system, J
$\dot{G}_{chp}$ – mass stream of cooling water, kg/h
$\dot{G}_e$ – mass stream of consumed fuel, kg/h

Corresponding author, e mail: z.matuszak@am.szczecin.pl

$\dot{G}_o$ – mass stream of lubricating oil, kg/h
$\dot{G}_p$ – mass stream of charging air, kg/h
$\dot{G}_s$ – mass stream of exhaust gases kg/h,
$\dot{G}_w$ – mass stream of cylinder cooling water, kg/h
L – mechanical or electric work performed by the system, J
N_e – maximum continuous output, kW
T – temperature of medium, K,
T_0 – temperature of the surroundings, K
T_p – temperature of environmental air, K
W_d – fuel calorific value, kJ/kg
$\dot{Q}_{chcyl}$ – heat losses of cylinder cooling, kJ/h, kJ/s
$\dot{Q}_{cho}$ – heat taken away by lubricating oil, kJ/h, kJ/s
$\dot{Q}_{chp}$ – heat losses of charging air cooling, kJ/h, kJ/s
$\dot{Q}_{pal}$ – energy delivered with fuel, kJ/h, kJ/s
$\dot{Q}_{pow}$ – energy delivered with charging air, kJ/h, kJ/s
$\dot{Q}_s$ – heat of exhaust gases losses, kJ/h, kJ/s
$\dot{Q}_r$ – sum of unaccounted heat losses, kJ/h, kJ/s
ΔB_u – increase in the system exergy, J
ΔB_{zr} – increase in the exergy of external heat source being in contact with the system, J
δB_w, δB_z – internal and external loss of exergy, J

1. Introduction

The increase of energy of energetic plant, generally understood as a technical system, is caused by the transition from the initial state to the terminal one and is independent of the way of transition between the states, but presents the contrast between the initial and the terminal energy [6]:

$$\Delta E_u = E_{uk} - E_{up}\,, \tag{1}$$

where:

E_{uk} – the terminal energy of the system;

E_{up} – the initial energy of the system.

In the present paper it was made an attempt to estimate the exergy balance of a ship's main diesel engine.

The main engine MAN B&W k90ME-C6 (fig.1) presents a low-speed, two-stroke engine, supercharged, fed with residual fuel oil with electronic control of fuel injection. The basic technical parameters of the engine are: maximum continuous output – 27420 kW at 104 rpm; rated rotational speed – 104 rpm; number of cylinders – 6; cylinder diameter – 900 mm; piston stroke – 2300 mm.

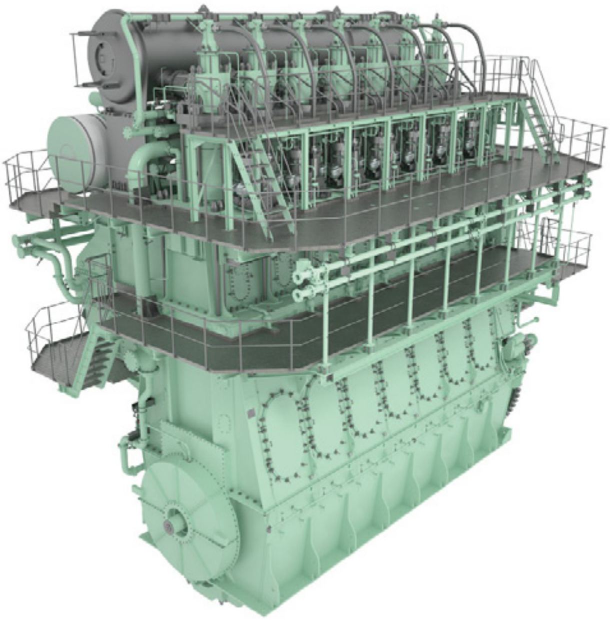

Fig. 1. General view of the main engine MAN B&W k90ME-C6 [8]

2. Estimation of components of the ship's main engine exergy balance

Generally the exergetic analysis may be presented in the form of exergy balance. Equation of exergy balance has the form:[1,2,3,7]:

$$B_d = \Delta B_u + B_{wu\dot{z}} + L + \sum \Delta B_{zr} + \delta B_w + \delta B_z \,, \tag{2}$$

where:

B_d – exergy of fluids put into the system,

ΔB_u– increase in the system exergy,

$B_{wu\dot{z}}$– useful exergy of fluids put out of the system,
L – mechanical or electric work performed by the system,
ΔB_{zr}– increase in the exergy of external heat source being in contact with the system,
δB_w, δB_z – internal and external loss of exergy.

If the temperature of the heat source is higher than the environmental temperature, the direction of the heat and exergy flow are compatible. Nevertheless, if the temperature of the heat source is lower than the cooled space ($T < T_0$), exergy is increased.

The dependences necessary to estimate exergy balance of the main engine are given below. They were received, after taking into account, the energy and the exergy of the working mediums (energy carriers) of the main engine. Thus the following forms of energy were included: the chemical energy (fuel), energy of charging air, energy of lubricating oil, energy of cylinder cooling water (high temperature cooling system) and charging air cooling water (low temperature cooling system) and energy of exhaust gases.

- Heat corresponding to the maximum continuous output is [5]:

$$Q_e = 3600 \cdot N_e \text{, kJ/h,} \tag{3}$$

where:

3600 – equivalent of the heat energy, kJ/kWh,
N_e – maximum continuous output, kW.

- Exergy, corresponding to the maximum continuous output is:

$$\Delta B_e = Q_e \frac{T - T_0}{T} \text{, kJ/h ,} \tag{4}$$

where:

T – temperature of medium, K,
T_0 – temperature of the surroundings, K.

- Exergy put into with fuel is:

$$\Delta B_{pal} = \dot{G}_e \cdot W_d \frac{T - T_0}{T} \text{, kJ/h,} \tag{5}$$

where:

$\dot{G}_e$ – mass stream of consumed fuel, kg/h,
W_d – fuel calorific value, kJ/kg.

- Exergy delivered with charging air is:

$$\Delta B_{pow} = \dot{G}_p \cdot c_p \cdot T_p \frac{T - T_0}{T}, \text{ kJ/h,} \tag{6}$$

where:

$\dot{G}_p$ – mass stream of charging air, kg/h,
c_p – mean specific heat of charging air, kJ/kgK,
T_p – temperature of environmental air, K.

- Exergy of exhaust gases losses is:

$$\Delta B_s = \dot{G}_s \cdot c_s \cdot \Delta T \frac{T - T_0}{T}, \text{ kJ/h,} \tag{7}$$

where:

$\dot{G}_s$ – mass stream of exhaust gases, kg/h,
c_s – mean specific heat of exhaust gases, kJ/kgK,
ΔT – difference between exhaust gasses temperature after turbine and temperature of the surroundings, K.

- Exergy taken away by lubricating oil is:

$$\Delta B_{cho} = \dot{G}_o \cdot c_o \cdot \Delta T \frac{T - T_0}{T}, \text{ kJ/h,} \tag{8}$$

where:

$\dot{G}_o$ – mass stream of lubricating oil, kg/h,
c_o – mean specific heat of lubricating oil, kJ/kgK,
ΔT – difference between main engine lubricating oil inlet and outlet temperatures, K.

- Exergy of cylinder water cooling losses is:

$$\Delta B_{chcyl} = \dot{G}_w \cdot c_w \cdot \Delta T \frac{T - T_0}{T}, \text{ kJ/h,} \tag{9}$$

where:

$\dot{G}_w$ – mass stream of cylinder cooling water, kg/h,
c_w – mean specific heat of water, kJ/kgK,
ΔT – difference between main engine cylinder cooling water inlet and outlet temperatures, K.

- Exergy of charging air water cooling losses is:

$$\Delta B_{chp} = \dot{G}_{chp} \cdot c_{chp} \cdot \Delta T \frac{T - T_0}{T}, \text{ kJ/h,} \tag{10}$$

where:

$\dot{G}_{chp}$ – mass stream of cooling water, kg/h,

c_{chp} – mean specific heat of water, kJ/kgK,

ΔT – difference between charging air cooler water inlet and outlet temperatures, K.

On the basis of the working parameters, components of energy and then exergy balance of the main engine MAN B&W k90ME-C6 were estimated in tables no 1, 2, 3.

Table 1. Temperature of the main engine working mediums [8]

	Main engine outlet, K	Main engine inlet, K
Cylinder cooling water temperature	370	353
Lubricating oil temperature	325	318
Charging air cooling water temperature	319	309
Exhaust gases temperature	518	-

Table 2. Specific heat of working mediums, kJ/kgK [6]

Mean specific heat of exhaust gases c_s	1,075
Mean specific heat of cooling water c_w	4,19
Mean specific heat of lubricating oil c_o	1,88
Mean specific heat of charging air c_p	1,005

Table3. Flows, kg/h [4]

Mass stream of exhaust gases $\dot{G}_s$	268 200
Mass stream of cylinder cooling water $\dot{G}_w$	200 000
Mass stream of lubricating oil $\dot{G}_o$	579 500

Mass stream of charging air cooling water $\dot{G}_{chp}$	384 000
Mass stream of charging air $\dot{G}_{p}$	263 532

The other parameters were as follows [8]: fuel consumption – 4 606 kg/h; the main engine power – 27 420 kW; fuel calorific value – 40 370 kJ/kg; temperature of exhaust gases – 518 K.

In table 4 components of energy balance at the environmental temperature 25oC (298 K) and 45oC (318 K) were presented.

Table 4. Components of the main engine energy balance at two environmental temperatures (25°C and 45°C)

	25°C		45°C	
	kJ/h	kJ/s	kJ/h	kJ/s
Heat corresponding to the maximum continuous output	98 712 000	51 651	98 712 000	27 420
Energy delivered with fuel $\dot{Q}_{pal}$	185 944 220	51 651	185 944 220	51 651
Energy delivered with charging air $\dot{Q}_{pow}$	78 925 198	21 923	84 222 191	23 395
Heat of exhaust gases losses $\dot{Q}_{s}$	63 429 300	17 619	57 663 000	16 017
Heat taken away by lubricating oil $\dot{Q}_{cho}$	7 626 220	2 118	7 626 220	2 118
Heat losses of cylinder cooling $\dot{Q}_{chcyl}$	14 246 000	3 957	14 246 000	3 957
Heat losses of charging air cooling $\dot{Q}_{chp}$	16 089 600	4 469	16 089 600	4 469
Sum of unaccounted heat losses of $\dot{Q}_{r}$	98 931 936	27 481	75 829 591,88	21 063

In table 5 assumed components of exergy balance of the main engine MAN B&W k90ME-C6 at the environmental temperature of 25oC (298 K) and 45oC (318 K) are given. All operating data were registered on board the ship during sea voyages in tropical and polar climatic conditions.

Table 5. Components of the main engine exergy balance at two environmental temperatures (25°C and 45°C)

Exergy	25°C		45°C	
	kJ/h	kJ/s	kJ/h	kJ/s
of consumed fuel ΔB_{pal}	46 719 653	12 977	36 908 526	10 252
of charging air ΔB_{pow}	17 031 227	4 730	13 519 878	3 755
of cylinder cooling water ΔB_{chcyl}	2 772 194	770	1 963 637	545
of lubricating oil ΔB_{cho}	633 562	176	140 791	39,11
of charging air cooling ΔB_{chp}	1 059 189	294	16 089 600	4 469
of exhaust gases ΔB_{s}	26 939 084	7 483	22 152 388	6 153
of maximum continuous output ΔB_{e}	98 712 000	27 420	98 712 000	27 420

Fig. 2 summarizes components of exergy balance of the main engine at two environmental temperatures of 25oC(298 K) and 45oC (318 K).

3. Final remarks

This attempt to estimate the exergy balance of a marine main engine, may have a simplified character. It is limited to only the main energetic (exergetic) components, characterizing the engine operation. The authors are aware of the complexity of the issue, but the assumptions have been presented simpler. Viewing the problem from the other aspect, we consider it advisable to analyze different issues of the balance for the autonomous energetic plants and systems situated in marine power plants.

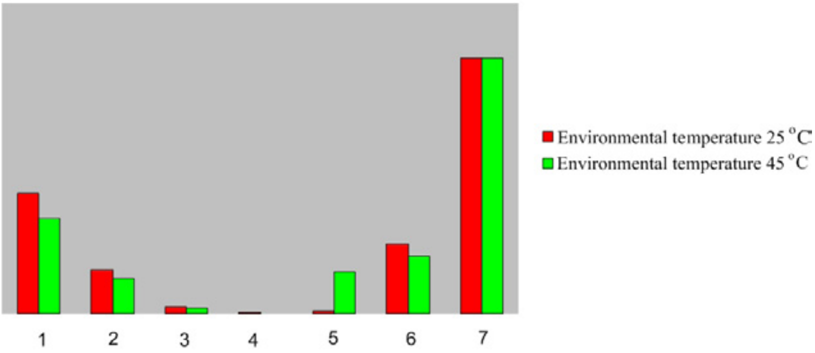

Fig. 2. Exergy of the main engine exergy balance components at two environmental temperatures: 1 – chemical exergy of consumed fuel; 2 – exergy of charging air; 3 – exergy of cylinder cooling water; 4 – exergy of lubricating oil; 5 – exergy of charging air cooling; 6 – exergy of exhaust gases; 7 – exergy corresponding to maximum continuous output

The presented results should be viewed as preliminary, the purpose of their constant verification is the realization of the detailed model of energy and exergy balance of marine diesel engine in real operating conditions during sea service. The present paper continues the research, described in the works [1, 2, 3, 4].

References

[1] MATUSZAK Z: Egzergia jako miara jakości urządzenia energetycznego. Mieżdunarodnyj sbornik naucznych trudow „Nadiożnost i effektiwnost techniczeskich sistem", Kaliningradskij gosudarstwiennyj techniczeskij uniwersytet, Izdatelstwo KGTU, Kaliningrad 2005, s. 162-167.
[2] MATUSZAK Z: Straty egzergii w urządzeniach energetycznych siłowni okrętowej. Mieżdunarodnyj sbornik naucznych trudow „Nadiożnost i effektiwnost techniczeskich sistem", Kaliningradskij gosudarstwiennyj techniczeskij uniwersytet, Izdatelstwo KGTU, Kaliningrad 2005, s. 168-173.
[3] MATUSZAK Z.: Losses of energy in a Marine oil-fired boiler. Archives of thermodynamics. Vol. 29 (2008), No. 4, s. 97-107.
[4] MATUSZAK Z.: Wybrane zagadnienia bilansu energetycznego silnika spalinowego. Mieżduna-rodnyj sbornik naucznych trudow „Nadiożnost i effektiwnost techniczeskich sistem", Kalinin-gradskij gosudarstwiennyj techniczeskij uniwersytet, Izdatelstwo KGTU, Kaliningrad 2009, s. 87-93.
[5] MICHALSKI R.: Siłownie okrętowe – obliczenia wstępne oraz ogólne zasady doboru mechanizmów i urządzeń pomocniczych instalacji motorowych. Wyd. Uczelniane Politechniki Szczecińskiej, Szczecin 1997.
[6] SZARGUT J.: Termodynamika. Państwowe Wydawnictwo Naukowe, Warszawa 1980.
[7] SZARGUT J.: Egzergia. Poradnik obliczania i stosowania. Wydawnictwo Politechniki Śląskiej, Gliwice 2007.
[8] http://www.manbw.dk/project_guides/printed/k90mec6.pdf

Journal of Energy Science, Vol. 1, No. 1, 2010, pp.103-110

Determination of temperature distribution in the gas flame using the thermovision technique

DOROTA MUSIAŁ[1], RAFAŁ WYCZÓŁKOWSKI[2], MAREK GAŁA[3]

[1]Czestochowa University of Technology, Faculty of Materials Processing Technology and Applied Physics, 19. Armii Krajowej AV., 42-200 Czestochowa, Poland
[2]Czestochowa University of Technology, Faculty of Materials Processing Technology and Applied Physics, 19. Armii Krajowej AV., 42-200 Czestochowa, Poland
[3]Czestochowa University of Technology, Faculty of Electrical Engineering, 17. Armii Krajowej AV., 42-200 Czestochowa, Poland

The article presents the results of a study on an original methodology for the determination of temperature distribution using the thermovision technique. The proposed method consists in the examination of the thermograms of elements placed within the space of a flame. The difficulties and limitations of this method and the directions of further studies on this subject are indicated.

Symbols

$\Theta_{bx,y}$ - reduced temperature of the point x lying on the line y of the thermogram examined;

$t_{bx,y}$ - temperature of the element at the point x on the line y of the thermogram examined, °C;

$t_{b\max,y}$ - maximum temperature recorded on the line y of the thermogram, °C.

1. Introduction

One of the basic quantity, determined during the examinations of flames, is the temperature [1,3]. Many different methods of measuring this quantity are described in the literature on the subject. These are either contact methods, where thermocouples and resistance sensors are employed, or contactless methods. In the latter case, radiation emission phenomena are utilized for the determination of the flame temperature [4]. An original methodology for the determination of the flame temperature, using a thermovision camera, is proposed in the present article.

2. Description of the examination methodology

The thermovision technique has been increasingly often used recently for temperature measurements [2,5]. As thermovision cameras are designed for recording infrared radiation emitted from the surface of solids, it is not possible to examine the flame temperature in a direct manner with their use.

Therefore, work was undertaken on the application of the thermovision technique to the examination of flames by an indirect method. To this end, the temperature distribution of objects positioned within the flame space was measured. The measurement consisted in placing a test piece within the flame, heating it up until a stationary condition was obtained and recording the temperature field at the moment of putting out the flame. Thus obtained thermogram is shown in Fig. 1. It represents a temperature field on the surface of steel sheet placed within a kinetic gas flame, as obtained also using a Bunsen burner. Adjacent to the thermogram is a diagram representing the variation of temperature along the line Li1, plotted on this thermogram, which coincided with the burner's axis. As can be noticed, the maximum recorded temperature is 548°C. This value is much lower (more than by half) than the actual flame temperature. This results from the losses of heat from the sheet surface to the environment.

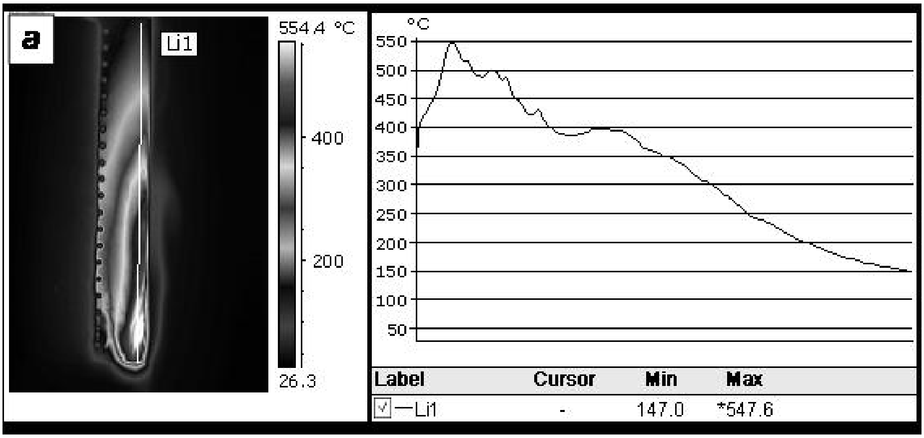

Label	Cursor	Min	Max
☑ —Li1	-	147.0	*547.6

Fig. 1. A thermogram of steel sheet placed within the gas flame and a temperature distribution along the line Li1

A decision was made therefore to modify the proposed measurement method. In further examinations, based on the thermovision measurements of the temperature field of test pieces placed in within the flame, their reduced temperature was determined. The reduced temperature was defined as:

$$\Theta_{bx,y} = \frac{t_{bx,y}}{t_{b\max,y}} . \tag{1}$$

It was assumed that, based on the value of the parameter $\Theta_{bx,y}$, it was possible to determine the distribution of the actual temperature in the flame. This required, however, the flame temperature measurement to be carried out using a contact sensor, such as a thermocouple. The measurement had to be taken at the flame point, where the highest temperature had been found to occur based on the thermogram. Thus the value of the determined temperature (designated by the symbol $t_{\mathrm{tr,max}}$) was then multiplied by the value of the reduced temperature to obtain again a temperature distribution, $t_{\mathrm{px,y}}$, expressed in °C. The conversion operation is expressed by the equation:

$$t_{px,y} = \Theta_{bx,y} \cdot t_{tr,\max} . \tag{2}$$

The proposed examination methodology requires therefore the following activities to be performed:

- placing within the flame space a test piece, on which, after it has been heated up, a thermogram will be recorded;
- recording the thermogram;
- removing the test piece and then placing it at the flame point, where the highest value thermocouple temperature has been found on the thermogram;
- measuring the temperature with the thermocouple.

Compared to the traditional method of measuring the temperature distribution within the flame using contact instruments, the arduous probing process is eliminated.

To evaluate the accuracy of the results obtained by the method described above, a series of tests were carried out on a laboratory stand. The tests included thermovision measurements of the temperature field of selected test pieces placed within a gas flame. The test pieces introduced to flames were: a steel sheet, a chamotte plate, and a ceramic unwoven fabric plate. The tests were performed for two flame types: diffusion and kinetic. To verify the obtained results, a temperature measurement was also taken for each flame with a thermocouple. The results of tests performed by the contact method provided reference data, to which thermovision measurement results were compared.

For the contact measurement of flame temperature, a system consisting of two thermocouple, a measuring card and a computer was used. Sheathed thermocouples type K (NiCr-NiAl) of a sheath diameter of 0.5 mm, were used. The terminals of both thermocouples were at the same height, with one of them being positioned in the burner axis, while the other on the burner perimeter. When traversing the flame, both thermocouples were moved simultaneously. Successive measurements were taken every 5 mm. The measurement results were recorded using a 10 Hz measuring card, type DAQ54, to obtain 600 readings for each of the measurement points. As the examined flames were characterized by low stability, considerable fluctuations in temperature values were recorded at particular points. Therefore, the average temperature value was calculated for each point based on the recorded data.

3. Analysis of the obtained results

The results of analysis of the thermograms recorded for steel sheet deviated substantially from the actual flame temperature distribution. This was caused by the relatively high thermal conductivity of the steel sheet, which resulted in equalizing of temperature. As a consequence, the observed temperature distribution radically differs from the actual flame temperature distribution. This observation suggests that a test piece to be placed in the flame may not be made of a material being a good thermal conductor.

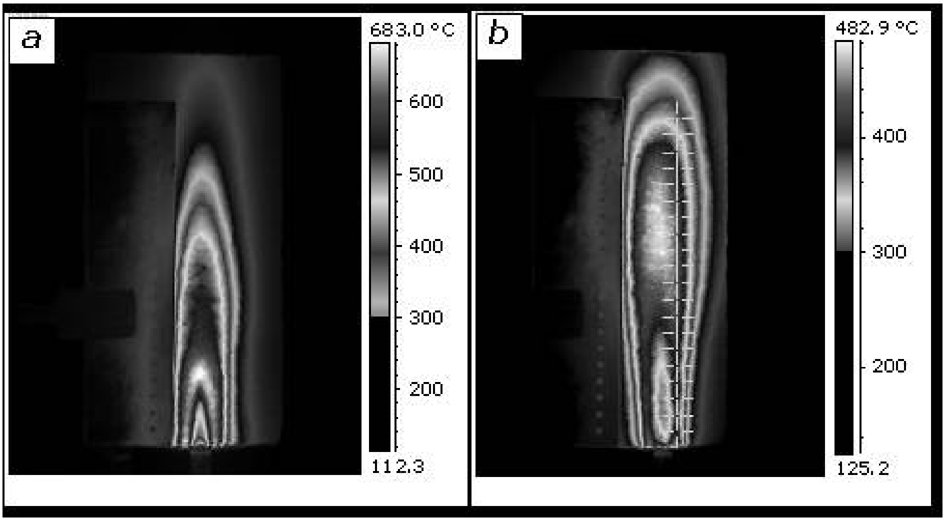

Fig. 2. Flame picture thermograms obtained on the chamotte plate for:
a) a kinetic flame b) a diffusion flame

Fig. 2 shows flame picture thermograms, as obtained on the chamotte plate. For each of the thermograms, temperatures were red out along two lines being an extension of the burner axis and the burner edge, respectively. In the latter case, this corresponded to the thermocouple measurements on the burner perimeter.

Based on the temperatures red out from the thermograms shown in Fig. 2, reduced temperatures, $\Theta_{bx,y}$, were determined for the lines examined. The variation of reduced temperature values as a function of the flame height is illustrated in Fig. 3. The values relating to the burner axis are indicated by squares, whereas the values concerning the burner perimeter are marked by circles.

It can be noticed that the variations of reduced temperature for both flames are different. In the case of the kinetic flame, the maximum temperature occurs at a distance of 4 cm from the burner outlet. Up to that point, the behaviour of reduced temperature variation in the axis and on the perimeter line is different. Higher temperatures were noted on the perimeter. Whereas beyond the 4 cm, the reduced temperature variations for both lines are nearly coincident. Moreover, the reduced temperature values decrease nearly linearly as a function of the flame height.

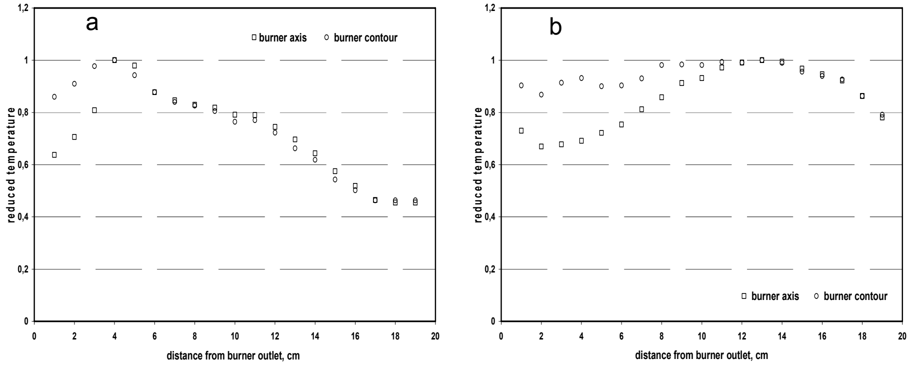

Fig. 3. Variations of reduced temperatures, as obtained on the chamotte plate, as a function of the flame height for: a) the kinetic flame b) the diffusion flame

In the case of the diffusion flame – Fig. 3a), the behaviour of reduced temperature variation, as a function of the flame height, is different. Due to the greater length of this flame, the maximum temperatures occur between the 8th and 14th centimetre. Similarly as for the kinetic flame, below the maximum point, the reduced temperatures for particular lines differ from each other. Higher reduced temperature values were obtained on the flame perimeter.

Whereas, upon attaining a maximum value, the examined temperature variations for both lines are practically coincident.

The reduced temperature variations obtained for the ceramic unwoven fabric show a behaviour similar to that of the results for the chamotte plate.

In order to obtain the temperature distributions of the examined flames in the Celsius temperature scale, it was necessary to convert the reduced temperature values according to relationship (2). As the $t_{tr,\max}$ temperatures, values measured with thermocouples at specified flame points were used. Thus converted temperature distributions are shown in Fig. 4 and Fig. 5. The results are grouped by flame type.

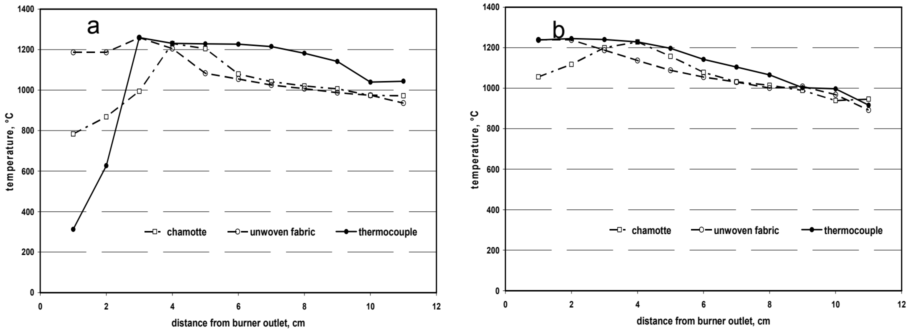

Fig. 4. Variations of temperatures in the kinetic flame: a) in the flame axis, b) on the flame perimeter

In the case of the results obtained for the flame axis, up to the point of occurrence of the maximum temperature, the values obtained from the analysis of thermographs are considerably overestimated compared to those indicated by the thermocouple. This is caused by the overheating of the plate edges. During testing, these plates were positioned so that their lower edge was at the same height as the burner outlet. The obtained results may suggest that the plate edge should be positioned below the burner outlet. In turn, for points situated above the maximum point, the discrepancy in the variations of particular temperatures is already much smaller. It ranges from 150 to 200°C. Temperatures red out from the thermograms slightly decrease as a function of the flame height, whereas the temperature indicated by the thermocouple remains almost constant over a section of several centimetres. There is also a section (between the 3rd and 5th centimetre), within which the values of all temperatures are very close to each other. This indicates that the proposed testing technique, after some modifications, might prove very effective. The lack of appropriate consistence between the results for the upper section of the flame is due to the fact that, because of their geometry, the plates used were not situated ideally in the flame axis. Therefore, the plate area that was intended to correspond to the flame axis was not sufficiently intensively heated. This drawback could be eliminated through the optimization of the plate shape.

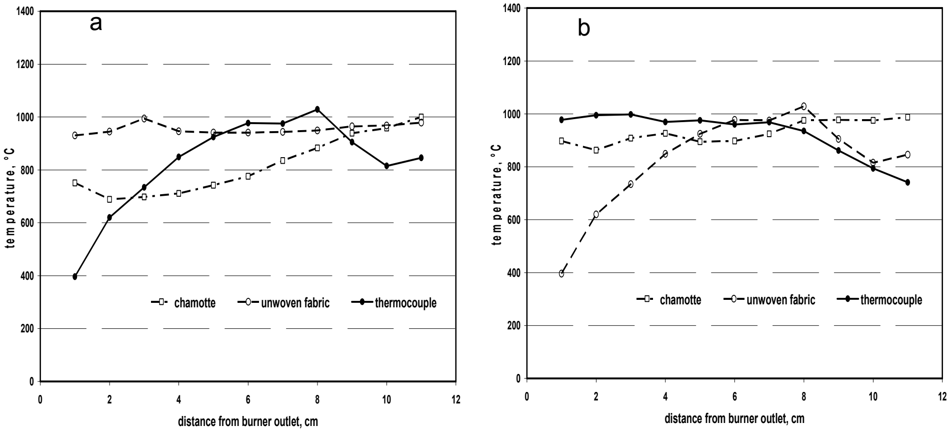

Fig. 5. Variations of temperatures in the diffusion flame: a) in the flame axis, b) on the flame perimeter

Much closer to the actual temperature variation of the kinetic flame are the results obtained for the flame perimeter. The discrepancy between the values ranges in this case from 100 to 50°C. In addition, the courses of particular lines are closer to each other.

The results obtained for the diffusion flame are shown in Fig.9. By analysing the variations of particular temperatures, one can come to conclusions similar to those drawn from the results discussed previously. To improve the accuracy of readings in the flame axis, a correction is needed both to the shape of the plates and to their positioning relative to the burner. Much greater consistence of results was reached for the temperatures determined on the flame perimeter. In addition, in the lower flame part, higher accuracy was reached for chamotte, while in the upper flame part – for unwoven fabric.

The best material, which might find application in the proposed testing methodology, has turned out to be ceramic unwoven fabric, which is due to its lowest thermal conductivity, as compared to other types of materials. At the same time, this material has the lowest thermal inertia; therefore, testing results obtained with its use are significantly dependent on the correct positioning of the plate relative to the flame.

4. Summary

The article has presented the results of investigation into the possibility of using the thermovision technique for the determination of temperature distribution within the gas flame. An original measuring methodology has been put forward, which involves the analysis of the temperature distribution of objects introduced into the flame space. The results obtained at this stage, in spite of the limitations and difficulties found, provide the grounds for stating that it is of purpose to continue studies on the proposed testing method. An improvement in the accuracy of the method could be achieved through the optimization of the shape, dimensions and the type of material of which the test pieces introduced to the flame are made.

References

[1] KOWALEWICZ A.: Podstawy procesów spalania. Warszawa 2000.
[2] MINKINA W.: Pomiary termowizyjne – przyrządy i metody. Częstochowa 2004.
[3] PEDELA R.: Paliwa i ich spalanie część III, Płomień. Gliwice 1982.
[4] Pod redakcją FODEMSKIEGO R., D.: Pomiary cieplne część II. Warszawa 2001.
[5] ThermaCAM P65. FLIR SYSTEMS, 2004.

Journal of Energy Science, Vol. 1, No. 1, 2010, pp.111-120

Experiments on the upper explosion limits of gaseous alkanes-oxygen mixtures at elevated conditions of T and p in a spherical vessel

G. RARATA[1], J. SZYMCZYK[2], P. WOLAŃSKI[3]

[1] Institute of Aviation, Space Technology Department,
Al. Krakowska 110/114, 02-256 Warsaw, Poland *
[2] Warsaw University of Technology, Division of Pumps, Drives and Plants,
Nowowiejska St. 21/25, 00-665 Warsaw, Poland
[3] Warsaw University of Technology, Division of Aeroengines,
Nowowiejska St. 21/25, 00-665 Warsaw, Poland

This experimental work has been completed in the Institute of Heat Engineering Laboratories of Warsaw University of Technology. The article reports on the explosion pressure data and the influence of chosen physical parameters on the value of the Upper Explosive Limit (UEL) of gaseous alkanes-oxygen mixtures. Such explosion behavior data of common gases for different initial conditions are essential for a quantitative risk assessment in many industrial environments. A number of higher alkanes-oxygen mixtures were examined (up to n-butane). Summarized research data is presented in the paper. All the presented data have been obtained from the experiments conducted in a 2.3 dm^3 spherical, steel vessel. Exploding wire was used as the mean of ignition source. It released about 0.1 J energy each time. The pressure histories in the combustion vessel have been recorded by means of piezoelectric pressure transducer. The influence of the increased initial temperatures of the tested mixtures on their value of UEL was investigated in the range of 20°C up to 200°C. Further experiments on the influence of elevated pressure, as well as the position of the ignition source, were carried out too. The experiments allowed the authors to find a distinct dependencies in the values of obtained UEL under *elevated conditions* of pressure and temperature.

---

* Corresponding author, e-mail: grarata@ilot.pl

1. Introduction

The upper explosion limits (UEL) data of common gases, such as gaseous alkanes in their mixtures with air and oxygen at elevated conditions, are essential for a factual risk assessment. Many industrial processes involve the mixing of these flammable gases with oxygen at standard and elevated conditions [1]. Mixtures of light alkanes and oxygen can be converted into many useful products (such as acetylene) by partial combustion (oxidation) in excess of fuel at moderate conditions of temperature and pressure. The flammability limits, for all commonly used gaseous fuels including those used in experiments here, are rather well documented in the literature. However, the data available almost always applies to ambient temperature and pressure conditions, Thus, despite the fact of extensive research on explosibility limits have been carried out for nearly 200 years now, there is only limited data on the influence of pressure and temperature on upper explosion limits even common gaseous fuels[2].

The determination of the UEL is more difficult compared to the lower explosion limit (LEL). The UEL value changes significantly over a wide range to higher fuel composition with pressure and temperature [3]. Various research explosion centers have published explosion limits values which often differ quite significantly from each other [4,5,6]

The report presents the explosion pressure data for four gaseous alkanes homologues-oxygen mixtures; i.e. methane, ethane, propane and n-butane (all at the upper flammable limit) at both; standard and elevated conditions of pressure and temperature. All the presented data have been obtained from the experiments conducted in the steel spherical explosion vessel of 2,3 dm^3 volume, equipped with external heating/cooling system. The initial temperatures of the examined mixtures have oscillated from 20°C up to 200°C and the initial pressures varied from 1 been 6 bar for methane and ethane.

The pressure histories in the combustion vessel have been recorded by means of special pressure transducer with additional cooling system. The effects of higher initial temperature or pressure of the mixture on the pressure curves have also been investigated and qualitatively analyzed. The effect of the ignition position on the explosion pressure history has been explored as well. The results are plotted as functions of time, with respect to the ignition configuration, temperature and pressure.

2. The research stand

The experimental set-up consist of following parts: spherical steel vessel, fusing wire ignition system, data acquisition system with pressure transducer, amplifier, acquisition card and computer, bottle with mixture and vacuum pomp. To control the initial conditions i.e., pressure and temperature, electronic precise manometer and a type K thermocouple were used. The pressure transducer (together with cooling system) used in this research was manufactured by Kistler.

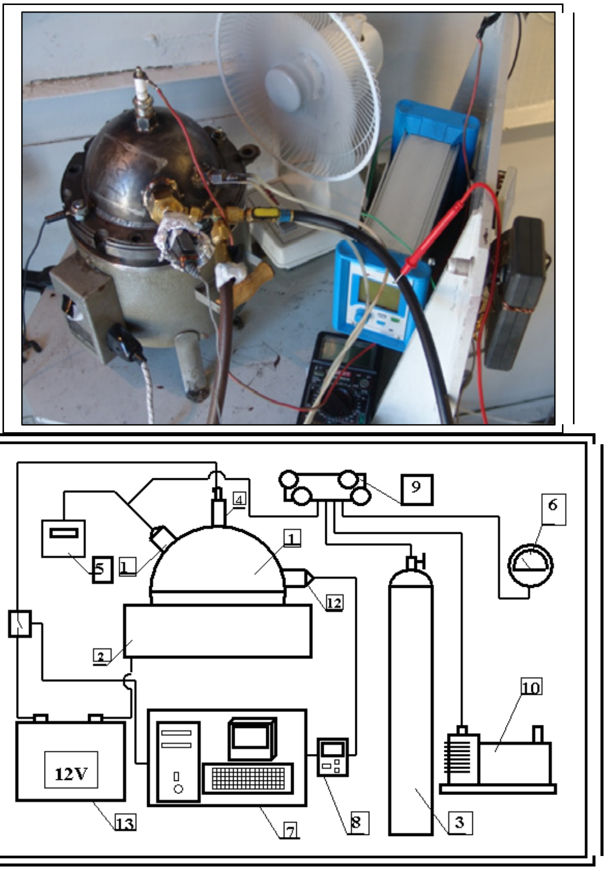

Fig. 1. Photography of the experimental test stand and its schematic diagram

Location of the ignition was changeable, that is was inserted in the center or on the bottom of the vessel in order to evaluate its position on the course of oxidation process.

A general view of the research stand and its schematic diagram is presented in Fig. 1. The explosion vessel (1) was placed on hemispherical electrical heater (2). The ignition system were assembled at the top of the vessel (4), and connected via cable with the battery (13) as well as with the data acquisition system and computer (7). Piezoelectric pressure transducer (12) was mounted in the vessel wall and connected to the amplifier (8), and then to the computer (7). The thermocouple was also placed in the vessel close to the wall (5). The same valve was used to fill vessel with fresh mixture and evacuate the products.

3. Experimental procedure

Before each experiment, the vessel was evacuated by vacuum pump and then filled with test mixture. The gas mixture was allowed to come to rest by waiting at least 5 min. before executing each test. All the test mixtures were prepared at least one day in advance, by using the partial pressure method. The stand for mixtures preparation was equipped with steel bottles, a vacuum pump and a set of precise manometers of high reading accuracy. The first step of the experimental procedure was evacuating the test chamber and then filling it in with the appropriate mixture, then preheating the test vessel containing the mixture to the required temperature, igniting the quiescent test mixture and recording the explosion overpressure inside the chamber. The test mixture was considered as an explosive one, if the measured explosion overpressure was equal to (or greater) than the overpressure formed by the ignition source itself (signal at the level of the reading resolution of the instruments), and exceeded 7% of the initial mixture pressure.

During tests the composition of all mixtures was continuously increased until no ignition was observed (lack of pressure rise). The mixtures were ignited by an exploding wire (aluchrome resistance wire, 0,2 mm diameter), with average energy ignition estimated ~ 0,1 J. The ignition source must be of sufficient energy to guarantee ignition, otherwise the property under investigation would be that of the limiting ignition energy and not of explosibility. Two positions of ignition were utilized during the research; centre and the bottom of the vessel. The limits were evaluated for initial pressure and temperature varied from 1 to 5 bar, and from 20°C to 200°C respectively. The pressure data were measured by water-cooled Kistler piezoelectric pressure transducer mounted in one of the side walls of the vessel. The data acquisition system was used to record all experimental data. The initial pressure of the mixture in the vessel was measured with high accuracy digital pressure manometer. The initial temperature of mixture was controlled by a K-type thermocouple located almost in the centre of the vessel. The temperature of the vessel was controlled by means of special electric heaters. The top half of the vessel was covered with an insulating material.

4. Experimental results

The increase of the initial mixture temperature causes a significant increase of the upper explosion limit in the case of all investigated mixtures. The change of that explosion limit versus the initial temperature of the mixture can be approximated by means of a linear function. Similarly, the increase of the initial mixture pressure causes a significant widening of the UEL, especially in the case of ethane-oxygen mixtures.

The table 1 presents bulk results on the upper flammability limit of methane-oxygen mixtures at elevated conditions of temperature and pressure (separately). The results are plotted as functions of molar percentage methane content, with respect to the pressure and temperature conditions. It can be seen that the upper explosibility limit increases along with the increase of the initial temperature/pressure of the methane-oxygen mixture. It was also found, that the upper explosion limit of methane-oxygen mixture does not depend on the residual time within investigated initial conditions of pressure and temperature.

Table 1. Qualitative results of the flammability of methane-oxygen mixtures in the spherical vessel of 2,3 dm^3 volume and central position of ignition source

UFL %[v/v]		**55**	**56**	**57**	**58**	**59**	**60**	**61**	**62**	**63**	**64**	**65**	**66**	**67**	**68**
1bar	20°C	↔	↔	↓	↓	↓	↓	↓	↓	↓	↓	↓	↓	↓	↓
1bar	50°C	↑	↑	↔	↓	↓	↓	↓	↓	↓	↓	↓	↓	↓	↓
1bar	100°C	↑	↑	↔	↓	↓	↓	↓	↓	↓	↓	↓	↓	↓	↓
1bar	150°C	↑	↑	↔	↔	↔	↔	↓	↓	↓	↓	↓	↓	↓	↓
1bar	200°C	↑	↑	↑	↔	↔	↔	↓	↓	↓	↓	↓	↓	↓	↓
20°C	2bar	↑	↔	↔	↑	↔	↔	↔	↓	↓	↓	↓	↓	↓	↓
20°C	3bar	↑	↑	↑	↑	↑	↔	↔	↔	↔	↓	↓	↓	↓	↓
20°C	4bar	↑	↑	↑	↑	↑	↑	↔	↔	↔	↔	↓	↓	↓	↓
20°C	5bar	↑	↑	↑	↑	↑	↑	↑	↑	↔	↔	↔	↓	↓	↓
20°C	6bar	↑	↑	↑	↑	↑	↑	↑	↑	↑	↑	↔	↔	↔	↓
↑ flammable, ↓ non-flammable, ↔ the ignitron occurred only once during 3 repetitions															

The UFL values for gaseous alkanes in their mixtures with oxygen at ambient conditions are given in the table 2. In the tables 3 and 4 the values of UFL at elevated conditions are presented, together with their graphical interpretation in the fig. 3.

Table 2. The UFL measured in the spherical vessel of 2,3 dm^3, central position of ignition source, 20°C

	methane	ethane	propane	n-butane
GGW [% v/v]	57	55	50	49

Table 3. The influence of mixture initial pressure on the UFL

Pressure bar	methane	ethane	propane	n-butane
1	57	55	50	49
2	59	61,5	51	52
3	62	64	53	□
4	63	65,5	54	□
5	65	66	□	□
6	66	66,5	□	□

Table 4. The influence of mixture initial temperature on the UFL

temperature °C	methane	ethane	propane	n-butane
20	57	55	50	49
50	57,5	55	50,5	49
100	58,5	55,5	51,5	49,5
150	59	55,5	51,5	49,5
200	60,5	56	52,5	50

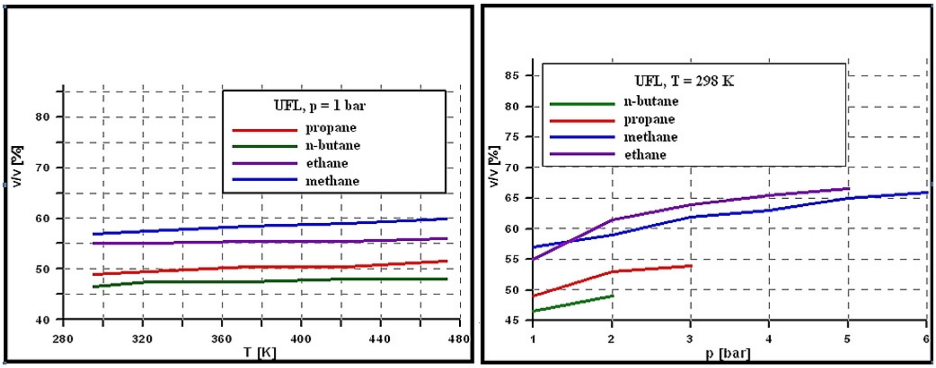

Fig. 2. The influence of elevated temperature and pressure on the UFL value

5. Discussion

The obtained values of the UFL are the consequence of many experimental measurements. The 7% initial pressure rise was used as a criterion of the UEL (Fig. 4). Experiments on the ignition of extremely fuel-rich methane, ethane propane and n-butane –oxygen mixtures in the 2,3 dm^3 spherical vessel at elevated initial pressure (up to 6 bar) and temperature (473 K) reveal significant influence of the ignition position on the maximum explosion pressure. Direct results of pressure course versus time for the examined mixtures in the UFL regime are shown in Fig. 5.

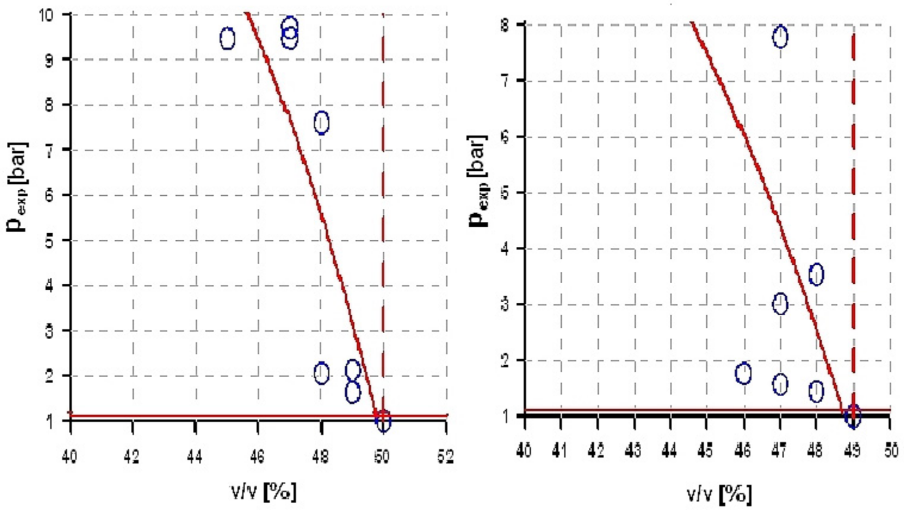

Fig. 4. The UEL approximation of propane-oxygen (left) and n-butane-oxygen (right) mixtures; 2,3 dm^3 vessel, 20°C, 1 bar, central ignition, 7% criterion

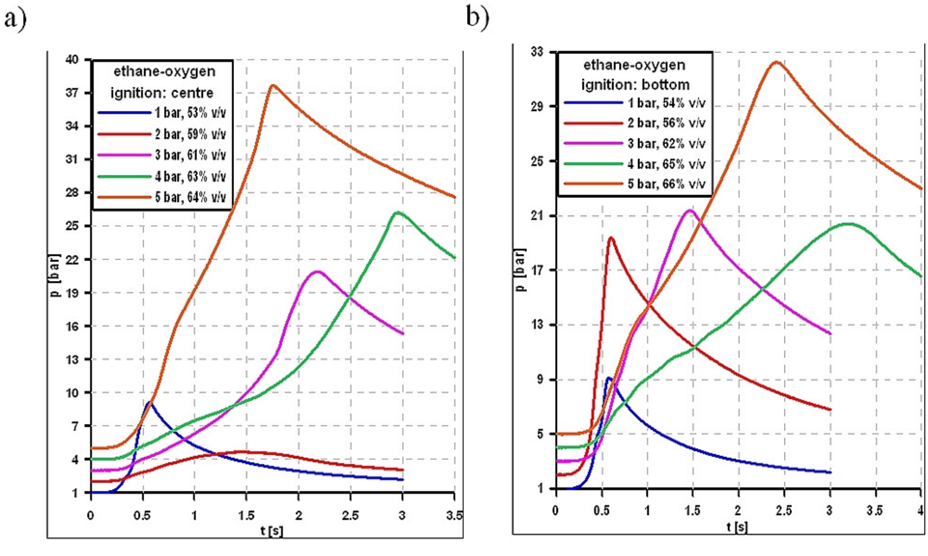

Fig. 5. The comparison of pressure rise for 5 different initial pressures for 2 ignition positions; 2,3 dm^3 vessel, 20°C

Maximum explosion pressure decreased as initial temperature increased in the case of all investigated mixtures. Examples are presented in Fig. 6. This was probably due to the decrease of the mass of mixture inside the chamber (at given initial pressure).

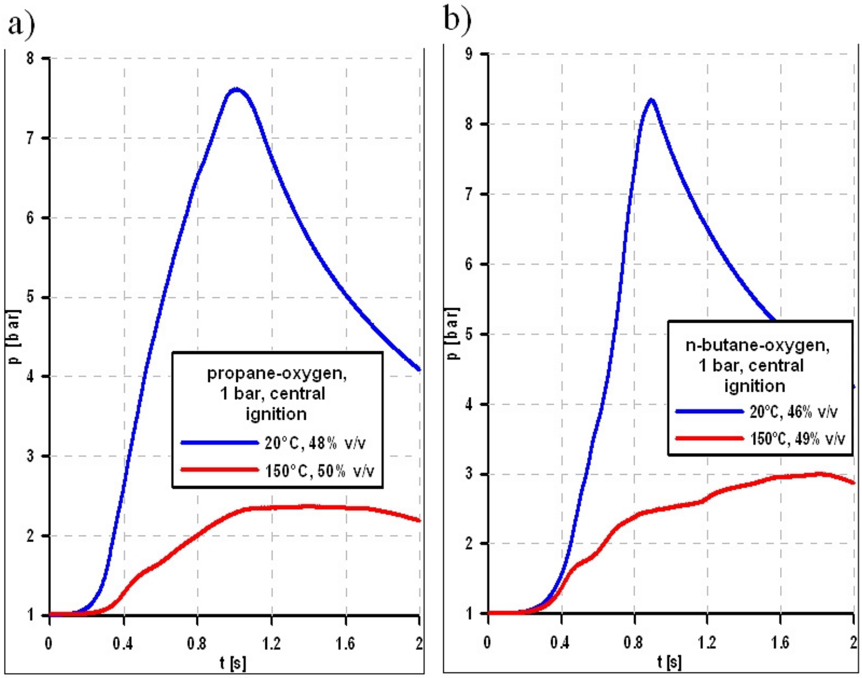

Fig. 6. The comparison of the pressure histories in the combustion vessel 2,3 dm^3 for two initial temperatures for central ignition position, 20°C

At higher initial pressure, mixture ignition occurred quite easily but the time of the explosion development lengthened. It means that the higher pressure, the slower flame propagation velocity. When increasing the initial pressure in a rich mixture, the expanding flame ball becomes more irregular in shape (Fig. 7).

The experimental results generally show an increase in soot volume fraction with increasing fuel content in the test mixture cases. Besides, it was possible to find the sooting tendency, that can be described as follows:

methane < ethane < propane < n-butane,

In some cases the soot volume fraction was very high, especially at higher pressure and lower temperature (Fig. 8).

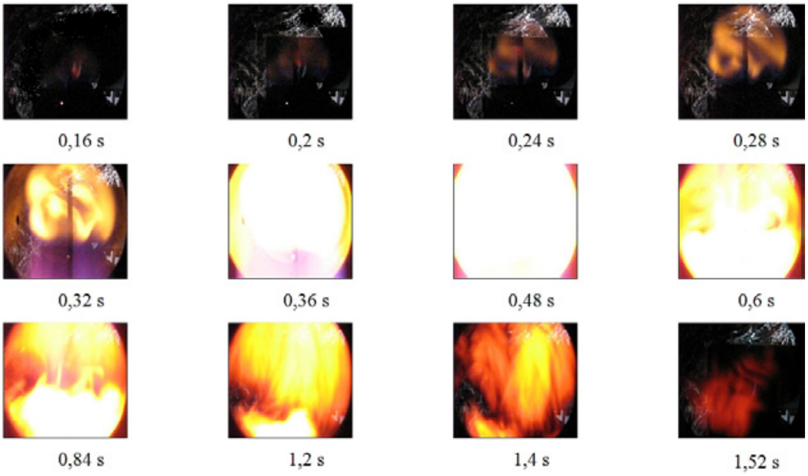

0,16 s 0,2 s 0,24 s 0,28 s

0,32 s 0,36 s 0,48 s 0,6 s

0,84 s 1,2 s 1,4 s 1,52 s

Fig. 7. The flame propagation in 2,3 dm^3 vessel; 62 mol.% ethane-oxygen mixture, bottom ignition (~ 0,1 J), 20°C, 3 bar

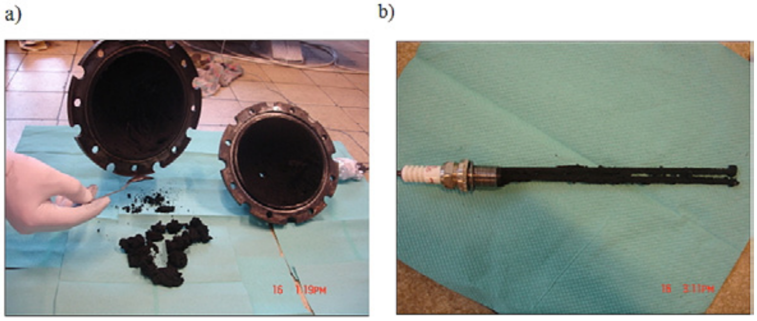

Fig. 8. The effect of soot formation; propane-oxygen mixture in 2,3 dm^3 vessel, 20°C, 3 bar

6. Conclusions

Methane, ethane, propane and n-butane in their rich mixtures with oxygen were examined during the experimental work. Key findings of this part of the research are:

- the upper explosion limits, in the examined range of the mixtures, strongly depend on the initial mixture temperature
- it was also observed that initial pressure has a significant influence on rich explosion limits, especially in the case of ethane-oxygen mixtures

- also the duration time of the explosion at rich limit increases significantly in the case of ethane-oxygen rich mixtures for higher initial pressures
- maximum explosion pressure decreases as initial temperature increases in the case of all investigated mixtures - due to the decrease of the mass of mixture inside the chamber (at given initial pressure)
- the change of the maximum explosion pressure versus initial mixture temperature can be approximated by means of a linear function for all oxygen mixtures
- the change of the upper explosion limit versus initial mixture pressure can be approximated by means of a linear function only for methane, ethane and propane -oxygen mixtures, not for ethane-oxygen mixtures
- lowering the ignition source position leads to easier ignition and higher explosion pressures for near upper limit mixtures, especially those with higher initial pressures – probably due to the fact that in this case more mixture is involved in combustion, and the whole process takes more time

Obtained results of the upper explosion limit for lower gaseous alkanes mixtures with oxygen as a function of initial pressure and temperature might be very useful not only for better understanding of explosive properties of this combustible mixtures but also would contribute to improve the safety conditions in many industry applications. The results of the study indicate that apparently inflammable mixtures can nevertheless become hazardous depending on the initial mixture conditions.

References

[1] A. A. PEKALSKI, E. TERLI, J. F. ZEVENBERGEN, S. M. LEMKOWITZ, and H. J. PASMAN, Combustion Institute Proceedings, 30, 1133–1139 (2005)

[2] L.G. BRITTON, Two hundred years of flammable limits, Process Safety Progress, 21, 1-11, (2002)

[3] K. HOLTAPPELS, V. SCHROEDER, A. KOBIERA, P. WOLANSKI, M. BRAITHWAITE, H.J. PASMAN, Gas explosion safety characteristics and anomalies at unusual conditions, Proceedings of the 12th international symposium on loss prevention and safety promotion in the process industries Edinburgh, UK, (2007)

[4] K.K. ELTSCHLAGER, et al. Technical Measures for the Investigation and Mitigation of Fugitive Methane Hazards in Areas of Coal Mining U.S. Department of The Interior Office of Surface Mining, Pittsburgh, 2001

[5] D.J. HALLIDAY Investigation of Natural Gas Explosions Forensic Science Service Metropolitan Laboratory, London, 2004

[6] J. DWYER, J.G. HANSEL, T. PHILIPS, Temperature Influence on the Flammability Limits of Heat Treating Atmospheres Air Products and Chemicals, Allentown, 2000

Journal of Energy Science, Vol. 1, No. 1, 2010, pp.121-131

Assessment of the effects of ignition of hydrogen leaking from untight installations

ANDRZEJ RUSIN[1*], KATARZYNA STOLECKA[1]

[1]Institute of Power Engineering and Turbomachinery, Silesian University of Technology
ul. Konarskiego 18, 44-100 Gliwice, Poland

Abstract: The limited resources of fossil fuels and the changing situation in economy and politics, lead to a higher interest in hydrogen as a fuel, with a wide range of use. It is currently used in the petroleum and automotive industries (in the latter to drive vehicle engines), and to heat households and provide them with electricity (fuel cells). Hydrogen is, at the moment, obtained from natural power resources, i.e. natural gas, petroleum, coal and water electrolysis. The methods most often used to obtain hydrogen are: steam reforming, coal gasification, partial oxidation of refinery residues and electrolytic water decomposition. Hydrogen is a relatively hazardous gas. Consequently, its manufacture, storing and transport pose a crucial problem. In case of a leakage it can be expected to form a combustible mixture more quickly than other fuels due to its higher diffusivity and rapid mixing with air. The paper presents an analysis of the effects of ignition of hydrogen leaking from untight installations. Calculations of the radiative heat flux value of burning hydrogen in the function of the outflow are presented. The change in the heat radiation in the function of distance from the leakage is determined. Potential heat radiation effects on people within its reach are assessed.

1. Introduction

Hydrogen is considered to be the most future energy carrier, especially in the context of the reduction in the emission of greenhouse gases. It can be obtained from materials such as natural gas, coal or biomass with the use of solar, wind or nuclear energy. It should also be noted that the production of energy, derived from hydrogen, does not contribute to an additional emission of CO_2 and the main potential source of hydrogen on Earth –water–is practically unlimited. Hydrogen is also gaining importance, because it is now being used

---

[*] Corresponding author, email: andrzej.rusin@polsl.pl

more and more extensively as a source of energy for driving car engines. This will cause a development of a hydrogen infrastructure including filling stations where it will be possible to refuel hydrogen. Hydrogen could be supplied to such stations by appropriate tankers, or it could be produced at these stations by means of gas reforming or electrolysis. Because of its high flammability, the assessment of risk involved with the use of hydrogen becomes a crucial problem. One of the potentially most dangerous scenarios of events related with hydrogen installations is its uncontrollable leakage, which could turn into a fire with a high level of heat radiation. An intensive research has been done in this area for several years [1÷7]. The paper presents an analysis of the potential effects of heat radiation caused by the burning of relatively small hydrogen leakages. Algorithms for the calculations of the value of the radiation are presented. The conditional probability of fatal burns in people being in the immediate vicinity of leaking installations is estimated with the use of what is referred to as probit functions.

2. Properties and obtaining of hydrogen

2.1. Properties of hydrogen

Hydrogen is the most common element in the universe discovered and described about 300 years ago. It is an important raw material used among others in refineries, in the petroleum industry and recently also more and more often in the power industry. Especially the present and future role of hydrogen as an energy carrier is mainly connected with its physical and thermodynamic properties [1,2]. Under normal conditions hydrogen is a gas of a very low density of 0.08374 kg/m^3. With increasing pressure the density of hydrogen rises, but not as fast as it could be expected from the equation of the state of ideal gas. At low temperatures particle hydrogen is low-reactive, which changes together with an increase in its temperature. The product of hydrogen burning is water and considerable amounts of released energy. The higher and lower combustion heat of hydrogen is:141.86 MJ/kg and 119.93 MJ/kg, respectively. These values are much higher than those of other gas fuels such as methane or propane. In comparison with other fuels the so-called energy density of hydrogen is relatively low, which necessitates a construction of high-volume tanks for the transport and storage of hydrogen. Some other properties of hydrogen, such as the ignition temperature of -253ºC and the self-ignition temperature of 585ºC, also are essential from the point of view of its practical application. The latter temperature is higher than the same temperature for petrol, methanol, propane or methane. A characteristic feature of hydrogen which has a great impact on the safety of its use is the wide range of its flammability in air – from 4 to 75% V/V, whereas for methane, for example, the range is only 5.3-15% V/V. Another of the values affecting the potential hazard of hydrogen catching fire is its low ignition energy, i.e. the minimum amount of outer energy, which, when supplied to hydrogen, can cause its ignition. The value for a stoichiometric mixture of hydrogen is only 0.02 mJ, whereas for other fuels the energies are more than ten times higher. Such a low value of the hydrogen ignition energy leads to a situation where any uncontrollable leakage might end in a fire, and the igniting spark can result from the friction of the hydrogen flux itself, or from the electrostatic influence of objects such as clothes.

Another important value characterising the burning process of hydrogen is the burning rate, i.e. the rate at which the flame spreads through the combustible mixture of hydrogen. It is much higher than for other fuels and ranges from 2.65 to 3.25 m/s. The flame of burning hydrogen is almost invisible and the phenomenon of soot formation does not occur in it. Heat is emitted in a narrow band of infrared primarily from steam. Adiabatic flame temperature of burning hydrogen exceeds 2300 K.

In the characterisation of properties connected with a safe use of hydrogen one must not overlook its considerable tendency to leakage and high diffusivity. The tendency to leakage, as compared to other fuels, results among others from the small size of hydrogen particles.

2.2. Obtaining of hydrogen

The production of hydrogen for chemical and recently for power purposes is growing steadily. Its sources are first of all natural gas, crude oil and coal, but also water [1,2]. The basic technology is among others coal gasification, which consists in the action of steam on coke which leads to a formation of gas composed of CO and H_2. The gas is subject to a further action of water in the presence of catalysts, which finally gives CO_2 and H_2.

Another technology for the production of hydrogen is steam reforming of methane. The action of steam on methane in the presence of catalysts results in the creation of a synthesis gas composed of 75% of H_2, and also of CO and CO_2. The further stages of the process are: the conversion of CO in the presence of H_2O to CO_2 and H_2, and the removal of CO_2. Hydrogen can also be obtained through a partial oxidation of heavy hydrocarbons forming refinery residues. The synthesis gas obtained here contains about 45% H_2, but also considerable amounts of CO, CO_2 and H_2S, which must undergo further treatment and removal processes. The oldest and the best known way to obtain hydrogen is water electrolysis which occurs according to the reactions:

cathode: $2H_2O + 2e^- \rightarrow H_2 + 2OH^-$, anode: $2OH^- \rightarrow H_2O + \frac{1}{2}O_2 + 2e^-$,

which in total gives: $H_2O \rightarrow H_2 + \frac{1}{2}O_2$.

Apart from these conventional methods of hydrogen production an extensive research is being done on new technologies. These include among others: the thermo-chemical dissociation of hydrocarbons, the thermo-chemical decomposition of hydrogen sulphide and water, or biological methods which make use of sunlight, water and biomass. For each of the methods mentioned above there exist appropriate installations in which hydrogen is obtained in the liquid or gaseous state. It can later be stored and transported. Due to the necessity to use high pressures reaching 35 and even 70 MPa in these processes, even the tiniest lack of tightness can lead to a hydrogen leakage. The leakage in the presence of even the smallest ignition energy could cause a fire whose effects in the form of thermal radiation are hazardous to people in the immediate vicinity.

3. Models of flame radiation of burning hydrogen

One of the possible effects of an uncontrolled release of gas from an untight installation is a fire hazard. What is referred to as jet fire is one of the most dangerous of all kinds of fires. Its effect is an extremely high heat radiation of the flame. An estimation of the radiation value is still a crucial research subject, and the proposed models, such as source models, multi-point models or the surface source models are approximate semi-empirical models.

In practice, the third model is the one which is used most often with an assumption that a part of the combustion heat radiates through the visible surface of the flame. The theoretical surface energy of heat radiation in a unit of time E_t can be calculated from the dependence:

$$E_t = \frac{Q_s}{A}, \tag{1}$$

where:

Q_s – combustion energy per time unit (J/s),

A – flame surface area (m^2).

Value Q can be calculated knowing the mass flow rate of the burning gas and heat of combustion H_c. Because only a part of this energy will be transferred through radiation, hence:

$$E = \eta_s E_t \,, \tag{2}$$

where: η_s describes the share of radiated energy in the total heat released from fire.

The value depends on the kind of fire and also on the kind of the burning substance.

A unit heat flux received by a surface at a certain distance from the flame can be calculated from the dependence:

$$q = EF\tau_a \,, \tag{3}$$

where: F is the configuration coefficient dependent on the distance and the location of the surface receiving the radiation in relation to the radiating flame area, and on the flame shape. Value τ_a describes atmospheric transmittivity between the receiver and the emitter, which is dependent mainly on steam and carbon dioxide content in air.

Other important features of the flame of the burning gas are its dimensions, i.e. its length L_f and its width W_f.

The reference literature presents various models which take into account more details for dependence (3). The simplest of them, which defines a unit heat flux at distance r from the flame centre, is described by the dependence [3]:

$$q = \frac{\eta \tau_a \dot{m}_e H_c}{4\pi r^2} \,. \tag{4}$$

In dependence (4) $\dot{m}_e$ denotes what is referred to as the effective gas flux smaller than the theoretical maximum flux $\dot{m}_{max}$ described for the case of a critical outflow by the formula:

$$\overset{\bullet}{m}_{\max} = A_o \sqrt{\rho_k p_k \kappa \left(\frac{2}{\kappa + 1} \right)^{\frac{\kappa+1}{\kappa-1}}} \,, \tag{5}$$

$$\dot{m}_e = c m_{max} \,. \tag{6}$$

Coefficient c usually assumes a value of approx. 0.3, or higher.

The experimental research of the hydrogen flame presented in [4,5] made it possible to work out the following empirical dependencies for a calculation of a unit heat flux at distance r from the flame:

$$q = \frac{a_s \dot{m}^{b_s}}{r^2}, \tag{7}$$

where a_s, b_s – constants established empirically, equalling $6 \cdot 10^5$ and 1.3, respectively. In the above dependence the mass flow rate should be expressed in kg/s; consequently, heat flux q will be expressed in W/m^2.

On the grounds of the research the relationships between the mass flow rate and flame length L_f were also established.

$$L_f = a_l m^{b_l}, \tag{8}$$

where a_1, b_1 are constants.

A more elaborate model also based on experimental research of the hydrogen flame was presented in works [6,7]. In it, a non-dimensional radiant power c* was defined, which describes the relative radiation along the flame length.

$$c^* = f(\frac{x}{L_f}). \tag{9}$$

It was found out that the maximum value c* of approx. 0.85 occurred for x/L_f contained in the range of 0.6 to 0.7. The value of unit radiation is described by the dependence [6,7]:

$$q = c^* \ \frac{S_{rad}}{4\pi r^2}, \tag{10}$$

where:

$$S_{rad} = \dot{m} H_c X_r. \tag{11}$$

Value X_r corresponding to the ratio of radiated energy to the total chemical energy of the burning gas was in turn made dependent on the grounds of the research on a value τ_f, which has a time dimension and is defined as follows:

$$\tau_f = \frac{\rho_f W_f^2 L_f f_s}{3\rho_o d_i^2 u_i}, \tag{12}$$

where ρ_f, W_f, f_s are the density, width and length of the flame. f_s corresponds to the ratio of the masses in the stoichiometric mixture of hydrogen and air, d_i is the diameter of the gas outflow hole, u_i – the rate of the outflow, and ρ_o the density of the gas flowing out. After time τ_f is established from dependence (12), X_r is calculated, and then, with the use of formulae 11 and 10, the unit heat flux in the function of distance r.

4. Assessment of the radiation effects

On the grounds of the algorithms presented above the calculations of the thermal effects of hydrogen leakage from an installation were carried out. It was assumed that in the installation there was hydrogen under the pressure of 35 MPa, and the leakage occurred through holes of equivalent diameters of approx. 1÷3 mm. Moreover, the following values were assumed in the calculations: $H_c = 141.9$ MJ/kg, $\tau_a = 1$, $\eta = 0.15$.

The obtaining of unit radiation value $\dot{q}$ is shown in Fig. 1 and 2. Fig. 1 presents the dependence $\dot{q}$ in the function of the leakage size $\dot{m}$. The particular curves in the figure correspond to various distances between the location of the receiver and the flame centre. Fig. 2 describes the dependence of the radiation $\dot{q}$ in the function of the distance from the radiation source.

To estimate the conditional probability of fatal burns depending on the volume of the received thermal radiation the so called probit functions are used of the following form:

$$P_r = a + b\,ln(D), \tag{13}$$

where:

P_r – probit function which is a measure of the population exposed to a particular injury caused by load D.

a, b – empirical constants dependent on the type of injury and type of load.

With a thermal load which lasts for time t, value D can be defined as:

$$D = \frac{tq^{4/3}}{10^4}. \tag{14}$$

The probit function coefficients then have the form a = -14.9 b = 2.56. With the use of the dependence presented above it is possible to determine the probit function value for a given radiation and the time it lasts, and then – the conditional probability of death of people exposed to a given effect.

By means of the results presented in Fig. 1 and 2 the values of the conditional probability of fatal burns were calculated. Fig. 3 presents the dependence of this probability in the function of the leakage size, and Fig. 4 – in the function of the distance from the flame centre. All the results relate to the time of exposure to the radiation of 120 s. On the grounds of the obtained results it can be estimated that with outflows exceeding 0.075 kg/s, the danger zone extends to approx. 6m from the leakage. With smaller leakages the zone extends to 3.5 to 4.5 m.

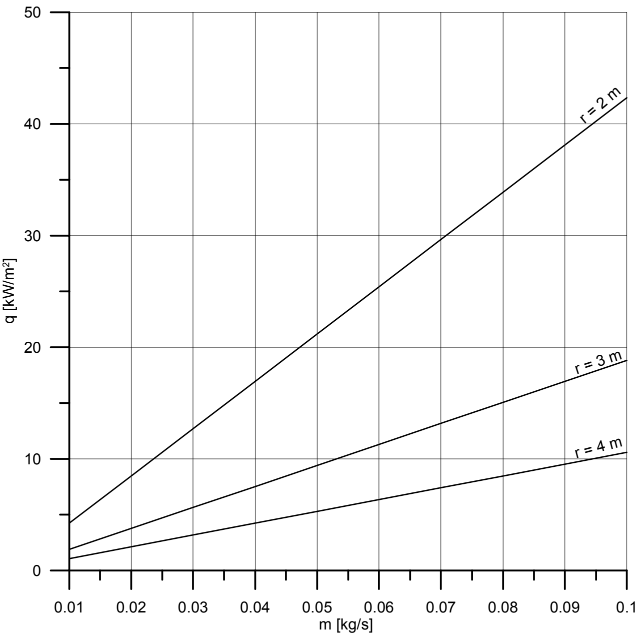

Fig. 1. Dependence of thermal radiation on mass flow rate of hydrogen flowing out

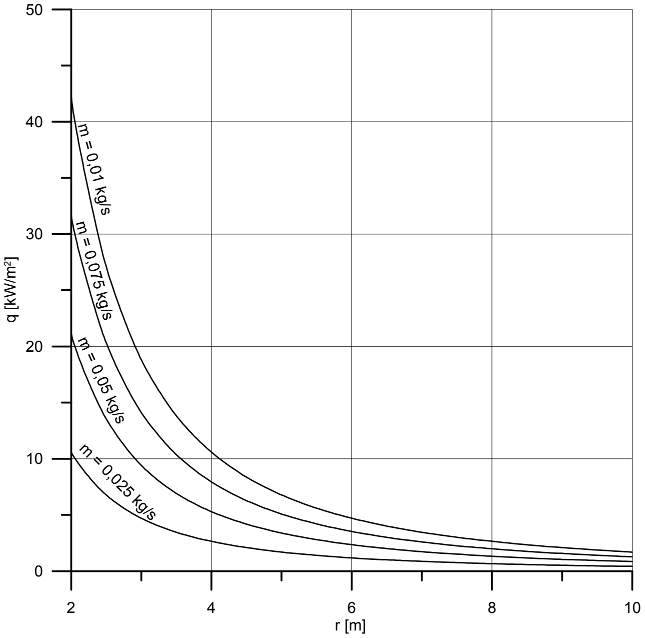

Fig. 2. Dependence of thermal radiation on distance from hydrogen flame centre

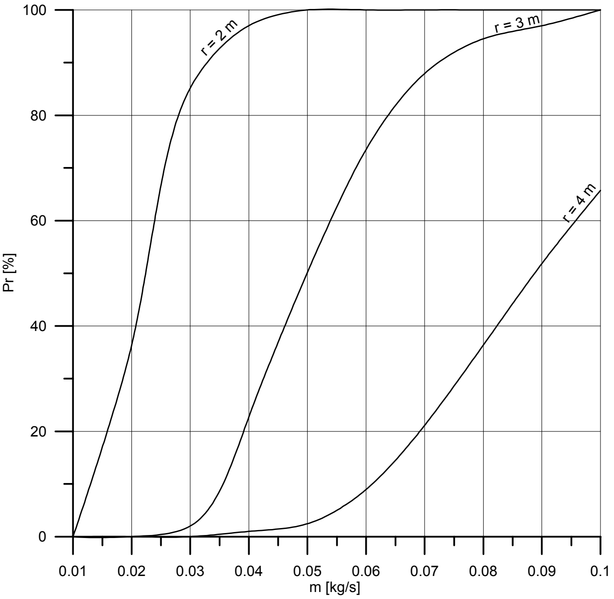

Fig. 3. Relative probability of fatal burns in the function of mass flow rate of flowing out hydrogen

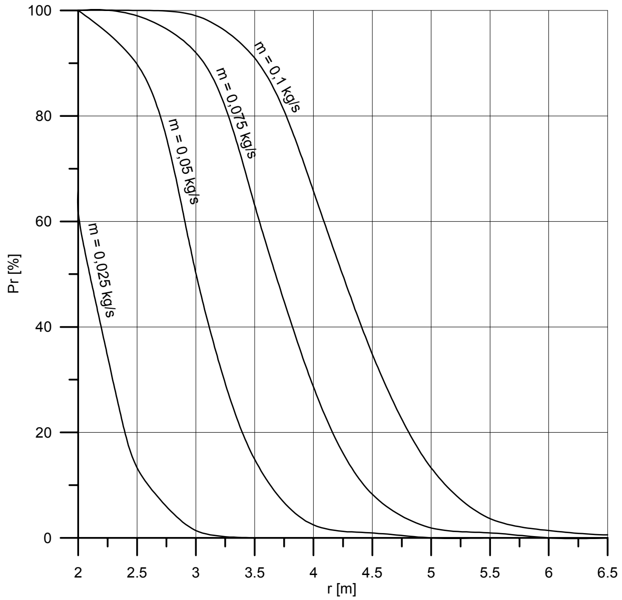

Fig. 4. Relative probability of fatal burns in the function of distance from flame centre

5. Conclusions

Hydrogen is definitely a gas with varied applications which plays, and which will play, an extremely essential role in the power and automotive industries. On the other hand, it is a dangerous gas. Its physical properties and the technical specifications of its storage and transport may lead to leakages, and consequently – to fires and explosions. The impact of hydrogen on construction materials, including steels, should also be remembered. Under some conditions and with a proper length of time of hydrogen contact with steel there may arise hydrogen embrittlement and damage to the component, which may in consequence lead to hydrogen leakage. Hence, it is vital that proper conditions for safety be assured both during hydrogen production and its storage and use. An important element of such actions is the assessment of potentially hazardous zones surrounding installations containing hydrogen. The analysis of the possible radiation level presented in this paper concerns relatively small hydrogen leakages which result from lack of tightness in various components of an installation such as pipe joints, valves, etc. The values obtained point out that the ranges of critical zones with such leakage volume do not differ substantially from the zones within installations for other gas fuels such as LPG [8].

REFERENCES

[1] SURYGAŁA J., Wodór jako paliwo, WNT, Warszawa, 2008

[2] ELVERS B. Handbook of Fuels, Viley-VCH, Wienhaim, 2008

[3] JO Y.-D., AHN B.J., Analysis of Hazard Area Associated with Hydrogen Gas Transmission Pipelines, International Journal of Hydrogen Energy, 31 (2006) p. 2122-2130.

[4] MOGI T., HORIGUCHI S., Experimental Study on the Hazards of High-pressure Hydrogen Jet Diffusion Flames, Journal of Loss Prevention in the Process Industries 22 (2009), p. 45-51.

[5] IMAMURA T., HAMADA S., MOGI T., WADA Y., HORIGUCHI S., MIYAKE A., OGAWA T., Experimental Investigation on the Thermal Properties of Hydrogen Jet Flame and Hot Currents in the Downstream Region, International Journal of Hydrogen Energy, 33 (2008) p. 3426-3435.

[6] HOUF W., SCHEFER R., Predicting Radiative Heat Fluxes and Flammability Envelopes from Unintended Releases of Hydrogen, International Journal of Hydrogen Energy, 32 (2007) p. 136-151.

[7] SCHEFFEF R.W., HOUF W.G., WILLIAMS T.C., BOURNE B., COLTON J., Characterization of High-pressure, Underexpanded Hydrogen-jet Flames, International Journal of Hydrogen Energy, 32 (2007) p. 2081-2093.

[8] RUSIN A., STOLECKA K., Zasięg stref krytycznych przy wypadkach cystern przewożących LPG, Rynek Energii nr 3 (88), 2010, str. 49-54.

Journal of Energy Science, Vol. 1, No. 1, 2010, pp.133-145

The prototype capacitance tomography sensor with increased sensitivity near the wall

MARIUSZ R. RZĄSA , BOLESŁAW DOBROWOLSKI

Politechnika Opolska , Katedra Techniki Cieplnej i Aparatury Przemysłowej.
45-271 Opole ul. Mikołajczyka 5

The paper presents a sensor for the capacitance tomograph used for tests of two-phase flows. Structure of the sensor was described, and the proposed solution was compared with typical sensors applied in capacitance tomography. Increase of sensitivity near the pipeline wall seems to be the most important advantage of the proposed solution. It is desirable because of phenomena occurring in during tests of two-phase gas-liquid flows, especially downward flows. The paper presents also the measuring system and the results obtained from the tests performed at the special measuring stand. The obtained test results were compared with the results for a typical capacitance sensor with the electrodes of the same dimensions.

Symbols

A– surface area, m^2
C– capacitance, F
R– resistance, Ω
$E(x,y,z)$ – distribution of the electric field, V/m
f– frequency, Hz
f_i^k– reconstruction field value
w_{ii}– element of the sensitivity matrix
$\varepsilon_r(x,y,z)$ – distribution of the dielectric permittivity, F/m
$\varphi(x,y,z)$ – distribution of the of the electric potential, V
$q\ (x,y,z)$ – distribution of electric charges, C

1. Introduction

There are many various structures of two-phase gas-liquid flows [1]. In capacitance tomography a magnitude measured at the electrode length is averaged, so capacitance tomographs should not be applied for bubble structures. Very good results are obtained for structures with phase separation

[2]. Fig. 1 shows two different stratified structures occurring in gas-liquid flows.

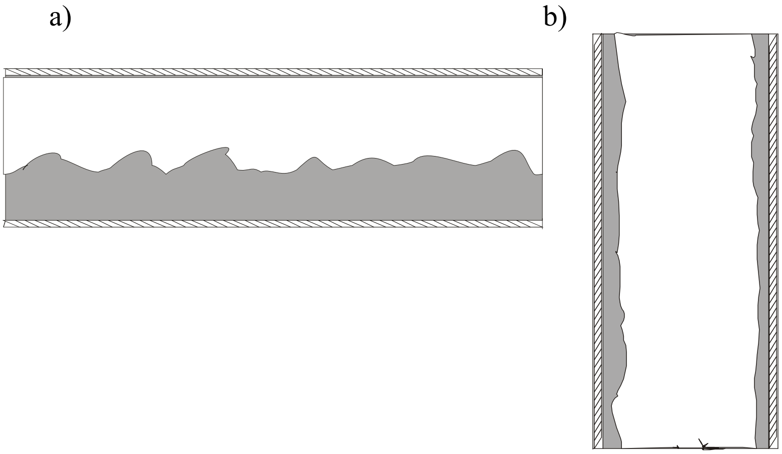

Fig.1. Gas-liquid structures in a) horizontal flow, b) co-current downward flow

The annular flow (see fig. 1b) can be asymmetric. In such flows, determination of thickness of the liquid layer flowing along the wall seems to be very important because it is decisive in determining the flow parameters. The capacitance sensor described in this paper is assigned mainly for tests of annular flows and it provides high sensitivity of measurements near the pipeline wall where the liquid layer occurs. However, the sensor of that type can be applied for tests of other flows, too.

2. The measuring sensor

The idea of capacitance tomography is based on measurements of capacitance variation between electrodes of the measuring sensor. The measured variation is caused by changes of structure of the material located in the measuring space. the measuring space.

Typical sensors applied in capacitance tomography are shown in fig. 2 [3,4]. They include rectangular electrodes arranged around the measuring section. Two metal screens are to reduce influence of disturbance. From the measurements of capacitance between all the possible combinations of electrodes, we obtain a picture of distribution of permittivity corresponding to gas and liquid distribution. Distribution of the electric field along the electrode length is not uniform, but it can be omitted when the electrode height is much bigger than its width, in the of, field nonlinearity.

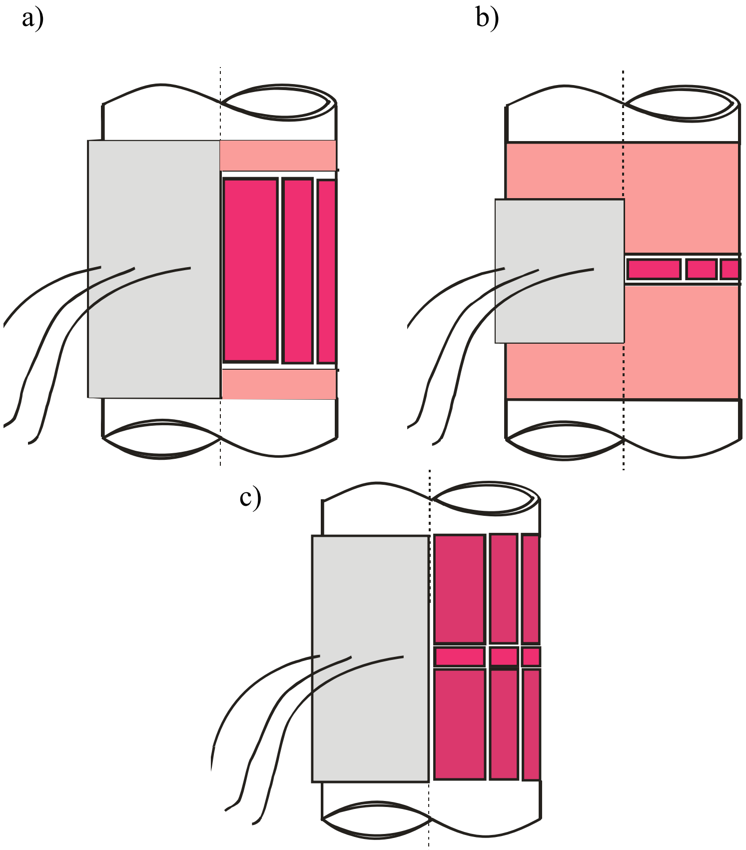

Fig.2. Capacitance sensors a) with long electrodes b) with small electrodes c) with compensatory electrodes

In the solution shown in fig. 2a, the electrode length is approximately equal to the sensor diameter. It ensures stability of measurements. However, a long electrode causes averaging of the value measured at the electrode length and it is sometimes unfavorable, especially for the bubble flows. Another sensor is presented in fig. 2b [3]. It includes big axial shields wound around the pipe above and below the electrodes. Both axial screens are connected electrically with the radial screen. Here, the electrodes have much smaller surface, and it causes averaging at a smaller interval of the pipeline, however, as the pipeline diameter rises, the measured capacitances decrease many times. Moreover, nonlinear distribution of the electric field at the electrode length is an additional inconvenience [4]. Thus, correct determination of the sensitivity map for such a sensor becomes difficult. Such difficulties can be eliminated by using the sensor shown in fig. 2c. It includes compensatory electrodes – while measurements they have the same potential as the measuring electrodes.

In all the above solutions, sensitivity inside the measuring sensor is conforming with distribution of the potential between the pairs of electrodes. Taking into account the previous considerations on structures of two-phase gas-liquid flows, or increase of sensitivity near the tomograph wall seems to be desirable. It should allow to detect thin liquid layers on the wall. In this order, the sensor presented in fig. 3 was elaborated.

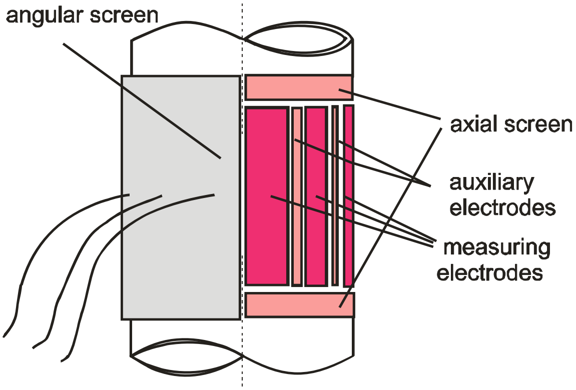

Fig.3. The capacitance sensor of high sensitivity near the wall

The sensor includes 17 measuring electrodes located on the pipeline 75 mm in diameter. Application of a great number of electrodes influences increase of the sensor sensitivity, but at the same time surface of the electrodes decreases and the measured capacitances are very small. Thus, it was necessary to increase the electrode length (electrodes equal to one diameter of the pipeline were assumed). As the electrodes were long, the electrodes compensating the electric field were not necessary.

In order to increase of sensitivity near the wall, stabilizing electrodes were applied as well. They were located between the measuring electrodes, and their width was many times smaller than the width of the measuring electrodes. In the tests it was found that good results were obtained for electrodes 15-20 times more narrow than the measuring electrodes. During the measurements, the auxiliary electrodes adjacent to the measuring electrode had the same potential as the opposite measuring electrode. Thus, the measured capacitance was equal to the substitute value of three component capacitances C_{Xp} C_{X1} C_{X2} (see fig. 4b).

$$C_X = C_{X1} + C_{X2} + C_{Xp} . \tag{1}$$

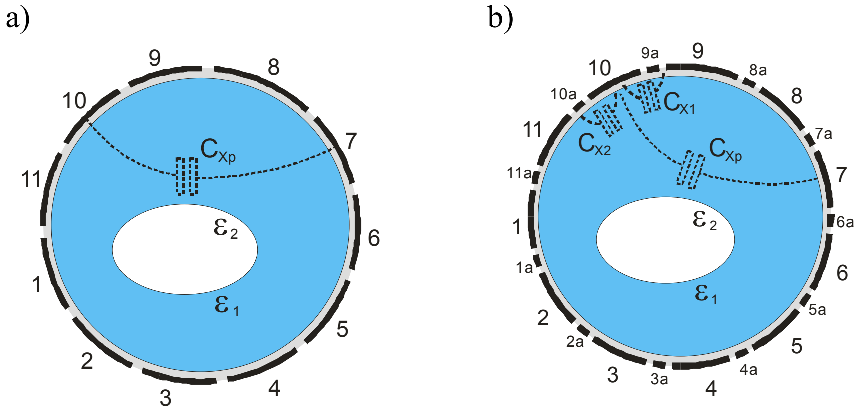

Fig.4. Idea of capacitance measurements a) for traditional sensor, b) for sensor with increased sensitivity near the wall

Since auxiliary and measuring electrodes are located close to each other, sensitivity near the pipeline wall becomes greater as compared to the sensor from the traditional solution (see fig. 4a).

3. The sensitivity map

The measured capacitance depends on the permittivity field inside the sensor. The permittivity for gas and liquid are different, so they can be used as a gas presence identifier. The electric charge accumulated between the selected electrodes is described by the Gauss law:

$$C = \frac{Q_{cx}}{V} = \frac{1}{V}\oiiint_A \varepsilon_r(x,y,z)E(x,y,z)\ dA\ , \qquad (2)$$

where: $\varepsilon_r(x,y,z)$ – distribution of the dielectric permittivity, $E(x,y,z)$ – distribution of the electric field, A – electrode area.

The electric field inside the measuring plane is expressed by the Poisson equation:

$$\nabla^2\varphi(x,y,z) + \frac{1}{\varepsilon_r(x,y,z)}\, grad\,\varphi(x,y,z) + grad\,\varepsilon_r(x,y,z) = \frac{q(x,y,z)}{\varepsilon_r(x,y,z)}\ , \qquad (3)$$

where: $\varphi(x,y,z)$ – distribution of the electric potential, $q\ (x,y,z)$ – distribution of electric charges.

In most cases, there are no charges in liquids, so the function of charge distribution q(x,y,z) is equal to zero. This assumption strongly simplifies solving the equation. Finally, we obtain the following equation expressing capacitance [2]:

$$C = \frac{\iint\limits_{A} \varepsilon(x,y,z)\, grad\,\varphi(x,y,z)\, d\,\hat{A}}{\int\limits_{S} grad\,\varphi(x,y,z)\, d\,\hat{s}} . \qquad (4)$$

The above relationships can be used for determination of sensitivity maps. The sensitivity maps are the most important in image reconstruction. In the case of the sensor with higher sensitivity near the wall, the sensitivity map was determined by calculating of permittivity distribution – Equation 3 was solved for three pairs of electrodes according to Equation 1 [9].

In order to compare the results obtained, simulations were performed. They included generation of electric field distribution between a pair of electrodes for the traditional sensor (see fig. 2a) and the sensor with auxiliary electrodes (see fig. 3). For calculations of the potential distribution and the sensitivity map the finite element method was applied using regular networks of the sensitivity map (see fig. 5).

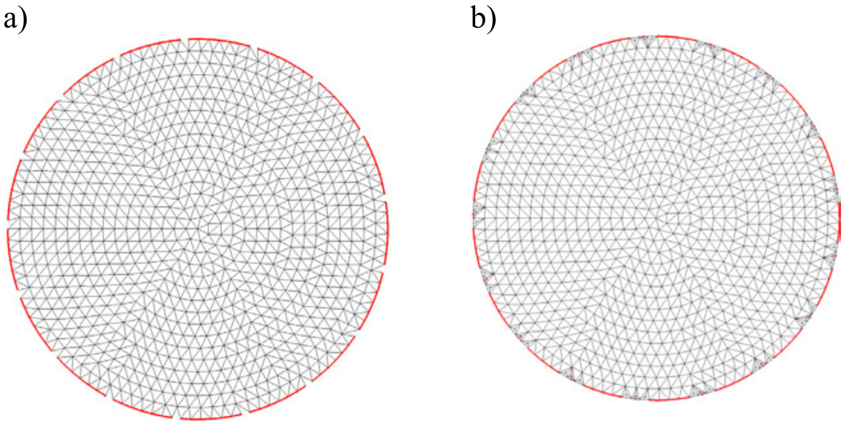

Fig.5. Network for determination of the sensitivity map a) for the sensor from fig. 2a b) for the sensor from fig. 4

Fig. 6 shows the results of generation of sensitivity distribution for the sensors presented in fig. 2a and fig. 3. The fields of the high sensitivity are red, and those of the low are blue. The map for the pair of electrodes for the sensor from fig. 2a (without auxiliary electrodes) shows the highest sensitivity in the central part; near the measuring electrodes a drop of sensitivity is observed. In the case of the sensor with auxiliary electrodes (see fig. 3), sensitivity strongly rises near the auxiliary electrodes. It means that the assumed structure of the measuring sensor is right.

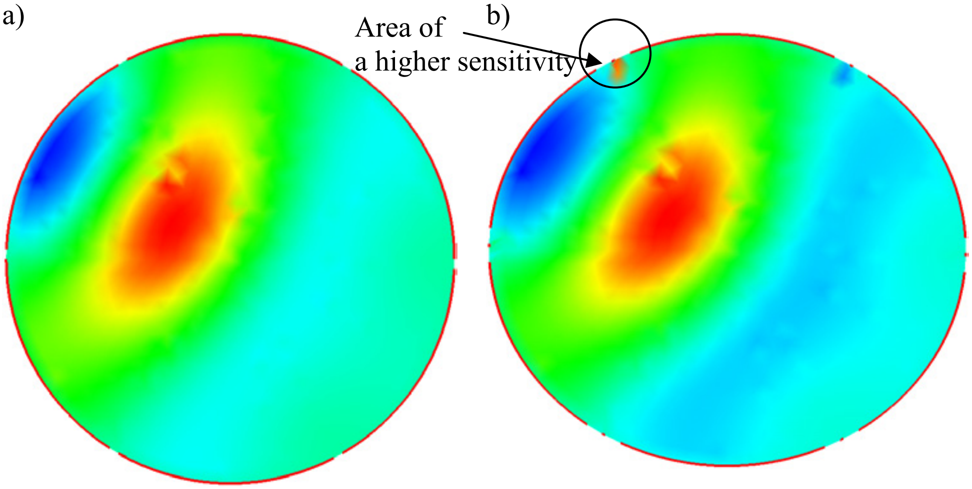

Fig.6. Sensitivity map a) for the sensor from fig. 2a b) for the sensor from fig. 3

4. The measuring system

The measuring system influences quality of the image obtained with the capacitance tomograph. Resolution of images obtained with the capacitance tomographs is rather low as compared with other techniques applied in processing tomography. It is caused, among others, by the limited sensitivity of converters [7] and linearity of conversion [8].

The converter applied in this paper is characterized by a large measuring range while linearity is kept at the level 5%. The measuring system uses RC oscillator with the Schmitt circuit [6] (see fig. 8). It is a converter changing the measured capacitance into frequency. The signal course at the output is rectangular. Owing to that, measurement of frequency of such a signal does not need the zero-detection system. Moreover, the converter can be joined directly to the processor, so the measuring system becomes much simpler.

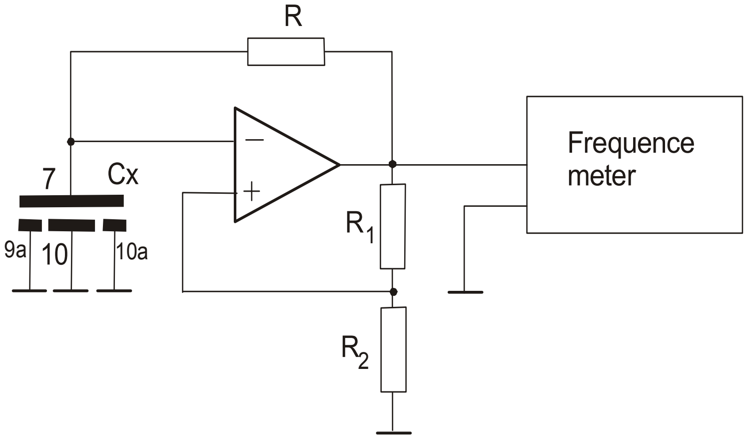

Fig.7. A scheme of the measuring system in the RC generator with the Schmitt circuit

Fig. 7 shows a scheme of such a converter where successive pair of measuring electrodes are joined instead of the condenser CX. For example, for the pair of electrodes from fig. 4b, numbers 9a, 10 and 10a, are related to the electrodes participating in measurements and influencing the value of capacitance CX. At the same time, the remaining electrodes (not used for measurements) are connected to high impedance in the system of switching the electrodes over. The converter charges the measuring condenser CX by the resistor R. Those elements form a negative feedback circuit. The positive feedback circuit with elements R1 and R2, switching the output of amplifier from the plus saturation state to the minus saturation state. The abrupt change of the output voltage causes charging and discharge of the measuring condenser. Frequency generated by the system is expressed as

$$f = \frac{1}{3RC_X \ln\left(1 + \frac{2R_2}{R_1}\right)}. \tag{5}$$

Fig. 8 shows characteristics of the converter conversion. The frequency value at the converter output is inversely proportional to the measured capacitance. The considered converter provides high stability of measurements, and its measuring range is very wide. Thus, it is possible to build a measuring system including the same converter for measurements of capacitance for both adjacent and opposite electrodes [6].

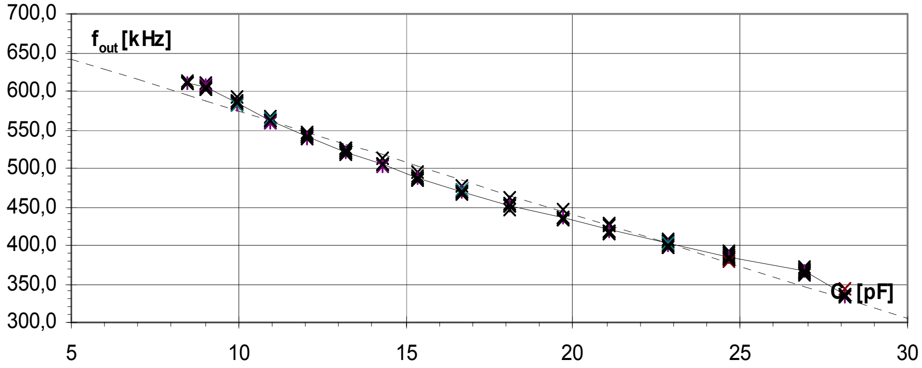

Fig.8. A scheme of the measuring system in the RC generator with the Schmitt circuit

5. The method of image reconstruction

The method of Linear Back-Projection (LBP) was used for image reconstruction [10]. The method is simple and does not require much time. In engineering applications, values of fi in particular areas of image are calculated from

$$\forall_{j=1..N} \qquad f_j = \frac{\sum_{i=1}^{M} w_{ij} \cdot C_i}{\sum_{i=1}^{M} w_{ij}} , \tag{6}$$

where: w_{ij} – element of the sensitivity matrix determined from the solved Poison equation C_i – standardized value of the measurement capacitance.

$$C_i = \frac{C_m - C_{\min}}{C_{\max} - C_{\min}} 100\% , \tag{7}$$

where: C_m – measured quantity C_{max} – measured quantity for the sensor fully filled with liquid C_{min} – measured quantity for the sensor fully filled with gas.

The considered method does not require much time, however the obtained images are sometimes of a bad quality. In order to improve reconstruction quality, the Iteration Back Projection (IBP) was used as well. The algorithm of IBP is very similar to LBP method. Modification consists in calculation of the reconstruction function error at each step according to the following relationship:

$$\underset{j \in <1, N>}{\forall} \quad \Delta f_j = \frac{\sum\limits_{i=1}^{M} w_{ij} \Delta C_i}{\sum\limits_{i=1}^{M} w_{ij}} . \tag{8}$$

Next, a new distribution of permittivity for each step is calculated according to:

$$\underset{j \in <1, N>}{\forall} \quad f_j^{k+1} = f_j^k + \lambda(\Delta f_j) , \tag{9}$$

where: λ – coefficient of relaxation

6. The method of image reconstruction

In order to compare influence of the sensor type on quality of the reconstructed image, tests were performed. In the tests, two typical structures occurring during two-phase flows were measured. A traditional sensor and a sensor with increased sensitivity were used for measurements. The stratified horizontal flow and the annular downward flow were measured. The results of reconstruction obtained with the use of LBP are shown in fig. 9. In the case of LBP, when a half of the pipeline is filled with water, no sensitivity is observed in the middle of the field. This disadvantage is much more visible when a sensor with increased sensitivity is applied.

As for the tests of the stratified flow, when 50% of the pipeline is filled with water, the best results are obtained for the traditional sensor (a better ratio of sensitivity in the middle to sensitivity near the wall). In the case of annular structures, application of the sensor with increased sensitivity near the wall seems to be a better solution. The traditional sensor gives distorted images.

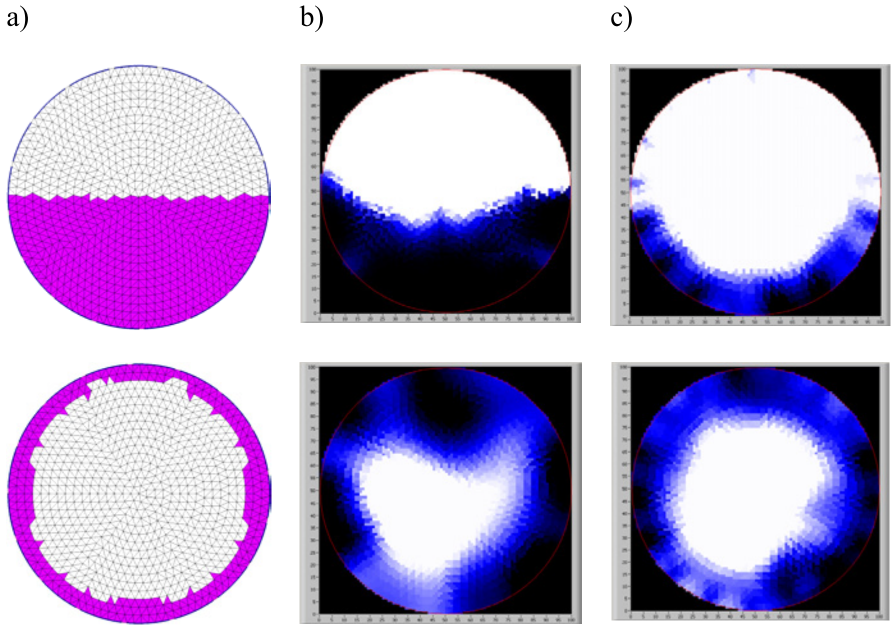

Fig.9. Examples of image reconstruction for two structures using the LBP method a) traditional sensor, b) sensor with increased sensitivity near the wall, c)sensor with switched electrodes

Fig. 10 shows the results of reconstruction for 20 iterations with the use of IBP. In the case of stratified structure, The results from both sensors are similar and the structure images are correct. In the case of annular structures, application of a traditional sensor gives incorrect results because air was not in direct contact with the pipeline wall. The correct results are obtained with the use of the sensor with a higher sensitivity near the wall although structures are a little deformed.

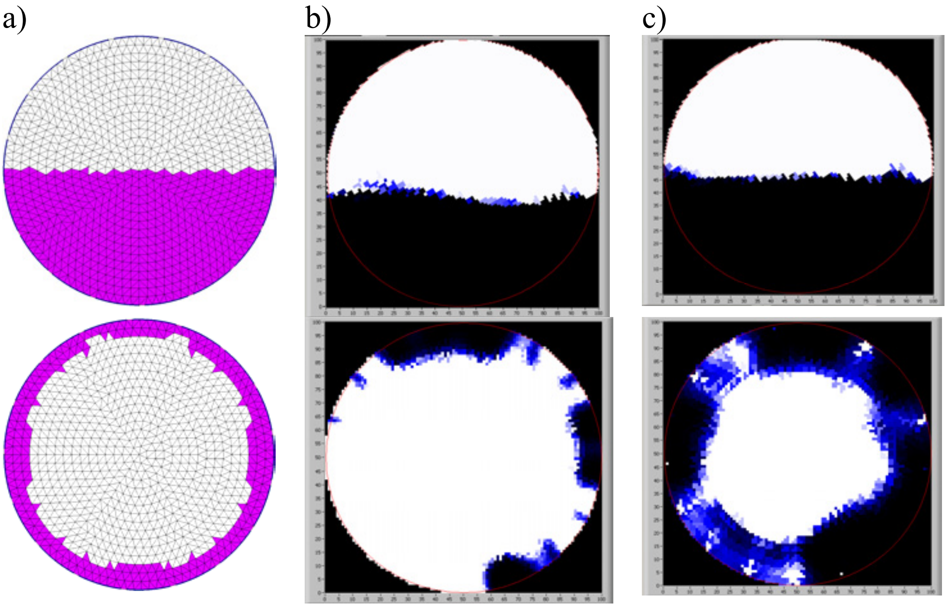

Fig.9. Examples of image reconstruction for two structures using IBP a) traditional sensor, b) sensor with increased sensitivity near the wall, c)sensor with switched electrodes

7. Conclusion

The paper presents a measuring sensor for the capacitance tomograph with increased sensitivity near the wall. The sensor can be applied for measurements two-phase gas-liquid downward flows. It can be also successfully applied for measurements of other flow structures. In such cases, iteration methods of image reconstruction should be applied. Introduction of additional measuring electrodes caused a necessity of elaboration of an atypical capacitance converter. The converter can be applied in other solutions of measuring sensor and capacitance measuring systems not connected with tomography.

References

[1] KIM S, PARANJAPE S S, ISHII M and KELLY J., Interfacial structures and regime transition in co-current downward bubbly flow 4th ASME_JSME Joint Fluids Engineering Conference, Honolulu, 2003 Hawaii USA

[2] LOSER T., PETRITSCH G. and MEWES D., Investigation of the Two-Phase Countercurrent Flow In Structured Packings Using Capacitance Tomography 1st World Congress on Industrial Process Tomography, Buxton, Greater Manchester, 1999

[3] HALOW J.S. and FASCHING G.E., Observations of a fluidized bad using capacitance imaging Chemical Ingineering Scince 48/1993 p.643-59
[4] KÜHN F.T., Electrical Capacitance Tomography Homburg 1998
[5] XIE C.G, HUANG S.M., HOYLE B.S,, THORN R., LENN C., SNOWDEN D. and BECK M.S., Electrical Capacitance Tomography for Flow Imaging: System model for development of image reconstruction algorithms and primary sensors IEE Proceedings-G 139/1992 p. 89-98
[6] RZĄSA M.R., Application of the capacity-to-frequency converter in the capacitance tomograph 4th World Congress on Industrial Process Tomography, Aizu, Japan 2005
[7] KÜHN F.T., SCHOUTEN J.C., MUDDE R.F., van den BLEEK C.M. and SCARLETT B., Analysis of chaos in fluidization using electrical capitance tomography Measurement Science and Technology 7/1996
[8] RZASA M.R., A New Transducer of Double Procesing for Capacitive Metrology and Measurement System, Vol. 14 2/2007
[9] RZASA M.R., WAJMAN R., GRUDZIEN K. and ROMANOWSKI A., The Capacitive Tomograph of Higher Sensitivity Near the Sensor Wall 5th World Congress on Industrial Process Tomography Bergen Norway 2007
[10] REINECKE N. and MEWES D. Recent developments and industrial/research applications capacitance tomography, Measurement Scince and Technology 3/1996 p. 233-46
[11] RZASA M.R., The measuring method for tests of horizontal two-phase gas–liquid flows, using optical and capacitance tomography Nuclear Engineering and Design 239/2009 p. 699-707

Journal of Energy Science, Vol. 1, No. 1, 2010, pp.147-160

Economical and ecological evaluation of the advanced electricity production technologies adapted for carbon dioxide capture

ANNA SKOREK-OSIKOWSKA[1*], ŁUKASZ BARTELA[1], JANUSZ KOTOWICZ[1]

[1] Silesian University of Technology, Institute of Power and Turbomachinery,
ul. Konarskiego 18, 44-100 Gliwice, Poland

Particularly interesting in ecological and environmental context, are two technologies: Integrated Gasification Combined Cycle (IGCC) systems and Supercritical Coal-fired Power Plant (SCPP). The main aim of the analysis was ecological and economical analysis of the selected technologies, both with and without CCS installation. The principal indicators of this evaluation was: break-even price of electricity, unit emission and CO_2 avoided cost. In the analysis the existing support mechanisms, mainly in the form of EU emission allowances trading scheme were, among other, taken in consideration. The results of the analysis show, that systems integrated with carbon capture installation can be competitive to the system without capture. Especially interesting in this light are IGCC systems. However, on the results of the analysis a lot of factors have influence, mainly fuel price, reliability of operation or auxiliary power rate. The evaluation of these parameters was qualitatively and quantitatively presented in the paper.

Symbols

C_{el}^{b-e}	-	break-even price of electricity, PLN/MWh,
e_{CO_2}	-	unit CO_2 emission, kg/MWh;
β_i	-	sensitivity coefficients

Indices

REF	-	reference
CCS	-	integrated with CCS

1. Introduction

In last years it have been observed some essential revaluations of the trends of popularity and development of particular energy technologies. One of the main reasons for that is the dynamic growth of ecologic requirements, for example in European Union countries affected by implementations of ecological directives [1,2]. In this light, Poland experienced emergency situation, first of all due to the great amount of still working, old and non-ecological energy sources. Additionally, in Poland about 95% of electricity production is based on utilization of coal, of which combustion causes a large emission of carbon dioxide. These factors, together with increasing energy demand, result in the need of investments in the energy sector. As a result of such a need, in nomenclature of energy technologies researchers, the expression Clean Coal Technologies has been popularized. In the case of coal-fired units it leads mainly to integration of power plants with CCS technologies.

European Emission Trading Scheme has a big importance for development of energy technologies is [1]. Poland is currently in the transition period that is characterized by, among other, continuous discussion about the role of greenhouse gases emission in the aspect of the greenhouse effect (which is the reason for legal instability and in consequence high investment risk), free allocations of greenhouse gases emission allowances (this system will be obligatory to 2027) and intensive research on CCS technologies.

Particularly interesting in Polish conditions, are two technologies: Supercritical Coal-fired Power Plants (SCPP) and Integrated Gasification Combined Cycle (IGCC) systems. In both these systems a carbon dioxide capture and storage (CCS) installation can be implemented in order to further improve ecological characteristics.

The main aim of the analysis was ecological and economical evaluation of the selected technologies both with and without CCS installation. The principal indicators of this evaluation were unit emission of carbon dioxide, break-even price of electricity and CO_2 avoided cost.

2. Characteristic of the selected systems

The purpose of the analysis, of which the results are presented in the present paper, was to evaluate the ecological and economical potentials of technologies, that for the Polish power sector are often referred to as prospective. Particularly important was to evaluate the validity of integration of these technologies with CCS installations, including the determination of boundary conditions for which such integration is economically justified.

In the first turn, the analysis included coal unit with supercritical steam parameters. Such solutions are well recognized in terms of utility, resulting in the erection in Poland of the first installations (Pątnów, Łagisza). It is expected, that in the coming years, investment in such systems will be constantly increasing. These technologies allow for energy production with high-efficiency, based on national energy resources and for achieving the commercial readiness of CCS they will provide the possibility to carry out a relatively easy integration with them. As a technology that has great potential, but in the long term considerations, integrated gasification combined cycle (IGCC) systems are also considered. In the analysis both technologies were examined as a stand-alone, as well as in the integration with CO_2 capture installations, although in the case of selected for study supercritical unit, its integration was made with membrane CCS installation, while in the case of the IGCC plant, the chemical absorption process with the use of amines was implemented. Although at the moment, Polish plants are expected to base on chemical absorption processes, it seems that about the direction of the development of CCS technology in the long term will decided next decade, which is probably going to be abundant in the research programs, including the installation of demonstration units using a wide range of solutions.

2.1. Supercritical Coal-fired Power Plant (SCPP) and Supercritical Coal-fired Power Plant with CCS installation (SCPP+CCS)

Adopted for the analysis unit has been widely used as a reference system in the already completed research project - Supercritical Coal Power Plants [3]. The detailed description of the system can be found, for example, in [3,4]. The main elements of the chosen for the analysis system, allowing to obtain high net efficiency of electricity production (nominally 44.27%), are: supercritical coal boiler with steam reheater (producing steam with parameters 28.5 MPa/600ºC/620ºC), extraction-condensing steam turbine and the set of 7 regenerative heat exchangers (realizing preheating of condensate and feed water). Gross power of the system is 602.2 MW_e. Scheme of the unit is presented in Fig. 1 (white background).

In the case of classical coal systems, carbon dioxide capture should follow the combustion process (post-combustion). In the system selected for analysis a membrane CCS installation is used. The results presented in [3] are used here. It was assumed, that the installation allows for 90% efficiency of CO_2 capture. Due to the large energy input required for the compression in capture process itself, as well as for preparation of the gas for transport and storage, a method for counteracting of the reduction of efficiency of the unit was proposed [3]. It consisted in interstage cooling of the compressed gas and using of the heat produced in such a way in the steam cycle, in order to replace low-pressure regenerative heat exchangers. In order to produce the required pressure difference in the membrane modules in the CCS installation two vacuum pumps (that produce a vacuum at 2.8 kPa after the membrane module) were used. In the calculations it was assumed, that the captured carbon dioxide is compressed to a pressure of 150 bar. In the process of compression two compressors take part. Scheme of the CCS installation, as well as its integration with the steam part of SCPP system is presented in Fig. 1 (gray background).

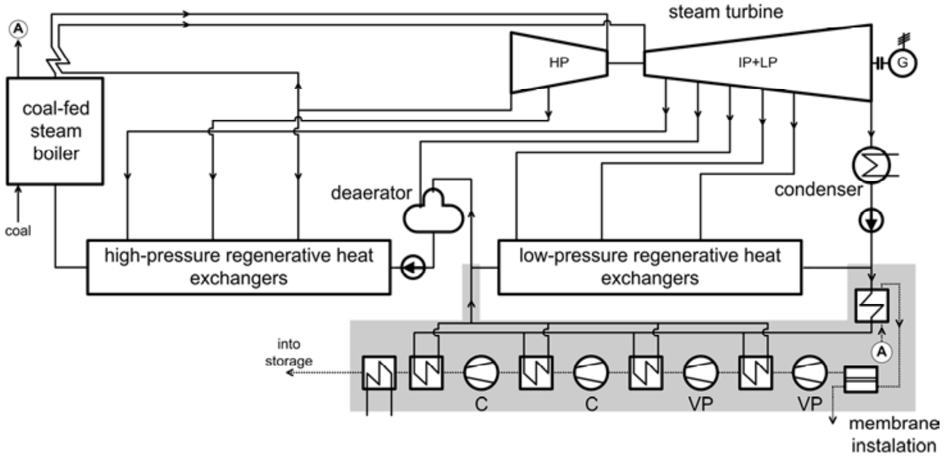

Fig. 1. Supercritical coal system and a conception of its integration with CCS installation

2.2. Integrated Gasification Combined Cycle (IGCC) system and Integrated Gasification Combined Cycle system with CCS installation (IGCC+CCS)

Currently, an emphasis is placed on the development of combined cycle systems integrated with coal gasification (IGCC). IGCC systems are characterized by high efficiency of electricity production and comparatively low pollutants emission. In the case of conventional systems, CO_2 emissions are relatively high. For the analysis it was assumed that in the system an entrained-flow gasifier powered by coal is operating. Oxidizing agents in the gasification process is oxygen and steam. Gasification pressure is at 18 bar and the temperature at 1700 K [5]. Raw synthesis gas is cooled, and generated in this way steam is supplied to the heat recovery steam generator. Produced steam is directed to the steam cycle. Cooled gas is subjected to purification, in which primarily particulates, alkali and sulfur compounds are removed. Deep cleaning of gas is required mainly for fulfilling the stringent requirements of gas turbines producers.

Integration of IGCC systems with CCS installations should be made before the combustion process. Energy and financial input on the capture, transport and storage of CO_2 in this case is much lower than for the methods of post-combustion type. In the case of IGCC+CCS system, it was assumed, that the capture process is carried out with the use of chemical absorption. It was also assumed, that the capture efficiency is the same as for the SCPP+CCS system, that is 90%. To enable the capture of CO_2 in the system, a double-stage conversion reactor of carbon monoxide to carbon dioxide (reactor Shift) was implemented. Captured CO_2 is compressed to a pressure of 150 bar. Simplified scheme of the system used in the analysis is shown in Fig. 2.

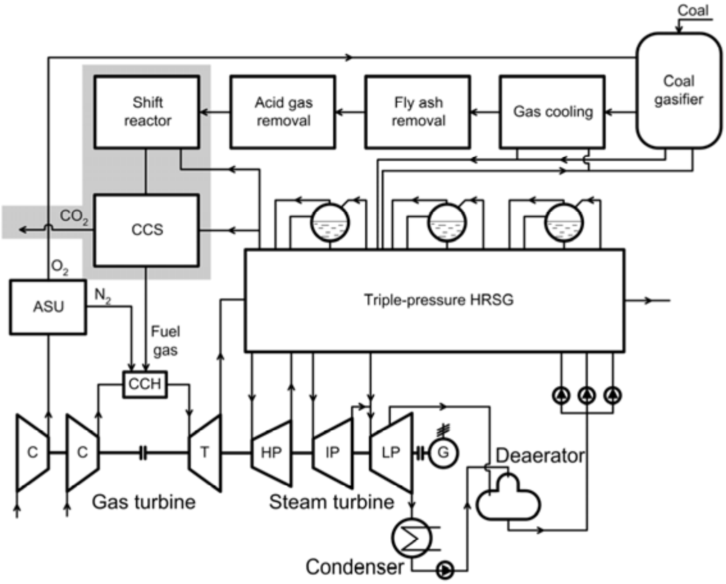

Fig 2. Integrated gasification combined cycle system with a conception of implementation of the CCS installation

3. Assumptions and results of the thermodynamic analyses

For the purposes of the analyses it was assumed, that the net electric power of the particular systems is the same and equals to 546.52 MW. Depending on auxiliary power of each systems, different is their gross output (Table 1).

All analyzed technologies use the same type of coal. Reference systems for the technologies with CCS installation (SCPP+CCS and IGCC+CCS) are suitable systems not prepared for carbon dioxide capture (SCPP and IGCC). Appropriate systems, constituting of the integration of electricity production technology with CCS installations cannot be treated as a physical complement of the reference systems, since the integration, due to the orientation of modeling on obtaining the same net power, boils down to scaling of the individual components being present in both cases. It was assumed, that in the two systems with the CCS installation, the efficiency of carbon dioxide capture is 90%, while after capture CO_2 is compressed to a pressure of 150 bar in order to prepare it for transport. Thermodynamic operational indices for analyzed systems are collected in Table 1. They results from modeling and carried out extensive literature review, in particular, [3,6-12].

Table 1. Selected characteristic ecologic and thermodynamic parameters of the analyzed technologies

Parameters, Units	Technologies			
	SCPP	SCPP+CCS	IGCC	IGCC+CCS
Gross power, MW	602.20	695.64	628.18	691.80
Auxiliary power, MW	55.68	149.12	81.66	145.28
Coal chemical energy flux, MJ/s	1234.52	1426.08	1236.47	1457.39
CO2 emission per unit chemical energy of coal, kgCO2/GJ	97.7	9.1	97.7	9.1
CO2 emission per unit of the electricity produced, kgCO2/MWh	794.5	85.5	795.7	87.36
Gross efficiency, %	48.78	48.78	50.80	47.47
Net efficiency, %	44.27	38.32	44.20	37.50

4. Assumptions for the economic analyses

The most important factor orienting European energy sector towards reducing of greenhouse gases emissions are the documents that are the basis of the implementation of appropriate mechanisms on the market. One of them is called Emissions Trading Scheme. This mechanism is responsible for the appearance within the cash flow of the company emitting greenhouse gases, a new category of costs, namely costs associated with the requirement of purchasing emission allowances. The company is obliged to present such allowances in the amount resulting from the real emission, and in the transition period (i.e. until the year 2027) with the quantity of free allowances allocated to a given installation in the so-called National Allocation Plan. In the light of the functioning of the EU Emissions Trading Scheme, extremely important factor, that in the future should settle the question of the economic justification of integration of energy systems with the CCS installations is the price of emission allowances. In the absence of unanimous predictions about the shape of the European energy market, in particular the uncertainty about the future of the Emission Trading Scheme, making economic efficiency analysis of energy systems is at present burdened with a huge risk. In the case of economic studies made for the energy systems integrated with the CCS installation, another risk factor is the adoption of strict scenarios of technological development, related both to capture and storage technology of separated carbon dioxide.

The economic effect of integration with the CCS installation is additionally highly dependent on the size of investments incurred for the CCS installation and the costs directly related to its operation, and therefore, widely understood exploitation costs associated with the capture itself, as well as with preparation of captured CO_2 to transport and storage. Definitely, the most important here are the costs associated with the production of energy required only for supply of the CCS installation. The required investment costs and exploitation costs are to a large extent dependent on the maturity of the considered solutions. What is important, the differences in investments for the integrated and the autonomic system are connected not only with the necessity of implementing more machines and devices, but also with the need to install higher gross power, in order to achieve the same level of net power.

Assumptions, that were used to evaluate the economic efficiency of the analyzed solutions, are the result of extensive literature review. In the economic analyses it was assumed, that the unit investment costs for the selected technologies are: 1600 USD/MWh for SCPP, 2900 USD/MWh for SCPP+CCS, 1800 USD/MWh for IGCC and 2500 USD/MWh for IGCC+CCS system. The construction time is 3 years for all technologies. The share of investments in the subsequent years of construction is 20%/30%/50%, respectively. The investment is self-financed in 20% and in 80% financed from a commercial credit, of which the actual interest amounts to 6%. Exploitation time is anticipated for 20 years. The discount rate amounts to 6.2%. The cost of repairs were determined to be 0.5% of the capital costs for the first five years of operation, 1% for the subsequent five years, 1.5% for the next five years, and 2% for the last years of exploitation. The annual operation time is equal to 7500 hours. The cost of exploitation of a CCS installation was assumed at 20 PLN/tonne of CO_2 captured [10]. Coal price was assumed at the average rate for industrial customers on the Polish market in the first half of 2010, i.e. 10 PLN/GJ. The emission allowances price was assumed at 150 PLN/tonne of CO_2. The depreciation equals to 6.7%, while the rate of income tax is 19%. The liquidation value of the designed systems is equal to 20% of the investment cost.

For the evaluation of economic effectiveness of the considered solutions, primarily the break-even price of electricity was used. This price allows for calculating of a so-called break-even point, i.e. a situation, in which losses are equalized with the incomes from sales. Break-even price of electricity was determined from the condition of *NPV*=0, where the *NPV* is a widely used indicator of economic efficiency evaluation, i.e. Net Present Value. It can be determined from general formula, which can be found, among others, in [12].

An interesting indicator in terms of evaluation of the integration of energy systems with the CCS installation is so-called the CO_2 avoided emission cost (*CAE*). Determination of the cost of avoided emissions requires a comparison of the integrated with CCS installation systems with the installation of the so-called reference systems, and thus unit without integration, however, built based on components and characteristics of the operation characterizing the system, in which CO_2 capture is realized. This indicator shows the value of the cost of removing carbon dioxide, but it takes into account a decrease of the efficiency of the system, resulting from the implementation of CCS installations. Cost of avoided CO_2 emission can be described by the relationship:

$$CAE = \frac{\left(C_{\mathrm{el}}^{\mathrm{b-e}}\right)_{\mathrm{REF+CCS}} - \left(C_{\mathrm{el}}^{\mathrm{b-e}}\right)_{\mathrm{REF}}}{\left(e_{\mathrm{CO_2}}\right)_{\mathrm{REF}} - \left(e_{\mathrm{CO_2}}\right)_{\mathrm{REF+CCS}}} . \qquad (1)$$

For systems integrated with the CCS installation the cost of avoided emissions was determined in relation to the corresponding systems without integration. This cost was calculated making assumption, that the market mechanisms in the form of the Emissions Trading Scheme do not exist. In this way, determined avoided emissions cost informs about the break-even price of emission allowances, when two compared solutions are characterized by the same economic effectiveness.

5. Results of the economic analysis

Table 2 presents the values of the defined in the preceding paragraph indicators of economic efficiency evaluation, obtained for the considered technologies. In the case of break-even price of electricity the calculations were made for the situation, for which the free allowances allocation is considered as well as for the scenario in which they are not taken into account. On the basis of calculation of the second case and the unit carbon dioxide emissions per net energy produced characteristic for the studied systems (Table 1) the cost of avoided emission was calculated.

Table 2. Break-even price of electricity and the avoided emission cost for the considered technologies

Evaluation indices	Case	Unit	Technologies			
			SCPP	SCPP+CCS	IGCC	IGCC+CCS
$C_{\mathrm{el}}^{\mathrm{b-e}}$	With Emission Trading System	PLN/MWh$_e$	277.2	289.1	291.2	262.3
	Without Emission Trading System	PLN/MWh$_e$	158.0	276.2	171.8	249.2
CAE		PLN/MgCO$_2$	-	166.7	-	109.1

For the accepted emission allowances price at 150 PLN/tonne, the lowest break-even price of electricity (262.3 PLN/MWh$_e$) is achieved for the IGCC system integrated with carbon dioxide capture installation, and the highest (289.1 PLN/MWh$_e$) for the IGCC system without the CCS installation. The results obtained for systems with supercritical boiler are located between the results obtained for systems that use coal gasification technology. It can be therefore concluded, that the popularity of IGCC systems will grow with the development of CCS technology.

Adapting of the CCS installation in the considered coal-fired systems increases auxiliary power, and consequently decreases their net efficiency. The avoided emissions cost for the system with supercritical coal-fired boiler is equal 166.7 PLN/tonne, while in the case of the integrated gasification combined cycle system is 109.1 PLN/tonne, which indicates a lower cost of the implementation of the CCS installation into the IGCC system. Moreover, these results indicate a lack of economic justification of integration of the SCPP units with the CCS installation for the adopted for analysis emission allowances price at the level of 150 PLN/Mg. A different situation occurs in the case of IGCC+CCS system where, for a given level of allowances prices economic justification of the integration is observed. It should be noted, however, that the analysis was performed for two different technologies of coal chemical energy conversion, which are also at different stages of development, with the use of different methods of carbon dioxide capture. For these reasons, there is a restriction in the formulation of clear conclusions about the superiority of one of the technologies in consideration.

Fig.3 presents the results of calculation of break-even prices of electricity as a function of emission allowances price. The resulting levels of CO_2 emission avoided costs, which are identical to the prices of emission allowances, under which the economic effects of the respective systems without and with the CCS installation are equal. Presented characteristics shows the undoubted advantage of the systems integrated with the CCS installation in relation to the systems without such integration, which is smaller sensitivity of the economic effect on the price of emission allowances. This allows for eliminating of the investment risks associated with the lack of accurate forecasts on the future of the Emissions Trading Scheme.

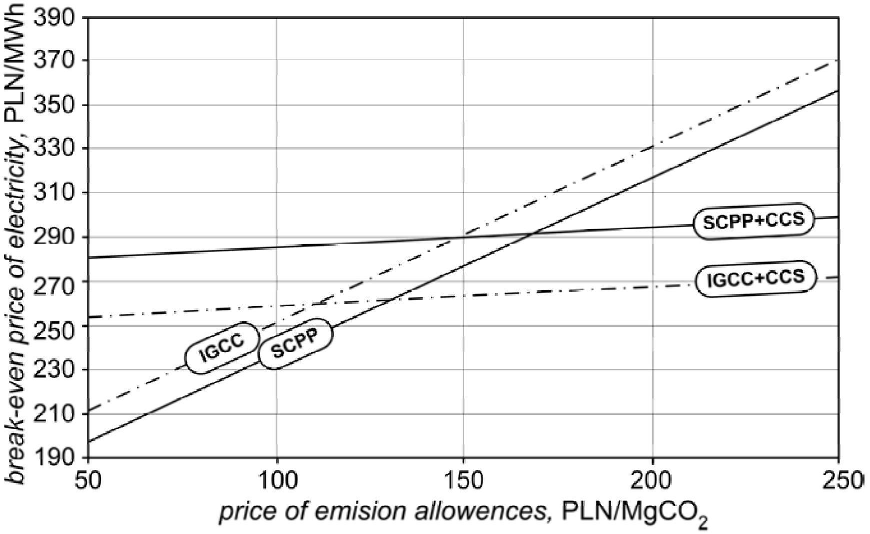

Fig. 3. Break-even price of electricity as a function of emission allowances price

The paper also examines the influence of changes of selected parameters on the change of break-even price of electricity. These parameters were: investment costs, coal prices and the price of emission allowances. The evaluation of the influence of the particular parameters of the break-even price of electricity is based on the analysis of sensitivity coefficients β_i of the changes of break-even price $C_\mathrm{el}^\mathrm{b-e}$ to a change of an independent parameter x_i, presented in a dimensionless form. For this purpose following formula was used:

$$\beta_\mathrm{i} = \frac{\partial C_\mathrm{el}^\mathrm{b-e}}{\partial x_\mathrm{i}} \frac{x_\mathrm{i}}{C_\mathrm{el}^\mathrm{b-e}}. \tag{2}$$

The sensitivity coefficient, defined in such a way, determines how does the relative break-even price change as a result of changes of the independent parameter x_i. The results of calculations of sensitivity coefficients of the analyzed system, when changing the price of CO_2 emission allowances, coal prices and investment cost are shown in Fig. 4.

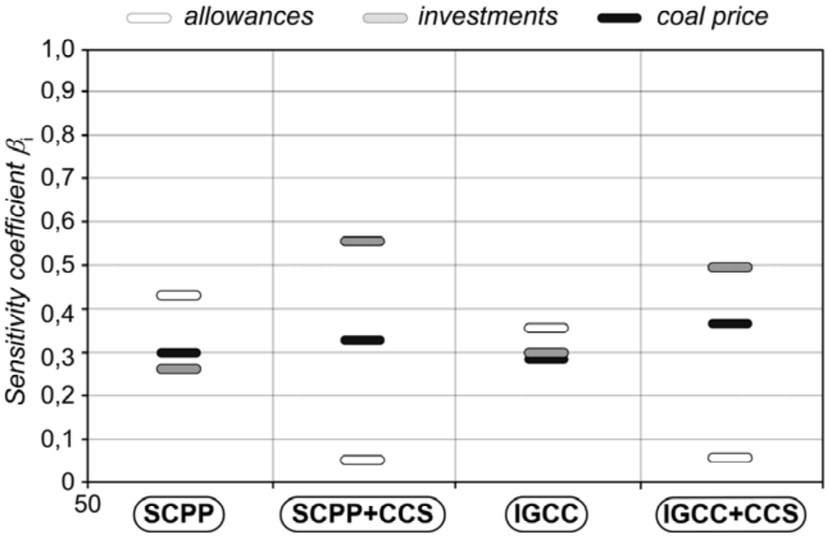

Fig. 4. Sensitivity coefficients for the analyzed systems, when changing the price of CO2 emission allowances, coal prices and investment cost

Coefficients close to zero indicate little effect of a change of a given parameter on the break-even price of electricity. This means, that some variations of this parameter from the current values influence relatively weakly the value of the break-even price of electricity. It may be noted, that in the case of systems with integrated carbon dioxide capture installation, a change of the price of emission allowances has the smallest impact on the change of the break-even price, while for systems without capture this influence is the most important. At the same time it can be observed, that the most important in the context of the achieved economic effects in the case of systems integrated with the CCS installation are changes of the investment costs. It should be therefore expected, that the development of CCS installations and, in consequence, the decrease of the investments will significantly increase the economic potential of carbon dioxide capture technologies.

6. Summary and conclusions

The main objective of the analysis presented in the paper was to evaluate modern systems of electricity production based on coal, along with the corresponding systems integrated with carbon dioxide capture installations. Selected for analysis technologies, i.e. supercritical coal system and integrated gasification combined cycle system, are characterized by, first of all, high efficiency of electricity production and relatively low pollutants emissions. Selected systems are considered to be the most prospective for Poland in the perspective of the next few decades. As a key indicator in the analysis a break-even price of electricity was assumed, which determines the minimum of the profitability of selling electricity, and thus, presents in an illustrative manner the economic viability of investment.

Economic analyses presented in the article suggest, that the systems ready for implementation of carbon dioxide capture installation, and in particular IGCC, can be competitive with other advanced systems for electricity generation, particularly facing the Emissions Trading Scheme. It consists of many elements, of which the most important are the price of emission allowances and unit investment costs. Analyses show, that for the assumptions made, IGCC systems integrated with the CCS installation are characterized by the lowest of all the technologies, break-even price of electricity. However, it should, be taken into account, that such systems are currently still in the initial phase of implementation, which creates an unfavourable economic environment, such as the required high investments. In addition, technological immaturity, manifested mainly by the relatively low reliability, reduces the competitiveness of IGCC technology in relation to conventional systems, which, at this stage of development, characterized among others by a large number of commercial implementations, can be considered a supercritical coal-fired systems. Undoubtedly, the popularity of IGCC systems, which are particularly predisposed for integration with the CCS installation, will increase. At the moment, however, there is still lack of sufficient operational experience, which causes, that the investments in this area are associated with an increased risk, that was not included in the carried out analyses.

The results of economic analysis are affected by many factors, of which the most important is the price of emission allowances. Low price of allowances contributes to the low competitiveness of the systems with carbon dioxide capture installation. It should be noted, however, that systems with low CO_2 emissions are slightly sensitive to the changes in emission allowances prices, which is their unquestionable advantage in the face of fluctuations in the price of allowances. Moreover, in the future, facing the gradual shift to auctioning system of emissions allowances trading, the decrease of prices of allowances should not be expected, but rather their growth.

Systems of electricity production, analyzed in the article, certainly belong to prospective technologies. Which of them will be developed and will play the most important role in energy production sector in Poland and in the world, will decide a number of factors. The most important among them are inter alia, prices of coal, development of the technology of CO_2 capture and European legislation, which determines, among others, a framework of the Emissions Trading Scheme. It can be expected, that with the rising costs of carbon dioxide emissions into the atmosphere, a decisive meaning will gain technologies integrated with capture (primarily IGCC, due to the lowest cost of implementation of capture installation), and technologies based on non-carbon fuels, including e.g. natural gas. Certainly, increasing ecological requirements, contained in the consecutive European Union directives, will be forcing the use of high-efficiency technologies of energy production.

Acknowledgements: The investigations presented in this paper have been carried out within the frame of the research project no. No. N N513 360537 for the years 2009-2012, financed by the Ministry of Education and Science.

References

[1] Directive 2003/87/EC of the European Parliament and of the Council of 13 October 2003 establishing a scheme for greenhouse gas emission allowances trading within the Community and amending Council Directive 96/61/EC. Official Journal of the European Union L 275/32 25.10.2003.

[2] Directive 2009/29/EC of the European Parliament and of the Council of 23 April 2009 amending Directive 2003/87/EC so as to improve and extend the greenhouse gas emission allowance trading scheme of the Community. Official Journal of the European Union L 140/63 5.6.2009.

[3] Praca zbiorowa pod redakcją T. CHMIELNIAKA i A. ZIĘBIKA. Obiegi cieplne nadkrytycznych bloków węglowych, Andrzeja Ziębika. Wydawnictwo Politechniki Śląskiej, Gliwice 2010.

[4] KOTOWICZ J., CHMIELNIAK T., and JANUSZ-SZYMAŃSKA K. The influence of membrane CO_2 separation on the efficiency of a coal-fired power plant, Energy, 35 (2010), 841-850.

[5] SKOREK-OSIKOWSKA A., BARTELA, Ł. and KOTOWICZ J. Modelling and Analysis of Gas Generator in the Integrated Gasification Combined Cycle Systems. 23rd International Conference on Efficiency, Cost, Optimization, Simulation and Environmental Impact of Energy Systems (ECOS), June 14-17, 2010, Lausanne, Switzerland.

[6] STIEGEL G. J. Overview of Coal Gasification Technologies. NSTAR Meeting Pittsburgh, PA, October 27, 2006.

[7] Intergovernmental Panel on Climate Change: Carbon Dioxide Capture and Storage Cambridge University Press, 2005.

[8] RAKOWSKI J. Obecne możliwości technologiczne ograniczania emisji CO_2 z elektrowni węglowych. 20th Word Exergy Council, Rome 2007.

[9] CHEN C. and RUBIN E.S., CO_2 control technology effects on IGCC plant performance and cost. Energy Policy 37 (2009), 915–924.

[10] DAVID, J. and HERZOG H., The Cost of Carbon Capture, presented at the Fifth International Conference on Greenhouse Gas Control Technologies, Cairns, Australia, August 13-16 2000.

[11] RUBIN E.S., CHEN C. and RAO B. Cost and performance of fossil fuel power plants with CO_2 capture and storage. Energy Policy 35 (2007), 4444–4454.

[12] ZAPART L., ŚCIĄŻKO M. and DRESZER K., Szacowanie kosztów inwestycji przyszłościowych technologii konwersji węgla. Polityka energetyczna, Tom 10, Zeszyt specjalny 2, (2007).

[13] KOTOWICZ J., Elektrociepłownie gazowo-parowe. Wydawnictwo Kaprint. Lublin 2008.

Journal of Energy Science, Vol. 1, No. 1, 2010, pp.161-170

Application of exergy analysis for evaluation of operation of steam power unit on the emission of CO_2

WOJCIECH STANEK[*], MICHAŁ BUDNIK

Politechnika Śląska, Instytut Techniki Cieplnej, ul. Konarskiego 22, 44-100 Gliwice

Szargut proposed the algorithm of determination influence of irreversibility of components of thermal process on the emission of CO_2. In the presented paper, basing on Szargut's proposal, the example of analysis of influence of operational parameters of coal fired power plant on the local increase of CO_2 emission is presented. The influence of operational parameters on the local exergy losses appearing in components of investigating power plant are simulating making use of the theoretical-empirical model of power plant.

Symbols

$\dot{B}$ – exergy flow, kW
c – mass fraction of c element in fuel
$\dot{m}$ – mass flow, kg/s
M – molar mass, kg/kmol
p – emission, kg CO_2 / kW
Wd – lower heating value, kJ/kg
Wg – higher heating value, kJ/kg
α – ratio of chemical exergy to chemical energy (LHV)
β – ratio of chemical exergy to chemical energy (HHV)
δ – losses

Subscripts

F – fuel
P – product
int – internal
ext – external
B – exergy

---

[*] Corresponding author, e-mail: wojciech.stanek@polsl.pl

1. Introduction

According to 3x20 package, it is planned to lower the emission of the greenhouse gases (include CO_2) by 20% in relation to emission level from 1990 year. Reduction of greenhouse gases can be achieved by improvement of thermal processes, energetic and exergetic efficiency or by CO_2 sequestration or oxy-combustion. The second mentioned group of measures is however power-consuming and should be only applied after running out of capability of thermal processes perfection improvement. It is known that the CO_2 emission form combustion processes is proportional to fuel consumption. Minimal fuel consumption would occur during ideal process characterized by lack of exergy losses (both internal and external). Minimal fuel energy consumption is always associated with unavoidable CO_2 emission. Each increase of internal or external exergy losses, in considered component of energy system, leads to increase of component's exergetic cost and in the end to increase of overall fuel consumption and CO_2 emission above earlier defined level of unavoidable emission. Having a mathematical model of process which allow to connect operational parameters with local exergy losses or local exergetic cost it is possible to investigate influence of thermodynamic perfection of these components on overall emission in considered system. That analysis allow to detect places which are especially responsible for local increase of CO_2 emission. In these work methodology to investigation of influence of operational parameters on local exergetic cost has been presented.

2. Application of exergy analysis to determination of local increase of CO2 emission

Due to the second law of thermodynamics real processes are nonreversible. This means that each real process is more or less responsible for degradation of energy resources [4,5,7,8]. Considering the process, that is supplying with the stream of resources exergy $\dot{B}_F$ (fuel) and within this process the flow $\dot{B}_P$ (product) of useful of exergy is producing, the exergy balance [4, 5] can be simply formulated as follows:

$$\dot{B}_F = \dot{B}_P + \delta\dot{B}\,.$$

Where $\delta\dot{B}$ means the sum of internal and external losses.

The flow of fuel $\dot{B}_F$ is proportional to the exergy losses $\delta\dot{B}$, by keeping the constant production $\dot{B}_P$.

The minimum consumption of flow of fuel $\dot{B}_F$ could be obtained in the ideal reversible process [6]. It means that the following conditions are fulfilled;

$$\delta\dot{B} = \delta\dot{B}_{int} + \delta\dot{B}_{ext} = 0\,, \tag{1}$$

or

$$\dot{B}_F = \dot{B}_P\,, \tag{2}$$

where

$\delta\dot{B}_{int}$ - internal exergy losses,

$\delta\dot{B}_{ext}$ - external exergy losses.

Fulfillment of the conditions (1) and (2) ensures the minimum flow of required exergetic fuel for the considered process [6]:

$$\dot{m}_{F\,min} \cdot b_F = \dot{B}_P\,. \tag{3}$$

For such conditions exergetic efficiency

$$\eta_B = \frac{\dot{B}_P}{\dot{B}_F} = 1\,, \tag{4}$$

as well as the local unit exergetic cost

$$k_B = \frac{\dot{B}_F}{\dot{B}_P} = \frac{1}{\eta_B} = 1\,. \tag{5}$$

Szargut proposed that the emission corresponding to the hypothetical riverside process fulfilling the conditions (1) or (2) should be treat as a minimum unavoidable emission [6]. Such emission can be expressed as follows:

$$p_{CO_2} = \frac{\dot{m}_{F\,min}}{\dot{B}_P} \cdot c \cdot \frac{M_{CO_2}}{M_C}\,, \tag{6}$$

where:

$\dot{m}_{F\,min}$ – hypothetical minimum flow the exergy of fuel feeding the analyzed energy system, c – mass fraction of c element in fuel,

M_{CO_2}, M_C – molar mass of CO_2 and C-element.

The chemical exergy of fuel b_F appearing in Eq.(3) can be expressed by means of LHV or HHV:

$$b_F = \alpha W_d = \beta W_g , \tag{7}$$

where:

W_d – Lower heating value (LHV),

W_g – Higher heating value (HHV),

α, β – ratio of chemical exergy to chemical energy expressed as LHV or HHV [4, 5].

Introducing (3) and (7) into (6) the unavoidable emission proposed by Szargut [6] can be expressed as follows[4]:

$$p_{CO_2} = \frac{c}{\alpha W_d} \cdot \frac{M_{CO_2}}{M_C} . \tag{8}$$

In real process the conditions (4) and (5) are not fulfilled. Each component of analyzed system are characterized by local exergy losses δB_i comprising both internal as well as external exergy losses. The local exergy losses leads to the increase in flow of exergy of fuel appearing in the balance shield of analyzed system. The relation between local exergy losses δB_i and the increase of flow of fuel Δm_i delivered to the system and resulting from irreverisibilities of *i*-th component can be expressed as follows:

$$\frac{\delta \dot{B}_i}{\dot{B}_P} = \frac{\Delta \dot{m}_{F,i} \cdot b_F}{\dot{B}_P} , \tag{9}$$

assuming the constant production of whole system.

Basing on the condition (9) the increase of emission of CO_2 resulting from irreversibility of *i*-th component of the system can be expressed:

$$\Delta p_{CO_2} = \frac{\Delta \dot{m}_{F,i}}{\dot{B}_P} \cdot \frac{c}{M_C} \cdot M_{CO_2} = \frac{\delta \dot{B}_i}{\dot{B}_P} \cdot \frac{1}{b_F} \cdot \frac{c}{M_C} \cdot M_{CO_2} , \tag{10}$$

$$\Delta p_{CO_2} = \frac{\delta \dot{B}_i}{\dot{B}_P} \cdot \frac{1}{\alpha W_d} \cdot \frac{c}{M_C} \cdot M_{CO_2} . \tag{11}$$

Introducing (8) into (11):

$$\Delta p_{CO_2} = \frac{\delta \dot{B}_i}{\dot{B}_P} \cdot p_{CO_2} \,. \tag{12}$$

And the total system CO_2 emission can be evaluated as:

$$p_{CO_2,tot} = p_{CO_2} + \sum_{i=1}^{n} \Delta p_{CO_2,i} \,. \tag{13}$$

3. Model of the plant

For the simulative calculation of influence of operational parameters on the exergetic cost, the mathematical model of the plant has to be applied. A mathematical model can be achieved in two ways. Using the physical laws an analytical model is formulated. Carrying out the measurements with the application of the identification methods, an empirical model is determined [3]. A development of the measuring techniques and a computer technology causes a wider application of the mathematical modelling of the processes basing on registered measurements data. The advantages of constructing models on the basis of the process identification methods prevail:

- the analytical models are impossible or extremely difficult and time-consuming

to construct (for example modelling of the processes proceeding in the steam power stations),

- real-time optimisation of the process parameters.

The models obtained on the basis of the identification of the processes have some features which differ from the analytical models:

- their application is limited (can be applied in a specific range, extrapolation is the most often inadmissible),
- they do not explain physical meaning of the process,
- they are quite easy to elaborate and apply.

The mathematical models obtained as a result of the identification are used to:

- simulate and optimise the processes,
- regulate and control the objects,
- diagnose the process.

A conventional power unit is a complex energy system. Such a system comprises a boiler, a turbine, a condenser, the regenerative heat exchangers and a cooling tower. A useful tool which identifies complex systems can be an integration of the analytical modelling techniques with the artificial intelligence techniques in a hybrid model [2]. An elaborated model of a power unit contains models of: a boiler, a steam-water cycle and a cooling tower. Fig. 1. presents a diagram of the hybrid model of a power unit.

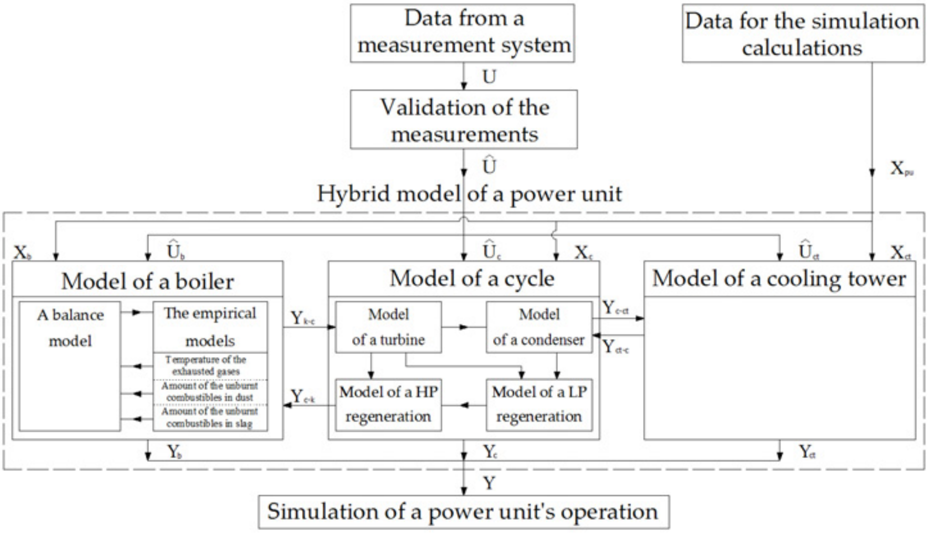

Fig. 1. The diagram of the simulation model of the power unit

The developed hybrid model of the boiler includes a balance model as well as the empirical one worked out by the means of the regression and the neural techniques. The balance model has been built basing on DIN-1942 standard [2]. The neural model describes the dependence between the flue gas temperature and the main operating parameters of the boiler. The regression models describing a dependence of a mass fraction of unburnt carbon in slag and dust on the boiler operating parameters. These models were developed by using a step-wise regression method.

A model of a steam-water cycle comprises a model of a turbine, the models of the heat exchangers and a model of a condenser [1]. A model of a turbine contains the mass and energy balances for each part of the turbine, the models of the steam expansion lines for each group of turbine’s stages and the auxiliary empirical functions. There are methods which use a flow modelling or methods based on the steam flow capacity and efficiency of the process equations applied for the evaluation of the steam expansion line in a turbine. Combining these methods is also possible. However, the flow computations demand knowledge of a flow system geometry. Such computations are time-consuming and require the complex models. The computations on the basis of the steam flow capacity and efficiency of the process equations are simpler and less time-consuming but require the identification of the empirical coefficients of the equations.

4. Results of calcualtions

The simulative calculations of the influence of operational parameters on exergy losses and emission of CO_2, have been carried out for the conditions of one of Polish Power plant. Analyzed system is the 370 MW power unit with double steam reheat – 17,65 MPa /535ºC/535ºC. Investigated steam-water cycle include the steam turbine, the condenser (CON), the high- temperature (HP1-4) and low-temperature regeneration system (LP1-4), the feed water tank with deaerator (WT), the auxiliary turbine and pumps (AUXT). The steam turbine consist of tree section: high-pressure part (HP), medium-pressure part (MP), low-pressure part (LP), with six bleeds (Fig. 2, streams no. 12, (18+21), 24, 27, 29, 31). The low-temperature regeneration system contain four regenerative exchangers ($i = 12 \div 15$) and are feed with the steam form low- and medium-pressure part of the turbine. The high-temperature regeneration system comprises two parallel threads with two heat exchanger installed on the each. The heat exchangers HP3 ($i = 21$) and HP4 ($i = 22$) are feed with the steam from the outlet of the high-pressure part of the turbine, whereas the heat exchangers HP1 ($i = 19$) and HP2 ($i = 20$) are feed with the steam from the first bleed (12) of the medium-pressure part of the turbine. The schematic diagram of the system is presented in Fig. 2.

Table 1 presents the results of calculation of:

- exergy efficiency η_b
- local exergetic cost k,
- exergy losses δb (internal and external) and
- increase of CO_2 emission Δp_{CO2}

The results have been carried out for two states of investigated power unit:

- reference x_0,
- operational x_1.

The difference between states x_0 and x_1 is caused by the increase of the pressure in condenser by $\Delta p = 0,2$ kPa. The flows of exergy $\dot{B}_j$ in each characteristic point presented in fig 2 have been evaluated using the simulator described in section 2.

The obtained results show, first of all, that in the investigated system the boiler and condenser are characterized by the lowest exergy η_b and local exergetic cost *k*. The boiler is responsible for the greatest exergy destruction and for this reason is the main source of the increase of emission. The increase of emission Δp_{CO2} caused by the boiler as well as that one caused by the all components are greater than the unavoidable emission. Among the components of steam-water cycle the highest increase of CO_2 emission is due to irreversibility of condenser and than that one of turbines an hest exchangers.

Table 1. Results of calculation of increase of CO_2 emissions

		η_b		k		δb		Δp_{CO2}, kg/GJ	
	Component *i*	$x=x_0$	$x=x_1$	$x=x_0$	$x=x_1$	$x=x_0$	$x=x_1$	$x=x_0$	$x=x_1$
1 -	Boiler	0,4645	0,4646	2,1531	2,1522	0,5355	0,5354	119,1869	120,8183
2 -	Turbine HP	0,9293	0,9318	1,0761	1,0732	0,0083	0,0080	1,8544	1,8034
3 -	Turbine MP I st	0,9590	0,9586	1,0428	1,0431	0,0024	0,0025	0,5440	0,5581
4 -	Turbine MP II st	0,9586	0,9578	1,0432	1,0441	0,0021	0,0022	0,4723	0,4884
5 -	Turbine MP III st	0,9635	0,9647	1,0379	1,0365	0,0015	0,0014	0,3257	0,3198
6 -	Turbine LP I A st	0,9025	0,8701	1,1080	1,1492	0,0040	0,0052	0,8839	1,1821
7 -	Turbine LP I B st	0,9025	0,8701	1,1080	1,1492	0,0014	0,0018	0,3060	0,4050
8 -	Turbine LP II A st	0,9025	0,8701	1,1080	1,1492	0,0015	0,0021	0,3440	0,4649
9 -	Turbine LP II B st	0,9025	0,8701	1,1080	1,1492	0,0036	0,0048	0,8069	1,0869
10 -	Turbine LP III st	0,9025	0,8701	1,1080	1,1492	0,0034	0,0045	0,7498	1,0144
11 -	Condenser	0,0285	0,0286	35,1476	34,9803	0,0370	0,0378	8,2310	8,5309
12 -	Heat Exchanger LP1	0,9490	0,9483	1,0537	1,0545	0,0002	0,0002	0,0357	0,0369
13 -	Heat Exchanger LP2	0,8657	0,8656	1,1552	1,1552	0,0007	0,0007	0,1521	0,1547
14 -	Heat Exchanger LP3	0,8260	0,8253	1,2107	1,2117	0,0020	0,0020	0,4431	0,4531
15 -	Heat Exchanger LP4	0,8897	0,8910	1,1239	1,1223	0,0011	0,0010	0,2341	0,2364
16 -	Deaerator	0,9727	0,9583	1,0280	1,0435	0,0005	0,0008	0,1111	0,1765
17 -	Feed water turbopomp	0,5574	0,5547	1,7939	1,8028	0,0058	0,0059	1,2850	1,3232
18 -	Turbopomp's condenser	0,0221	0,0221	45,2872	45,2872	0,0027	0,0027	0,5954	0,6082
19 -	Heat Exchanger HP1	0,8929	0,8928	1,1199	1,1201	0,0008	0,0008	0,1755	0,1800
20 -	Heat Exchanger HP2	0,8896	0,8895	1,1240	1,1242	0,0008	0,0008	0,1755	0,1801
21 -	Heat Exchanger HP3	0,9296	0,9291	1,0758	1,0763	0,0009	0,0009	0,1903	0,1960
22 -	Heat Exchanger HP4	0,9298	0,9293	1,0756	1,0760	0,0009	0,0009	0,1982	0,2039
23 -	Generator	0,9780	0,9780	1,0225	1,0225	0,0084	0,0083	1,8753	1,8753
33 -	Feed water mixer	0,9995	0,9995	1,0005	1,0005	0,0000	0,0000	0,0099	0,0101
	System	0,3746	0,3694	2,6696	2,7070	0,6254	0,6306	139,1860	142,3067
	Unavoidable emission							83,3666	83,3666
	Total emission							222,5526	225,6733

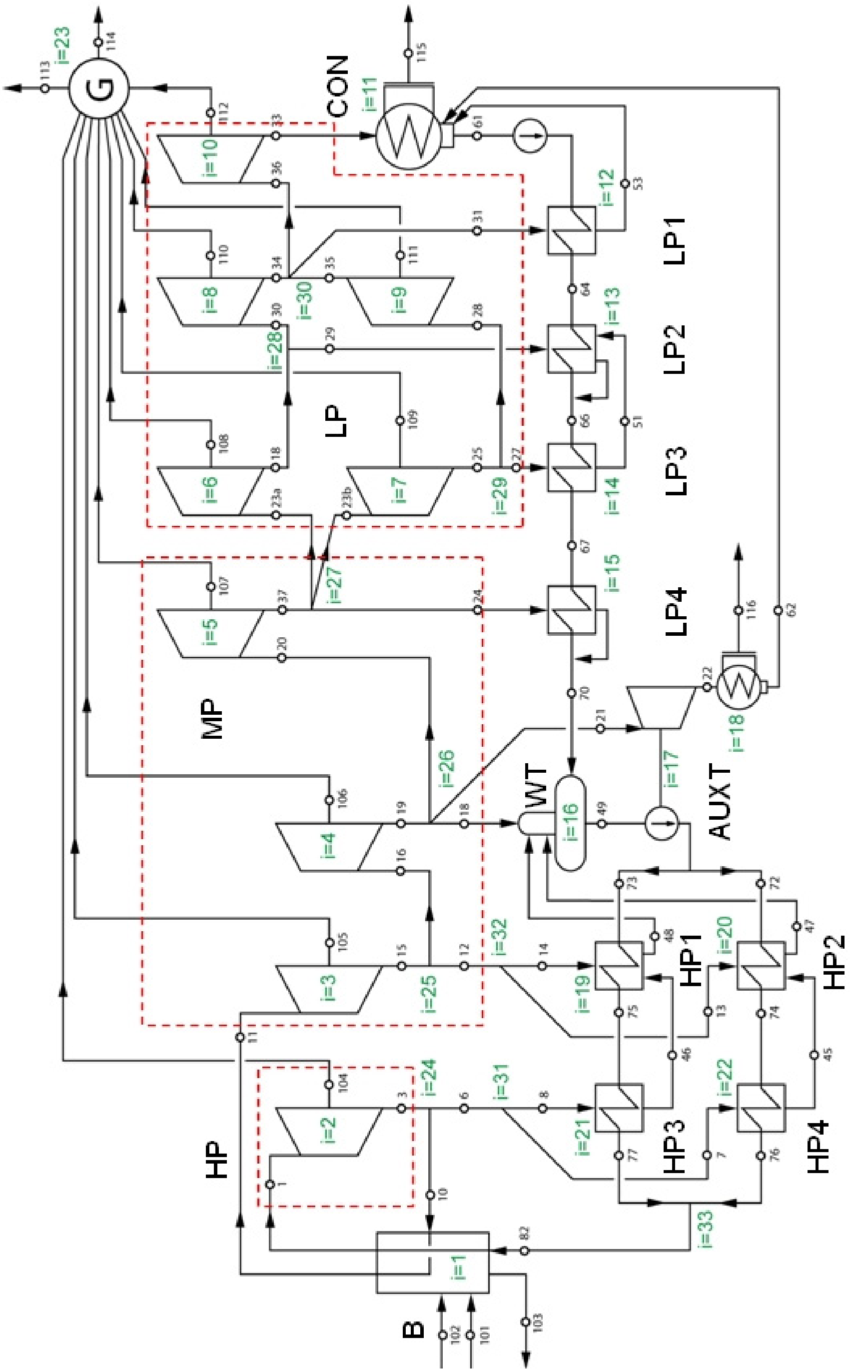

Fig 2. Schematic diagram of analyzed power plan

5. Summary

The authors applied the Szargut's methodology of CO_2 emission evaluation basing on exergy losses. The methodology has been introduced into the simulative hybrid model of the condensating power unit. The algorithm, developed by the authors, let to investigate the influence of operational parameters of each single component of power unit on increase of emission of CO_2. Using the algorithm the authors carried out example calculation for one of modern Polish power plant. Results of simulation shown that boiler is responsible for the highest increase of CO_2 emission upon the level of unavoidable emission. It is worth to stress that the increase of CO_2 emission is greater than the unavoidable one. The application of simulative hybrid model of the power unit with inclusion of Szargut's method of exergetic evaluation of CO_2 emission ensure to investigate the influence of operational parameters on the total emission of CO_2. In the presented work the example calculation have been done for two states (reference and operational), in general the proposed methodology can be applied for any sate of power unit work. Moreover it can be applied for sensitivity analysis of CO_2 emission caused by power unit parameters changes.

References

[1] RUSINOWSKI H., SZAPAJKO G., STANEK W.: Hybrid model of the conventional power unit. Mechanics Vol. 27 (2008) No. 3, 120-130

[2] RUSINOWSKI H., STANEK W.: Hybrid model of steam boiler. Energy, Vol.2, Feb. 2010

[3] STANEK W., RUSINOWSKI H.: Application of empirical modellng for construction of auxiliary models of steam boiler. Archives of Thermodynamics Vol. 29(2008), No. 4, 165-176

[4] SZARGUT J.: Egzergia. Poradnik obliczania i stosowania. Wydawnictwo Politechniki Śląskiej, Gliwice 2007

[5] SZARGUT J.: Exergy metod – Technical and ecological applications. WIT-Press 2005.

[6] SZARGUT J.: Wpływ nieodwracalności działania ogniw procesu cieplnego na emisję CO2. Energetyka listopad 2007.

[7] VALERO A. 2006a. The thermodynamic process of cost formation. Encyclopedia of Life Support systems. EOLSS Publishers, Oxford UK, www.eolss.net

[8] VALERO A, TORRES C. 2006b. Application of thermoeconomics to operation diagnosis of energy plants. EOLSS Publishers, Oxford UK, 2006, www.eolss.net

Journal of Energy Science, Vol. 1, No. 1, 2010, pp.171-178

Two dimensional numerical model vertical axis wind turbine

DANIEL TRZEBIŃSKI, ZBIGNIEW BULIŃSKI, IRENEUSZ SZCZYGIEŁ

Institute of Thermal Technology, Silesian University of Technology

In this paper the two-dimensional numerical model of the Savonius vertical axis wind turbine is presented. The numerical model was built and all simulations were carried out using the ANSYS FLUENT CFD (Computational Fluid Dynamics) software. The dynamic mesh capability of the software was fully exploited to model the flow around the moving rotor of the turbine. This allowed us to simulate turbine operation under prescribed load conditions.

1. Introduction

Energy consumption is continuously increasing in the world. Many countries, like China or India, are undergoing fast economic development, which consequence is dramatic increase in electric power consumption. The biggest share in the global electric power production have fossil fuels, eg.: coal, oil, natural gas or uranium. However, allowable sources of the fossil fuels are getting smaller. Hence there is great need to increase the energy production from renewable sources. The most important source of the renewable energy is the Sun.

Except of saving of the fossil fuels the important advantage of renewable utilization is no carbon dioxide production during the operation. This is especially important as the new regulations regarding the carbon dioxide emission are going to be established in the European Union. Moreover, they entail no future liabilities associated with the decommission of obsolete plants. Therefore the number of installed wind power plants in the world has been increasing annularly by almost 30% for a few last years.[0]

1.1. Historical overview

One of the means of utilization of this source potential is the application of the wind turbines to recover the energy form the wind. The wind has been used for propelling different machines for a very long time. The first known windmills are dated to tenth century. They were built by Persians and they had a vertical revolution axis. In the Middle Ages, the horizontal axis windmills were commonly used for pumping water or grinding grain. These windmills had four blades and a yawing system. They were mounted on a huge structures. Windmills lost their important role during the industrial revolution in Europe in 18th and 19th century due to increasing popularity of the steam engines. At the same time they were becoming more and more popular in United States, where they were mainly used on farms. [0]

1.2. Nowadays

Nowadays, the most popular are horizontal axis wind turbine (HAWT). They are usually placed on high towers with two or three blades. The alternative construction to them are the vertical axis wind turbines (VAWT). The most known of them are: the Darrieus turbine, the H-rotor turbine and the Savonius turbine. The first one was patented by a French aeronautical engineer Georges Jean Marie Darrieus in 1931. Second one was patented also by Darrieus in 1927. The Savonius turbine was invented by Finnish engineer S.J. Savonius in 1922.

1.3. Theoretical background

Cost effectiveness of wind-turbines increases with size. Recently the size of the state-of-the-art wind units has been increasing systematically but the actual technology of horizontal-axis wind turbines would ultimately reach the limits. There are number of problems in rotor design that arise while increasing the rotor size, e.g. high velocity on end of the wings up to 200-300 km/h. [0]

Horizontal turbines need air flows with approximately constant velocity. The minimal wind speed to start energy production is around 3-4 m/s. While the maximal velocity for which turbine operation is still safe is about 25 m/s. Usually, the nominal power output is reached at wind speed in the range 10-12 m/s and it decreases rapidly when the wind speed differs from those numbers. For example, at 4 m/s the net power can be as much as 6-7 times lower than at 12 m/s. Similar situation is above the nominal air velocity. On the other hand, the vertical wind turbines don’t need to be stopped even for high wind speeds. Literature reports that they could run with wind speed up to 60 m/s without any faults. Therefore they can be successfully utilized in the geographical regions which are characterized by strong winds, e.g.: Antarctica or Arctic. The main designing difference between horizontal and vertical turbines is that the second ones are omni-directional. It means that they accept wind from any direction. Hence, they do not require the yaw system, which directs a turbine towards the wind and it includes control system and drive mechanism. The yaw system increases both investment and operational costs of a turbine operation. In the omni-directional turbines there are no power loses to run the yaw system during wind direction changes. Therefore they can be placed in the mountain sites where the wind changes its direction very often.

The generator in the VAWTs could be located on the ground level. So the construction tower may be lighter and the generator maintenance is easier. Moreover, its weight and dimensions are not so important as in the HAWTs, where the generator is placed at the top of the tower.

The generator in the vertical wind turbine is directly connected with the turbine rotor through shaft, without any gearbox with breakdown in the system. The gearbox is needed in the horizontal wind turbines because the rotor angular velocity is about 15-30 rpm, while generator shaft is 1500 rpm. The gearbox and the breakdown system need maintenance during operation. Malfunction of one of these systems can destroy a turbine during high wind speeds. The lack of the gearbox and the yaw system influences considerably the vertical axis wind turbines construction. Most of the operating equipment is situated at the bottom of the tower, in many cases it is on the ground. Therefore, the tower could be lighter which is huge advantage of this type of turbines.

Other important advantages of the vertical axis wind turbines comparing to the horizontal axis wind turbines are: [0]

- low sound emission (they operate at lower tip speed ratios),
- insensitivity to wind direction,
- increased power output in skewed flow,
- simple construction,
- high starting torque,
- ability to run with strong wind,
- generator or other energy converter might be placed on the ground level,
- lower threat for birds and other flying animals,
- maintenance operations are considerably simplified.

The main disadvantages of this type of wind turbines are: [0]

- difficulties in utilization for the production of electric energy, especially when the energy is directly transferred on the distribution network,
- in many cases lower efficiency.

The Savonius wind turbines have high starting torque or high coefficient of static torque. That is why they are used as starters for other types of wind turbines i.e. Darrieus or H-rotor. The starting torque of the Savonius wind turbines is high but in the same time it is non uniform along the all rotor angels. The conventional Savonius rotor (one stage) has negative coefficient of static torque for angles in ranges from 135^o to 165^o and from 315^o to 345^o. Two or three stage conventional Savonius can overcome this problem. In most cases two or three bladed wind turbines are preferred, principally because of their higher efficiency.

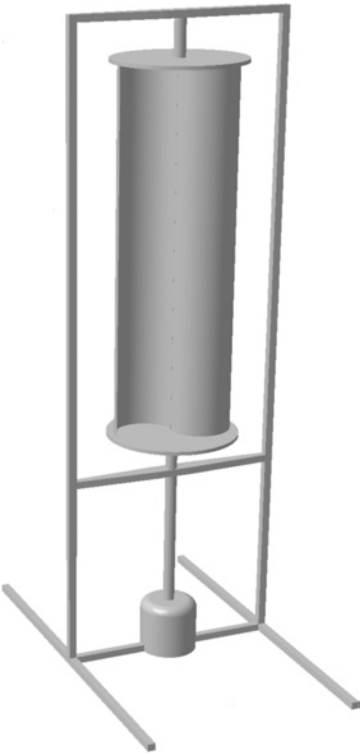

Fig. 1. Savonius turbine visualisation

2. Mathematical model

The mathematical model of the wind turbine was built using commercial Computational Fluid Dynamics (CFD) software *ANSYS Fluent*. It was assumed that the flow is incompressible, isothermal and fluid is Newtonian, hence it can be described by the unsteady set of flow equations only, i.e. [4]:

- continuity equation

$$\nabla \cdot \mathbf{w} = 0 . \tag{1}$$

- Navier-Stokes equation

$$\rho\frac{\partial \mathbf{w}}{\partial t}+\rho\nabla\cdot(\mathbf{ww})=\rho\mathbf{g}-\nabla p+\mu\nabla^2\mathbf{w}+\mathbf{S}_t\,. \tag{2}$$

In above equations $\mathbf{w}$ is the velocity vector, ρ is the density, p refers to the pressure, t is the time, μ represents the dynamic coefficient of viscosity and **g** is the gravitational acceleration vector. The last term on the right-hand side of the Navier-Stokes equations $\mathbf{S}_t$, describes momentum source/sink due to the turbulence. It arises from the Reynolds averaging of the instantaneous Navier-Stokes equations and it requires additional modelling [5,6]. This is continuously developing field of science and there are number of models are described in the literature of the subject. However, in this work a few most well established and widly used models were considered [5,6,7]:

- standard k-ε model,
- Wilcox k-ω model,
- Menter SST k-ω,
- Reynolds stress model (RSM).

At this stage it is hard to verify which of the above models is the most adequate for this problem, it needs further experimental validation. Numerical model was made as 2D with Ansys software. Simulations were done with two meshes: one with about 14000 cells, second with 180000 cells. Both mesh consists triangular and quadratic elements. Blade thickness is 1mm with aluminium as a material. Dynamic mesh capability was also used.

3. Results

The most important factor for the wind turbine operation is the resultant force moment with respect to the turbine axis. Having the pressure field around the turbine blade this quantity can be calculated by the integration of the elementary moment over the whole blade surface:

$$\mathbf{M}=-\int_{A_{blade}} p\mathbf{r}\times d\mathbf{A}\,. \tag{3}$$

In above equations **r** is the radius, **A** is the blade area and **M** is the force moment. First simulations were done with constant angular velocity 2Π rad/s, which is equal to one revolution per second, to compare force moment with different viscosity model in Fluent software. Wind velocity was set to 10 m/s.

As it was mentioned the most important factor is force moment with respect to turbine axis. Force moments comparison from different viscosity models is shown in Fig. 2. As it can be noticed in each model force moment tendency is similar. Differences between values form different models are below 0,25 Nm with respect to 2,5 Nm between maximal and minimal force moment value. More differences, up to 0,5 Nm, appear with Reynolds Stress model

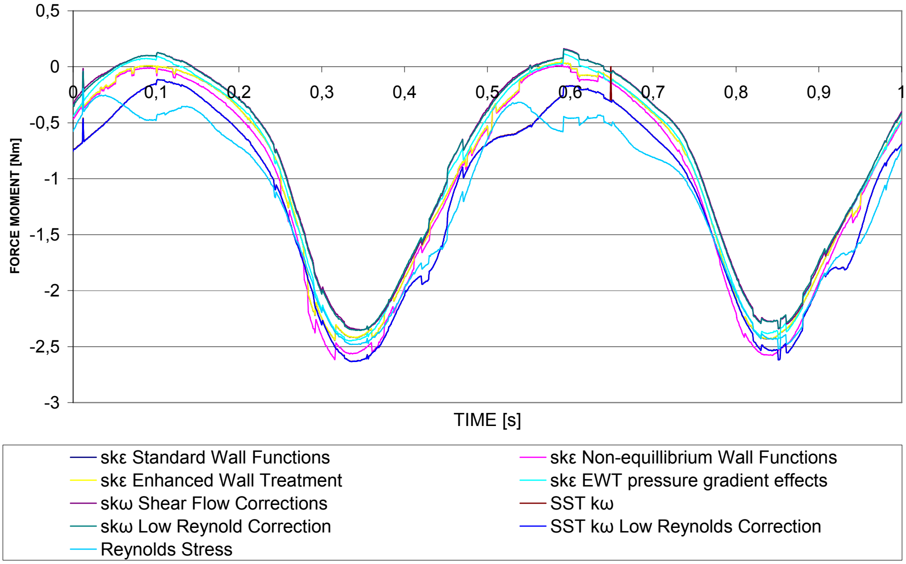

Fig. 2. Comparison of force moment with respect to revolution time for different viscosity models (mesh - 14000 cells)

Second simulations were done with angular velocity resulting from pressure field around the rotor. Wind velocity was also set to 10 m/s. Viscosity model: standard k-epsilon Standard Wall Functions.

In this case there is no force resistance in bearings and generator so the angular velocity is very high - 60 rad/s (9,5 revolution per second). Maximal theoretical angular velocity, when end of blades has the same velocity as wind, is 66,7 rad/s. In real conditions blade velocity is lower. Bearings and current generator work as a brake for wind turbine. Blade revolution is clockwise. Angle 0^{o} means blade situated perpendicular to wind direction. This is also initial position for all simulations. Angle in figures as abscissa mean angle between perpendicular line to wind direction and line draw through the end of one blade. It is shown in fig. 3. Comparison of force moment calculations for two meshes is shown in fig. 4. It can be noticed differences between two models. Values for 14000 cells mesh are quite higher than for 180000 mesh but the differences are less than 0,2 Nm. The force moment tendency is similar in both cases.

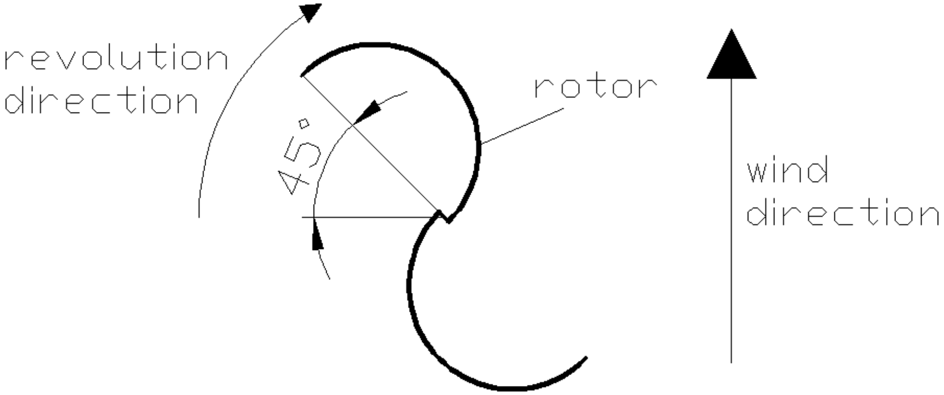

Fig. 3. Revolution direction of the rotor

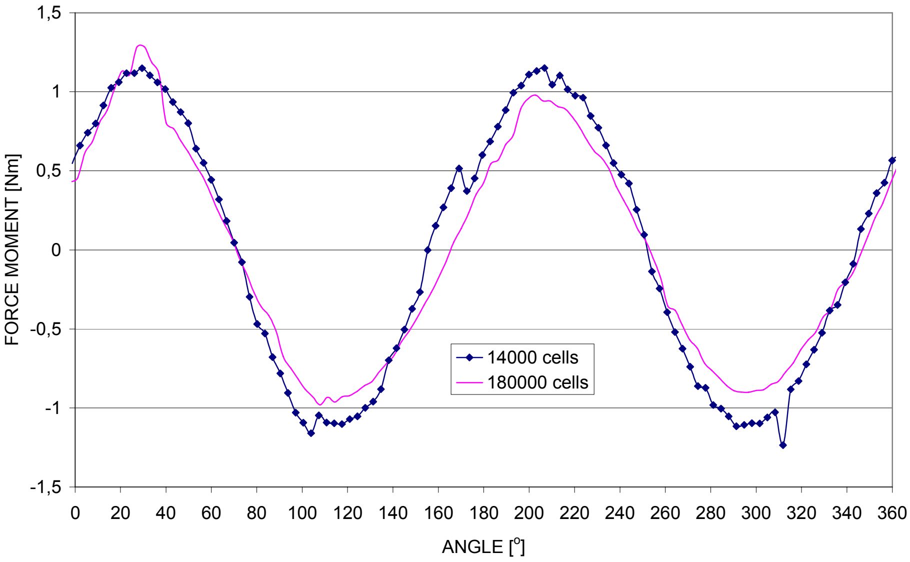

Fig. 4. Comparison of force moment with respect to revolution angle for different meshes

As it can be found in literature, such kind of turbine (one stage, 2 blades) could have problem with start when angular blade is between 75° and 160° or 255° and 345° – in these positions force moment is negative. To get rid of this problem usually two stage turbines are built. Investigation of the turbines with more than one stage are planned in the future.

4. Conclusions

In this paper numerical analysis of vertical wind turbines are presented. This simulations were conducted to check results obtained with different viscosity models. Numerical analysis were performed without resistance in bearings and in current generator. The resistance will be build in next simulations with full 3D model. Simulations of different blade geometry are also planned.

References:

[1] ERIKSSON S., BERNHOFF H., LEIJON M.: Evaluation of different turbine concepts for wind power, Renewable and Sutainable Energy Reviews 12, 2008, 1419-1434

[2] MENET J.L.: A double-step Savonius rotor for local production of electricity: a design study, Renewable Energy 29, 2004, 1843-1862

[3] PONTA F.L., SEMINARA J.J., Otero, A.D.: On the aerodynamics of variable-geometry oval-trajectory Darrieus wind turbines, Renewable Energy 32, 2007, 35-56

[4] WHITE F.M.: Fluid mechanics, McGraw-Hill, New York, 5th edition, 2003.

[5] VERSTEEG H.K., MALALASEKERA W.: An introduction to computational fluid dynamics. The finite volume method, Pearson Education Limited, Harlow, 2nd edition, 2007.

[6] POPE S.B.: Turbulent flow, Cambridge University Press, Cambridge, 2000.

[7] ANSYS Fluent documentation, www.ansys.com, 2010.

Journal of Energy Science, Vol. 1, No. 1, 2010, pp.179-190

The ORC power unit driven by the exhaust gas heat of a gas turbine power set and the system power output as influenced by the ORC characteristic parameters

SŁAWOMIR WIŚNIEWSKI*, ALEKSANDRA BORSUKIEWICZ-GOZDUR

West Pomeranian University of Technology, Faculty of Mechanical Engineering and Mechatronics, Department of Heat Engineering, Al. Piastów 19, 70-310 Szczecin, POLAND

The authors presented problems related to utilization of the waste heat, carried by the exhaust gases of the gas turbine power set, with a goal to achieve an additional electricity generation. A relevant solution is then discussed, in which the gas turbine power set is thermally coupled with an ORC power unit that uses organic fluids as its working medium. The solution offers an increase in the electricity generation efficiency and in the electric power output. The rate of the waste heat utilization, converts directly into the degree of the increase in the generation efficiency and power output, and depends on the ORC characteristic parameters. Effects on the thermally coupled power system performance of several ORC parameters and of possible ORC cycle solutions were then analysed. Variations in the organic vapour pressure and temperature at the ORC turbine inlet, in the steam condensation temperature, and for four different organic fluids (benzene, cyclohexane, decane and toluene) were examined. With account to the varying parameters calculations of the simulated combined power systems were performed. As result, diagrams to illustrate the influence of individual ORC parameters and of the type of organic fluid on the combined power system performance (efficiency, power output) were elaborated.

Symbols

c_{ps}	– average specific heat of the exhaust gas, J/(kgK)
$\dot{Q}_d$	– heat flow supplied to the ORC cycle, W
$\dot{m}$	– mass flow of a substance, kg/s
N	– power, W
h	– specific enthalpy, J/kg
l	– specific work, J/kg
t	– temperature, °C

---

* Corresponding author: e-mail: slawomirwisniewski@zut.edu.pl

η	– efficiency, %
Δn	– power increase coefficient, %

Subscripts

c	– organic fluid
s	– exhaust gas

1. Introduction

Among top priorities of any country there is one to assure its energy supply safety. Therefore, for a number of countries, their energy policy aims not only towards increasing the share of the renewable energy resources in the country total energy balance but also towards improvements in the performance effectiveness of the existing power (and heat) plants. Much pressure is then put to apply new energy conversion technologies of higher efficiency. More efficient installations bring in turn measurable profits as less fuel need to be burnt, less environmental pollution is emitted, and the whole economy of the subject processes is improved.

A way to increase the performance effectiveness of a gas turbine power set is discussed in the present paper. Recently, installations incorporating gas turbines have been more and more popular. Their cumulative installed output power grows continuously since nineties of the last century [1]. One drawback of the gas turbine power plants, when only simple gas turbine cycle is in place, lies in their relatively low efficiency of the electricity generation. Depending on the size of the plant output power the electricity generation efficiency varies then between a dozen or so up to some 40%. There are ways to increase the gas turbine efficiency as, among others, to apply interstage overheating of the exhaust gases (additional combustion chamber for the two stage gas turbines), to apply interstage air coolers (for the gas turbine air compressors), or to inject additional working fluid, e.g. water upstream of the combustion chamber, [2]. Another way to improve the effectiveness of the gas turbine power set is analysed by the Authors of the present paper. Here, utilization of the residual heat of the gas turbine exhaust gases has been taken into consideration. To this end, the gas turbine power set is thermally coupled with an ORC power unit that runs with an organic working fluid in the supercritical Clausius-Rankine cycle.

Both the previous works, [3], and the results of the thermodynamic and flow calculation obtained within the present work indicate that there is an opportunity to improve the effectiveness of the gas turbine performance when the exhaust gas enthalpy is utilized to drive an ORC unit. This is possible due to the high temperature of the exhaust gases, which exceeds 500 ^{O}C. Such level of the temperature is suitable to form the upper heat source for subsequent thermodynamic cycles.

Variations in the characteristic parameters of the ORC cycle have been included in the present analysis. Influence of the individual cycle parameters and of application of several organic fluids on improvement of the system power output could then be determined. A diagram of the combined system under consideration is presented in Fig. 1.

2. Characteristics of the combined power system

The present analysis is based on the commercially available gas turbine power set that is fired with natural gas and delivers 5.25 MW of electric power. Nominal parameters of this gas turbine power set, according to the catalogue data [2], read: electric power generation efficiency – 30.5%, exhaust gas mass flow rate – 20.8 kg/s, exhaust gas temperature – 530 ^{O}C. The exhaust gases with that high temperature are suitable for further utilization, comp. Fig. 1.

According to the scheme given in Fig. 1 the turbine exhaust gases are directed to a heat exchanger that forms an element of thermal coupling between the gas turbine power set and the ORC power unit. In the heat exchanger, heat of the exhaust gases is transferred to the working fluid of the ORC power unit. It is an assumption adopted by the Authors of the present paper that the ORC power unit is working in the supercritical cycle, i.e. that the pressure of the working fluid in the heat exchanger is higher than its critical pressure. The fulfillment of the critical cycle is possible due to the high temperature of the upper heat source (hot exhaust gases). The Clausius-Rankine thermodynamic cycle of the ORC power unit, as plotted on a T-s diagram, is shown in Fig. 2.

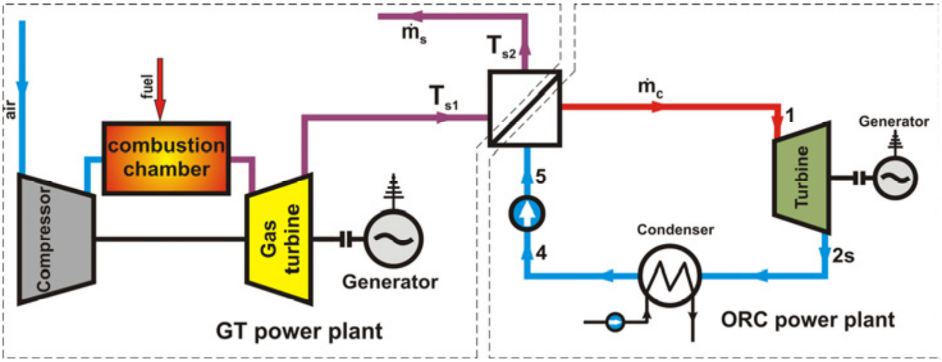

Fig. 1. Thermal coupling of the gas turbine power set and ORC power unit

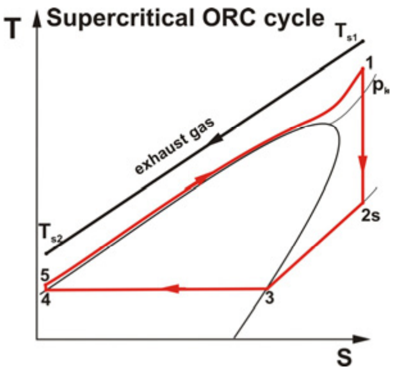

Fig.. 2. Clausius-Rankine conversion cycle of the ORC power unit (T-s diagram)

Now, various organic fluids of the dry fluids group [4], were analyzed as possible working fluids. Organic fluids of that group are characterized by their entropy factor I>1. That means that the fluid vapour expansion in the turbine (izentropic process) ends within the superheated vapour region. This results due to the shape of the fluid saturation line x = 1, comp. Fig. 2 and 3.

Out of many fluids referenced by the Refprop database the following four organic fluids were adopted for further analysis: benzene (t_k = 288.9 °C, p_k = 4.89 MPa), cyclohexane (t_k = 280.49 °C, p_k = 4.07 MPa), decane (t_k = 344.5 °C, p_k = 2.10 MPa) and toluene (t_k = 318.6 °C, p_k = 4.13 MPa).

Actual shapes of the saturation lines for two exemplary organic fluids are presented as their T-s plots in Fig. 3.

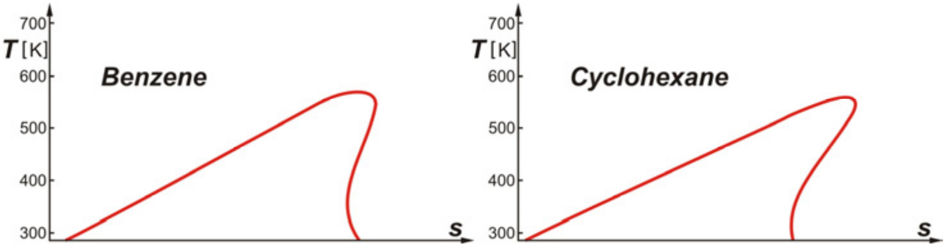

Fig. 3. Saturation lines of the analysed fluids (T-s diagram)

Next, several values of the turbine inlet steam pressure and temperature were analysed to determine the influence of the individual ORC cycle parameters on the power performance of the combined system. On top of that, several values of the condenser pressure were taken into account. The actual range of the parameter variations, and the corresponding calculation results are presented in Sec. 4.

3. Algorithm of calculations

To perform the analysis the Authors adopted the characteristics of the gas turbine power set as given in the catalogue data of the manufacturer [5]. Additionally, it was assumed that the temperature difference between the exhaust gas and the organic fluid equals to $\Delta T = 30$ K at inlet and outlet of the countercurrent heat exchanger. The organic fluid vapour after expansion, would condense at the temperature of 35°C to 55°C. Thermal and calorific state parameters of the organic fluids (at characteristic points of the ORC cycle) were determined on the basis of the Refprop 7.0 database [6]. The main formulas used in calculations are given below.

The heat flow extracted from the exhaust gas in the heat exchanger is determined from :

$$\dot{Q}_s = \dot{m}_s c_{ps} \left(T_{s1} - T_{s2} \right). \tag{1}$$

Average value of the exhaust gas specific heat for the temperatures in the range of T_{s1} to T_{s2} is obtained on the basis of the table data [7]. Variation in the temperature of the exhaust gas specific heat at constant pressure, is by using those table data, presented in Fig. 4. It should be noted here that the exhaust gas heat capacity is very close to that of air. This results from the very high content of air within the turbine exhaust gas (combustion of natural gas occurs at a considerable excess of air).

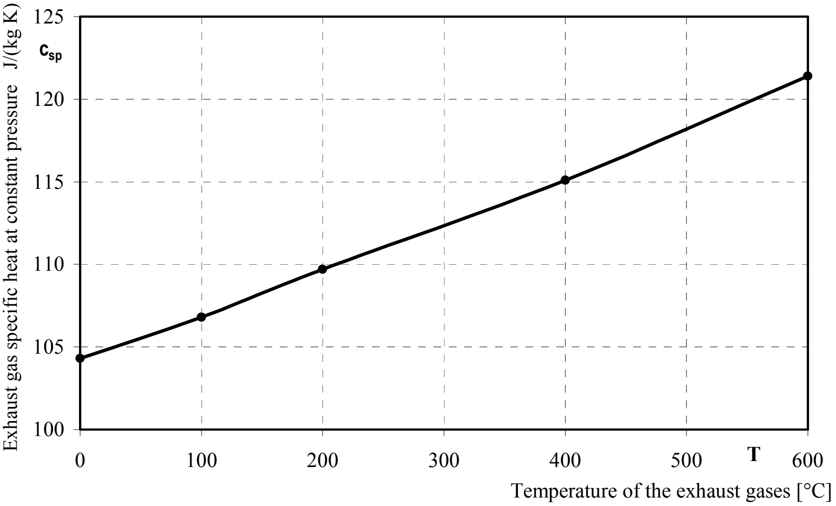

Fig. 4. Exhaust gas specific heat vs. temperature, for natural gas, [7]

The heat flow delivered to the organic fluid in the heat exchanger is determined from:

$$\dot{Q}_c = \dot{m}_c(h_1 - h_5). \tag{2}$$

The organic fluid mass flow is calculated from the energy balance of the heat exchanger on assumption that the environmental heat loss is negligible. With account to Eqs. (1) and (2) the value of the organic fluid mass flow reads:

$$\dot{m}_c = \frac{\dot{m}_s c_{ps}(T_{s1} - T_{s2})}{h_1 - h_5}. \tag{3}$$

Specific work of the ORC vapour turbine amounts:

$$l_{1-2s} = h_1 - h_{2s}. \tag{4}$$

Specific work of the ORC liquid pump amounts:

$$l_{4-5} = h_5 - h_4. \tag{5}$$

The results of previous works carried out at the Chair of Thermal Engineering, West Pomeranian University of Technology, and devoted to the ORC cycles proved that, in contrast to traditional water steam cycles, the amount of work needed to rise the organic fluid cycle pressure should not be neglected [8]. In line with that, the Clausius-Rankine cycle power of the ORC power unit was calculated from:

$$N_{C-R} = \dot{m}_c(l_{1-2s} - l_{4-5}) = \dot{m}_c(h_1 - h_{2s} - (h_5 - h_4)). \tag{6}$$

The electric generator power output of the ORC power unit was calculated with assumption of the following efficiency values: turbine internal efficiency η_i=0.80, turbine mechanical efficiency η_m=0.98, electric generator efficiency η_g=0.97 [9]:

$$N_{el_c} = \eta_i \eta_m \eta_g N_c. \tag{7}$$

The total electric power output of the combined system (gas turbine power set + ORC power unit) was determined as the sum of the respective power outputs:

$$N_{el} = N_{el_c} + N_{el_z} \,. \tag{8}$$

Increase in the combined system power output, with reference to the gas turbine power output, was defined by means of the power increase coefficient Δn:

$$\Delta n = \frac{N_{el} - N_{el_z}}{N_{el_z}} \,. \tag{9}$$

The electricity generation efficiency for the combined system consisting of the gas turbine power set and ORC power unit was determined from:

$$\eta_{el} = \frac{N_{el}}{\dot{Q}_d} 100 = \frac{N_{el_c} + N_{el_z}}{\dot{Q}_d} 100 \,. \tag{10}$$

According to the catalogue data [2], the energy flow the gas turbine set was supplied with equaled to $\dot{Q}_d = 17.21$ MW.

4. Results of calculation

Four organic fluids from the dry fluids group were taken into account in the present analysis. Comparative calculation results obtained with those fluids are presented below for the ORC power unit working at the following cycle parameters: inlet vapour temperature t_1=350 ^{O}C, inlet vapour pressure p_1=5 MPa, vapour condensing temperature t_3= t_4=35 ^{O}C.

As result of the whole analysis it was found, that out of the four organic fluids under consideration the most profitable effects were obtained for benzene and toluene. For the cycle parameters specified above, the comparative global calculation results are presented on the diagram in Fig. 5.

Because of the limited volume of the present paper the detailed calculation results are given for toluene only. However, the calculation results for all the remaining fluids display an analogous trend.

Influence of the ORC cycle parameters on the power output and electrical efficiency of the thermally coupled power system is presented in Fig. 6 for the case where toluene was adopted as working medium in the ORC power unit.

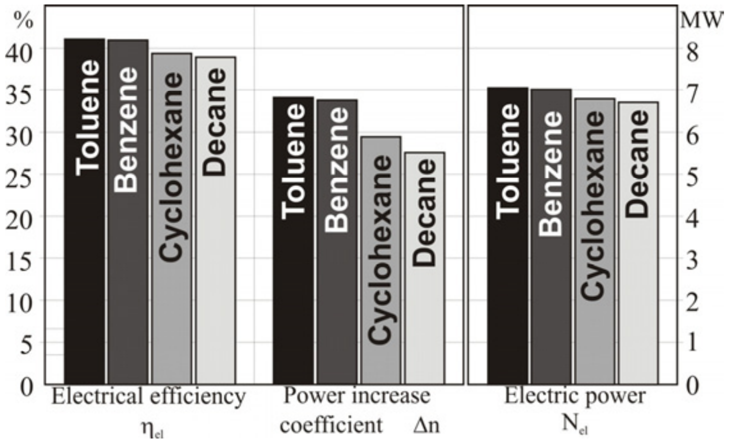

Fig. 5. Influence of the organic fluid type on effectiveness of the combined system performance

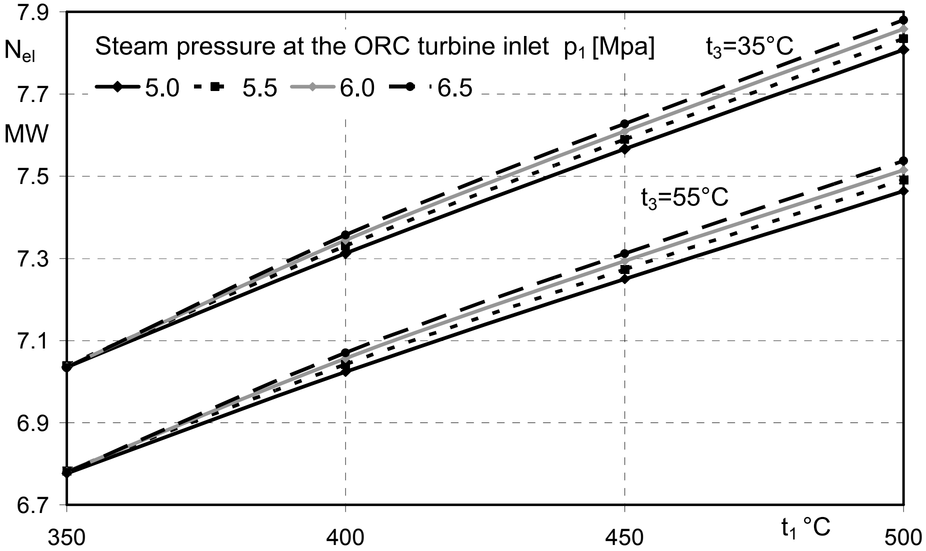

Fig. 6a. Influence of the ORC cycle parameters, for toluene, on effectiveness of the combined system performance

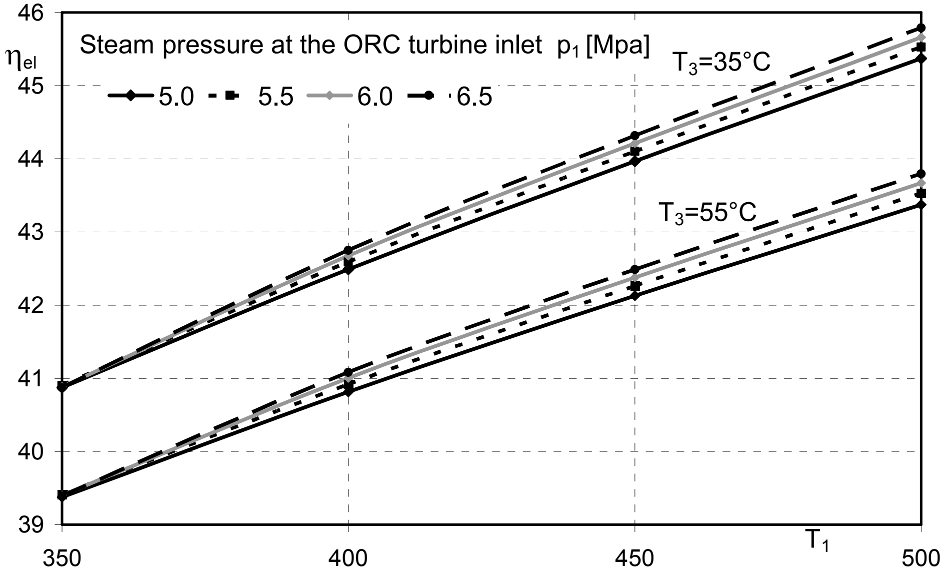

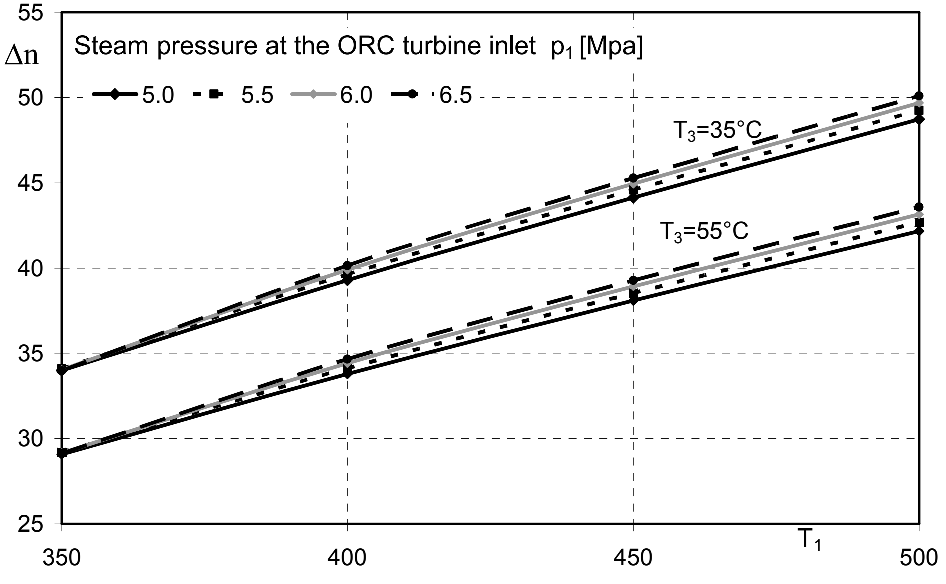

Fig. 6 b,c. Influence of the ORC cycle parameters, for toluene, on effectiveness of the combined system performance

Table 1. Calculation results for toluene

Temp. t_1	Press. p_1	Temp. $t_3 = t_3$	Temp. t_{s2}	$\dot{q}_d$	$l_{1\text{-}2s}$	$l_{4\text{-}5}$	m_c	N_{C-R}	N_{el_c}	N_{el}	η_{el}	Δn
°C	MPa	°C	°C	kJ/kg			kg/s	MW			%	
350	5	35	144	824.5	273	5.8	8.78	2.35	1.78	7.03	40.9	34
		45	155.1	806.9	255.5	5.9	8.7	2.17	1.65	6.9	40.1	31.5
		55	165.3	789	238.9	6	8.62	2.01	1.53	6.78	39.4	29.1
	5.5	35	130.4	794	264.4	6.4	9.12	2.35	1.79	7.04	40.9	34.1
		45	141.4	776.5	247.4	6.5	9.04	2.18	1.66	6.91	40.1	31.6
		55	151.7	758.5	231.3	6.6	8.96	2.01	1.53	6.78	39.4	29.2
	6	35	117.4	764.4	254.9	7	9.47	2.35	1.79	7.04	40.9	34
		45	128.4	746.8	238.5	7.1	9.4	2.18	1.65	6.9	40.1	31.5
		55	138.7	728.9	223	7.2	9.33	2.01	1.53	6.78	39.4	29.2
	6.5	35	110.6	749.1	250.2	7.6	9.67	2.35	1.78	7.03	40.9	34
		45	121.6	731.5	234.1	7.7	9.6	2.17	1.65	6.9	40.1	31.5
		55	131.9	713.6	218.8	7.8	9.53	2.01	1.53	6.78	39.4	29.1
400	5	35	207.8	979.4	320.4	5.8	8.62	2.71	2.06	7.31	42.5	39.3
		45	219	961.8	300.2	5.9	8.55	2.52	1.91	7.16	41.6	36.4
		55	229.4	943.9	281.1	6	8.48	2.33	1.77	7.02	40.8	33.8
	5.5	35	202.2	968.5	320.1	6.4	8.72	2.73	2.08	7.33	42.6	39.6
		45	213.3	950.9	300.2	6.5	8.65	2.54	1.93	7.18	41.7	36.8
		55	223.7	933	281.3	6.6	8.58	2.36	1.79	7.04	40.9	34.1
	6	35	196.6	957.1	319.2	7	8.82	2.75	2.09	7.34	42.7	39.9
		45	207.7	939.5	299.5	7.1	8.75	2.56	1.95	7.2	41.8	37.1
		55	218.1	921.6	280.8	7.2	8.68	2.38	1.81	7.06	41	34.4
	6.5	35	190.9	945.1	317.7	7.6	8.93	2.77	2.11	7.36	42.7	40.1
		45	202	927.5	298.2	7.7	8.87	2.58	1.96	7.21	41.9	37.3
		55	212.4	909.6	279.8	7.8	8.8	2.39	1.82	7.07	41.1	34.7
450	5	35	260.2	1114.6	357.3	5.8	8.67	3.05	2.32	7.57	44	44.1
		45	271.6	1097.1	334.9	5.9	8.61	2.83	2.15	7.4	43	41
		55	282.3	1079.1	313.8	6	8.54	2.63	2	7.25	42.1	38.1
	5.5	35	255.9	1107.2	359	6.4	8.73	3.08	2.34	7.59	44.1	44.6
		45	267.3	1089.6	336.8	6.5	8.66	2.86	2.18	7.43	43.2	41.5
		55	277.9	1071.7	315.8	6.6	8.6	2.66	2.02	7.27	42.3	38.5
	6	35	251.7	1099.7	360.1	7	8.79	3.1	2.36	7.61	44.2	44.9
		45	263	1082.1	338.1	7.1	8.72	2.89	2.2	7.45	43.3	41.8
		55	273.6	1064.2	317.3	7.2	8.66	2.69	2.04	7.29	42.4	38.9
	6.5	35	247.6	1092	360.9	7.6	8.85	3.13	2.38	7.63	44.3	45.3
		45	258.9	1074.4	339.1	7.7	8.79	2.91	2.21	7.46	43.4	42.2
		55	269.5	1056.5	318.4	7.8	8.73	2.71	2.06	7.31	42.5	39.3
500	5	35	309.5	1248.1	391.3	5.8	8.73	3.36	2.56	7.81	45.4	48.7
		45	321.2	1230.6	366.9	5.9	8.67	3.13	2.38	7.63	44.3	45.3
		55	332	1212.6	343.8	6	8.62	2.91	2.21	7.46	43.4	42.2
	5.5	35	305.7	1242.3	394.1	6.4	8.77	3.4	2.58	7.83	45.5	49.2
		45	317.3	1224.8	369.8	6.5	8.71	3.17	2.41	7.66	44.5	45.9
		55	328.1	1206.8	346.9	6.6	8.66	2.95	2.24	7.49	43.5	42.7
	6	35	302	1236.4	396.3	7	8.81	3.43	2.61	7.86	45.7	49.7
		45	313.6	1218.9	372.2	7.1	8.76	3.2	2.43	7.68	44.6	46.3
		55	324.4	1201	349.5	7.2	8.7	2.98	2.27	7.52	43.7	43.2
	6.5	35	298.5	1230.7	398.3	7.6	8.85	3.46	2.63	7.88	45.8	50.1
		45	310.1	1213.1	374.4	7.7	8.8	3.23	2.45	7.7	44.8	46.7
		55	320.9	1195.2	351.7	7.8	8.74	3.01	2.29	7.54	43.8	43.6

Detailed results of the analysis with toluene being the ORC working fluid are given in Table 1. Four different values of the vapour pressure and temperature at the turbine inlet and three different vapour condensing temperatures are specified.

5. Recapitulation and conclusions

The results of the analysis, as presented in the preceding Section, revealed that the power effectiveness of the combined power system was noticeably influenced by the organic fluid chosen to work in the ORC power unit. Calculation results for the four organic fluids (benzene, cyclohexane, decane and toluene) yielded differences, that could reach a few percent in the combined system electric power efficiency and even somewhere from ten to twenty percent in the combined system electric power increase. Best results were obtained for toluene.

Additionally, it was proven that, on top of the organic fluid choice, also the ORC characteristic cycle parameters affect the performance of the combined power system. Here, influence of the organic vapour pressure and temperature at the turbine inlet, as well as the vapour condensing temperature, were analysed. The results given in Table 1 and Fig. 6 indicate that a considerable influence on the electricity generation efficiency and the electric power output of the combined power system, was exerted by the two parameters: vapour temperature at the turbine inlet and the temperature of the vapour condensation. For the case of the supercritical ORC cycle the vapour pressure at the turbine inlet did not significantly affect the combined power system performance. The effects of such vapour pressure increase are more prominent only for higher vapour temperatures (450°C to 500°C).

It was shown that, for the combined power system with application of the ORC power unit, the utilization of enthalpy of the gas turbine exhaust gases can significantly improve the effectiveness of the system performance. Next, for the supercritical ORC cycle, the usage of dry organic fluids results in very high vapour temperatures at the turbine outlet. As it can be seen (Table 1), such vapour outlet temperature may exceed 300°C. This circumstance was not a subject of the present analysis. It can be, however, considered as an additional opportunity to improve the power system performance. Second ORC cycle can be then added, for which the upper heat source would be created by the turbine outlet vapour of the present ORC power unit. Technical and economic analysis of such cascade type systems is in progress.

References

[1] CHMIELNIAK T.: Energy technologies, Wydawnictwo WNT, Warszawa 2008.

[2] WĘDZKI A.: Combined systems of the production of electricity, Part I. Technical issues, Energetyka,Numer 5 (623) / Rocznik 59, Maj 2006, pp. 323-329

[3] WIŚNIEWSKI S., BORSUKIEWICZ-GOADUR A.: Ocena efektywności pracy zespołu turbiny gazowej sprzężonej z nadkrytyczną siłownią ORC, XII Forum of Power Engineers, Elektryka z. 64, nr 336/2010, pp. 131-132

[4] BORSUKIEWICZ-GOZDUR A., NOWAK W.: Comparative analysis of natural and synthetic refrigerants in application to low temperature Clausius-Rankine Cycle, Energy 32 (2007), pp. 344-352

[5] Industrial Gas Turbines - Siemens

[6] NIST. Refprop 7.0, Standard Reference Database 23, Reference Fluid Thermodynamic and Transport Properties. National Institute of Standards and Technology, Gaithersburg, MD, USA, 2002.

[7] GOGÓŁ W.: Heat transfer, boards and graphs, WPW, Warszawa 1979

[8] BORSUKIEWICZ-GOZDUR, A.. Efektywność pracy elektrowni geotermalnej z organicznym czynnikiem roboczym. Praca doktorska, Politechnika Szczecińska, Szczecin 2008.

[9] SZARGUT J.: Thermodynamics, Wydawnictwo Naukowe PWN, Warszawa 1998

Journal of Energy Science, Vol. 1, No. 1, 2010, pp.191-200

Concept of a system for waste heat recovery from flue gases in a coal-fired power plant

KAZIMIERZ WÓJS[*], PIOTR SZULC, TOMASZ TIETZE, ANDRZEJ SITKA

Wroclaw University of Technology, Institute of Heat Engineering and Fluid Mechanics,
Wybrzeże Wyspiańskiego 27, 50-370 Wrocław, Poland

The paper presents an analysis of methods of recovery and utilization of waste heat from flue gases of power units in coal-fired power plants in Poland and worldwide. Systems for waste heat recovery from flue gases and methods of utilizing the waste heat in Polish coal-fired power plants were described. An analysis showing advantages and disadvantages of the heat recovery systems currently in use was been performed. A concept of waste heat recovery and utilization with condensation of the steam contained in flue gases was proposed. This concept is characterized by a larger stream of the recovered waste heat as compared with the methods without condensation.

1. Introduction

Currently, research studies are conducted to develop a construction of a power boiler with supercritical parameters of live steam, which would be additionally equipped with systems for flue gas treatment (catalytic denitrification), desulphurization with the use of the wet limestone method, dust removal with the use of electrostatic precipitators and flue gas heat recovery systems. Besides losses resulting from incomplete and partial combustion and radiation losses, the efficiency of a power boiler is affected by outlet losses [1]. Considering the fact that outlet losses are a predominating part of the total losses in the boiler, one of the methods significantly improving the efficiency, consists in using a flue gas heat recovery system. The problem of waste heat recovery is associated with the ongoing research on reducing emissions of carbon dioxide and other greenhouse gases. Flue gas waste heat recovery systems are widely used in the 'oxyfuel' technology that is under development.

---

[*] Corresponding author, e-mail: kazimierz.wojs@pwr.wroc.pl

This technology consists in separation of nitrogen and argon before the combustion process and thereby the combustion process takes place in pure oxygen. A negative effect of combustion in pure oxygen is an increase of the temperature in the combustion chamber above 2000°C. In addition, the increase of the flue gases temperature, causes higher outlet losses. Flue gas recirculation is used to reduce the temperature in the combustion chamber. Cooling flue gases below, their dew point temperature results in the most efficient heat recovery [2]. Additionally, a considerable impact of the excess air factor on the dew point temperature of carbon can be observed. However, the 'oxyfuel' technology causes a fivefold increase in the content of sulphurous anhydride (SO_2), as compared with conventional combustion. In connection with this fact, there arises another problem, which consists in the occurrence of sulphur corrosion, because below 250°C, the dew point of sulphuric acid (H_2SO_4) is reached [3]. Hence, flue gas ducts and heat recovery systems must be made of a corrosion-resistant material. In addition to sulphur corrosion, surfaces are polluted as a result of the presence of ash fraction of ash in flue gases. In the case of the OP-650k boiler, the increase in the ash content from 15 to 40% causes as much as four-fold increase in the erosivity [4].

Another example of utilization of flue gas waste heat is the IGCC (Integrated Gasification Combined Cycle) technology. The ICGG unit consists of two parallel process lines containing a gas generator, a gas turbine and a waste-heat boiler. The waste-heat boiler produces steam from the heat received from flue gases from the gas turbine [5,6].

There are a many methods of utilizing flue gas waste heat, mainly for heating the feed water in high-pressure regeneration or condensate in low-pressure regeneration, as well as for heating the intake air [7]. As a result of heating the intake air and feed water, the efficiency of the power unit increases while CO_2 emissions decrease. A decrease in CO_2 emissions is proportional to the increase in the efficiency of the power unit both for hard coal and brown coal. On the other hand, the steam jet flowing from turbine bleeds to regeneration heaters decreases as a result of heating the condensate, which causes an increase in the power of the turbine set for the same capacity of the boiler. Currently, intensive research work aiming at utilization of waste heat for coal drying is underway.

This paper presents an analysis of the methods for recovery and utilization of flue gas heat, which are used in power plants both in Poland and worldwide. A concept of waste heat recovery with condensation of the steam contained in flue gases was also presented.

2. Methods of recovering and utilizing flue gas waste heat

2.1. Recovery and utilization of flue gas waste heat for heating treated flue gases

In currently operated power units, much attention is paid to the heated exhaust gas in order to protect cables and equipment from corrosion caused by condensation of sulphur-containing gases. This happened especially after installing flue gas desulphurization systems. The temperature of flue gases in these systems is significantly reduced in order to ensure adequate conditions for the flue gas desulphurization process. Flue gases, after leaving a flue gas desulphurization system, have a temperature lower than the dew point and they flow through a duct system to the chimney. However, in order to protect the flues against condensation and thus against corrosion of chimney walls, treated flue gases should be heated to a temperature of at least 10°C above the dew point. In such a case, an effective way to raise the temperature of flue gases is to bring a hot air jet from the regenerative rotary air heater and mix it with treated flue gases (Fig.1). The advantage of this system is that an increase in the temperature of flue gases above the saturation temperature is ensured. Whereas, main disadvantages include: an increase in the flue gas stream, a possibility of contamination of flue gases with the dust carried by hot air from rotary air heaters and a possibility of penetration of hot air into the flue gas desulphurization system, which results in irreversible damage to the lining of the absorber.

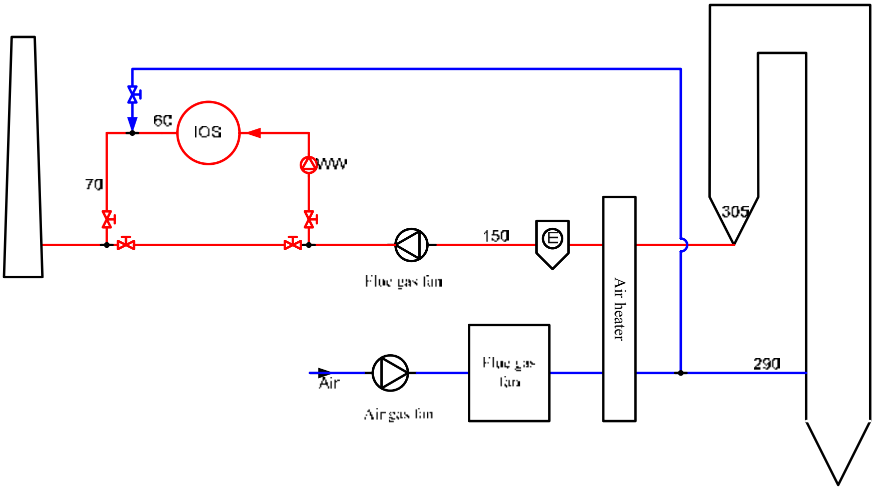

Fig. 1. The system for heating treated flue gases with the use of hot air

Another method for raising the temperature of treated flue gases, which has been used since recently, is a system for heating treated flue gases with the use of raw flue gases (Fig.2). In this system, before the flue gas desulphurization system, there has been installed a cross-flow heat exchanger, the task of which is to cool flue gases to a temperature that ensures the effectiveness of the desulphurization process and, on the other hand, to increase the temperature of treated flue gases to a temperature above the dew point. Therefore the system simultaneously recovers and utilizes flue gas waste heat, which undoubtedly is its advantage. The heat exchanger installed in the system is made from fluorine plastics, which are characterized by a high corrosion resistance and a low susceptibility to contamination. The disadvantage of the system are significant overall dimensions of the heat exchanger and the need to use inside the exchanger the systems for rinsing pipes from the remaining dust carried by flue gases.

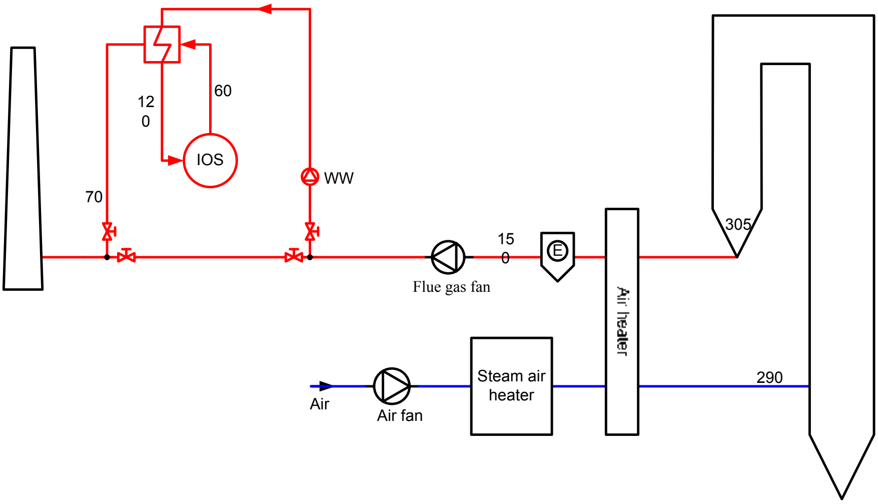

Fig. 2. The system for heating treated flue gas with the use of a cross-flow heat exchanger

Another system, designed for recovery and utilization of waste heat for heating treated flue gases, is shown in Fig.3. Two heat exchangers have been installed in this system - one before and second after the flue gas desulphurization system it. The task of the heat exchangers, like in the previous case, is to cool raw flue gases before the flue gas desulphurization system and to heat the treated flue gases to a temperature above the dew point. The difference in relation to the previously described example consists in the use of a liquid that transfers heat between the heat exchangers. Unquestionable advantages of this system include small dimensions of heat exchangers as compared with a cross-flow heat exchanger, the ability to transfer heat on longer distances, and the fact that water can used as the transfer liquid. The main problems include the necessity to use a system for preparing the transfer water and the need to add chemicals for water treatment. Water treatment is associated with possible penetration of sulphur compounds to the water.

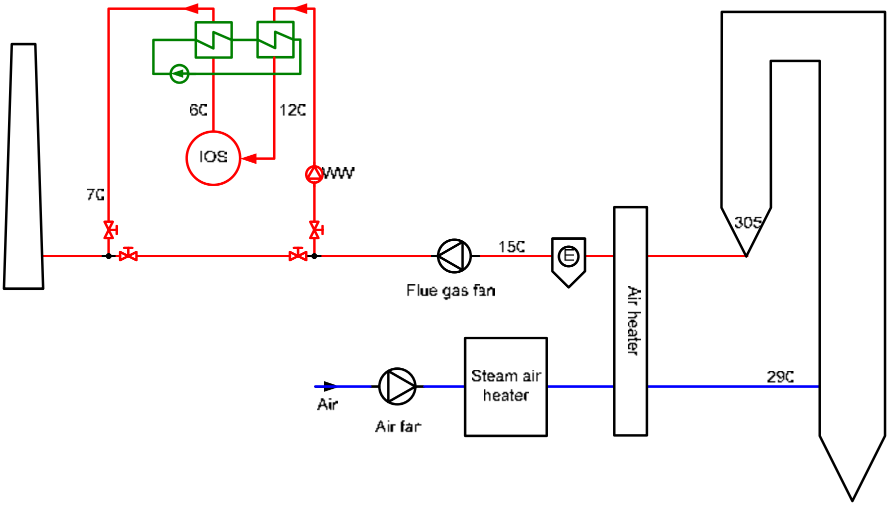

Fig. 3. The system for heating treated flue gases with the use of transfer liquid

Fig. 4 presents the concept of heat recovery proposed by Babcock Borgis Power. The essence of this concept consists on a two-stage heat recovery before the flue gas desulphurization system. In the first stage, flue gases are partly cooled and the recovered heat is transferred with the use of the transfer liquid to treated flue gases flowing out from the flue gas desulphurization system. The purpose of this operation, like in the previously described cases, is to heat treated flue gases to a temperature above the dew point. In the second stage of cooling, another heat stream is recovered from flue gases, which is also transferred with the use of the transfer liquid to the exchanger that heats air flowing into the combustion process. As it can be noticed, this system is more complex as compared with the systems already described. An unquestionable advantage in this case is much more efficient use of flue gas waste heat. A disadvantage of this system consists in very high costs of building it.

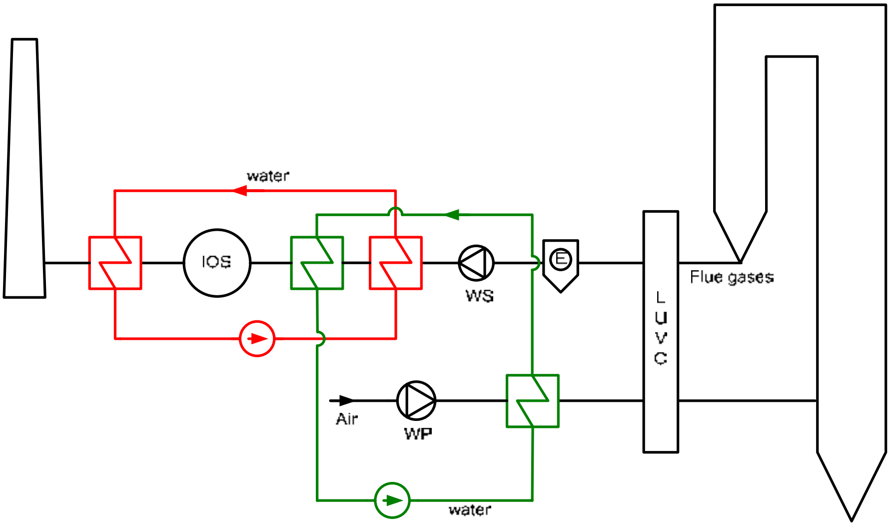

Fig. 4. The system of recovery and utilization of waste heat proposed by Babcock Borsig Power

2.2. Recovery and utilization of flue gas waste heat for heating intake air, feed water and condensate

When describing systems for recovery and utilization of flue gas waste heat, the first system to be considered should be the system used in the Niederaussem Power Plant in Germany [8]. Flue gas heat in this system is used to heat feed water in high-pressure regeneration, condensate in low-pressure regeneration, and the air flowing to the combustion process. This system is presented in Fig. 5.

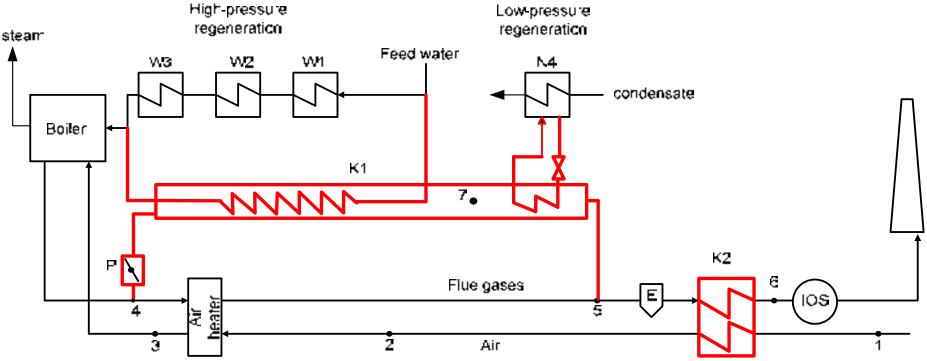

Fig. 5. Diagram of the heat recovery system in the Niederaussem Power Plant

The essence of this solution consists in the fact that there are installed two heat exchangers, designated in the figure as K_1 (flue gases-water) and K_2 (flue gases-air). Before the rotary air heater, the flue gas stream flowing from the boiler is divided into two parts. The first part of the stream flows to the rotary air heater and the second part (up to 30%) flows to the heat exchanger K_1. This exchanger heats the feed water and condensate. After leaving the heat exchanger K_1, flue gases merge to form one stream and flow to the heat exchanger K_2 via the electrostatic precipitator. The role of this exchanger is to heat the intake air. With such an arrangement, less bleed steam is required to heat the feed water and condensate, and thus the power produced by the generator is increased.

Another interesting solution is the flue gas heat recovery system in a supercritical power unit with a fluidized bed boiler proposed by Foster Wheeler. The diagram of the system is shown in Fig. 6. In this system, flue gases are divided into two streams before the rotary air heater. The first stream flows to air heaters, while the second flows to the heat exchanger that heats the condensate in the low-pressure regeneration system. Flue gases merge after the exchanger and flow via the electrostatic precipitator to the flue gas cooler.

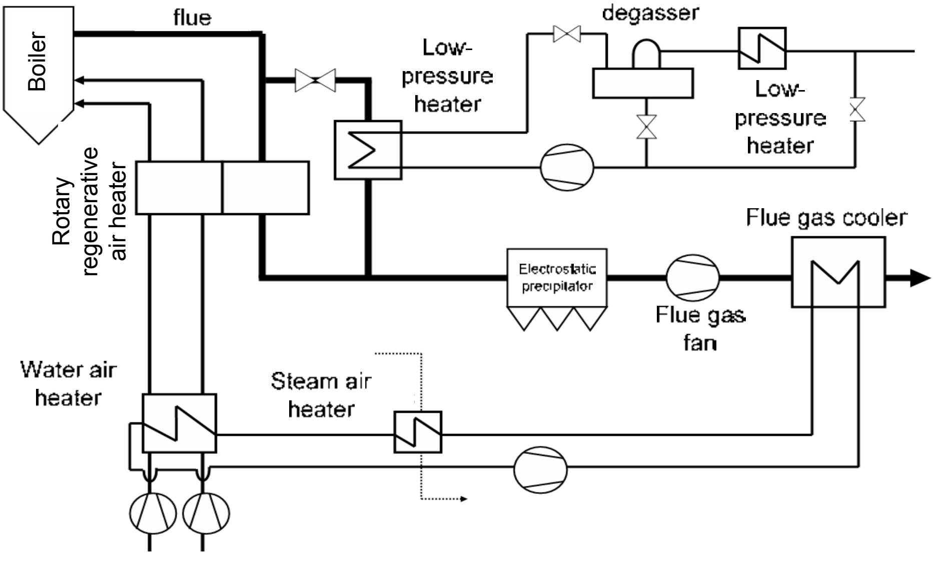

Fig. 6. The flue gas heat recovery system in a power unit with the power of 460 MW [8]

The temperature of flue gases is reduced in the cooler to approx. 85°C and the recovered heat with the use of the transfer liquid preheats the air for combustion. After having left the cooler, flue gases are discharged to the atmosphere via a cooling tower. According to the performed calculations, the use of such a flue gas heat recovery system increases the efficiency of the power unit by approx. 0.3%.

Another interesting solution is the system shown in Fig. 7, in which flue gas waste heat is used for heating the intake air as well as for heating the condensate in the main steam-water cycle. According to the assumptions, this system should operate at a variable amount of the heat being transferred, taking into account seasonal variations in temperatures of the outside air (–25°C to 35°C). In addition, the system should ensure a minimum air temperature (35 ° C) before the air heater, which will allow increasing the boiler efficiency by approx. 2% (from 93% to 95%). It is expected that the heat recovery system will be installed at the section after the rotary air heater and before the flue gas desulphurization system.

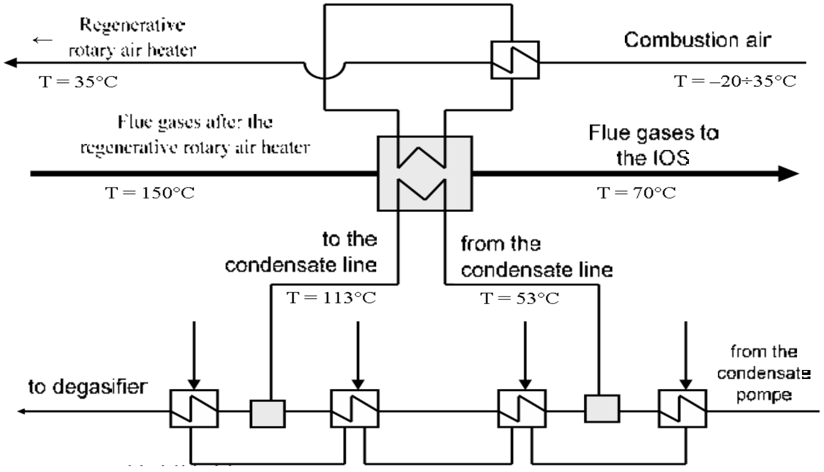

Fig. 7. Diagram of the flue gas heat recovery system for heating the intake air and feed water

As it appears from the analysis of the literature, it is often impossible to install waste heat recovery systems in existing power units. This result from the lack of space in a system or is connected with too high costs of installing a system of such a type. The situation is different in the case of newly built power units. In such power units, the space for building such a system can be foreseen just at the design stage. And so it is in the case of the power unit with the power of 858 MW built in PGE Elektrownia Bełchatów SA. It will be the largest and the most modern power unit in Poland. Apart from the highest power, the unit will be characterized by the use of clean coal technologies. Its anticipated net efficiency should reach 41%. Such a high efficiency will be achieved, among other things, thanks to the use of supercritical steam parameters, modern turbine blade systems, a cooling system with a cooling tower, as well as thanks to limiting the power unit auxiliaries to below 5.7%, full automation of the process, and a flue gas heat recovery system. The essence of the operation of this system will consist in cooling flue gases before the flue gas desulphurization system and transferring the heat with the use of a transfer liquid for heating the condensate in low-pressure regeneration of the power unit. In relation to the cases already described, waste heat is not used for example for heating the air flowing to the combustion process.

2.3. Flue gas heat recovery system with condensation

The authors proposed a concept of low-temperature recovery and accumulation of flue gas waste heat from coal-fired power units [9]. This concept consists in installing a new-generation heat exchanger in the outlet part of a power boiler, which will allow recovering the heat from flue gases. This exchanger should be characterized by a cross flow of mediums and have a high efficiency and small overall dimensions. It should cool flue gases between the electrostatic precipitator and the flue gas desulphurization system below the dew point temperature. Another problem associated with the construction of the heat exchanger is developing a method for discharging the condensate and cleaning the heat exchange surface. Fig. 8 presents a flowchart of the system with a two-stage heat exchanger installed between the electrostatic precipitator and the flue gas desulphurization system. The heat recovered from flue gases is used for heating the intake air as well as for heating the flue gases above the dew point temperature.

The use of a heat exchanger with condensation allows recovering a larger heat stream. The recovered heat, apart from heating the flue gases and intake air, can be used in the processes of the steam-water cycle, for heating feed water, power plant utility water, as well as for brown coal drying or for heat accumulation systems. It is also possible to convert the flue gas heat into electricity with the use of a low temperature ORC system.

3. Summary

An analysis of the flue gas heat recovery systems, which are currently used in coal-fired power plants, was presented in this paper. An important advantage of the flue gas waste heat recovery is a reduction of the stream of the combusted coal mass, which leads to a better efficiency of a power unit, decreases greenhouse gas emissions, and allows drying the flue gases flowing to the flue gas desulphurization system as well as heating the treated flue gases. The use of cross flow in the heat exchanger results in decreasing the overall dimensions of the heat exchanger and in increasing the heat exchange efficiency.

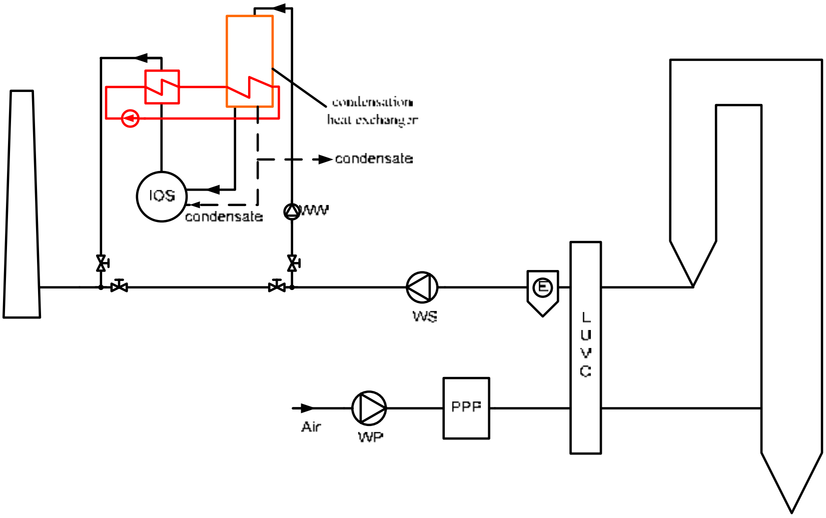

Fig. 8. The flue gas waste heat recovery system with single-stage cooling and condensation

References

[1] Olkuski T., Mokrzycki E., "Miejsca powstawania strat energii chemicznej zawartej w węglu w procesach pozyskiwania węgla oraz wytwarzania energii elektrycznej", Polityka Energetyczna, vol.6, Special Issue, Kraków, 2003, pp.389-398

[2] Ziembicki P., Zastosowanie techniki kondensacyjnej w istniejących instalacjach grzewczych, Scientific Journals No. 136, Inżynieria Środowiska No. 16, the University of Zielona Góra, 2009, pp.202-216

[3] Rombrecht H.B.; Krautz H.J., Proces Oxyfuel – przyszłością spalania węgla?. XII International Scientific and Technical Conference "Nowoczesne urządzenia zasilające w energetyce", Kazimierz Dolny, March 2009

[4] Mokrzycki E., Tumidajski T., Olkuski T., "Wpływ wzbogacenia wegla na procesy spalania w elektrowniach", Inżynieria mineralna – Special Issue No. 3, Kraków, 2003, pp. 194-199

[5] Rakowski J., Obecne możliwości technologiczne ograniczania emisji CO2 z elektrowni węglowych, Energetyka, June 2008. No. 06 (648), Annual 61, pp.395-408

[6] Bartnik R., Efektywność energetyczna i ekonomiczna modernizacji elektrowni węglowych przez nadbudowę turbiną gazową w układzie szeregowym i równoległym, Seminar "Kogeneracja w energetyce przemysłowej i komunalnej", 10 October 2003, Gliwice

[7] Budowa bloków 5 i 6 w PGE Elektrowni Turów SA – aspekty gospodarcze, środowiskowe i społeczne, edited by Czesława Rusik-Dulewska, Grzegorz Kusz, Opole, 2009, pp.31-33

[8] Ralf J. Heitmuller, Hans Fischer, Johann Sigg, Kocioł parowy na węgiel brunatny o mocy 1000 MW dla Elektrowni Niederaussem, Jubileuszowa Konferencja Kotłowa '99, Gliwice, Racibórz 1999, pp. 113-130

Journal of Energy Science, Vol. 1, No. 1, 2010, pp.201-225

Numerical investigations of the four-path separator

JACEK WYDRYCH[1*]

[1]Opole University of Technology, Department of Thermal Engineering and Industrial Facilities,
Mikołajczyka 5, 45-271 Opole, Poland

In the pneumatic conveying systems of large power boilers, the required separation of the dust-air mixture to particular burners has to be obtained. This problem is very important in consideration of limitation of losses connected with incomplete combustion, life of many elements of the furnace system and NO_x emission. The realized design works on dust pipes are usually based on the assumption that dust concentration in the section is approximately the same and there is no segregation of dust particles. However, in many cases in the pneumatic conveying systems for coal dust, diversified concentration and out-of-control segregation of particles take place. Such segregation leads to diversification of propagation, disturbance in the combustion process and accelerated erosion of the installation elements. This paper presents numerical investigations on the air-coal dust mixture flow through the four-path separator system. Diversification of concentration and particle segregation behind the separator are determined by the elbow presence just before the inlet to the separator. The elbow presence causes diversification of concentration on the mixture silt to the four-path separator located directly over the elbow. It is a reason of the diversified silt of the dust on the boiler corners and the accelerated erosion of separators. The author tried to assess influence of configuration of the pipe delivering the medium to the separator on uniformity of dust separation behind the separator. Numerical investigations were performed for six positions of the inlet interval before the separator at different velocities and dimensions of the dust particles. In order to realize calculations for three-dimensional geometry, the Euler model was selected for description of the gaseous phase motion, and the Lagrange model was used for description of the particle motion. From analysis of the performed calculations it appears that the inlet configuration in relation to the separator strongly influences the proper dust separation to outlets. The best dust separation can be observed for the inlet location angle in the range 60÷90°.

Symbols
C_D - coefficient of aerodynamic drag
D_p - particle diameter, m
f - correction factor

---

[*] Corresponding autor, e-mail: j.wydrych@po.opole.pl

F_i - mass force, N
k - turbulent kinetic energy
m_P - particle mass, kg
p - pressure, Pa
Re_p - Reynolds number related to particle
S_m - mass source
S_{fi} - momentum source
t - time, s
u_j - component velocity, m/s
$\overline{u}$ - mean velocity, m/s

Greek symbols
δ_{ij} - Kronecker delta
ε - dissipations of turbulent kinetic energy
μ - viscosity, Pa·s
μ_t - turbulent viscosity
μ_{ef} - effective viscosity
ρ - density, kg/m^3
τ_{ij} - diffusion terms
σ_k - effective Prandtl numbers for k
σ_ε - effective Prandtl numbers for ε

1. Introduction

In the pneumatic conveying systems of large power boilers, the required separation of the air-dust mixture to particular burners has to be obtained. This problem is very important because of limitation of losses of incomplete combustion, life of many furnace elements and NO_x emission.

The design problems connected with the pneumatic conveying systems are the subject of many research works [1,2]. In many papers we can find equations determining linear and local resistances of different elements of the installation [5,9]. They include, among others, influence of the dispersed phase, the substitute diameter of particles and spatial location of the elements on losses of pressure [11,12,18]. Much attention was paid to conditions under which the dust can accumulate in the installation [7,10]. This problem is very important because of the required mixture separation and work safety. Many papers were devoted to different separators included into dust-pipe installations [3,6,16], . In the furnace installation in the Opole Power Plant there are two-path separators with mobile baffles, allowing to control distribution. Such structures were subjected to numerical investigations, many measurements were done, too.

The realized design works on dust pipe installations are usually based on the assumption that the dust concentration distribution in the section is approximately the same and there is no segregation of dust particles [8]. However, in many cases, in the pneumatic conveying system for coal dust diversification of concentration and out-of-control particle segregation take place [13,17],. In a consequence, they lead to diversification of propagation, disturbance in the combustion process and accelerated erosion of the installation elements [14].

This paper presents numerical investigations on the air-coal dust mixture flow through the four-path separator system. Diversification of concentration and particle segregation behind the separator are determined by the elbow presence just before the inlet to the separator [8]. Presence of that element causes diversification of concentration on the mixture silt on the four-path separator located directly above the elbow. It is a reason of diversified dust silt to the boiler corners and accelerated erosion of separators.

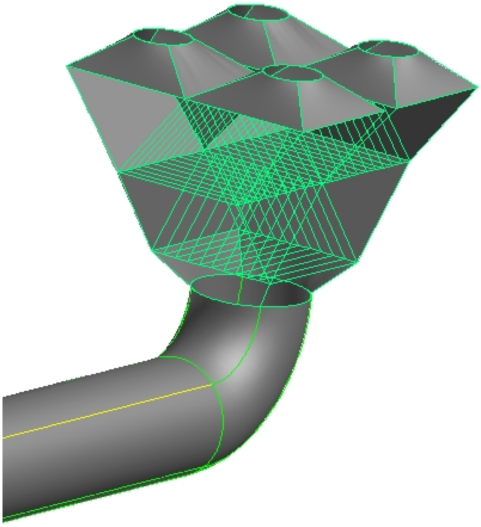

Fig. 1. General view of the examined four-path separator system

The considered flow system is shown in Fig. 1. It is the outlet straight interval of the dust tube from the mill together with the elbow. The four-path separator is located just above the elbow. The tests of gas and dust separation show the problem of non-uniformity of their distribution. Table 1 presents dust distribution (in %) to four outlets above the separator. From the results it appears that particle distribution to particular outlets is non-uniform under different service conditions of the system.

Table 1. Dust separation (in %) to particular outlets

Inlet velocity	Outlet 1	Outlet 2	Outlet 3	Outlet 4
m/s	%	%	%	%
30	24.5	21.8	27.6	26.1
37.5	24.6	21.1	29.5	24.7
45	25.5	18.9	27.5	28.1

The paper concerns influence of configuration of the tube delivering the medium to the separator on uniformity of dust separation behind the separator. Numerical investigations were carried out for six locations of the inlet before the separator, different velocities and dust particle dimensions. In order to realize calculations of the three-dimensional geometry the Euler model was applied for description of the gaseous phase motion, and the Lagrange model was used for description of the particle motion.

2. Simulation of the multiphase gas-solid flow

Presence of particles in the gas stream influences the gas motion, that influence depends on the particle concentration. In the simplest case, the mixture motion can be described introducing the equivalent density to equations of motion. However, such approach does not provide identification of points where the particles collide with the walls. During simulation of motion of the diluted gas-particle mixture two methods are applied:

- the particle phase is replaced by the fictitious fluid with suitably defined properties (the Euler method),
- particular particles are treated as the material points displacing in the space, and their interactions with gas and walls are taken into account (the Lagrange method).

The Lagrange method was chosen for description of the solid phase motion.

2.1. Model of the gas motion

The equations of mass and momentum conservation for incompressible fluid flows are written as [1,15]:

$$\frac{\partial p}{\partial t}+\frac{\partial(\rho u_i)}{\partial x_i}=S_m \quad , \qquad (1)$$

$$\frac{\partial \rho u_i}{\partial t} + \rho u_j \frac{\partial u_i}{\partial x_j} = F_i + \frac{\partial \tau_{ij}}{\partial x_j} + S_{fi} \,, \tag{2}$$

where u_j is the component velocity, F_i - mass force, S_m - the mass source, p - pressure, ρ - density, t - time, x_j - the direction, τ_{ij} - the diffusion terms, and S_{fi} is the momentum source. Since it is possible to analyse motion of the polydispersion mixture gas – particles, in this work the PSICell method was used. Phase changes were neglected, and it was assumed that both phases were incompressible, the flow was isothermal and steady [4]. Using average velocity and pressure, these equations can be written as

$$\frac{\partial p}{\partial t} + \frac{\partial (\rho u_i)}{\partial x_i} = 0 \,, \tag{3}$$

$$\frac{\partial (\rho u_i)}{\partial t} + \frac{\partial (\rho \bar{u}_i \bar{u}_j)}{\partial x_j} = F_i - \frac{\partial p}{\partial x_i} + \frac{\partial}{\partial x_j}\left[\mu\left(\left(\frac{\partial \bar{u}_i}{\partial x_j} + \frac{\partial \bar{u}_j}{\partial x_i}\right) - \rho \overline{u'_i u'_j}\right)\right] + \overline{S_{u_i,p}} \tag{4}$$

where $\bar{u}$ is the mean velocity and μ is viscosity. The turbulent stresses $\overline{\rho u_i u_j}$ and mean strain fields are assumed to be connected by the effective viscosity hypothesis:

$$-\rho \overline{u'_i u'_j} = \mu_{ef}\left(\frac{\partial \bar{u}_i}{\partial x_j} + \frac{\partial \bar{u}_j}{\partial x_i}\right) - \frac{2}{3}\rho k \delta_{ij} \,, \tag{5}$$

where μ_t is the turbulent viscosity and $\mu_{ef} = \mu + \mu_t$ is the effective viscosity, δ_{ij} - the Kronecker delta, k - the turbulent kinetic energy, and ε is the dissipation of the turbulent kinetic energy. In equation (5), turbulent viscosity is defined as:

$$\mu_t = \rho C_\mu \frac{k^2}{\varepsilon} \,. \tag{6}$$

The two turbulence quantities appearing in the above equation, k and e, are obtained from the following transport equations [2]:

$$\frac{\partial k}{\partial t}+\overline{u}_i\frac{\partial k}{\partial x_j}=\frac{1}{\rho}\frac{\partial}{\partial x_j}\left(\frac{\mu_t}{\sigma_k}\frac{\partial k}{\partial x_j}\right)+\frac{\mu_t}{\rho}\left(\frac{\partial\overline{u}_i}{\partial x_j}+\frac{\partial\overline{u}_j}{\partial x_i}\right)\frac{\partial\overline{u}_i}{\partial x_j}-\varepsilon \quad , (7)$$

$$\frac{\partial \varepsilon}{\partial t}+\overline{u}_i\frac{\partial \varepsilon}{\partial x_j}=\frac{1}{\rho}\frac{\partial}{\partial x_j}\left(\frac{\mu_t}{\sigma_\varepsilon}\frac{\partial \varepsilon}{\partial x_j}\right)+\frac{C_1\mu_t\varepsilon}{\rho k}\left(\frac{\partial\overline{u}_i}{\partial x_j}+\frac{\partial\overline{u}_j}{\partial x_i}\right)\frac{\partial\overline{u}_i}{\partial x_j}-C_2\frac{\varepsilon^2}{k} \quad .(8)$$

The quantities σ_k and σ_ε are the effective Prandtl numbers for k and ε. The turbulence model constants have the values: $C_1 = 1.44$, $C_2 = 1.92$, $\sigma_k=1.0$ and $\sigma_\varepsilon=1.3$. In order to capture the viscous effects, two equation turbulence models based on intensity and length scale with standard wall functions are employed.

In the PSICell method it is assumed that the disintegrated phase particles are sources of mass, momentum and energy occurring as additional components of $\overline{S_{u_i,p}}$ in equations of the continuous gas phase. $\overline{S_{u_i,p}}$ term is given by [13]:

$$\overline{S_{u_i,p}}=\frac{1}{V_E}\eta_j\int_{\delta t_j}\frac{\mu C_D Re_p D_p}{8\pi}\left(\overline{u}_i-u_{pi}\right)dt \quad , \qquad (9)$$

where D_p is the particle diameter, Re_p – the Reynolds number and C_D is the coefficient of aerodynamic drag.

2.2. Model of the disintegrated phase motion

Prediction of flows involving a dispersed phase requires separate calculation of each phase with the source terms generated to account the interaction between the phases [7]. Let us consider a discrete particle travelling in a continuous fluid medium. The equation of motion for particle in fluid flow [4], for which detailed derivations are available is written as [13,14]:

$$m_p\frac{du_p}{dt}=\frac{3}{4}C_D\frac{\rho m_P}{\rho_p dp}\left|u-u_p\right|(u-u_p)+g \quad , \qquad (10)$$

where m_P is a particle mass. The coefficient of aerodynamic drag is related to the Reynolds number for the particle diameter and sliding interphase velocity [5]:

$$Re_p = \frac{d_p \left| \vec{u} - \vec{u}_p \right|}{\nu}\,, \tag{11}$$

with:

$$\left| \vec{u} - \vec{u}_p \right| = \sqrt{\left(u - u_p\right)^2 + \left(v - v_p\right)^2 + \left(w - w_p\right)^2}\,. \tag{12}$$

If $Re_p \leq 1$, the value of C_D is calculated from the Stokes equation:

$$C_{Dr} = \frac{24}{Re_p}\,. \tag{13}$$

For higher values of Re_p, the empirical correction f is usually introduced [15]. Then:

$$C_{Dr} = \frac{24}{Re_p} f\,. \tag{14}$$

In this paper, the following equation [4] was proposed for calculations of the function f

$$f = \begin{cases} 1 + 0{,}15\,Re_p^{0{,}687} & 0 < Re_p \leq 200 \\ 0{,}914\,Re_p^{0{,}282} + 0{,}0135\,Re_p & 200 < Re_p \leq 2500 \\ 0{,}0167\,Re_p & Re_p > 2500 \end{cases} \tag{15}$$

The model considers only spherical inert particles, where particle–particle interactions are not considered. The equation of motion for particles is very complicated for particle shapes other than spherical.

The case when a particle collides with the solid wall should be treated with a special attention. In such a case, components of the particle velocity vector after a collision are calculated from the following equations:

$$u_{p1} = e_t u_p\,, \qquad v_{p1} = -e_n v_p\,, \tag{16}$$

where et and en determine the coefficient of restitution in shear and normal directions to the wall surface, up, vp, are advanced velocities in x and y directions. In Eq. (16), the subscript 1 means the component of particle velocity after collision [1,2].

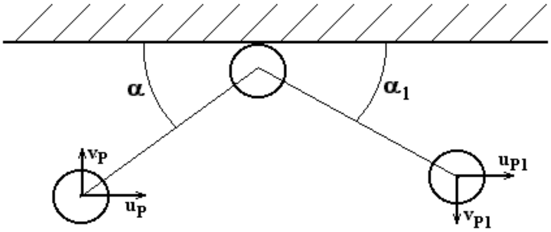

Fig.2. Configuration of particle-wall collision with velocity notation

The coefficient of restitution e is strongly dependent on the coefficient of kinetic friction, particle velocity, glancing angle and properties of materials used for the particle and the wall. From the tests it results that the coefficient of restitution is strongly dependent on the wall surface smoothness and the particle shape. The restitution coefficients are determined experimentally according to flow, particle velocity and particle glancing angle for the given material pairs. If the target material is 410 stainless steel, inert particles like sand/ash impacting on this surface, then the expression for normal and tangential restitution coefficient ratios are written as:

$$\begin{aligned} e_t &= 0.988 - 1.66\alpha + 2.11\alpha^2 - 0.67\alpha^3 \\ e_n &= 0.993 - 1.76\alpha + 1.56\alpha^2 - 0.49\alpha^3 \, . \end{aligned} \quad (17)$$

In the above models it is assumed that a particle is spherical. In the case of non-spherical particles, determination of restitution coefficient becomes much complicated [18].

3. The results of numerical calculations

Influence of configuration of the tube delivering the medium to the separator on uniformity of gas separation was tested for six locations of the inlet before the separator, at different velocities and dimensions of the dust particles. In the calculation area a complicated internal structure of the separator (see Fig.1) was taken into account. In order to perform calculations, the continuous flow systems were replaced by the calculation areas containing non-structural calculation networks. The network contains 779996 calculation elements, $5.59 \cdot 10^{-6} \div 1.88 \cdot 10^{-4}$ m^3 in volume. The tested locations of the inlet in relation to the four-way separator are presented in Fig.3. The paper presents the results for different angles of inlet location φ. The vertical inlet from the figure is marked as the system 0°, and the successive inlet locations are 30°, 60°, 90°, 120° and 150°. Fig.3 presents a top view of the flow system, the outlet sections are also visible.

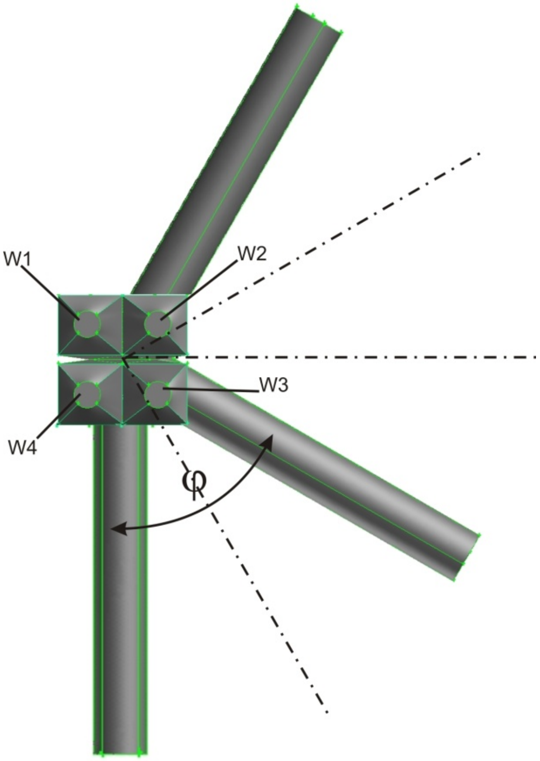

Fig. 3. The tested system „inlet-four-path separator" for different inlet locations

Numerical calculations were performed with use of the Fluent program, that allows to solve the system of equations of mass transport, gas momentum and the solid phase extended with equations of turbulence models.

The tests concerned disintegrated coal particles of 5, 10, 25, 50 and 100µm. The calculations were performed for the stationary flow with the interfacial coupling. At the inlet to the calculation area, three stationary velocity distributions of the gaseous phase were assumed. The inlet velocities 25, 30 and 35m/s were assumed for calculations.

The successive figures show the velocity distributions and trajectories of particles for the chosen service conditions in all the six flow systems. In these figures, the four-path separator is always presented in view from one direction, but the inlet position varies. The outlets for which the tests of solid particle separation were performed, are noted as: W1 – back left outlet, W2 – back right outlet, W3 – frontal right outlet, and W4 – frontal left outlet.

Fig.4 shows distributions of the gas velocity modulus for the system 90°, at the inlet velocities 25 and 35m/s. A lower inlet velocity causes that velocity distributions in the outlets are more uniform, but the velocity increase in the inlet causes increase of non-uniformity of velocity distributions in the outlets.

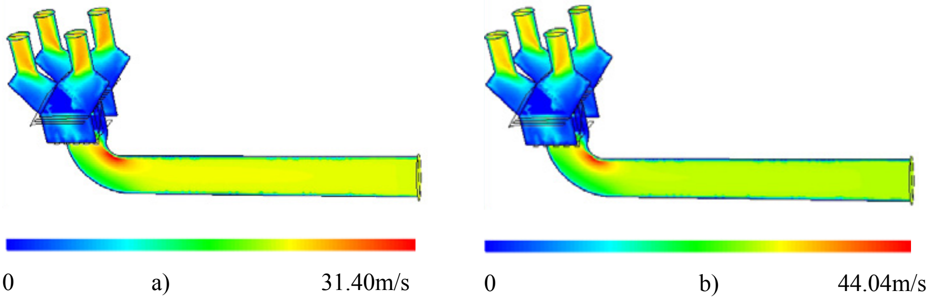

Fig. 4. Velocity distributions for the system 90° for inlet velocities a) 25m/s and b) 35m/s

When convergence of the velocity field solutions is obtained, and solid particle presence and coupling between phases are taken into account, the trajectory of coal dust particle motion is calculated; the coal dust density is 1300kg/m^3. The calculation results for trajectories of the particles delivered to the system from the point inlets of the system 90° for two inlet velocities are presented in Figs. 5 and 6. In these figures, different colours show the particle velocities corresponding to the gaseous phase velocities. Fig. 5 shows trajectiories of the particles 100µm in diameter for vertical locations of the point inlets of the supplying section for the inlet velocities 25m/s and 35m/s.

Fig. 6 presents trajectories of the particles 100µm in diameter, for the horizontal orientation of the point inlets of the supplying section for the same inlet velocities.

From the presented results it appears that the dust separation to particular corners influenced by location of the dust inlet points and velocity at the system inlet, is diversified. In the case of particles for which trajectories of their motion have been presented we can state that before the elbow the particles accumulate in the lower part of the pipeline, and next they are thrown away in direction of the external arc of the elbow [15]. Such effect causes non-uniform distribution of concentration in the section before the separator and, in a consequence, non-uniform dust separation to particular outlets. Moreover, the effect of increased concentration of particles in some zones of the system can lead to greater wear of its walls located directly near these zones.

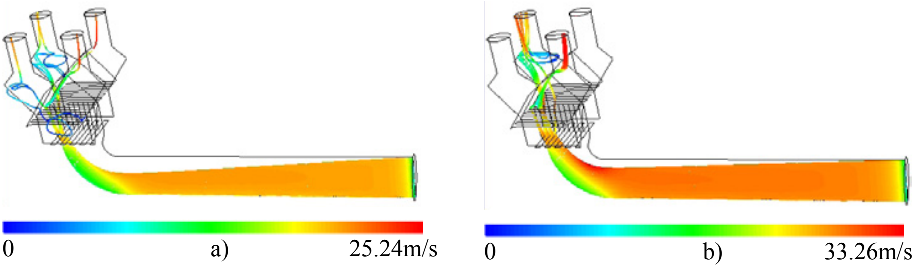

Fig. 5. Trajectories of the particles 100μm in diameter for the system 90° at the inlet velocities a) 25m/s and b) 35m/s for the linear vertical inlet of the particles

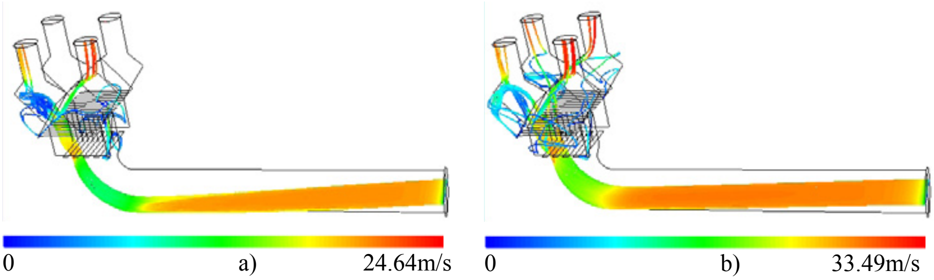

Fig. 6. Trajectories of the particles 100μm in diameter for the system 90° at the inlet velocities a) 25m/s and b) 35m/s for the linear horizontal inlet of the particles

Figs. 7÷11 present comparison of the calculation results for all the six flow systems at the inlet velocity 25m/s. The results are shown in the way allowing to assess influence of the inlet location in relation to the separator on the gas motion parameters, especially the component velocities and trajectories of the particles.

Distributions of the velocity moduli for all the systems shown in Fig.7 testify similarities between them. However, there are differences between the maximum velocity moduli in these systems, which in connection with different directions of the particle flow into the separator area can cause differences in the dust particle trajectories.

The next figure presents influence of diversification of the flow system on the vertical components of the gaseous phase velocity vz. Like in the case of velocity moduli, distributions of the vertical component are similar in spite of differences between geometries of the calculation systems. The extreme values of these quantities change. The maximum velocity varies in the range 24.84÷25.96m/s, and it means the change to 4.5%. The minimum velocity varies in the range -10.08 ÷ -7.52m/s, i.e. the range reaches even 40%. Analysis of variations of the vertical component of the gas velocity allows to assume that the gas velocity strongly influences trajectories of the solid particle motion.

Figs. 9÷11 present trajectories of the particles 5, 25 and 100μm in diameters in six flow systems for the inlet velocity 25m/s. Fig. 9, concerning the particles 5μm in diameter, allows to state that location of the inlet tube in relation to the separator strongly influences trajectories of the particles and their non-uniform separation to particular outlets. In the system 30°, the highest number of particles reaches the outlet W1, where their quite an uniform distribution over all the outlet surface can be seen. A similar situation can be observed in the system 90°, but in this case the greatest number of particles reaches to the outlet W2.

The next figure shows trajectories of the particles 25μm in diameter, thus, their mass and inertia are much greater. Quite an uniform distribution of particles on the inlet surface occurs in the case of geometry 90° for the outlet W4. In this case, a low number of the particles reaches the outlet W3. As for the remaining geometries, the particles concentrate on small surfaces of the outlets. Moreover, we can observe diversification of trajectories in the main part of the four-path separator. Only in the case of 0°, the particles fluently flow in the separator area without any perturbations.

Fig. 11 shows trajectories of the particles 100μm in diameter, which often move along the paths forming „cords" concentrated on small surfaces – it is a reason of local increase of concentration. Like in the case of the particles 25μm in diameter, for geometry 0° the particles fluently flow in the area of separator without any perturbations. However, in this system no particles reach the outlet W3. In the case of other tested geometries, we can also observe similar by-passing some outlets, namely the system 30° - the outlet W3 is not reached, the system 60° - the outlet W4 is omitted, the system 150° - the outlet W1 is by-passed by the particles.

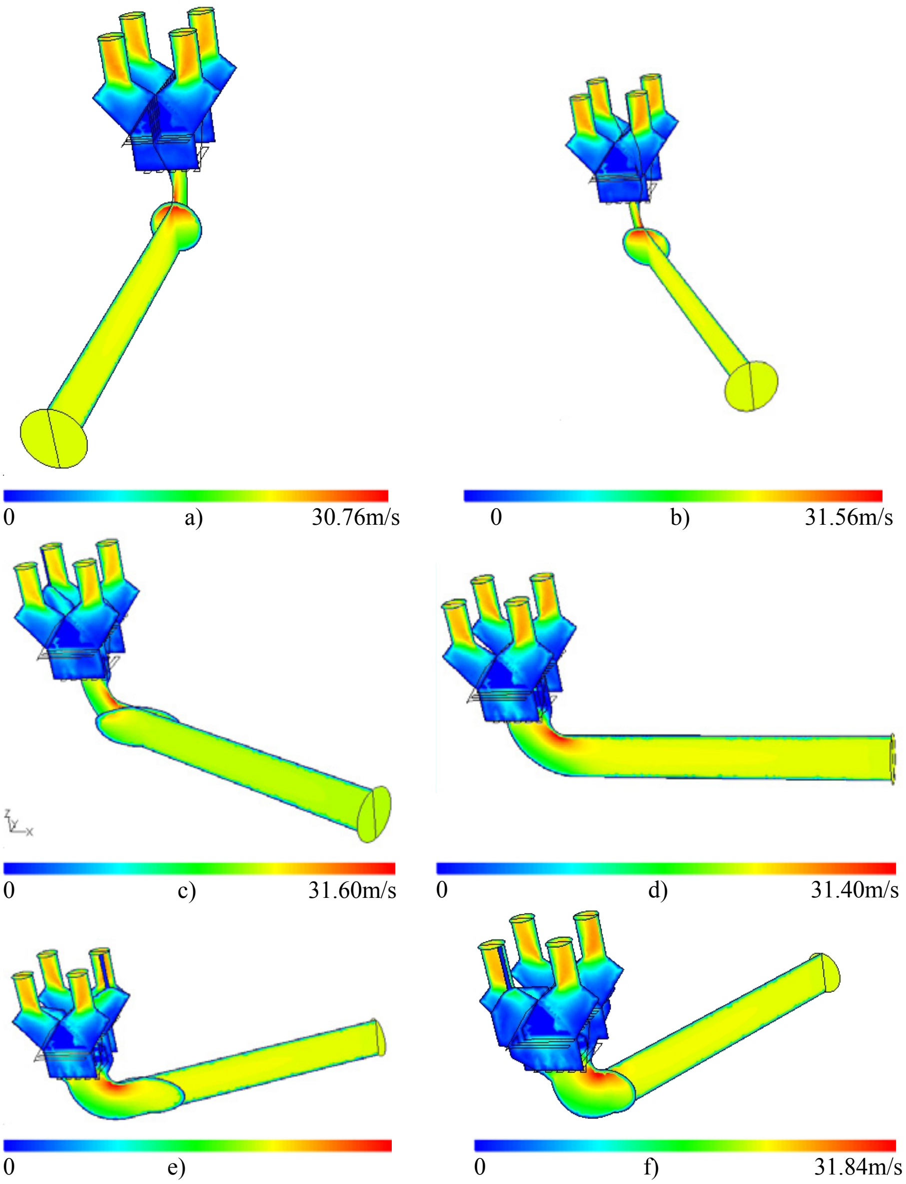

Fig. 7. The gas velocity distributions at the inlet velocities 25m/s for the systems:
a) 0°, b) 30°, c) 60°, d) 90°, e) 120° and f) 150°

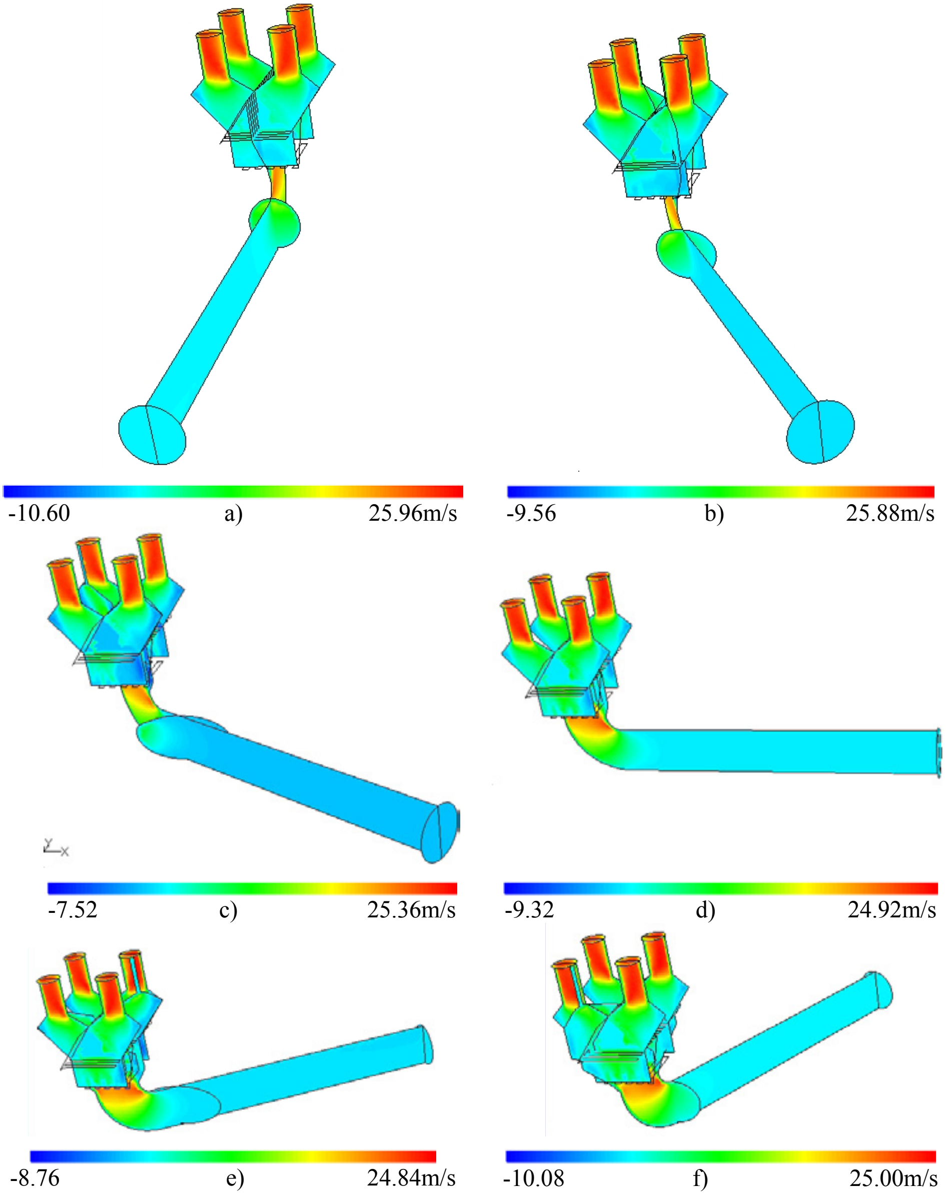

Fig. 8. Distributions of the vertical component of the gas velocity at the inlet velocitiy 25m/s for the systems a) 0°, b) 30°, c) 60°, d) 90°, e) 120° and f) 150°

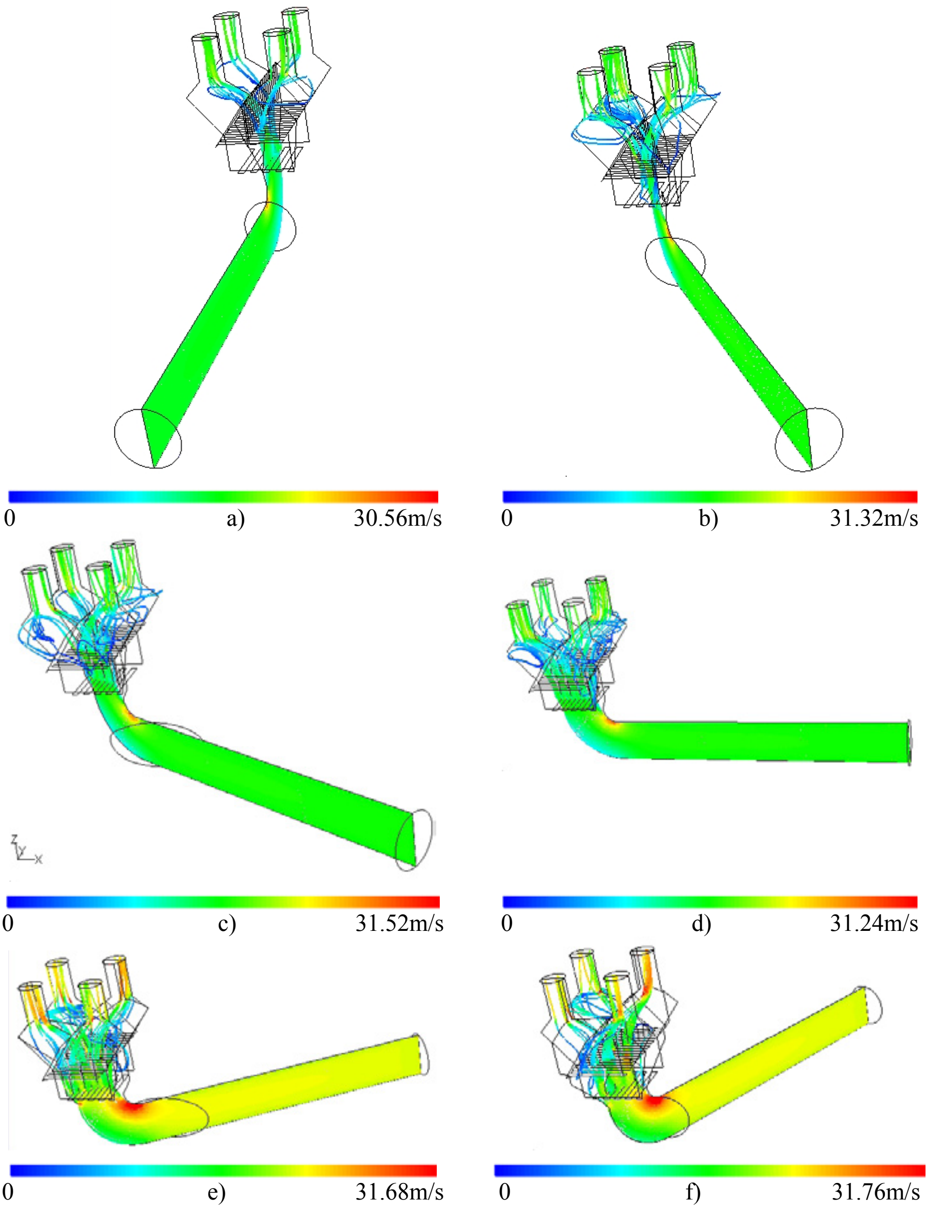

Fig. 9. Trajectories of the particles 5µm in diameters at the inlet velocity 25m/s for the systems a) 0°, b) 30°, c) 60°, d) 90°, e) 120° and f) 150° (colours mean velocity of the particles)

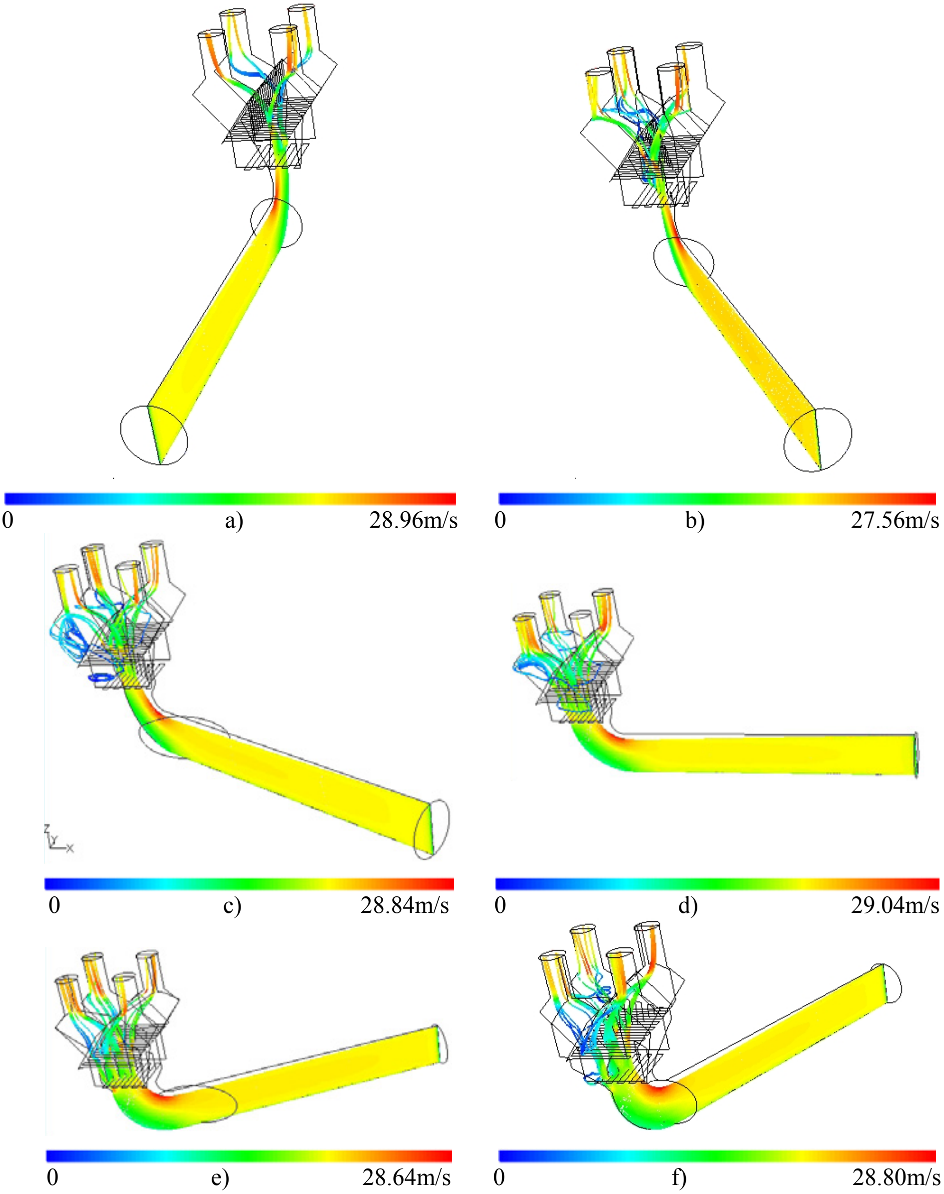

Fig. 10. Trajectories of the particles 25μm in diameter at the inlet velocity 25m/s for the systems: a) 0°, b) 30°, c) 60°, d) 90°, e) 120° and f) 150° (colours mean the particle velocities)

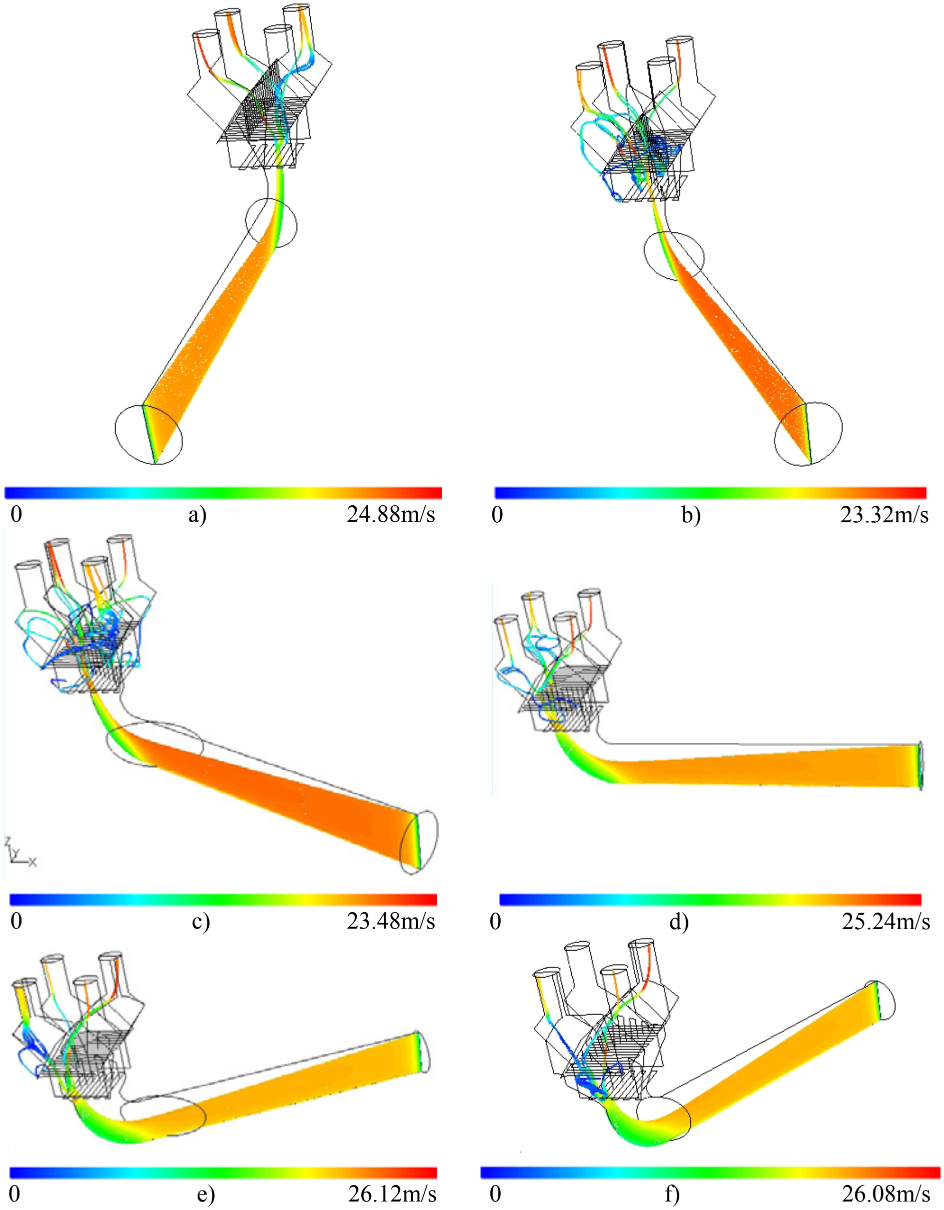

Fig. 11. Trajectories of the particles 100μm in diameter at the inlet velocity 25m/s for the systems: a) 0°, b) 30°, c) 60°, d) 90°, e) 120° and f) 150° (colours mean velocities of the particles)

4. Analysis of the numerical results

The calculated gas velocity fields and solid particle trajectories allowed to estimate the disintegrated phase distribution to particular outlets for the tested systems. The trajectories of 120600 particles started from the inlet where 2412 points of the entry of the solid particles were assumed. The particles starting their motion in the tested system passed through the separator and reached one of the four outlets. Table 2 presents separation of the dust particles 5μm in diameter for particular outlets of the system 0° for all the tested systems at the inlet velocity 25m/s. Such statements were elaborated for all the tested diameters and inlet velocities.

Table 2. Numbers of particles for particular outlets of the system 0° for the inlet velocity 25m/s and diameter of particles 5μm

Inlet angle	Outlet W1	Outlet W2	Outlet W3	Outlet W4
deg	%	%	%	%
0	33919	31092	24968	30621
30	28346	29377	28346	34531
60	28496	33585	25443	33076
90	31078	31078	28295	30150
120	27199	28226	33357	31818
150	29390	27363	31417	32430

The complete set of the data for the tested velocities and diameters of the particles allowed to elaborate graphs where particle distribution to particular outlets was presented as percentage of the total number of particles. Fig.12 presents the particle percentage for particular outlets for the system 0° at different inlet velocities.

Let us note diversification of separation dependent on the angle of location of the inlet tube in relation to the four-path separator φ, and reduction of diversification of the angle φ about 100° in the case of the inlet velocity 30m/s and the angle φ about 90° for the velocity 35m/s.

Assuming that uniform separation (25% particles for each outlet) provides the best service conditions of the boiler installation, at the next stage deviations of the calculated separations from the expected were estimated according to the following relation:

$$ED = \frac{D-25}{25} \cdot 100 , \qquad (19)$$

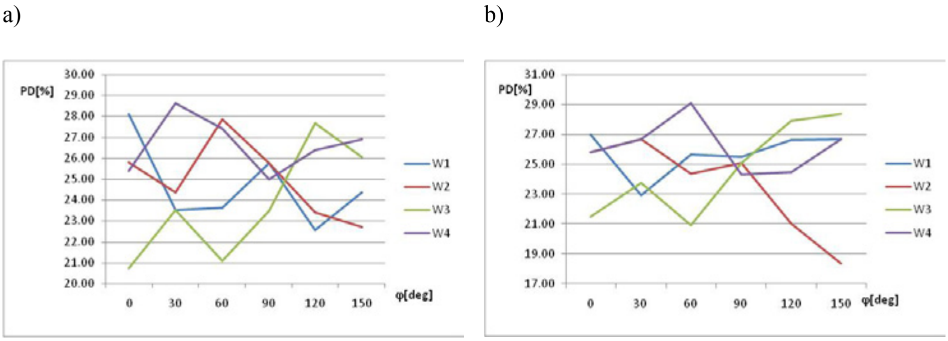

Fig. 12. Particle percentage in particular outlets of the system 0° for particles 5μm in diameter at the inlet velocities a) 30m/s, b) 35m/s

where *D* is the calculated separation, and *ED* deviation of separation from the expected value. The calculated deviations are shown in Fig.13.

From Fig.13 it appears that increase of the inlet velocity causes increase of uniformity of the particle separation to particular outlets, especially for the systems where the angle between the inlet and the separator is included into the range 50-100°. In the case of lower velocities, improvement of separation occurs at the angle φ about 90°.

Fig.14 presents the moduli of deviation for all the outlets from the expected value for all the considered particle diameters and all the locations of angle φ.

In all the graphs in Fig. 14 we can see improvement of separation uniformity for the angle φ within 50÷100°. More precise information about the optimum angle φ can be obtained from analysis of particular curves shown in the graphs. The particles 25μm in diameter are the best separated at the inlet velocity 25m/s in the system 90°, at the inlet velocity 30m/s in the range of the angle φ 60÷120°, and at the inlet velocity 35m/s in the system 120°. As for the particles 100μm in diameter, the best separation occurs at the inlet velocity 25m/s in the system 60°, at the inlet velocity 30m/s for the angle φ 30° and in the range 90÷120°, and at the inlet velocity 35m/s in the system 90°. Thus, for each diameter and under different inlet velocities it is possible to find the optimum angle of the inlet location, φ , taking into account the best dust separation to particular outlets.

In the true dust-pipe systems, the flowing mixture contains the particles of different fractions and different participations of these fractions. Thus, it is necessary to estimate the total particle fractions in particular outlets and their deviations from the expected values, and their their deviations from the expected values taking into account their fractions in the mixture. Fig. 15 shows percentage of particles of particular dust fractions obtained with the Rosin-Rammler-Sperling method.

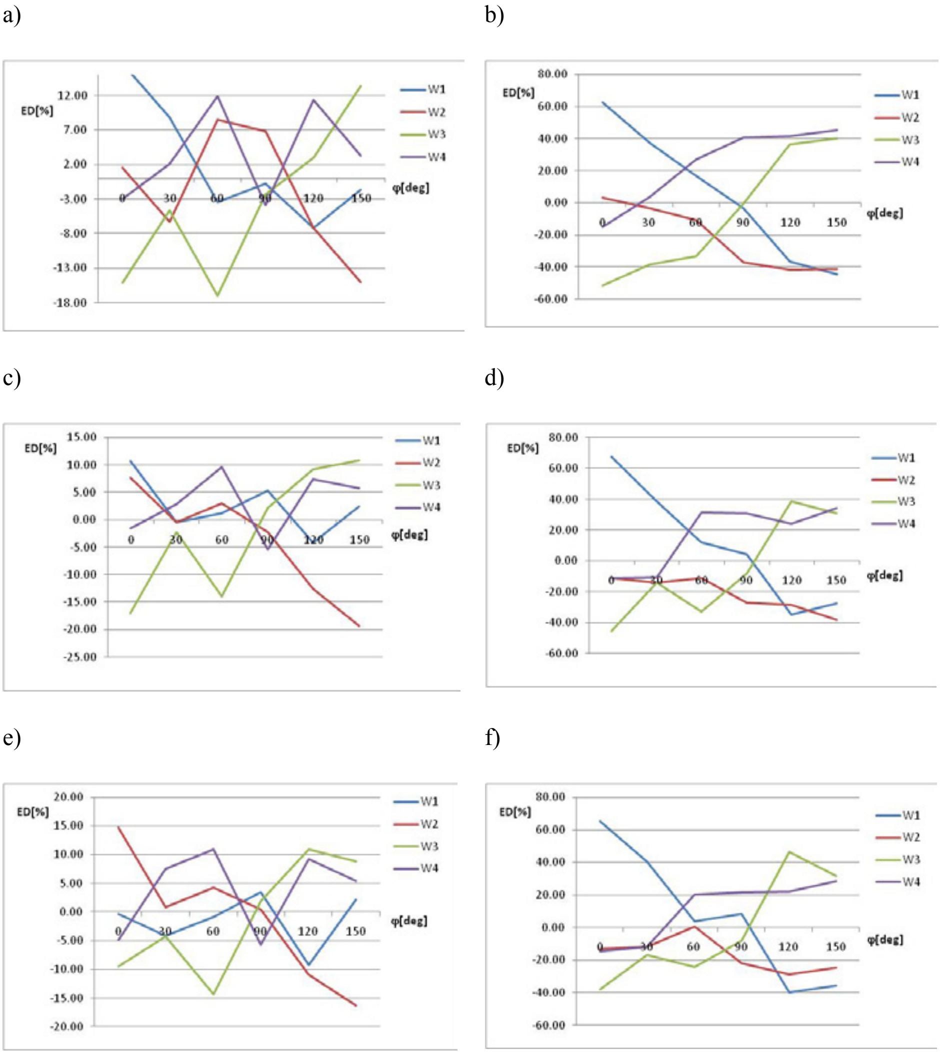

Fig. 13. Deviations from the expected values in particular outlets of the tested systems for: a) v=25m/s, D_p=10µm, b) v=25m/s, D_p=50µm, c) v=30m/s, D_p=10µm, d) v=30m/s, D_p=50µm, e) v=35m/s, D_p=10µm, f) v=35m/s, D_p=50µm

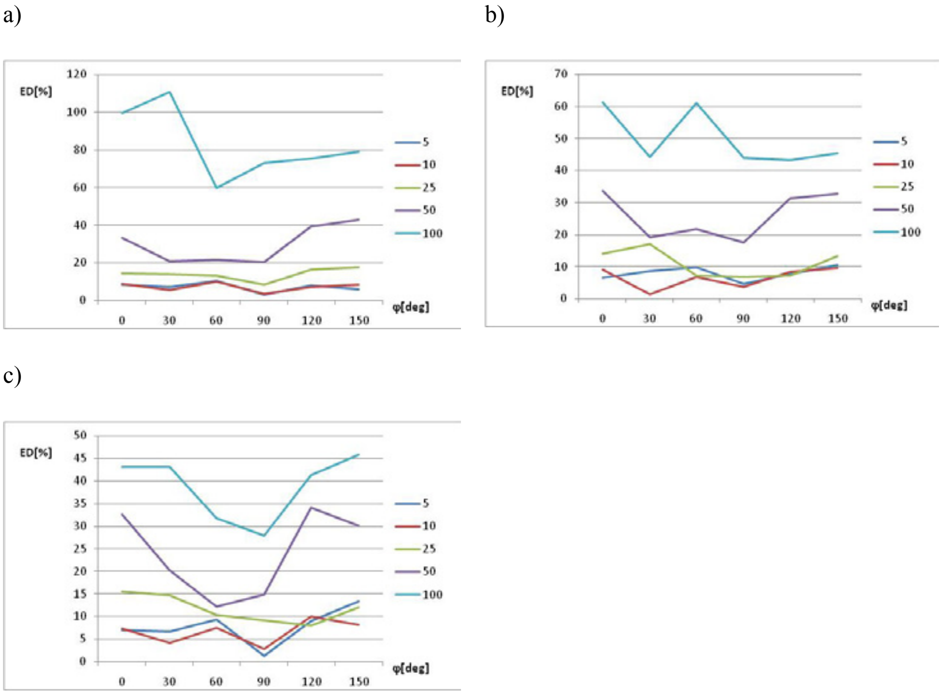

Fig. 14. Deviations from the expected value depending on the particle diameter for the inlet velocities a) 25m/s, b) 30m/s, c) 35m/s,

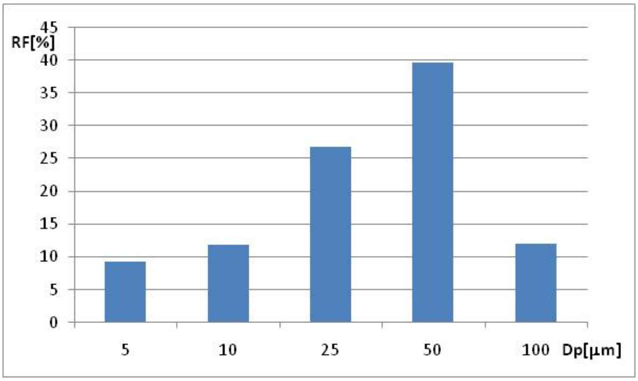

Fig. 15. Percentage of the particles of particular coal dust fractions

Fig. 16 presents deviations from the expected value for all the polydispersion mixture for some selected flow systems. Let us note that increase of velocity stabilizes the particle separation to particular outlets. At the same time, geometry of the flow system influences a change of the particle separation to the outlets in a greater degree than velocity.

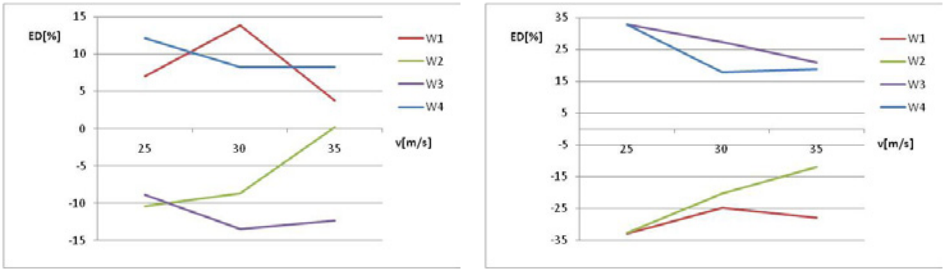
a)
b)

Fig. 16. Deviation from the expected value of all the mixture for the system a) 60deg, b) 150deg

The previously presented results allowed to elaborate the sets of moduli of the averaged deviations from all the outlets for all the mixture. Then, the elaborated graph presented changes of these moduli together with the changes of velocity and angle of inlet location φ (Fig. 17). Application of the least inlet velocity to the system causes occurrence of the greatest non-uniformities in dust distribution to the outlets. At this velocity, the angle $\varphi=60°$ is the optimum inlet angle in relation to the separator. Increase of the inlet velocity to 30m/s causes a change of the optimum inlet angle to 80°. At the highest tested inlet velocity 35m/s, the optimum inlet angle reduces to 70°. Such results testify strong influence of the inlet system on effectiveness of particle separation by the four-path separator. Moreover, we can find that particular inlet locations are optimum for the given service loadings, and a change of these conditions can cause a worse separation of particles to particular outlets.

The further part of analysis includes an attempt of determination of a relation between deviations of particle separation from the expected values and gas velocities for different inlet-separators systems. Fig.18 shows changes of separation deviations, maximum gas velocities, maximum, minimum and component vertical gas velocities caused by changes of locations of the inlet angle φ.

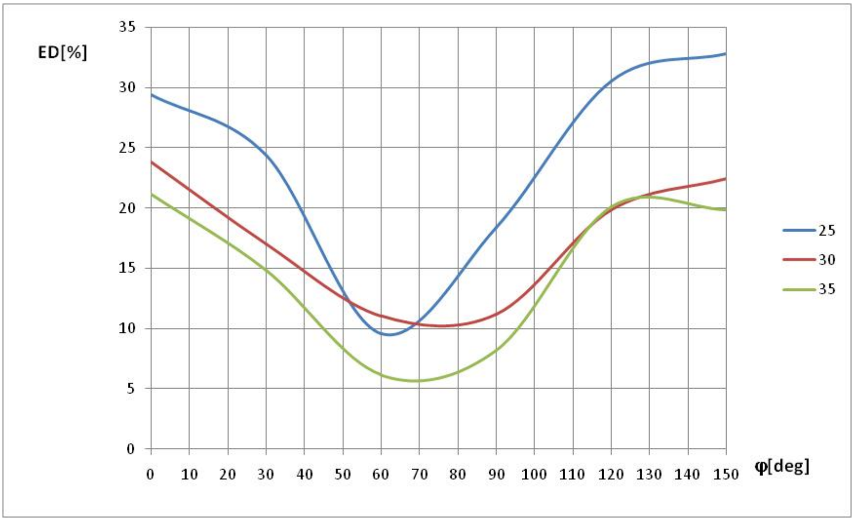

Fig. 17. Modulus of the averaged deviation for all the outlets

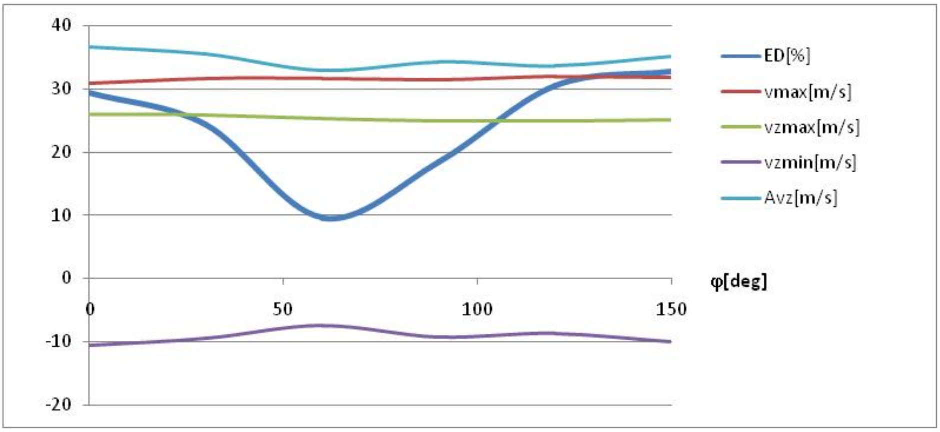

Fig. 18. Changes of deviations, extreme velocities and velocity amplitudes versus the inlet location angle φ

The data presented in Fig. 18 allowed to determine correlations between them, and the calculation results were presented in Table 3. The calculated correlation coefficients allow to state that there are not important relations between the maximum moduli v_{max} and vertical component vz_{max} gas velocities and separation deviations. On the other side, high convergence between the minimum values vz_{min} and amplitudes A_{vz} of vertical velocity components with separation deviations from the expected values can be seen.

Table 3. The data for calculation of correlation between separation deviation and gas velocity components togeterer with the values of correlation coefficients

	0	30	60	90	120	150	Coeff. of correlation
	deg	deg	deg	deg	deg	deg	-
ED[%]	29.41	24.35	9.62	18.42	30.56	32.81	-
v_{max}[m/s]	30.76	31.56	31.60	31.40	31.96	31.84	0.060
vz_{max}[m/s]	25.96	25.88	25.36	24.92	24.84	25.00	-0.030
vz_{min}[m/s]	-10.60	-9.56	-7.52	-9.32	-8.76	-10.08	-0.756
Avz[m/s]	36.56	35.44	32.88	34.24	33.60	35.08	0.602

5. Conclusions

From the performed analysis it appears that the applied method allows to determine geometry of the four-path separator system which provides the optimum conditions of dust particle distribution to particular outlets.

The maximum vertical velocity varies in the range 24.84÷25.96m/s, and it means a change to 4.5%. The minimum velocity varies in the range -10.08 ÷ -7.52m/s, and it means a change reaching even 40%.

From analysis of the particle trajectories it results that in the case of some diameters the particles move along the paths forming distinct "cords" concentrated on small surfaces. It is a reason of local increase of concentration.

In the case of geometry 0°, the particles of all diameters fluently flow through the separator with no disturbances in its area. At the same time, in all the systems at different velocities we can observe large non-uniformities causing that no particles reach some outlets. It has been found that application of the lowest inlet velocity to the system causes occurrence of greatest non-uniformities in dust separation to the outlets. At such velocity, the angle $\varphi=60°$ is the optimum inlet angle in relation to the separator. A change of the inlet velocity causes a change of the optimum inlet angle. These results show a strong influence of the inlet system on effectiveness of particle separation by the four-path separator.

References

[1] BORSUK G., DOBROWOLSKI B. and WYDRYCH J., Gas - solids mixture flow through a two - bend system, Chemical and Process Engineering, vol. 27, nr 3/1, (2006), 645-656.

[2] DOBROWOLSKI B. and WYDRYCH J., Evaluation of numerical models for prediction of areas subjected to erosion wear, Int. J. of Applied Mechanics and Engineering, vol.11, No.4 (2006), 735-749.

[3] DONG K.J., GUO B.Y., CHU K.W., YU A.B. and BRAKE I., Simulation of liquid–solid flow in a coal distributor, Minerals Engineering, 21 (2008), 789–796.

[4] FIDAROS D.K., BAXEVANOU C.A., DRITSELIS C.D. and VLACHOS N.S., Numerical modelling of flow and transport processes in a calciner for cement production, Powder Technology, 171 (2007), 81–95.

[5] GIDDINGS D., AROUSSI A., PICKERING S.J. and MOZAFFARI E., A 1/4 scale test facility for PF transport in power station pipelines, Fuel, 83 (2004), 2195–2204.

[6] RAJENDRAN S., NARASIMHA M., DUTTA A., SINHA M.K. and MISRA A., Modelling of feed distributor at coal washeries, Int. J. Miner. Process., 81 (2006), 178–186.

[7] SAKAI M. and KOSHIZUKA S., Large-scale discrete element modeling in pneumatic conveying, Chemical Engineering Science, 64 (2009), 533 – 539.

[8] SCHNEIDER H., FRANK Th., PACHLER K. and BER K., A Numerical Study of the Gas-Particle Flow in Pipework and Flow Splitting Devices of Coal-Fired Power Plant, 10th Workshop on Two-Phase Fow Predictions, 9-12 April 2002, Martin-Luther-Universität Halle-Wittenberg, Halle (Saale), Germany, pp. 227-236.

[9] SZMOLKE N. and WYDRYCH J., Badania przepływowe kotła małej mocy na ziarno energetyczne, In: Termodynamika w nauce i gospodarce, Politechnika Wrocławska, Wrocław, 2008, pp. 384-389.VUTHALURU H.B., PAREEK V.K. and VUTHALURU R., Multiphase flow simulation of a simplified coal pulveriser, Fuel Processing Technology, 86 (2005), 1195– 1205.

[11] WYDRYCH J. and SZMOLKE N., Numerical simulation of fluidization between the tubes, Archives of thermodynamics, vol. 27, No. 4, (2006), 245-253.

[12] WYDRYCH J. and SZMOLKE N., Reciprocal correlation in fluid flows, International Conference of Modeling and Simulation – Virtual Forum, Italy , Napoli, 12-26.07.2010.

[13] WYDRYCH J., Computational and experimental analysis of gas-particle flow in furnance power boiler instalations with respect to erosion phenomena, Journal of theoretical and applied mechanics, vol.45, No.3 (2007), 513-538.

[14] WYDRYCH J., DOBROWOLSKI B. and SKULSKA M., Numerical modelling of erosion wear of components of cyclone separators, Archives of Energetics, vol.XXXVIII, nr 2 (2008), 63-70.

[15] YILMAZ A. and LEVY E.K., Formation and dispersion of ropes in pneumatic conveying, Powder Technology, 114 (2001), 168–185.

[16] ZHANG J. and COUTHARD J., Theoretical and experimental studies of the spatial sensitivity of an electrostatic pulverised fuel meter, Journal of Electrostatics, 63 (2005), 1133-1149.

[17] ZHANG Y, CHEN L., ZHANG C., YU L., WEI X., MAB L. and GUAN C., CFD analysis of pneumatic conveying in a double-tube-socket (DTS_) pipe, Applied Mathematical Modelling, 34 (2010), 3085–3097.

[18] ZHU H.P., ZHOU Z.Y., YANG R.Y. and YU A.B., Discrete particle simulation of particulate systems: A review of major applications and findings, Chemical Engineering Science, 63 (2008), 5728 – 5770.

Journal of Energy Science, Vol. 1, No. 1, 2010, pp.227-239

Thermodynamic analysis of COP achieved by adsorption heat pump

BARTOSZ ZAJĄCZKOWSKI, ZBIGNIEW KRÓLICKI, BOGUSŁAW BIAŁKO

Wroclaw University of Technology, Institute of Heat Engineering and Fluid Mechanics,
Wybrzeże Wyspiańskiego 27, 50-370 Wrocław, Poland

Adsorption heat pumps (SSHP) (solid-liquid/gas) have potential to be competitive if one compares them with absorption heat pumps (liquid-liquid/gas) or vapor compressor heat pumps. Benefits follow from the type of a heat pump drive source. SSHP utilize a waste heat of industrial processes as a heat source and fully ecological substances as working pair. For physical adsorption silica gel – water and zeolite – water can be used. For chemical adsorption it can be salt – ammonia (or its derivatives). However, low efficiency (COP < 1) and constant work difficulties seem to be the basic problem.In this paper a COP model of an adsorption heat pump system is discussed: basic two-adsorber system, system with recuperation and with regeneration. The results of theoretical analysis of several types of sorption systems using different working pairs have been evaluated for the highest coefficient of performance.

1. Sorption heat pump for continuous operation

Solid sorption heat pumps (SSHPs) are devices, which operate refrigeration cycle with consecutively occurring processes of adsorption and desorption (Fig. 1) [10]. Thermodynamic cycle of adsorption system is defined by two isosteres and two isobars (Fig. 2).

In a simple single adsorber SSHP, the effective heating occurs only during adsorption of the working fluid. Under assumption that the time of adsorption is equal to the time of desorption, heating takes place during less than a half of the working cycle. This periodicity is a consequence of SSHP's working principle – heating period is mainly defined by the isoster 1-2 (concetration of adsorbate on adsorbent is constant) in Fig. 2 [4, 7]. Valves are closed and the working fluid does not flow through condenser, throttling valve and evaporator. Hence, no heat is being transfered from the low temperature source and no heat is released in the adsorber.

The continuity of operation can be obtained with two adsrobers working out-of-phase. Transitions 1-2 and 1-3 can occur simultaneously and alternatingly in the two adsorbers. Such working cycle consists two distinct half-cycles.

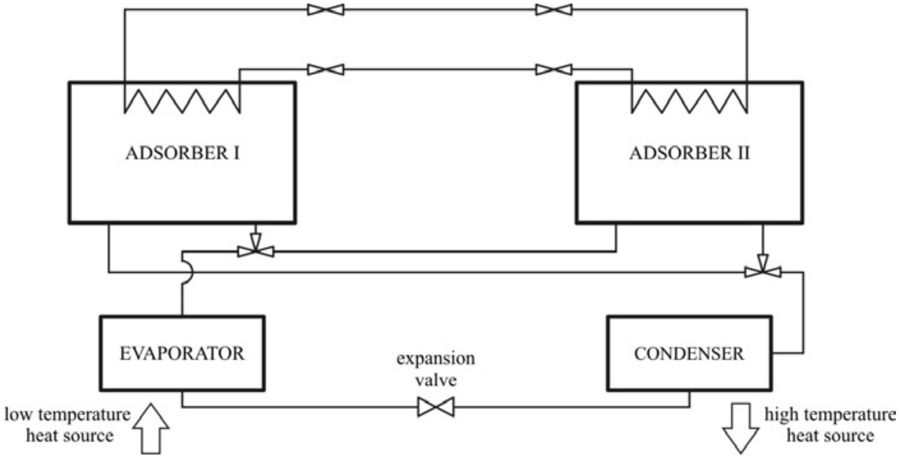

Fig. 1. Outline of the solid sorption heat pump with two adsorbers (and heat recuperation) [7]

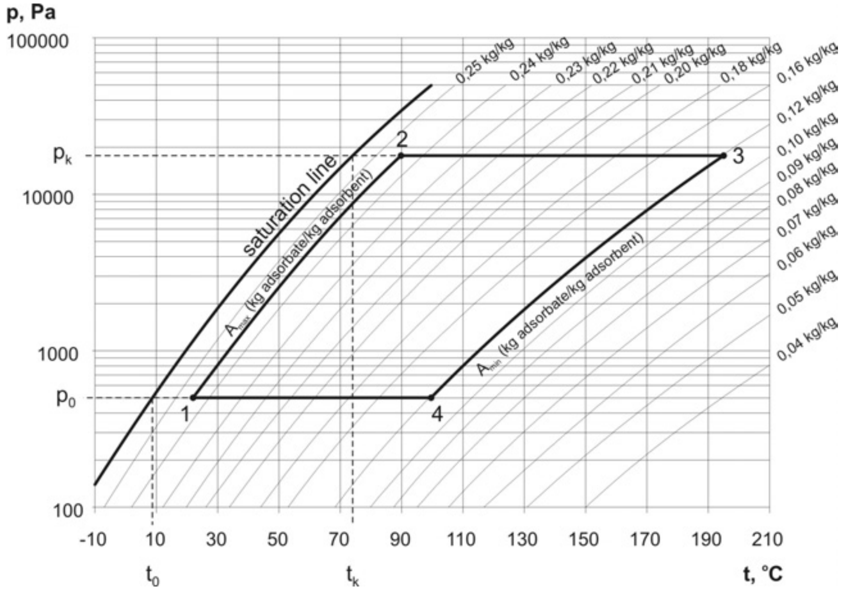

Fig. 2. Example thermodynamic adsorption cycle of zeolite 4A and water [8]

The time of effective heating almost doubles in two adsorber system, because during regeneration (desorption) phase in the first adsorber, the second one generates heat (adsorption). However, this system also has transient periods, when the working fluid does not flow through condenser nor evaporator and both adsorbers undergo isosteric transitions.

The continuity of operation can be attained with increased number of adsorbers – e.g. four or more [7]. However, this leads to complicated (thus less reliable) designs, increased cost and weight, larger space requirements. Therefore, the other possible solutions were introduced and researched, such as the system with recuperation [5] or the system with „thermal wave" (regeneration) [3, 5, 12].

2. Sorption heat pump with heat recuperation

The analysis of SSHP's working cycle shows that, at the end of each half-cycle, one adsorber is at higher temperature and pressure, while the other is at lower ones. In order to start the next half-cycle, thermodynamic conditions in both adsorbers have to be reversed. Pressure in the first adsorber has to be increased to the condensation pressure, while pressure in the second one has to be reduced to the evaporation pressure. During these processes, the working fluid does not flow to or from condenser and evaporator [3,12]. All the heat, introduced to or removed from the adsorbers, is used to change the conditions in the adsorbers. The efficiency can be increased if the heat of adsorption is recovered and used to desorbs the other adsorber (Fig. 1). This will decrease the required amount of high temperature heat, thus will increase overall efficiency of the system.

3. Sorption heat pump with heat regeneration („thermal wave")

Another way to increase COP is introduction of additional heat transfer fluid loop between two adsorbers [1,6,8].

Heat transfer fluid leaves cooler (heat exchanger I – low temperature heat source) at low temperature and enters adsorber I. As it passes through the adsorber I, the bed is gradually cooled and the fluid is heated. Thermal resistance of the bed and limiting heat transfer coefficient, between bed and fluid, cause the temperature gradient in the bed – „the thermal wave" [6]. Next, the heat transfer fluid leaves adsorber I, is heated in heat exchanger II (high temperature heat source) to the desorption temperature and enters adsorber II. As it passes through adsorber II, the fluid is cooled and the bed is gradually heated again, causing the thermal wave. Then, the fluid is directed to heat exchanger I completing first half of the cycle. During the other half, the direction of the flow is reversed. Adsorber II is cooled and adsorber I is heated.

The ability to regenerate the heats of adsorption and desorption processes reduces required energy input (via heat exchanger II in Fig. 3) and improves overall system efficiency. Highly efficient thermal wave require steep temperature gradient, which is possible only if the bed has high equivalent thermal conductivity. The overview of the thermal regeneration is presented in Fig. 4.

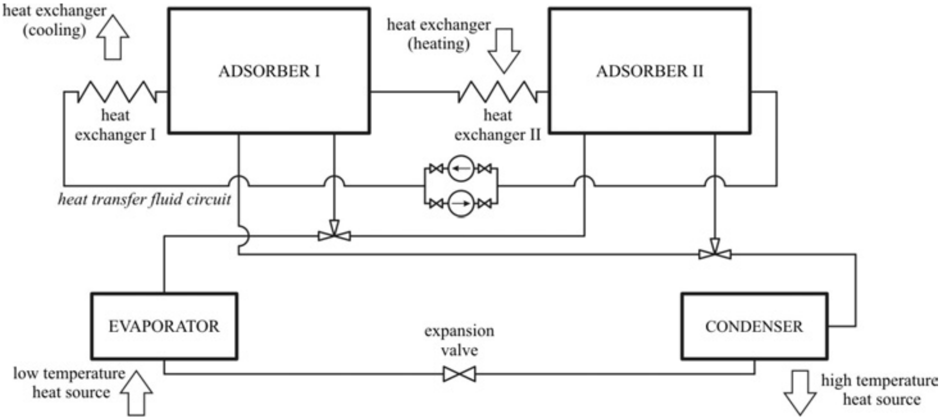

Fig. 3. Schematic representation of a sorption heat pump with heat regeneration

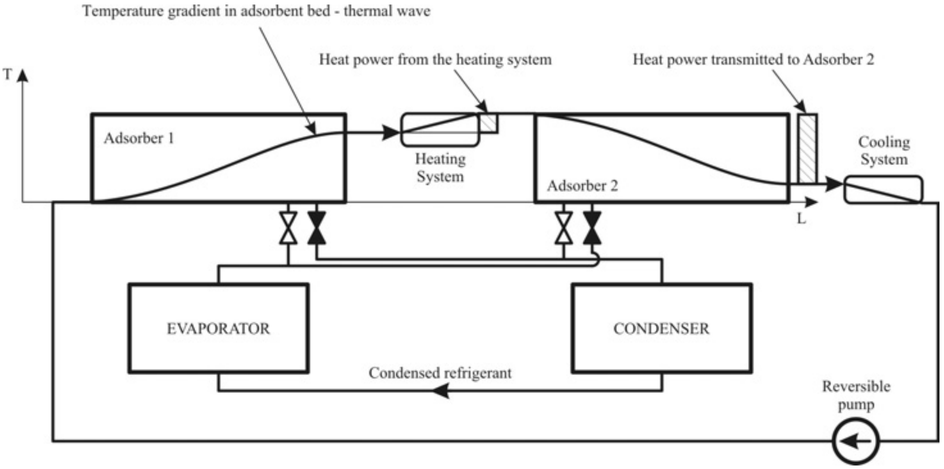

Fig. 4. Temperature gradients in a SSHP with thermal wave [6]

4. Working fluids and adsorbents

SSHPs allow use of working fluids and adsorbents characterized by high latent heat of vaporization and generally known as environmentally neutral [2,8,9] The choice of a working pair is determined by operational parameters of sorption cycle (temperatures and pressures) and physicochemical properties of components. The choice of working pair is also determined by the type of adsorption process – physical or chemical [2]. Physical adsorption occurs at the interface of two phases, where cohesive forces act between molecules (Van der Walls forces). Chemical adsorption is driven by valence forces and lead to chemical bonding between involved molecules [12].

Physical adsorption typically uses water, alcohols, hydrogen, ammonia and its derivatives [12] as a working fluid and active carbons, silica gels and zeolites as an adsorbent [5,8,9]. Adsorbents are characterized by the pore size and the thermal conductivity of a bed [2,8,9] and are capable of adsorption of large variety of substances. Example list of substances adsorbed by zeolites is presented in Table 1.

Table 1. Various compounds adsorbed by zeolites [8]

Type	**Adsorbates**
3A	Water
4A	As above plus CO_2, NH_3, CH_3OH, C_2H_4, C_2H_2
5A	As above plus hydrocarbons and alcohols (up to 20 carbon atoms in chain), ethylene oxide, ethylamine
10X	As above plus izoparafiny, proste połączenia naftenowe i węglowodory aromatyczne, związki organiczne azotu, siarki i tlenu
13X	As above plus complex naphthalene and aromatic hydrocarbons and their derivatives

Substances suitable for chemical adsorption have to meet the requirement of reversibility of reaction, which is a necessary condition for sorption system operating in cycles. There are several suitable working pairs [3,9,12]:

Water systems (hydroxide/oxide, salt hydrate/salt, salt hydrate/salt hydrate, etc.)

Ammonia systems (ammonia/salt, methylamine/salt, etc.)

Sulphur dioxide systems (sulphite/oxide, pyrosulphate/oxide)

Carbon dioxide systems (carbonate/oxide, barium oxide/barium carbonate)

Hydrogen systems (hydride/hydride, hydride/metal)

One of the other parameters determining the choice of working pair is the temperature of a heat source. Some compounds react or decompose in high temperature and create non-condensing gases which reduce efficiency [9], e.g at methanol decompose at temperatures above 120°C. Examples of temperature ranges for sorption systems are presented in Table 2.

Table 2. Parameters of different sorption cycles for refrigeration and heat pumping [8]

Sorption system	**Temperature range [T_o/T_c i T_a/T_d]**
Active carbon – methanol (ice production)	-6°C / 28°C 24,5°C / 87°C
Active carbon – methanol (ice production)	-5°C / 35°C 35°C / 110°C
Active carbon – methanol (heat pump)	5°C / 35°C 40°C / 80°C
Zeolite 4A – water (air conditioning)	0°C / 25°C 25°C / 110°C
Zeolite 4A – water (heat pump)	12°C / 42°C 60°C / 200°C

5. Efficiency of sorption systems

Sorption systems are typically analyzed with Claussius-Clapeyron diagram (ln p – -1/T) (Fig. 5) [2,4] in which solid-gas and liquid-vapor equilibrium lines are straight. The sorption cycle consists of four transitions: isosteric heating (A_1=idem, $T_1 \rightarrow T_2$), isobaric desorption (p_K=idem, $T_2 \rightarrow T_3$), isosteric cooling (A_2= idem, $T_3 \rightarrow T_4$) and isobaric adsorption (p_0= idem, $T_4 \rightarrow T_1$). $Q_{i,h}$ and $Q_{i,c}$ are consequently the heat of heating and the heat of cooling of adsorber [8,12].

Assuming reversibility of all the processes, coefficient of performance of the heat pump COP_{HP} can be calculated as [1,3,4]:

$$COP_{HP} = \frac{Q_a + Q_c}{Q_d}. \qquad (1)$$

Which is a ratio of the heats of adsorption Q_a and condensation Q_c to the heat submitted for regeneration/desorption Q_d.

Complete thermodynamic description of the sorption cycle involves heats of intermediate phases of the cycle. If there is no recuperation or regeneration, coefficients of performance COP and COP_{HP} are calculated as:

$$COP = \frac{Q_o + Q_d + Q_{ih}}{Q_d + Q_{ih}} \quad COP_{HP} = \frac{Q_c + Q_a + Q_{ic}}{Q_d + Q_{ih}}. \qquad (2)$$

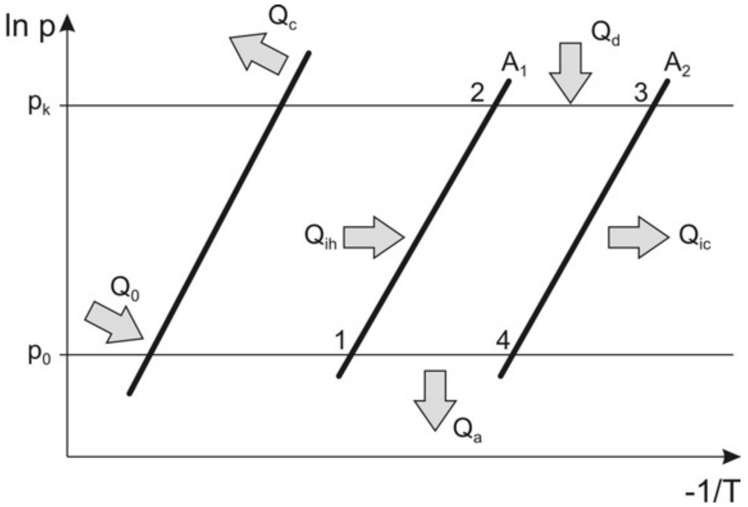

Fig. 5. Gas-solid and vapor-liquid equilibrium lines [12]

Where Q_{ih} is the heat submitted to the adsorber in order to increase its internal pressure from p_e to p_c, Q_{ic} is the amount of heat extracted from the adsorber in order to decrease its internal pressure from p_c to p_e.

Total heat of condensation Q_c is a sum:

$$Q_k = Q_v + Q_{cond} + Q_{ac} \, . \tag{3}$$

Where Q_v is the heat released during cooling of the adsorbate (from the temperature of desorption T_d to the temperature of condensation T_c), Q_{cond} is the heat of the phase change and Q_{ac} is the heat of after cooling.

Decrease of the temperature of gaseous adsorbate (from the temperature of desorption T_d to the temperature of condensation T_k) gives the amount of heat Q_v:

$$Q_v = r_m \cdot m_{ads} \cdot \int_{T_d}^{T_k} c_{p,g}\left(T\right) dT \, . \tag{4}$$

Heat of condensation Q_{cond} is calculated as:

$$Q_{cond} = r_m \cdot m_{ads} \cdot \Delta H_k\left(T_k\right) . \tag{5}$$

Where ΔH_k is calculated as a difference between enthalpy of saturated liquid $H_k(T_{k,sat-l})$ and enthalpy of saturated vapor $H_k(T_{k,sat-v})$ at the temperature of condensation T_k.

$$Q_{cond} = r_m \cdot m_{ads} \cdot \left[H_k \left(T_{k,sat-l} \right) - H_k \left(T_{k,sat-v} \right) \right]. \tag{6}$$

Heat of aftercooling Q_{ac}:

$$Q_{ac} = r_m \cdot m_{ads} \cdot \int_{T_k}^{T_t} c_{p,l} \left(T \right) dT. \tag{7}$$

Where $c_{pl}(T)$ is specific heat of adsorption (as a function of temperature). Since the temperature range of after cooling undercooling is small, specific heat can be assumed as constant.

Actual exothermic heat of adsorption Q_a is the heat of adsorption process Q_{ads} minus the heat transferred to adsorbate Q_{ca} and to metal components of the adsorber Q_r.

$$Q_a = Q_{ads} - Q_{ca} - Q_r. \tag{8}$$

Adsorption is much slower than evaporation. Therefore, certain amount of cold adsorbate (at the temperature of evaporation T_e) is being transferred to the adsorber. Therefore some of the generated heat is used for heating of vapor (up to temperature of adsorption). Assuming that the entire vapor has to be heated up, necessary amount of heat Q_{ca} is calculated from equation:

$$Q_{ca} = m_{ads} \cdot r_m \cdot \int_{T_o}^{T_{ads}} c_{p,g} \left(T \right) dT. \tag{9}$$

It is assumed that the temperature of adsorber 1 surface T_r is equal to the temperature of adsorption T_{ads} and the heat accumulation in metal components could be neglected ($Q_r = 0$).

The exothermic heat of adsorption is calculated as:

$$Q_{ads} = m_{ads} \cdot v_{am} \cdot \Delta H_{ads}. \tag{10}$$

Where ν_{am} is a coefficient ($\nu_{am} = 1$ for physical adsorption and it is equal to the stoichiometric coefficient of reaction for chemical adsorption), ΔH_{ads} is the enthalpy of adsorption (or reaction) [3,12].

Total heat of desorption Q_d is expressed as:

$$Q_d = Q_{des} + Q_{\Delta des}. \tag{11}$$

Where Q_{des} is he heat of chemical reaction taking place during adsorption is:

$$Q_{des} = m_{ads} \cdot \nu_{am} \cdot \Delta \mathrm{H}_R. \tag{12}$$

During the first stage of desorption, temperature of adsorber (active compounds and construction elements) is determined by the equation of state at the pressure pk [12]. Desorption occur at the temperature Td + ΔTdes, thus, an additional amount of heat is required to increase the temperature of the system above its equilibrium state. If we assume that specific heats of all involved elements are temperature dependent, required amount of heat QΔdes is calculated as:

$$Q_{\Delta des} = m_{ads} \cdot \int_{T_d}^{T_{des}} c_{p,ads,przereagowane}(T)\,dT + m_{ads} \cdot r_m \cdot \int_{T_d}^{T_{des}} c_{p,g}(T)\,dT + m_r \cdot \int_{T_d}^{T_{des}} c_{p,r}(T)\,dT \tag{13}$$

Where the integrals represent the heat required to increase the temperature of adsorbent, adsorbate and metal elements.

Intermediate phases of the SSHP working cycle are important to determine operating pressure of the phase (either adsorption or desorption). During isosteric heating the temperature of the adsorber is increased. The system aims to balance, thus the pressure in the adsorber increases from p_e to p_c). During isosteric cooling this process is reversed. Heat is removed from adsorber and its internal pressure decreases from p_c to p_e. Assuming that the heats are equal Q_{ic}=Q_{ih}=Q_i, required amount of heat can be obtained from equation:

$$Q_i = m_{ads} \cdot \int_{T_1}^{T_2} c_{p,ads}(T)\,dT + m_r \cdot \int_{T_1}^{T_2} c_{p,r}(T)\,dT. \tag{14}$$

In case of heating $Q_i = Q_{i,h}$, $T_1 = T_a$, $T_2 = T_d$, while in case of cooling $Q_i = Q_{i,c}$, $T_1 = T_d$, $T_2 = T_a$ (Fig. 6). It is assumed that starting temperature of isolated adsorber T_1 equals T_{ads} not T_a, because adsorption takes place at the temperature $T_{ads} = T_a - \Delta T_{ads}$. This influences the integrals in equation (14), and thus system's COP.

In chemisorption heat pump, the reaction between adsorbent and gaseous adsorbate will not take place in equilibrium conditions. The temperature difference has to be imposed [1]. If the temperature of the bed is higher than its equilibrium temperature in given pressure, the desorption will occur, otherwise the vapor is adsorbed [12].

Working pressure in chemisorption systems are typically couple orders of magnitude higher than in physical adsorption systems. According to Lu et al [3], for the pressures higher than 4 bar, the heat transfer coefficient of adsorbent becomes the main limiting factor, replacing the mass flow resistance of the porous structure.

The amount of heat, taken from the low temperature heat source $Q_{0,}$ is calculated as the difference between the heat of evaporation Q_{evap} and the heat introduced during throttling Q_{cv}:

$$Q_o = Q_{evap} - Q_{cv} \,. \tag{15}$$

Assuming that evaporated amount of adsorbate is enough to saturate all available adsorbent, total heat of evaporation is calculated as:

$$Q_{evap} = r_m \cdot m_{ads} \cdot \Delta H_o \,. \tag{16}$$

Enthalpy of evaporation ΔH_o is defined as a difference between enthalpy of the saturated vapor at temperature of evaporation $H_o(T_{o,sat\text{-}v})$ and the enthalpy of saturated liquid at temperature of evaporation $H_o(T_{o,sat\text{-}l})$. Therefore, equation (16) can be written as:

$$Q_{evap} = r_m \cdot m_{ads} \cdot \left[H_o\left(T_{o,sat-v}\right) - H_o\left(T_{o,sat-l}\right) \right]. \tag{17}$$

Assuming that saturated liquid is being throttled, total cooling effect Q_0 is decreased by the Q_{cv} which is the difference between enthalpy of saturated liquid at the temperature of condensation $H_k(T_{k,sat\text{-}l})$ and enthalpy of saturated liquid at the temperature of evaporation $H_o(T_{o,sat\text{-}l})$.

$$Q_{cv} = r_m \cdot m_{ads} \cdot \left[H_k\left(T_{k,sat-l}\right) - H_o\left(T_{o,sat-l}\right) \right]. \tag{18}$$

Introduction of the equations (16) and (17) into equation (15) leads to:

$$Q_o = r_m \cdot m_{ads} \cdot \left[H_o\left(T_{o,sat-v}\right) - H_k\left(T_{k,sat-l}\right) \right]. \tag{19}$$

6. Performance of sorption system for continuous operation

The equations presented above become base for a computational algorithm [12], that was used for analysis of the performance of different sorption systems. The algorithm allowed selection of the working pair for several SSHPs [8,10,12].

Experimental setup has been build and several working pairs were chosen for analysis of physical sorption: zeolite 4A – water, silica gel – water, active carbon – methanol [8]. Temperature of desorption has been defined within the range t_{des}= 120 – 200°C. It was assumed that the adsorber is powered by the waste heat and then cooled by the airflow. Temperature of adsorption was defined between t_{ads}= 85 – 105°C, temperature of evaporation t_0= 5°C, and condensation t_k= 35°C. Condenser is cooled by the airflow. Latent heat of desorption is 3611 kJ/kg. Specific heat of zeolite is 0.31 kJ/kgK.

The results of mathematical modeling and experiments [8] for selected working pairs in a system with two adsorbers (working out of phase) are presented in Fig. 6. Registered differences between mathematical and experimental values (up to 18%) are the result of non-uniform heating of the bed. Lumped parameter model do not consider temperature gradients inside adsorbers. For comparison the theoretical analysis of other SSHPs are presented in Fig. 7.

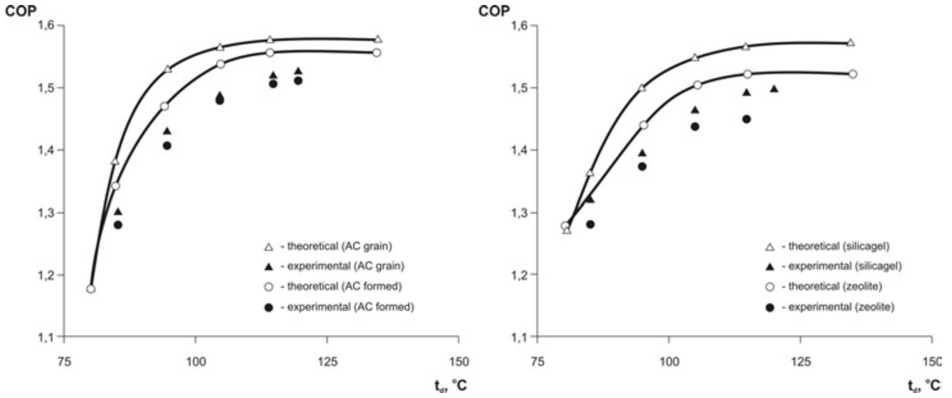

Fig. 6. The influence of temperature of desorption on SSHP's performance: a) active carbon – methanol, b) zeolite 4A – water, silica gel – water

7. Summary

The efficiency of sorption system highly depends of proper selection of the working pair, the amount and design of adsorbers, porosity and thickness of adsorber bed and the method of heat management within the system. Presented thermodynamic analysis is a useful tool, allowing estimation of the efficiency and comparison of different sorption systems.

When compared to other solutions, SSHP is still not economically feasible. The performance of the system has to be at least 1 and it has to utilize waste heat sources. Otherwise vapor compression system will remain cheaper, more reliable solution. The main advantages of the sorption system are ability to directly utilize heat sources available on the spot, especially when there is no electric power available. Sorption systems are also more ecological and present very small imprint on the environment.

REFERENCES

[1]. GOETZ,V.,ELIE,F.,SPINNER,B., Structure and performance of single effect solid-gas chemical heat pumps. Heat Recovery Systems& CHP, 1993,13(1), 79-96

[2]. KRÓLICKI Z., WILK T., ZAJĄCZKOWSKI B., KACZMARCZYK J., Research on adsorption characteristics of active carbon and silica gel and application in solar refrigeration and heat pump, 61st ATI National Congress – International Session "Solar Heating and Cooling", Perugia, Włochy, 14-18 września 2006, 129

[3]. LU, H-B, MAZET, N.,Modeling of gas-solid reaction-coupling of heat and mass transfer with chemical reaction, Chemical Engineering Science,1996,519(15),3829-3845

[4]. MUENIER F.: Solid sorption: an alternative to CFC, Heat Recovery Systems & CHP, 13, 1993, 289

[5]. NEVEU P., CASTAING J., Solid-gas chemical heat pumps: field of application and performance of the internal heat of reaction recovery process, Heat Recovery Systems & CHP, 1993, 13(3), 233

[6]. PONS,M.,FENG.Y., Characteristic parameters of adsorptive refrigeration cycles with thermal regeneration, Applied Thermal Engineering 1997 ,17(3), 289-298

[7]. TENG Y., WANG R.Z., WU J.Y., Study of the fundamentals of adsorption systems. Applied Thermal Engineering 17, 1997, 327-334

[8]. WILK T.: Wpływ własności par roboczych zespołu adsorpcyjnego na efektywność słonecznej wytwornicy lodu, Praca Doktorska, ITCIMP Politechnika Wrocławska, Raport serii PRE nr 27/ 2006

[9]. WONGSUWAN W., KUMAR S., NEVEU P., MUENIER F.: A review of chemical heat pump technology and applications, Applied Thermal Engineering 21, 2001, 1489

[10]. ZAJĄCZKOWSKI B., KRÓLICKI Z., BIAŁKO B., Modelling of solid sorption chemical heat pumps and refrigeration systems, Inżynieria Chemiczna i Procesowa, 27, 2006, 1035

[11]. ZAJACZKOWSKI B.,KRÓLICKI Z., JEŻOWSKI A.:New type of sorption composite for chemical heat pump and refrigeration systems, Applied Thermal Engineering 30(2010) p.1455-1460

[12]. ZAJĄCZKOWSKI B.: Przenoszenie ciepła i masy w reaktorze sorpcyjnej chemicznej pompy ciepła, Praca Doktorska, ITCIMP Politechnika Wrocławska, Raport serii PRE 12/ 2008

Guidelines for authors

The language of the journal is English. Manuscripts should not extent 20 printed pages in length and should submitted by e-mail in the form a DOC file, or by post in two hard- copies. Upon receipt, the paper is sent to reviewers. The opinion constitutes a basis for the decisions of the Editorial Committee to publish the paper.

1. Paper considered for publication in Journal of Energy Science should not have been previously published elsewhere. They should deal with original research and may contain either theoretical or experimental results.

2. Manuscripts must be written according to the example from the website.

www.energyscience.pwr.wroc.pl

3. The title of the paper should be as short as possible.
4. Paper should be divided into sections appearing in the following order:
   - title, authors names and affiliations and complete address for the corresponding author including telephone and fax numbers as well as an e-mail address;
   - abstract (not exceending150 words), indicating the scope of the of the research and principal findings;
   - keywords (3-5 words);
   - introduction;
   - material and methods;
   - results;
   - discussion;
   - conclusions
5. References should be listed according to the example below.
6. One proof will be sent to the first-name author or to the name direction author. The editor reserves the right to make a charge for alterations in proof other than correction of printer's errors.
7. The electronic source files of the manuscript can be sent by e-mail or alternatively mailed on a CD or DVD diskette. The preferable format for the text is MS Word, but TeX or LaTeX is also acceptable. Separate files for figures should be provided in one of the following formats: BMP, TIF, JPEG, PDF, EPS or PostScript (color or black-white or gray).

Edited - Printed and Copyright by
Wrocław University of Technology
Department of Periodics Publications
Wybrzeże Wyspiańskiego 27, 50-370 Wrocław
Tel./fax 4871 320 4130, e-mail: energyscience@pwr.wroc.pl